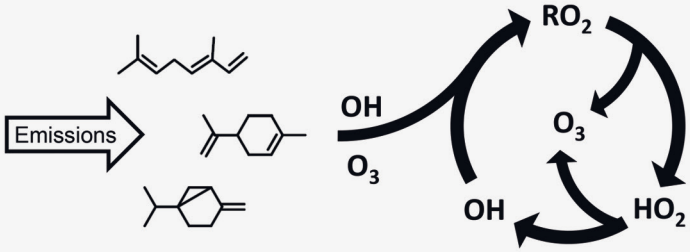

The Chemical Budget of Radicals and Reaction Mechanisms of the Atmospheric Oxidation of Monoterpenes Investigated in the Atmospheric Simulation Chamber SAPHIR

Yat Sing Pang

Energie & Umwelt / Energy & Environment
Band / Volume 623
ISBN 978-3-95806-742-4

Mitglied der Helmholtz-Gemeinschaft

JÜLICH
Forschungszentrum

Schriften des Forschungszentrums Jülich
Reihe Energie & Umwelt / Energy & Environment Band / Volume 623

Forschungszentrum Jülich GmbH
Institut für Energie- und Klimaforschung (IEK)
Troposphäre (IEK-8)

The Chemical Budget of Radicals and Reaction Mechanisms of the Atmospheric Oxidation of Monoterpenes Investigated in the Atmospheric Simulation Chamber SAPHIR

Yat Sing Pang

Schriften des Forschungszentrums Jülich
Reihe Energie & Umwelt / Energy & Environment Band / Volume 623

ISSN 1866-1793 ISBN 978-3-95806-742-4

Bibliografische Information der Deutschen Nationalbibliothek.
Die Deutsche Nationalbibliothek verzeichnet diese Publikation in der
Deutschen Nationalbibliografie; detaillierte Bibliografische Daten
sind im Internet über http://dnb.d-nb.de abrufbar.

Herausgeber und Vertrieb:	Forschungszentrum Jülich GmbH Zentralbibliothek, Verlag 52425 Jülich Tel.: +49 2461 61-5368 Fax: +49 2461 61-6103 zb-publikation@fz-juelich.de www.fz-juelich.de/zb
Umschlaggestaltung:	Grafische Medien, Forschungszentrum Jülich GmbH
Titelbilder:	Wald: pixabay.com – Bergadder SAPHIR-Kammer: Forschungszentrum Jülich – Sascha Kreklau Pflanzenkammer: Forschungszentrum Jülich – Yat Sing Pang
Druck:	Grafische Medien, Forschungszentrum Jülich GmbH
Copyright:	Forschungszentrum Jülich 2024

Schriften des Forschungszentrums Jülich
Reihe Energie & Umwelt / Energy & Environment, Band / Volume 623

D 468 (Diss. Wuppertal, Univ., 2023)

ISSN 1866-1793
ISBN 978-3-95806-742-4

Vollständig frei verfügbar über das Publikationsportal des Forschungszentrums Jülich (JuSER)
unter www.fz-juelich.de/zb/openaccess.

Abstract

Volatile organic compounds (VOCs) play an important role in the atmosphere. VOCs are mostly emitted from the land surface and are oxidized by oxidants such as hydroxyl radicals (OH) and ozone (O_3) upon their emissions into the atmosphere. The oxidation of VOCs has wide-ranging impacts for example on local-scale air quality and climate. The chemistry of the oxidation of VOCs depends on environmental conditions such as temperature and concentrations of pollutants like nitric oxide (NO). The NO concentration affects the chemistry of organic peroxy (RO_2) radicals produced from the oxidation of VOCs by competing with other reaction pathways of RO_2 radicals such as unimolecular reactions and the reaction with hydroperoxyl radicals (HO_2) and other RO_2 radicals.

This thesis aims to investigate the oxidation of monoterpenes including limonene and sabinene by OH radicals and ozone at different NO concentrations. Experiments were conducted in the outdoor atmospheric simulation chamber SAPHIR (Simulation of Atmospheric PHotochemistry In a large Reaction chamber). A large set of analytical instruments was used in the experiments, including the measurements of OH, HO_2, and RO_2 radicals, VOC species, and OH reactivity. The analysis of experiments focus on these measurements in this study.

In oxidation experiments for both limonene and sabinene, product yields of VOC species such as formaldehyde (HCHO) and acetone were determined at different NO concentrations. The results were compared to other laboratory studies and yield values expected from the proposed oxidation mechanism. The chemical budget of OH radicals was calculated for different experiments, which reveals if there could be a missing OH source from for example the unimolecular reaction of RO_2 radicals during the oxidation of monoterpenes.

Results from the limonene oxidation experiments were compared to model simulations using a semi-explicit model Master Chemical Model version 3.3.1 (MCM). Model simulations using the standard MCM mechanism suggested the model could not reproduce OH, HO_2, and RO_2 radicals, and the OH reactivity. The discrepancy between model simulations and measurements of HO_2 and RO_2 radicals increases when NO concentrations decrease. To improve the model-measurement agreement, additional reaction pathways converting RO_2 to HO_2 radicals with a reaction rate constant of $(1 – 5) \times 10^{-2}$ s^{-1} are required. The additional RO_2 loss might be explained by fast unimolecular reactions for RO_2 radicals derived from limonene oxidation, followed by the increased loss rate from the reaction with other RO_2 radicals.

For the sabinene oxidation experiment, the Arrhenius equation of the OH-oxidation reaction was determined for the first time with an absolute rate method by OH reactivity measurements. The setup allowed for the measurement of the reaction rate constant of the photooxidation of VOCs at a temperature range of 10 °C to 70 °C. The reaction rate constant at 298 K calculated from the Arrhenius equation determined in this experiment agrees with value found in the only other available laboratory study.

In addition to conducting oxidation experiments with single monoterpene species, four oxidation experiments involving VOC emissions from sweet chestnut (*Castanea sativa*) trees, a strong monoterpene-emitting species, were conducted using the SAPHIR-PLUS plant chamber, from which emitted VOCs were transferred to and oxidized in the SAPHIR chamber. The analysis of sweet chestnut emissions suggests that β-ocimene was the main emission by OH reactivity, consistent with previous measurements of emission from sweet chestnut trees of similar age in another study. The OH reactivity calculated from measured VOC concentrations showed a good agreement within measurement uncertainties when compared to the OH reactivity measurements before the oxidation phase of the experiment. However, the OH reactivity calculated from VOC concentrations was lower than the measured values during the oxidation of the plant emission especially in the ozonolysis experiment, which could be explained by unmeasured ozonolysis products of β-ocimene. The chemical budget of OH radicals was calculated for the oxidation of β-ocimene. This suggests that there could be a small missing OH source.

The results presented in this thesis contribute to the understanding of radical chemistry during the oxidation of different monoterpene species, which can help the development of oxidation mechanisms for monoterpenes needed for air quality and climate models.

Acknowledgements

There are many people who supported me throughout my doctoral degree. Therefore, I would like to express my gratitude to them.

First and foremost, I would like to thank Prof. Dr. Andreas Wahner and Prof. Dr. Astrid Kiendler-Scharr for the opportunity to work at the Institute of Energy and Climate Research: Troposphere (IEK-8) in Forschungszentrum Jülich. Astrid Kiendler-Scharr, who is regrettably no longer with us, her dedication to the institute and her enduring support to young scientists will be forever missed.

I would like to express my heartfelt gratitude to my scientific supervisor Prof. Dr. Hendrik Fuchs for the invaluable support and encouragement throughout the process of the PhD. The thesis would not be possible without his guidance and the opportunity working in Forschungszentrum Jülich.

I would also like to thank Prof. Dr. Peter Wiesen for accepting the supervision of this thesis as Doktorvater at the Bergische Universität Wuppertal. Furthermore, I would like to thank my committee members for reviewing this thesis.

I want to thank Dr. Philip Carlsson and Dr. Anna Novelli for the co-supervision of the monoterpene oxidation projects. The inspiring discussion on the monoterpene oxidation mechanism and OH radical measurements helped me to complete the manuscripts and this thesis.

I gratefully appreciate the support from Dr. Frank Holland, PD Dr. Andreas Hofzumahaus, Michelle Färber, Florian Berg, and all members of the LIF groups who contributed significantly to the completion of this thesis.

I want to acknowledge the support of the whole SAPHIR team during the experiments, and also for Dr. Birger Bohn for his valuable comments when writing the manuscripts.

I want to thank Dr. Luc Vereecken for the discussion on the limonene oxidation mechanism and unimolecular reaction chemistry, as well as the opportunity to be involved in the development of Chekimomi.

Many thanks to the VOCs group, Sergej Wedel for the support on the GC instrument and René Dubus for the measurements during the sabinene experiments and plant emission experiments.

Many thanks to the aerosol group, Dr. Thorsten Hohaus and Stefanie Andres for all the work that involved the SAPHIR-PLUS chamber during the plant emission experiments.

Lastly, I want to show my deepest gratitude to my friends Kathy Lam, Hauyi Li and her cat Tokki for their support and motivation, which made this work possible.

Contents

1. Introduction

The troposphere is the lowest layer of the atmosphere which spans from the surface of the Earth to 8 – 16 km above sea level. Chemical and physical processes that occur in the troposphere greatly impact the biosphere and humans. On the other hand, activities of the biosphere and humans largely determine the chemical composition of the atmosphere. The impact on the troposphere is large due to the proximity to the land and sea surface, where most of the activities take place.

The atmosphere composes mainly of nitrogen (78.1%), oxygen (21.0%), argon (0.9%) and a highly variable water vapor with mixing ratios of up to 4%. It also includes trace gases that can have mixing ratios from the parts per million (ppm) range down to below parts per trillion (ppt). The impact of trace gases on the atmosphere and the biosphere is huge, albeit their low concentrations. For example, global warming is largely attributed to the increase in carbon dioxide concentrations from 280 to 420 ppmv since industrialization (IPCC, 2022), and emissions of nitrogen oxides from anthropogenic activities lead to the formation of secondary air pollutants that are detrimental to human and ecosystem health. The emission and formation of aerosols from the reaction of trace gas species can affect the radiative budget of the Earth, as well as the precipitation pattern on a local or regional scale.

The composition of trace gases in the troposphere is influenced by their local production and destruction processes and transportation. The shorter the lifetime of the species in the atmosphere, the more important is the local production and destruction for the abundance of that species. Local production of trace gases includes emissions from the land and sea surface and productions from chemical reactions.

One example of the production of trace gases is the emission of biogenic volatile organic compounds (BVOCs) by plants. BVOCs emitted by plants are reactive compounds that have typical lifetimes ranging from hours to days in the atmosphere (Section 1.2.3). The chemical transformation of BVOCs in the atmosphere produces secondary pollutants such as ozone (O_3) and formaldehyde (HCHO). Due to the short lifetime of BVOCs, their chemical transformation is largely controlled by local reaction conditions such as temperature and the abundance of pollutants like nitrogen oxides ($NO_x = NO_2 + NO$). Air quality questions are for example also of high interest in urban environments and indoors, where chemical conditions can be much different from natural environments.

Despite their localized influence on air quality and compositions, reactions of BVOCs are still collectively affecting air quality and composition on a global scale as plants are ubiquitous. The chemistry of these plant-emitted VOCs can be different at different locations with different chemical and physical conditions. Therefore, it is essential to investigate the oxidation of BVOCs at different conditions for accurate predictions of air quality.

This thesis aims to investigate the impact of plant emissions on air quality, precisely the oxidation mechanisms of monoterpenes (limonene and sabinene) by hydroxyl radicals (OH) and O_3 in the atmosphere are investigated at different NO concentrations, representing different pollution scenarios. Chamber oxidation experiments were performed under atmospheric-relevant conditions and with state-of-the-art measurement techniques. Results are compared to recently published chemical mechanisms. This work specifically focuses on radical species which are the key intermediates of atmospheric oxidation

processes. The better understanding of the oxidation mechanisms of monoterpenes will help to improve the atmospheric chemical mechanisms that are used in air quality forecast and chemical transport models.

In addition, the oxidation of biogenic emissions emitted directly from sweet chestnut trees (*Castanea sativa*) by OH radicals and O_3 were studied, as emission directly from plants can more realistically represent the chemical composition of ambient air than using a single monoterpene species for the study. Sweet chestnut is a strong monoterpene emitter which is commonly found in Europe. To measure the potential VOC emissions especially different monoterpene species from sweet chestnut, VOCs were measured by instruments including an offline gas chromatography (GC), an online GC, and an online proton-transfer-reaction time-of-flight mass spectrometer (PTR-TOF-MS). In the part of the PhD work, the online GC instrument was calibrated and its measurements were compared to the online PTR-TOF-MS. The VOC composition of plant emissions and oxidation products were compared to the total OH reactivity measurements, which can be used to identify potential missing OH reactants that are emitted.

1.1 Biogenic volatile organic compounds (BVOCs) in the atmosphere

Volatile organic compounds (VOCs) play an important role in the chemistry in the troposphere. They are mostly emitted from the land surface, from both anthropogenic sources and natural sources. Biogenic volatile organic compounds (BVOCs) are the most abundant VOCs. It is estimated that about 760 Tg of BVOCs is annually emitted into the atmosphere (Sindelarova et al., 2014). The main source of BVOCs is from terrestrial vegetation (Guenther et al., 2012). Limonene and sabinene, which are the BVOCs investigated in this study, are emitted by pine trees (Bai et al., 2017), beech trees (Tollsten and Müller, 1996; Van Meeningen et al., 2016), oak trees (Staudt and Bertin, 1998), and other trees.

The primary purpose of the BVOCs emission by vegetation is to relieve environmental stress (Holopainen and Gershenzon, 2010). For example, BVOCs can relieve oxidative stress on plant tissues by reacting with atmospheric oxidants (e.g., Loreto et al., 2001; Vickers et al., 2009), relieve biotic stress by deterring insect herbivores and attracting predators of insect herbivores (e.g., Kessler and Baldwin, 2001; Kappers et al., 2005), and relieve heat stress from direct sunlight exposure (Sharkey et al., 2007) .

Small amounts of BVOCs are also emitted from soil (Kramshøj et al., 2018) and marine ecosystems (Exton et al., 2015). Apart from natural sources, BVOC species are also emitted from anthropogenic source. For example limonene is extensively used in volatile chemical products (VCPs) such as fragrances and cleaning products (Liu et al., 2004; Nazaroff and Weschler, 2004; McDonald et al., 2018; Gkatzelis et al., 2021a, b). Measurement campaigns conducted in New York City showed that limonene is the most abundant monoterpene species in winter, suggesting that VCPs can impact urban chemistry (Coggon et al., 2021). The emission rate of limonene from the usage of VCPs can locally exceed the emission from biogenic sources by two orders of magnitude (Rosales et al., 2022). Therefore, BVOC species can still greatly impact the air quality even in urban environments and indoors, where VCPs are largely used.

Emissions of non-methane anthropogenic VOCs (AVOCs) emission are less than that of BVOCs with emission rates about 100 Tg per year (Duan et al., 2023). The main source of AVOCs is biomass burning and the use of fossil fuels for energy production (Piccot et al., 1992).

Among all BVOCs, the most abundant species is isoprene, which contributes about 70% to the total BVOC emissions by mass, followed by small (< C_5) oxygenated VOCs such as methanol (12%), and monoterpenes (11%) (Sindelarova et al. (2014), Table 1). The highest isoprene and monoterpene emissions are found in tropical forests which have a dense vegetation. In temperate and boreal forests, the relative emissions of monoterpenes to isoprene is higher compared to that in the tropics, as the dominant vegetation in higher latitudes are strong monoterpene emitters. The emission rate of BVOCs is mainly controlled by meteorological variables such as temperature and radiation (Guenther et al., 1991), as well as by environmental stresses such as drought (Saunier et al., 2017) and insect infection (Faiola and Taipale, 2020).

When BVOCs are emitted into the atmosphere, they quickly react with atmospheric oxidants including OH radicals, O_3, and nitrate radicals (NO_3) (Section 1.2.1). During daytime, OH radicals are the most important atmospheric oxidants, whereas during nighttime O_3 and NO_3 are more important. The oxidation of BVOCs can produce secondary pollutants such as O_3 and oxygenated organic compounds like formaldehyde (HCHO), which are harmful to the respiratory system (Kim et al., 2011). Oxidation of large BVOCs such as monoterpenes followed by a repeating oxidation of the derived RO_2 radicals can rapidly produce highly oxidized molecules that can potentially form aerosols (Bianchi et al., 2019). Aerosols can grow in size through condensation and eventually are removed from the atmosphere by dry deposition (e,g, Farmer et al., 2021) and wet deposition (e.g., Knote et al., 2015) through precipitation. For small BVOCs (< C_5), stepwise oxidation often eventually forms carbon dioxide that has a very long lifetime in the atmosphere (Inman, 2008). The lifetime of BVOCs in the atmosphere differs among the BVOCs species and depends on the concentrations of atmospheric oxidants. It varies from minutes to days (Steiner and Goldstein, 2007; Section 1.2.3). Small oxygenated BVOCs are in general less reactive due to the lack of reactive functional groups. On the other hand, isoprene, monoterpenes, and sesquiterpenes are highly reactive due to the presence of reactive C=C double bonds.

Table 1-1. Global annual emission of selected VOCs averaged over the period of year 1980 – 2010 determined from model estimates by Sindelarova et al. (2014). Values for trans-β-ocimene, limonene, and sabinene are from Guenther et al. 2012, where are the estimated emissions in the year 2000 are reported.

VOCs	Emission (Tg $year^{-1}$)
Isoprene	594
α-Pinene	32
β-Pinene	17
Trans-β-ocimene	19
Limonene	11
Sabinene	9
Sesquiterpenes	20
Methanol	130
Acetone	37
Ethene and propene	33

1.2 VOCs oxidation chemistry in the troposphere

The atmospheric oxidation of VOCs involve radical reactions, which include the oxidation by OH radicals and NO_3 radicals (Atkinson et al., 1988). O_3 is a non-radical species that can oxidize VOCs, but the ozonolysis mechanism also involves radical chemistry. Oxidation of VOCs includes initialization, propagation, and termination of radical reactions. Figure 1-1 summarizes the important radical initialization, propagation, and termination reactions in the atmospheric oxidation of VOCs. Detailed descriptions of these reactions are included in Section 1.2.1, 1.2.2 and 1.2.4.

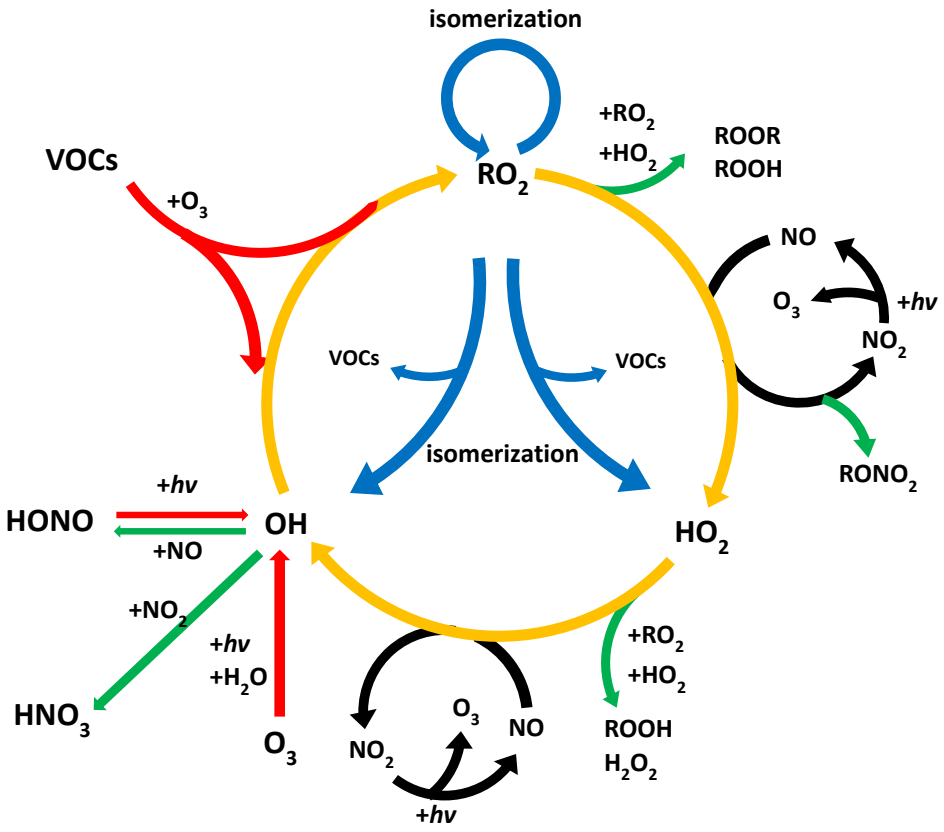

Figure 1-1. The main initiation (red arrows, Section 1.2.1), destruction (green arrows, Section 1.2.2), and propagation (orange arrows, Section 1.2.2) reactions of radicals in the oxidation of VOCs in the troposphere. The blue arrows indicate isomerization reactions of peroxy radicals (Section 1.2.4).

1.2.1 Initiation of the oxidation of VOCs

The atmospheric oxidation of VOCs is most often initiated by the reaction with a radical reaction partner (e.g., OH, NO_3 radicals), or sometimes by the reaction without a radical reaction partner if the VOC contains certain functional groups. For example, VOCs having a C=C double bond can be oxidized by O_3 (e.g., Yu et al., 1999), while some oxygenated VOCs can be photolyzed in the troposphere, where radiation with wavelengths longer than 290 nm is available (e.g., Calvert et al., 1972). The wavelength of 290 nm is the lower limit for radiation that can reach the lower troposphere without significant absorption for example by stratospheric O_3.

The oxidation of VOCs by a radical partner starts with an H-abstraction reaction or addition reaction on the C=C double bond. Using the OH-oxidation of limonene as an example (Fig. 1-2), the H-abstraction results in an alkyl radical whereas the addition reaction to the C=C double bond produces a hydroxyl alkyl radical. Addition of a NO_3 radical to a C=C double bond results in the production of a nitro alkyl radical. In general, the OH addition on the C=C double bond is preferred to H-abstraction, with the reaction rate constants of OH-additions are being order of magnitude faster than of H-abstractions (Vereecken and Peeters, 2001; Peeters et al., 2007). Alkyl radicals usually immediately react with an oxygen molecule under typical atmospheric conditions, which results in an organic peroxy radical (Fig. 1-2).

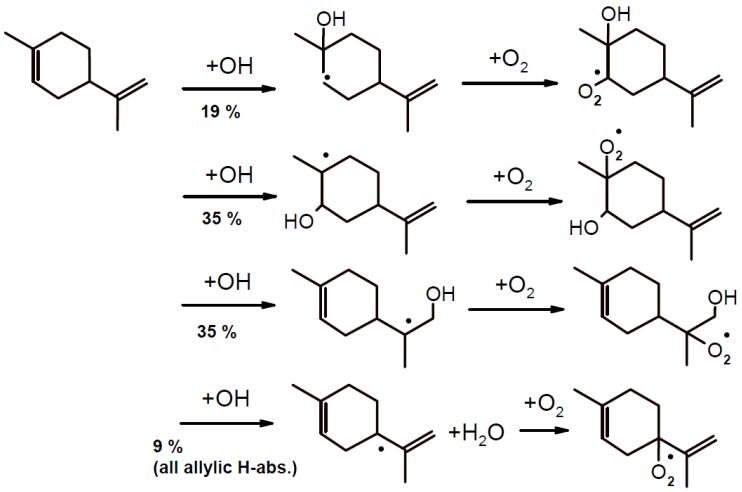

Figure 1-2. Example of the initiation of the oxidation of limonene by OH radicals forming organic peroxy radicals. The branching ratios of the OH-oxidation pathways of limonene are calculated from reaction rate constants of the OH-addition reactions (Peeters et al., 2007) and rate constants of H-abstraction reactions (Vereecken and Peeters, 2001).

O_3 is typically less reactive than OH and NO_3 radicals and it only reacts with VOCs with C=C double bonds. The reaction between ozone and VOCs in the atmosphere follows the Criegee mechanism (Fig. 1-3, Criegee, 1975). The addition of O_3 to the C=C double bond forms a primary ozonide (POZ) that quickly decomposes into a carbonyl product and a Criegee intermediate (CI*). Some of the Criegee intermediates quickly isomerize and a fraction of them is stabilized through collisions with air molecules resulting in a stabilized Criegee intermediate (sCI). The stabilized Criegee intermediate can react with other trace gases (e.g., H_2O, NO, CO, SO_2) in the atmosphere or can undergo isomerization reactions. The isomerization reactions of Criegee intermediates, before or after their stabilization, follow either the dioxirane pathway or the vinyl hydroperoxide (VHP) pathway. In the dioxirane pathway, the terminal oxygen of the carbonyl oxide bonds with the carbonyl carbon and forms a dioxirane, which can quickly isomerize into esters and acid. In the VHP pathway, the terminal oxygen abstracts an H-atom of the β-carbon of the carbonyl oxide (i.e., 1-4 H-shift), yielding a vinyl hydroperoxide. The vinyl hydroperoxide dissociates into an OH radical together with a β-oxoalkyl radical that eventually forms a peroxy radical in the reaction with oxygen (Fig. 1-3). The ozonolysis of VOCs is one significant source for OH radicals in the atmosphere. It is especially important at night, when there are no photolytic sources of OH (Paulson and Orlando, 1996).

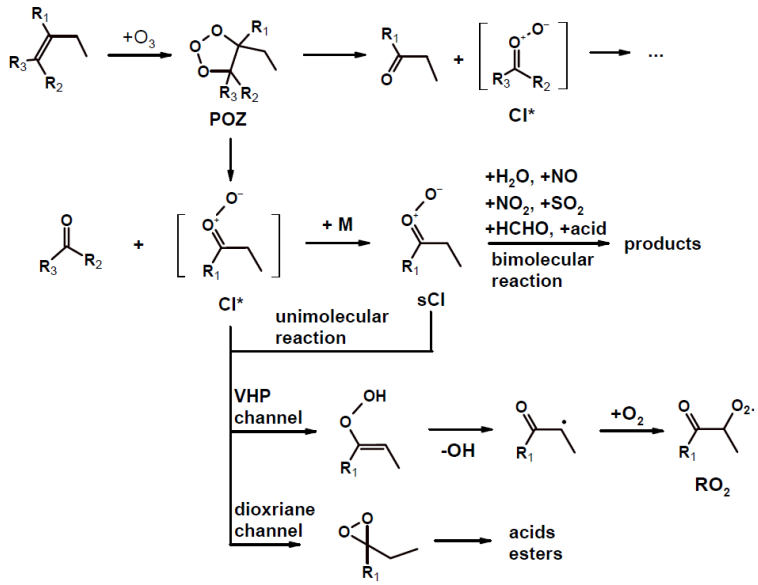

Figure 1-3. An example of the initiation of the oxidation of alkene by O_3. Stereoisomers of primary ozonide POZ, and the geometric isomers of the Criegee intermediates are not included in this simplified scheme. However, it should be noted that the chemistry of the geometric isomers of Criegee intermediates is largely affected by the position of the terminal oxygen in the carbonyl oxide functional group.

The photolysis of VOCs in the troposphere is less important than the oxidation of VOCs by radicals or O_3, as emitted BVOCs are mainly hydrocarbons (i.e., isoprene) that cannot be photolyzed by radiations with wavelengths longer than 290 nm. Photolysis by radiation available in the troposphere occurs mainly for oxygenated VOCs such as carbonyls, hydroperoxides, and nitrates (Atkinson et al., 2006). These photolysis reactions can act as sources for radicals that further oxidize of VOCs. For example, formaldehyde (HCHO) produces two HO_2 radicals in one of its photolysis pathways:

$$HCHO + h\nu \longrightarrow H + HCO \quad (\lambda < 340\ nm) \qquad \text{Reaction 1-1}$$

$$HCO + O_2 \longrightarrow HO_2 + CO \qquad \text{Reaction 1-2}$$

$$H + O_2 + M \longrightarrow HO_2 + M \qquad \text{Reaction 1-3}$$

$$HCHO + h\nu \longrightarrow H_2 + CO \quad (\lambda < 360\ nm) \qquad \text{Reaction 1-4}$$

Apart from the photolysis of VOCs, photolysis reactions of inorganic compounds are the main source of OH radicals. The most important OH radical production pathway is the photolysis of O_3 by radiation at wavelengths lower than 340 nm, forming $O(^1D)$:

$$O_3 + h\nu \longrightarrow O(^1D) + O_2 \quad (\lambda < 340\ nm) \qquad \text{Reaction 1-5}$$

$O(^1D)$ can either transit to the ground state $O(^3P)$ by molecular collisions (*M*, usually oxygen and nitrogen molecules) or can react with water vapor to produce OH radicals:

$$O(^1D) + H_2O \longrightarrow 2\ OH \qquad \text{Reaction 1-6}$$

$$O(^1D) + M \longrightarrow O(^3P) \qquad \text{Reaction 1-7}$$

Another source of OH radicals is the photolysis of nitrous acid (HONO). HONO is emitted from anthropogenic and natural sources (Oswald et al., 2013; Xue et al., 2021). In the atmosphere, HONO is produced from the gas-phase reaction of OH radical and NO, as well as from the heterogeneous NO_2 hydrolysis reaction on aerosol particles (Lu et al., 2018). The photolysis of HONO can locally contribute up to 20 % – 80 % of the total OH production rate during daytime in urban areas with high emissions of nitrogen oxides (Alicke, 2002; Hendrick et al., 2014; Kim et al., 2014).

$$HONO + h\nu \longrightarrow NO + OH \quad (\lambda < 400\ nm) \qquad \text{Reaction 1-8}$$

The other atmospheric oxidant O_3 is produced from the photolysis of nitrogen dioxides (NO_2) by solar radiation at $\lambda < 400$ nm. The photolysis of NO_2 produces a nitrogen oxide (NO) and an $O(^3P)$ atom. The $O(^3P)$ atom is then quickly captured by an oxygen molecule to form O_3, so that concentrations are in a chemical equilibrium.

$$NO_2 + h\nu \longrightarrow NO + O(^3P) \quad (\lambda < 400\ nm) \qquad \text{Reaction 1-9}$$

$$O(^3P) + O_2 \longrightarrow O_3 \qquad \text{Reaction 1-10}$$

NO_2 is produced from the reaction in NO with O_3 or peroxy radicals (Section 1.2.2), or directly from the emission of NO_2 in polluted areas.

1.2.2 Propagation and termination reactions of atmospheric radicals

Peroxy radicals produced from the oxidation or photolysis of VOCs react with trace gases and other radicals in the atmosphere. The reaction can follow different pathways depending on the environmental conditions. The main reaction partners of peroxy radicals include NO, HO_2, and other organic peroxy radicals.

The main radical propagation reaction in the troposphere is the reaction of peroxy radicals with NO (Fig. 1-1). In polluted regions with high NO mixing ratios, peroxy radicals react mainly with NO to form alkoxy radicals or organic nitrates ($RONO_2$).

$$RO_2 + NO \longrightarrow RO + NO_2$$ Reaction 1-11

$$RO_2 + NO \longrightarrow RONO_2$$ Reaction 1-12

The production of organic nitrates terminates the radical chain. Organic nitrates are removed in the atmosphere by wet and dry deposition. They can also be photolyzed and react with OH radicals and thereby taking part in the radical chain again (Roberts, 1990).

Alkoxy radicals (Reaction 1-11) further decompose into a close-shell organic product and an HO_2 or RO_2 radical in the reaction with an oxygen molecule, depending on their structures. Examples for the reactions of simple alkoxy radicals are:

$$CH_3O + O_2 \longrightarrow HCHO + HO_2$$ Reaction 1-13

$$(CH_3)_3CO + O_2 \longrightarrow CH_3COCH_3 + CH_3O_2$$ Reaction 1-14

The HO_2 radical produced in Reaction 1-13 can further react with NO and produce OH radicals.

$$HO_2 + NO \longrightarrow OH + NO_2$$ Reaction 1-15

The OH radical produced in Reaction 1-15 can then react with VOCs and repeat the OH-to-RO_2-to-HO_2 radical conversion cycle in the presence of NO (Fig. 1-1). The branching ratio of Reaction 1-11 and Reaction 1-12 generally depends on the size of the peroxy radical, with large (more C-atoms) peroxy radicals being prone to form organic nitrates (Jenkin et al., 2019). The branching ratio of Reaction 1-12 ranges from less than 1 % for methyl peroxy radicals (CH_3O_2, Butkovskaya et al., 2012) to about 20 % to 30 % for monoterpene-derived peroxy radicals (e.g., Rindelaub et al., 2015; Hantschke et al., 2021).

Other important reaction partners of organic peroxy radicals include HO_2 radicals and other RO_2 radicals. There are multiple reaction pathways possible for the reaction of RO_2 radicals with HO_2 radicals:

$$RO_2 + HO_2 \longrightarrow ROOH + O_2$$ Reaction 1-16

$$RO_2 + HO_2 \longrightarrow R_{-H}O + O_2 + H_2O$$ Reaction 1-17

$$RO_2 + HO_2 \longrightarrow RO + OH + O_2$$ Reaction 1-18

$$RO_2 + HO_2 \longrightarrow R_{-H}O + OH + HO_2$$ Reaction 1-19

Reaction 1-16 and Reaction 1-17 are radical terminating pathways whereas Reaction 1-18 and Reaction 1-19 are radical propagating pathways. For the majority of peroxy radicals (e.g., alkyl peroy radicals, β-OH peroxy radicals), Reaction 1-16 is the most dominant pathway (Jenkin et al., 2019). The other pathways

only apply to peroxy radicals with oxygenated functional groups near the peroxy radical site. With typical atmospheric HO_2 concentrations of 10^8 – 10^9 cm^{-3}, the lifetime of RO_2 with respect to the reaction with HO_2 is about several minutes, which is equivalent to the loss rate of RO_2 in the presence of about 0.05 ppbv NO. Therefore, the loss of RO_2 radicals in the reaction with HO_2 radicals only gain importance in regions with very low NO concentrations such as remote and forested areas.

Similar to the reaction with HO_2 radicals, RO_2 radicals can react with other RO_2 radicals. The reaction also has multiple reaction pathways:

$$RO_2 + R'O_2 \longrightarrow RO + R'O + O_2 \qquad \text{Reaction 1-20}$$

$$RO_2 + R'O_2 \longrightarrow R_{-H}O + R'OH + O_2 \qquad \text{Reaction 1-21}$$

$$RO_2 + R'O_2 \longrightarrow ROH + R'_{-H}O + O_2 \qquad \text{Reaction 1-22}$$

$$RO_2 + R'O_2 \longrightarrow ROOR' + O_2 \qquad \text{Reaction 1-23}$$

Reaction 1-20 is the only radical propagating channel, where alkoxy radicals are formed and further decompose into close-shell products and HO_2 radicals. Reaction 1-21 to Reaction 1-23 are radical terminating channels, in which close-shell products are formed. The branching ratios of Reaction 1-20 to Reaction 1-23 depend on the structure of the peroxy radical and its reaction partner. Based on the studies of RO_2 with less than 5 carbon atoms, radical termination pathways Reaction 1-21 and Reaction 1-22 are the most important pathways under typical atmospheric conditions. The sum of branching ratios of Reaction 1-21 and Reaction 1-22 for methyl peroxy radicals is 65 % at 298 K, the value reduces to 40 % for primary and secondary peroxy radicals, and further drops to 20 % for tertiary and acyl peroxy radicals (Jenkin et al., 2019). Formation of peroxides (Reaction 1-23) is not observed for small peroxy radicals. However, for large RO_2 radicals with at least 10 carbon atoms, it is suggested that the formation of peroxides gains in importance (Hasan et al., 2021).

1.2.3 Lifetimes of VOCs and their oxidants in the atmosphere

The lifetime of VOCs depends on the concentrations of the oxidants. Typical OH concentrations in the troposphere range from 10^6 to 10^7 cm^{-3} (Vaughan et al., 2012). The chemical lifetime of OH radicals range from 10 ms to 1 s, which is determined by the concentrations of their reactants such as VOCs. Because of the very short lifetime of OH, the chemical production and destruction rates of OH radicals are always balanced on atmospherically relevant time scales.

Typical O_3 concentrations in the troposphere range from 10 ppbv in unpolluted marine air (Ayers et al., 1992) to more than 150 ppbv in extreme ozone pollution events (Solberg et al., 2008). The production rate of O_3 depends on the ratio between the concentrations of VOCs and NO_x (e.g, Dunker et al., 2002). O_3 is mainly lost due to its photolysis reaction, reactions with organic compounds and deposition on surfaces. The typical lifetime of O_3 in the troposphere ranges from several days to weeks (Wild, 2007). Due to its much longer lifetime than the OH radical it can persist into the night if NO_x emissions are low. This makes O_3 one of the most important oxidants for VOCs during nighttime when the photolytic production of OH radical stops.

At sunset, O_3 converts NO into NO_2, followed by the conversion of NO_2 to NO_3 radicals. NO_3 radical is another important reactant of BVOCs during the nighttime. It is solely a nighttime oxidant as it is rapidly converted back to NO_x by its photolysis or reaction with NO during daytime. Typical nighttime concentrations of NO_3 radicals range from 10 pptv to 100 pptv in regions where reactive nitrogen oxide species are available (Platt et al., 1984).

Using typical concentrations of atmospheric oxidants, the lifetime of VOCs can be calculated using reaction rate constants of the VOCs oxidation reactions. Table 1-2 summarizes the atmosphere lifetime of VOCs species listed in Table 1-1. Terpenes have shorter lifetimes than smaller VOCs without a C=C double bonds, as C=C double bonds increase their reactivities towards OH and NO_3 radicals. Reaction rate constants of the ozonolysis reactions are more sensitive toward the presence of multiple non-conjugated C=C double bonds (e.g., limonene, trans-β-ocimene, and sesquiterpenes) than that reactions rates for OH- and NO_3- radical oxidation.

Table 1-2. Selected VOCs listed in Table 1-1 and their lifetimes in the atmosphere with respect to the oxidation of OH, O_3, and NO_3 under typical concentrations of oxidants. Reaction rate constants are retrieved from IUPAC recommended values for a temperature of 298 K (https://iupac.aeris-data.fr/, last access: 10 July 2023).

	Lifetime for reaction with		
VOCs	OH (2.0×10^6 cm^{-3})	O_3 (7.0×10^{11} cm^{-3})	NO_3 (2.5×10^8 cm^{-3})
Isoprene	1.4 h	1.3 days	1.6 h
α-Pinene	26 h	4.6 h	11 min
β-Pinene	1.8 h	1.1 days	27 min
Trans-β-ocimene	33 min	44 min	3.0 min
Limonene	49 min	2.0 h	5.6 min
Sabinene	1.2 h	4.8 h	6.7 min
Sesquiterpenes[a]	42 min	2.0 min	3.5 min
Methanol	6.4 days	/[b]	360 days
Acetone	2.1 days	/[b]	< 4 years
Ethene and propene	5.2 to 24 days	/[b]	< 2 years

[a]values of β-caryophyllene, [b]species do not react with O_3

1.2.4 Recent advances in atmospheric organic peroxy radical chemistry

The chemistry of bimolecular reactions between organic peroxy radicals and other atmospheric radicals have been studied for many decades (e.g., Adachi and Basco, 1979; Cox and Tyndall, 1980; Sander and Watson, 1980). With the development of new instruments and advancement in measurement techniques, also intermediates produced during the atmospheric oxidation of VOCs can be observed. In addition, the improvement of computing power allows for the evaluation of reaction pathways using computational chemistry.

One important discovery has been that isomerization reactions of isoprene-derived RO_2 radicals leading to the production of OH radicals without the presence of NO are of importance (Crounse et al., 2011; Fuchs et al., 2013; Peeters et al., 2014; Novelli et al., 2020). This partly explains the deficit of a factor of up to 10 in model calculations observed for noon-time OH concentrations in a measurement campaign in rain forest, if only OH productions from photolysis reactions, ozonolysis of VOCs, and HO_x recycling reactions were considered (Lelieveld et al., 2008; Whalley et al., 2011). An analysis of field campaigns in which OH concentrations were measured suggests modelled OH concentrations start deviating from measured OH concentrations when NO_x mixing ratios were less than 1 ppbv. Regions, in which models underestimated measured OH concentrations are located in subtropical and temperate forests (Rohrer et al., 2014).

The study conducted by Novelli et al. (2020) suggests that up to 50 % of OH radicals are regenerated from RO_2 isomerization reactions and the photolysis of isomerization products in the oxidation chain of isoprene at NO mixing ratio less than 0.2 ppbv, which is important in regions like tropical forests. The result implies that the global OH radical regeneration rate is higher than previously thought, which can affect the lifetime of greenhouse gases such as methane and pollutants like carbon monoxide.

The mechanism behind the additional OH production from the oxidation of isoprene at low NO mixing ratios was elucidated by theoretical studies (Peeters et al., 2014). It is found that the H-migration in the RO_2 radical derived from the OH-oxidation of isoprene can yield a hydroxy peroxy aldehyde, which can be photolyzed into products including OH radicals (Fig. 1-4).

Similar isomerization reactions were not observed in the RO_2 radicals derived from the OH-oxidation of simple hydrocarbons without specific functional groups, as H-shift reactions in peroxy radicals without the presence of other functional groups are generally not competitive ($k_{uni} < 10^{-3}$ s^{-1}, Vereecken and Nozière, 2020). In general, the presence of C=C double bonds and oxygenated functional groups such as carbonyl and hydroxyl groups increase the isomerization rate. The isomerization reaction rate could span values from 10^{-2} to 10^{3} s^{-1} (Vereecken and Nozière, 2020; Vereecken et al., 2021), which is equivalent to the RO_2 loss rate constant in the presence of 0.01 ppbv to 1000 ppbv of NO.

In some temperate forests with low NO mixing ratios dominated by non-isoprene BVOCs emission, missing HO_2 sources were observed (Hens et al., 2014; Kim et al., 2014), demonstrating that current state-of-the-art atmospheric chemistry models cannot correctly reproduce the HO_2 concentration in the degradation of monoterpenes. This has also been shown in the investigation of the degradation of α-pinene and β-pinene in chamber experiments (Eddingsaas et al., 2012; Kaminski et al., 2017; Rolletter et al., 2019). There is no definite conclusion on the mechanism behind the missing HO_2 sources during the oxidation of

monoterpenes, but it could be related to the isomerization of the RO_2 radicals derived from the oxidation of monoterpenes. Due to the complexity of the structure of monoterpenes, the degradation of monoterpenes involves multiple possibilities of unimolecular reaction pathways and the formation of intermediate organic compounds. As a result, the construction and evaluation of the degradation mechanism of a specific monoterpene are often difficult without the identification and quantification of intermediates.

Apart from explaining the missing HO_x sources observed in chamber experiments and field measurements, isomerization reactions of peroxy radicals can explain the observation of highly oxidized molecules (HOMs) in the oxidation of VOCs (e.g., Ehn et al., 2014; Mentel et al., 2015). HOMs have a high O:C atom ratio of up to one (Tu et al., 2016) and in general have a high molecular mass. As a result, HOMs have very low volatility and could readily condense and form secondary organic aerosol (SOA) in the atmosphere. HOMs were observed in laboratory studies and field measurements (Bianchi et al., 2019). The production of HOMs from isomerization reactions can be initiated by H-shift or cyclization reactions (Fig. 1-5), which yield a hydroperoxyl- or peroxyalkyl radical. Instead of dissociating like the hydroperoxyl alkoxy radical from isoprene (Fig. 1-4), the new alkyl radical reacts with O_2 to form a new RO_2 radical while retaining its oxygenated functional groups. Depending on the structure and function groups present in the RO_2 radical, the process can be repeated several times which resulted in RO_2 radicals with many oxygen atoms (more than 8).

In summary, the discovery of the additional production of OH radicals from the oxidation of isoprene revealed the importance of peroxy radical isomerization reactions. The isomerization reactions of peroxy radicals are used to explain the observation of missing HOx radicals during the oxidation of BVOCs, as well as the production of HOMs. As isomerization reactions are competing with their bimolecular reactions with NO, the investigation of peroxy radical isomerization requires experimental conditions with low NO concentrations.

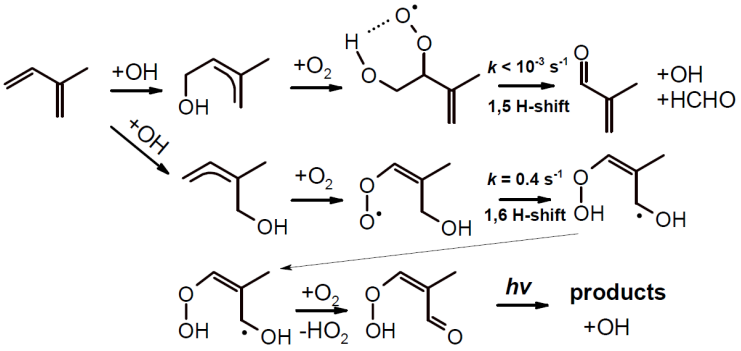

Figure 1-4. Example of the OH radical regeneration through isomerization of peroxy radical derived from the OH-oxidation of isoprene. The figure is adapted from Novelli et al. (2020).

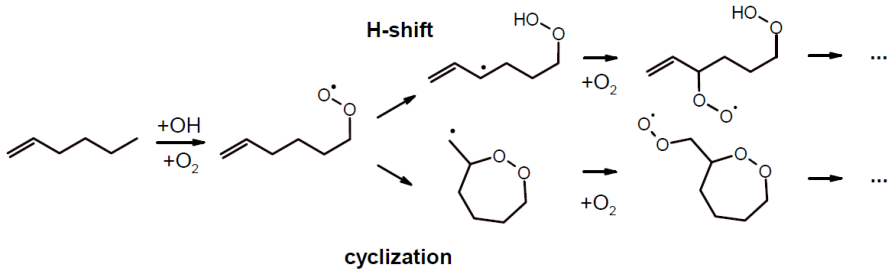

Figure 1-5. Example of an isomerization and oxidation of RO_2 radicals through H-shift or cyclization.

1.3 Objectives of the thesis

Investigations of the degradation of monoterpenes were mostly conducted for conditions with NO mixing ratios that are at least one order of magnitude (> 100 ppbv) higher than typical NO mixing ratios found in the ambient environment. In this case, the lifetime of peroxy radicals is very short. As a result, unimolecular reactions that may be competitive with bimolecular reactions for ambient conditions could be overlooked.

So far, only the oxidation mechanism of a few monoterpenes species have been investigated in the presence of ambient NO mixing ratios including α-pinene (Eddingsaas et al., 2012; Rolletter et al., 2019), β-pinene (Kaminski et al., 2017; Xu et al., 2019), myrcene (Tan et al., 2021), and Δ^3-carene (Hantschke et al., 2021). In total, these four monoterpenes species represent about 61% of the total global monoterpene emission (Sindelarova et al., 2014). Other important monoterpene species that are not well investigated include trans-β-ocimene (23 % of the total global emission rate), limonene (9 % of the total global emission rate), and sabinene (7 % of the total global emission rate). In addition, specifically limonene is also important in urban environments from anthropogenic sources as limonene is one of the most reactive compounds of volatile chemical products.

In this thesis, the oxidation of limonene and sabinene was investigated in simulation chamber experiments. Limonene is a monocyclic monoterpene with two C=C double bonds. When one of the C=C double bonds reacts with OH or O_3 to form a RO_2 radical, the RO_2 radical can undergo fast unimolecular reactions (e.g., cyclization, abstraction of allylic H atom) due to the presence of the second C=C double bonds (Møller et al., 2020; Chen et al., 2021). These reactions can be important even in polluted regions with moderate NO mixing ratios. The oxidation of limonene produces harmful organic compounds such as formaldehyde (HCHO), which could be a health threat indoors if limonene is emitted from the usage of VCPs.

To investigate the oxidation of limonene at different NO concentrations, experiments were conducted in the SAPHIR chamber with NO mixing ratios ranging from 0 ppbv to 10 ppbv. The yield of HCHO was calculated and compared to previous studies. In addition, modelled OH, HO_2, RO_2 radical concentrations, and the OH reactivity were compared to the observations to investigate whether current oxidation mechanism can reproduce the measurements (Chapter 4).

The oxidation of sabinene at different NO mixing ratios was also investigated in simulation chamber experiments. The chemical structure of sabinene is similar to that of β-pinene. Both are bicyclic monoterpenes with an exocyclic C=C double bond. It is expected that the oxidation of sabinene is similar to β-pinene. Unlike limonene which has two C=C double bonds, the oxidation of sabinene resulted in peroxy radicals that do not have another C=C double bond that enhances potential isomerization reactions. Therefore, it can be expected that isomerization reactions of peroxy radicals derived from the oxidation of sabinene may be less important, thereby resulting in less oxygenated peroxy radicals.

In this work, reaction rate constants of the OH reaction of sabinene was determined at different temperatures. Product yields of sabinene oxidation at different NO concentrations were calculated and compared to values expected from available oxidation mechanisms of sabinene. In addition, the chemical budgets of OH and RO_2 radicals during the oxidation of sabinene were analyzed (Chapter 5).

Lastly, the oxidation of a realistic mixture of BVOCs directly emitted from sweet chestnut trees (*Castanea sativa*) were investigated in experiments in the atmospheric simulation chamber SAPHIR. Emissions were collected in the plant chamber SAPHIR-PLUS and then transferred into the SAPHIR chamber. Sweet chestnut was selected as monoterpenes including sabinene are expected to be the major emission (Aydin et al., 2014). In contrast to oxidation experiments that only involve one precursor, plant emission experiments involve multiple precursor species that could better emulate the ambient environment. In summer 2022, several experiments were performed to investigate the change in plant emissions at different temperatures (Chapter 6). VOCs emitted by plants and their oxidized products were measured by online GC-MS/FID and PTR-TOF-MS in the SAPHIR chamber, as well as an offline GC-MS/FID in the SAPHIR-PLUS chamber. The online GC instrument was calibrated, and its measurements were compared to the online PTR-TOF-MS measurements as the part of this work. The measured VOC concentrations by the online measurements in the SAPHIR chamber were used to compare with the OH reactivity measurement if there was missing OH reactant in the VOC measurements. The chemical budget of OH radicals was also calculated in the experiments investigating the oxidation of the emissions from sweet chestnut trees.

2. Atmospheric Simulation Chamber SAPHIR

2.1 The atmospheric simulation chamber SAPHIR

Monoterpenes and plant BVOCs emission oxidation experiments were conducted in the SAPHIR chamber (Simulation of Atmospheric Photochemistry In a large Reaction Chamber) located at Forschungszentrum Jülich, Germany. It is a large cylindrical-shaped chamber (18 m length, 5 m diameter, 270 m^3 volume, with 1:1 volume to surface area ratio) made of a double-wall Teflon (FEP) film (Fig. 2-1). The chemical inertness of the Teflon film and the large volume-to-surface area ratio minimize the wall loss of gas phase species and aerosols. The Teflon film has a transmittance of 75 % on average for the whole spectrum of solar radiation (Bohn and Zilken, 2005), allowing photooxidation experiments to be conducted with natural sunlight. There is a shutter system that can be opened or closed to control whether the sunlight irradiates the chamber air. The chamber is filled with synthetic air produced from mixing evaporating ultra-pure liquid oxygen and nitrogen (Linde, > 99.99999 %). The chamber is operated under a slight overpressure of about 35 Pa above ambient pressure, such that contaminants from the ambient air cannot infiltrate into the chamber. The overpressure is maintained by continuously flowing pure synthetic air into the chamber to compensate for small leakages and consumption of air by instruments, which results in a dilution rate of trace gases of about 4 % h^{-1}. The temperature inside the chamber is similar to the ambient temperature when the shutter is closed, and the temperature can be about 5°C to 10°C higher than the ambient temperature when the shutter is opened. Two fans are installed at the opposite ends of the chamber to ensure a thorough mixing of the air. Instruments are located in sea containers underneath the chamber. Most instruments sample air through Teflon inlet lines to reduce the loss of analytes.

Figure 2-1. The SAPHIR chamber at Forschungszentrum Jülich. Copyright “Forschungszentrum Jülich / Sascha Kreklau”

2.2 Trace gas emissions from the chamber

Upon illumination, trace gases including nitrous acid (HONO), formaldehyde (HCHO), and acetone are formed and released from processes on the surface of the chamber. The emission rates of these trace gas species are characterized for the calculation of product yields and the chemical budget of OH radicals in this study. Emission rates of these trace gases species can be described by their source strength S_x, which depend on temperature (T, in K), relative humidity (RH, in %), and radiation. An empirical parameterization of the source strength for HONO was derived by Rohrer et al. (2005). Source strengths for HCHO and acetone were also derived similarly to that of HONO:

$$S_{\mathrm{HONO}} = c_{\mathrm{HONO}} \cdot j_{\mathrm{NO_2}} \left(1 + \frac{\mathrm{RH}}{11.6}\right)^2 \exp\left(-\frac{3950}{T}\right) \qquad \text{Equation 2-1}$$

$$S_{\mathrm{HCHO}} = c_{\mathrm{HCHO}} \cdot j_{\mathrm{NO_2}} (0.21 + 0.026\mathrm{RH}) \exp\left(-\frac{2876}{T}\right) \qquad \text{Equation 2-2}$$

$$S_{\mathrm{acetone}} = c_{\mathrm{acetone}} \cdot j_{\mathrm{NO_2}} (0.21 + 0.026\mathrm{RH}) \exp\left(-\frac{2876}{T}\right) \qquad \text{Equation 2-3}$$

The dependence of the source strength S_x on the radiation strength is expressed as a function of the photolysis rate constant of NO_2 (j_{NO2}). The empirical constants c_x are determined from the increase of trace gas concentrations during the zero-air phase of experiments in this work, when the clean chamber was illumined for about 30 minutes to 2 hours at the beginning of every experiment before the injection of VOCs. It is assumed that values of c_x do not change during an experiment within a day. Typical production rates of HONO, HCHO, and acetone from chamber sources are around 0.2 ppb hr^{-1} to 0.8 ppbv hr^{-1}.

2.3 The SAPHIR-PLUS Chamber

The SAPHIR-PLUS chamber is a gas exchange chamber housed in a sea container (dimension: 2.39 m × 3.84 m × 2.84 m) located next to the SAPHIR chamber. SAPHIR-PLUS can house the canopy of up to six trees in a Teflon bag under controlled conditions (Fig. 2-2). The detailed description of SAPHIR-PLUS can be found in Hohaus et al. (2016). In brief, SAPHIR-PLUS consists of three components, (1) the gas exchange chamber, (2) the interspace between the exchange chamber and the exterior, and (3) the lighting unit.

In the gas exchange chamber, biogenic emissions from plants are collected and then transferred to the SAPHIR chamber by a gas exchange flow. The volume of the Teflon bag that encloses the canopies is around 9 m^3 (dimension: 1.80 m × 3.52 m × 1.45 m). The bottom of the chamber has an aluminum surface with six holes, in which the stems of the trees are sealed against the gas-exchange volume. Therefore, emissions from the soil cannot enter the gas exchange chamber. During the collection of VOCs emitted by the plants, the gas exchange chamber is flushed with synthetic air mixed with CO_2, resulting in a CO_2 mixing ratio of 400 ppmv. The chamber is operated under a slight over-pressure of around 50 Pa above atmospheric pressure. When the valve that controls the air flow between the two chambers is opened,

emitted VOCs are transferred from the SAPHIR-PLUS chamber to the SAPHIR chamber due to the pressure difference.

The space underneath the aluminum plate constains the plant pots and connections of various sensors. For each plant pot, there is an automatic irrigation system and a soil humidity sensor. The temperature of the interspace and gas exchange chamber is controlled by heat exchange panels embedded in the walls of the SAPHIR-PLUS chamber. The interspace is flushed with synthetic air and the pressure is about 30 Pa lower than that of the gas exchange chamber, so that contaminants in the interspace cannot leak into the gas exchange chamber.

The lighting unit is installed at the ceiling of the chamber. Glass panes are installed to prevent the gas exchange chamber from heating up by the lighting. The spectrum of the light unit ranges from 400 nm to 700 nm, with a bimodal bell-shaped characteristic with maximum intensities at wavelengths of 440 nm and 570 nm. The intensity of the photosynthetically active radiation (PAR) can be adjusted between 0 to 800 µmol m^{-2} s^{-1} to emulate the change in light intensity within the diurnal cycle.

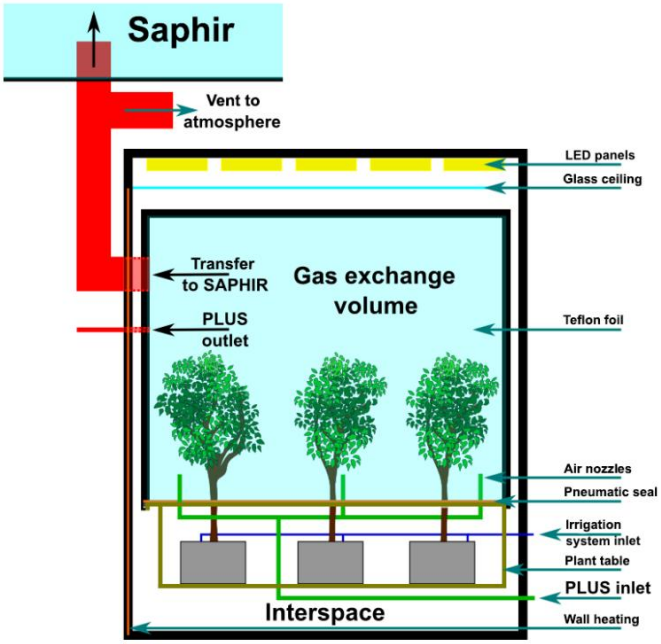

Figure 2-2. Schematic diagram of the SAPHIR-PLUS chamber. Figure adapted from Hohaus et al. (2016).

2.4 Instruments at the SAPHIR chamber

A large suit of instruments is available at the SAPHIR chamber. Table 2-1 summarizes the instruments that are involved in this study. This study focuses on the interpretation of measurements of radical and trace gas concentrations and the instruments are described in the following sections.

Table 2-1. Instrumentation for radical and trace-gas measurements that were used in the chamber experiments in this work.

Species	Method	Time resolution	1-σ precision	1-σ accuracy	Reference / Manufacturer
OH	DOAS[b]	205 s	0.8×10^6 cm^{-3}	6.5 %	Dorn et al. (1995)
	LIF[c]	47 s	0.3×10^6 cm^{-3}	13 %	Fuchs et al. (2011)
HO_2, RO_2	LIF	47 s	1.5×10^7 cm^{-3}	16 %	Fuchs et al. (2011)
OH reactivity	Laser flash photolysis + LIF	180 s	0.3 s^{-1}	0.5 s^{-1}	Fuchs et al. (2017)
NO	Chemiluminescence	60 s	20 pptv	5 %	Eco Physics
NO_2	Chemiluminescence + photolytical converter	60 s	20 pptv	5 %	Eco Physics
HONO	LOPAP[d]	300 s	3 pptv	10 %	Li et al. (2014)
O_3	UV absorption	180 s	60 pptv	5 %	Ansyco
C_9 and C_{10} VOCs[a]	PTR-TOF-MS[e]	40 s	10 %	[h]	Lindinger et al. (1998)
Limonene	GC-FID[f]	45 min	4 % – 8 %	5 %	Kaminski (2014)
Formaldehyde	Hantzsch	60 s	25 pptv	8.6 %	Glowania et al. (2021)
	DOAS	100 s	20 %	7 %	Hausmann et al. (1997)
	CRDS[g]	60 s	90 pptv	10 %	Glowania et al. (2021)
Acetone	PTR-TOF-MS	40 s	5 %	5 %	Lindinger et al. (1998)
	GC-FID	45 min	4 % – 8 %	5 %	Agilent
Photolysis frequencies	Spectroradiometer	60 s	10 %	18 %	Bohn et al., (2005)

[a]Including limonene, sabinene, and sabinaketone. [b]Differential optical absorption spectroscopy [c]Laser-induced fluorescence [d]Long path absorption photometer [e]Proton-transfer time-of-flight reaction mass spectroscopy [f]Gas chromatography coupled with flame ionization detector [g]Cavity ring down spectroscopy [h]limonene (14 %); sabinene (25 %); sabinaketone (50 %). Only the measurements of limonene was calibrated in the instrument. Concentrations of sabinene were determined by the OH reactivity increase right after its injections; concentrations of sabinaketone were determined based on the measurement sensitivity of structurally similar nopinone in the instrument.

2.4.1 Measurements of radical species

Two instruments were used for the measurement of radical concentrations in the SAPHIR. The instrument using differential optical absorption spectroscopy (DOAS) measures the concentration of OH radicals. Another instrument that is based on laser-induced fluorescence (LIF) measures the concentrations of OH, HO_2, and total RO_2 radicals.

The detection of OH concentrations with DOAS is based on the measurement of the absorption of UV radiation by OH radicals at 308 nm. In general, the absorption of the radiation is described by Beer–Lambert's law, which includes the absorption cross-section of the species of interest and the length of the optical path. The long optical path (2240 m, Schlosser et al., 2007) in the SAPHIR chamber allows a highly sensitive measurement, which is achieved by using a multiple-reflection cell. Additional light extinction attributed to Rayleigh scattering and Mie scattering, broad-band spectral absorption structures are separated from fingerprint, narrow-band spectral absorption lines by a mathematical fit procedure that is similar to a high pass filter. The obtained narrow-band spectral structure spectrum is then fitted to a superposition of reference absorption spectra of absorbers that are relevant in this wavelength region. Reference spectra are taken from literature or were determined in characterization experiments in the past. In this way, OH concentrations and trace gas (e.g., HCHO and SO_2) in the probed air are derived. The DOAS method is an absolute measurement, which does not require calibrations for the instrument. In SAPHIR, the DOAS instrument can also to measure the concentration of formaldehyde.

Measurement of OH concentrations using LIF is based on the measurement of the fluorescence signal emitted from excited OH radicals. In the SAPHIR chamber, about 1000 cm^3 min^{-1} of air is sampled into a low-pressure fluorescence cell. OH radicals are excited by a short laser pulse at 308 nm. The subsequent fluorescence signal is measured by a single photon-counting system (Fuchs et al., 2011). The instrument is regularly calibrated using OH radicals generated from the photolysis of water vapor at 185 nm using a mercury lamp. In general, OH concentrations measured by LIF agree with that of measured by DOAS within the combined 1σ accuracies of 13 % and 6.5 %, respectively (Fuchs et al., 2012; Cho et al., 2021).

HO_2 and total RO_2 concentrations are measured indirectly in two separate low pressure fluorescence cells of the LIF instrument. In the HO_x cell, where the HO_2 concentrations are measured, NO is added to the air to convert HO_2 radicals into OH radicals. The concentration of NO is carefully selected so that the potential formation of HO_2 from the concurrent conversion of RO_2 radicals is minimized (Fuchs et al., 2011). The total OH fluorescence signal measured reflects the concentrations of HO_x (the sum of OH + HO_2) in the air sample and the HO_2 concentrations can be derived from the difference in the fluorescence signals between the HO_x cell and OH cell after taking into account the differences in sensitivities. The measurement of RO_2 radicals concentrations is done in the RO_x cell, where the air sample is first converted to HO_2 by adding NO and CO in a conversion reactor. The air is then transferred into the low-pressure fluorescence cell, where HO_2 is converted to OH by excess NO, followed by the measurement of OH by LIF. The RO_2 concentrations can be derived from the difference in the fluorescence signal between the RO_x cell and HO_x cell after taking into account the differences in sensitivities.

2.4.2 Measurements of the OH reactivity (k_{OH})

The OH reactivity is the reciprocal of the chemical lifetime of the OH radical. It is measured using an instrument based on laser flash photolysis combined with laser-induced fluorescence (LP-LIF, Lou et al., 2010; Fuchs et al., 2011). In this instrument, OH radicals are generated in-situ in a flow tube from the photolysis of ozone in the presence of water vapor using a low repetition laser (1 Hz) at 266 nm. The OH produced from the flash photolysis reacts then with the OH reactants present in the sampled air which leads to a decay of the OH concentration. The decay in the OH concentration is observed with a high time resolution (1 ms). A small fraction of the air is sampled into a fluorescence cell after exciting them by short laser pulses at 308 nm with a high frequency of 8.5 kHz. The loss rate of the OH in the flow tube can be expressed as:

$$\frac{d[\mathrm{OH}]}{dt} = -\sum_i (k_{\mathrm{OH}+X_i}[X_i]\,[\mathrm{OH}]) \qquad \text{Equation 2-4}$$

where k_{OH+Xi} is the reaction rate constant of the reaction between OH and reactant X_i. Since the concentrations of OH reactant concentration are much higher than the OH concentrations, the reaction can be regarded as a pseudo-first order reaction ($[X_i]$ is a constant). By solving the differential equation Equation 2-4, the OH concentration in the flow tube exponentially decays with a decay constant of $\sum_i(k_{OH+Xi}[Xi])$:

$$[\mathrm{OH}] = [\mathrm{OH}]_0 \exp(\textstyle\sum_i (k_{\mathrm{OH}+X_i}[X_i])t) \qquad \text{Equation 2-5}$$

The decay constant $\sum_i(k_{OH+Xi}[X_i])$ is the OH reactivity and it can be determined by fitting the decay curve of the OH concentration to a single-exponential function.

$$k_{\mathrm{OH}} = \textstyle\sum_i (k_{\mathrm{OH}+X_i}[X_i]) \qquad \text{Equation 2-6}$$

2.4.3 Measurements of volatile organic compounds (VOCs) with PTR-TOF-MS

The concentrations of VOCs concerned in this study were measured online by proton-transfer-reaction time-of-flight mass spectrometry (PTR-TOF-MS). The measurement is based on the reaction target VOCs and H_3O^+ ions and the detection of $[VOC\text{-}H]^+$ ion by the mass spectrometer. It can measure both oxygenated and non-oxygenated VOCs such as monoterpenes and their oxidation products. The instrument has a high time resolution of 1 minute. However, it cannot resolve isomers such as different monoterpene species. This drawback is specifically apparent in the plant emission experiments, where a mix of monoterpene species were present during the experiment.

The instrument is regularly calibrated with commercially available gas standards. In chamber experiments of a single monoterpene species, concentrations of the injected species can be derived from OH reactivity measurement, if that species are not included in the gas standard. For species that are not injected into the chamber, their concentrations are calculated by their estimated measurement sensitvitiy.

In the sabinene oxidation experiment (Section 4), the injected sabinene concentration can be inferred from the increase in OH reactivity right after its injection using the reaction rate constant of the reaction

in sabinene with OH radicals (Equation 2-3). Therefore, the ion mass signal of the PTR-TOF-MS instrument can be scaled to match the increase of OH reactivity. For species that could not be determined by this method such as the oxidation product of monoterpene (e.g., sabinaketone). The measurement sensitivity can be estimated based on its molecular formula and functional groups. For sabinaketone, an oxidation product of sabiene, its concentrations were derived from the measurement sensitivity of nopinone in the PTR-TOF-MS instrument, assuming that the instrument has the same sensitivity for both compounds. This assumption has an uncertainty of 50 % based on the result in Sekimoto et al. (2017).

2.4.4 Measurements of VOCs by gas chromatography (GC)

As part of this PhD.work, GC measurements were established for the detection of monoterpenes in the chamber experiments. Online measurements were conducted with a GC (Agilent, Santa Clara, USA) equipped with a flame ionization detector (FID) and a mass spectrometer (MS) (Fig. 2-3).

Air sample is continuously sampled from the SAPHIR chamber and transferred to the GC. VOCs are first sampled in a cryogenic cooled thermal desorption system (GERSTEL, Germany) for about 15 minutes through enrichment on an adsorbent. The thermal desorption system is then heated and the VOCs are injected into two separate GC columns (DB-624, Agilent). The columns are heated with a programmed temperature ramp from -150 °C to 270 °C for 25 minutes. VOCs species are then separated based on their adhesion strength on the coating material inside the column. One GC column is connected to the FID detector that is used to quantify the analyte; another GC column is connected to the MS that is used to identify the analyte. The time resolution of the GC measurements is about 45 minutes.

The GC instrument is regularly calibrated with a gas standard containing 64 compounds which are diluted to concentirations range between 1 ppbv – 50 ppbv. For species that are not included in the gas standard, it is calibrated with a diffusion source if a liquid sample is available (Fig. 2-3). To calibrate the instruments with a diffusion source, a few grams of the liquid sample is placed in the diffusion source for a few days to stabilize under a controlled environment with a constant temperature and a constant carrier gas flow. The evaporation loss rate of the liquid sample, which can be used to calculate the gaseous concentration in the instruments, is then determined by successively weighting the liquid sample with a precise balance over time with a typical duration of several days. The method was applied to determine the for β-ocimenes required for the analysis of the plant emission experiments in the SAPHIR chamber (Section 2.6).

In addition to the online GC measurements in the SAPHIR chamber, an offline GC-FID/MS was setup to measure VOCs emitted from plants in the SAPHIR-PLUS chamber. A small amount of air was sampled from the SAPHIR-PLIS chamber and passed through a Tenax® TA Tube for 90 minutes to 150 minutes to collect the VOCs. The flow rate of the sampling line from the SAPHIR-PLUS to the Tenax® TA Tube was recorded for the calculation of the total volume of sampled air passing through the absorbent. Tenax® TA Tube used for the measurements were then analyzed with a GC instrument.

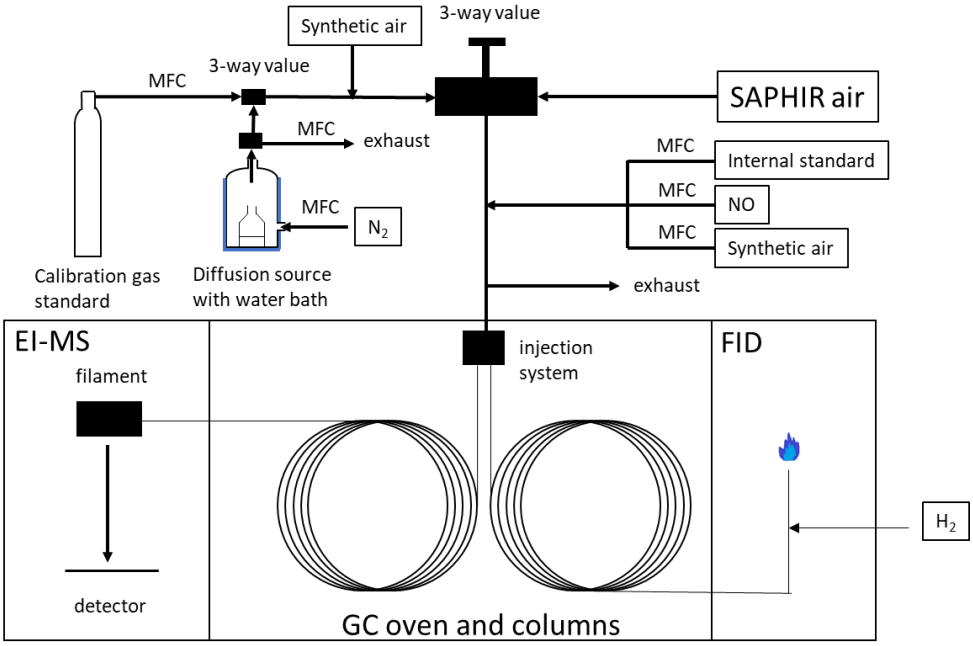

Figure 2-3. The simplified schematic diagram of the GC instrument at the SAPHIR chamber. A diffusion source was set up to measure to VOCs species that are not included in the gas standard. Abbreviation: MFC (mass flow controller); EI-MS (electron ionization mass spectrometer)

2.5 Monoterpene oxidation experiments in the SAPHIR chamber

To investigate the oxidation of monoterpene at atmospherically relevant conditions, experiments were conducted under NO mixing ratios from zero to 10 ppbv. Experiments can be divided into four groups, which are based on their NO mixing ratios:

- ozonolysis experiments (zero NO) (e.g., Fig. 2-4)
- photooxidation experiments with low NO mixing ratios (e.g., Fig. 2-5)
- photooxidation experiments with medium NO mixing ratios (e.g., Fig. 2-6)
- photooxidation experiments with high NO mixing ratios (e.g., Fig. 2-7)

Ozonolysis experiments were conducted in the dark chamber, so that there was no production of NO from the photolysis of HONO (Section 2.2). At the beginning of the ozonolysis experiments, about 5 ppbv of monoterpene was injected into the chamber followed by several injections of O_3 with concentrations ranging from 50 to 160 ppbv. The monoterpene was allowed to react with O_3 for several hours until it was nearly completely consumed. OH radicals were produced from the ozonolysis of monoterpenes and they also reacted with monoterpenes. Depending on the consumption rate of the monoterpene, additional monoterpene of several ppbv was injected into the chamber after 2 hours to replenish the consumed monoterpene. After four hours of the experiment, about 100 ppmv of carbon monoxide (CO) was injected into the chamber. CO scavenges the OH radicals produced from the ozonolysis reaction, such that the monoterpene reacted exclusively with O_3 after the injection of CO. With 100 ppmv of CO, over 95 % of the OH radical reacted with CO whereas less than 5 % of the OH radical reacted with monoterpene. O_3 was injected again into the chamber 15 minutes after the injection of CO for replenishing the loss of O_3 from dilution in the chamber and its chemical loss in the reaction with monoterpene. After the injection of CO, about 5 ppbv of monoterpene was injected to the chamber and allowed to react for another 4 hours. Again, depending on the consumption rate of monoterpene, an additional 5 ppbv of monoterpene was injected into the chamber one more time during this phase of the experiment. Figure 2-4 illustrates typical trace gas and radical concentrations of one of the ozonolysis experiments.

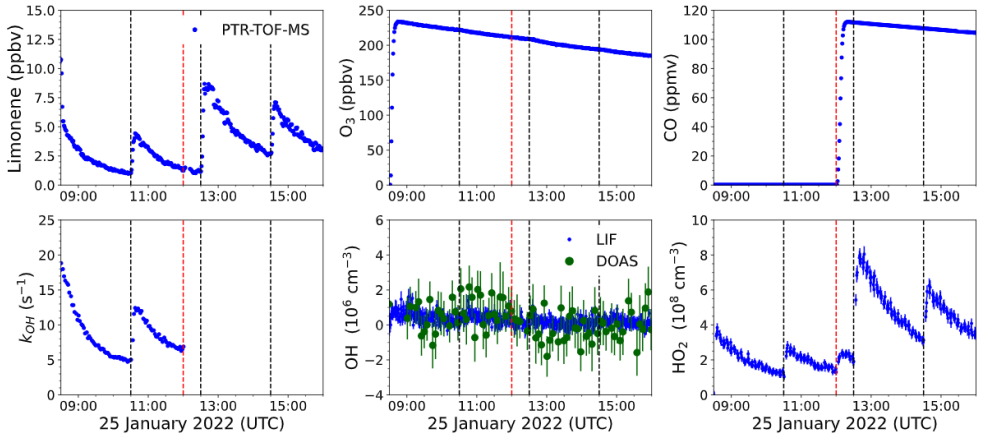

Figure 2-4. Overview of the radicals and trace gas measurements of one of the monoterpenes (sabinene) ozonolysis experiments. The black lines indicate when sabinene was injected into the chamber. The red line indicates when CO was injected into the chamber. The injection of CO suppressed the OH concentrations and increased the HO_2 concentration. OH reactivity (k_{OH}) was too high (~500 s^{-1}) to be measured after the injection of CO.

Photooxidation experiments were conducted in the illuminated chamber. Before the injection of monoterpenes, the chamber roof was opened for 30 minutes to 2 hours for determining the production rates of chamber-emitted species including HONO (Section 2.2). After that, about 2 ppbv to 6 ppbv of monoterpene was injected into the chamber to start the photooxidation experiment. Depending on the experiment, additional monoterpene (2 ppbv to 6 ppbv) was added into the chamber when nearly all monoterpene was oxidized. This was repeated once to twice over the course of an experiment.

In photooxidation experiments with medium NO mixing ratios, experiments were conducted following the procedure described above. NO mixing ratios were typically between 0.2 ppbv and 0.5 ppbv.

In photooxidation experiments with low NO mixing ratios, NO concentrations were further suppressed. This was achieved by adding about 60 ppbv to 100 ppbv of O_3 at the start of the experiment, so that NO mixing ratios were below 0.25 ppbv due to its reaction to O_3. The composition of RO_2 radicals in experiments with low NO mixing ratios was different from that in experiments with medium NO ratios, as the ozonolysis of monoterpenes gained importance at higher O_3 concentrations. Less than 10 % of monoterpene was lost in the reaction with O_3 in experiments with medium NO mixing ratio, whereas depending on the O_3 concentration, about 30 % to 60 % of monoterpene was lost in the reaction with O_3 in the experiments with low NO mixing ratios. Figure 2-5 and 2-6 illustrates typical trace gas and radicals concentrations of one of the photooxidation experiments at low NO mixing ratio and medium NO mixing ratio, respectively.

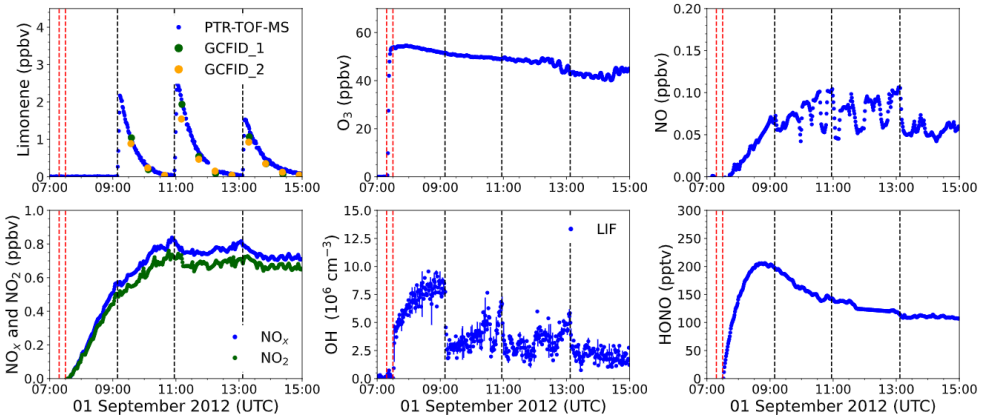

Figure 2-5. Overview of the radicals and trace gas measurements of one of the monoterpenes (limonene) photooxidation experiments with low NO mixing ratios. The black lines indicate when limonene was injected into the chamber. The leftmost red line indicates the injection of O_3 into the chamber; the second leftmost red line indicates the opening of chamber roof.

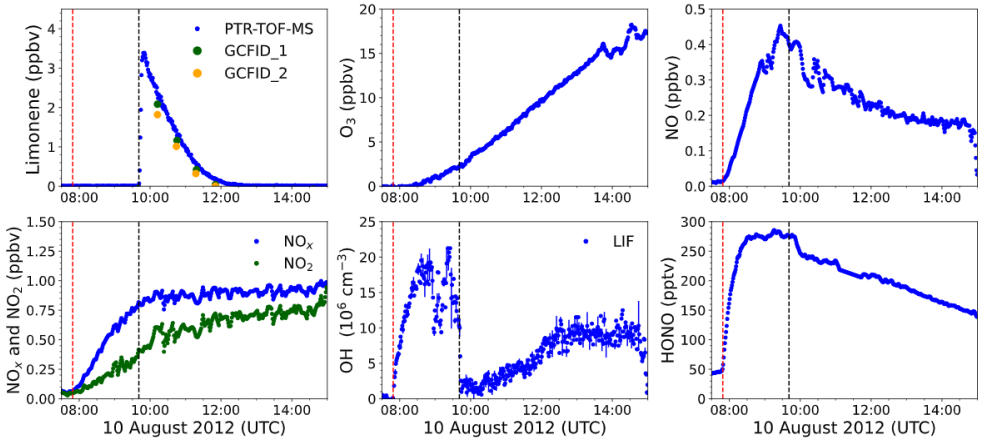

Figure 2-6. Overview of the radicals and trace gas measurements of one of the monoterpenes (limonene) photooxidation experiments at medium NO mixing ratios. The black line indicates when limonene was injected into the chamber. The red line indicates the opening of chamber roof.

Only one experiment was conducted to investigate the photooxidation of limonene under high NO mixing ratios (Section 4). In that experiment, NO concentrations were further elevated by injecting about 15 ppbv of NO during the zero-air phase of the experiment. About 10 ppbv to 12 ppbv of limonene was injected into the chamber (Fig. 2-7).

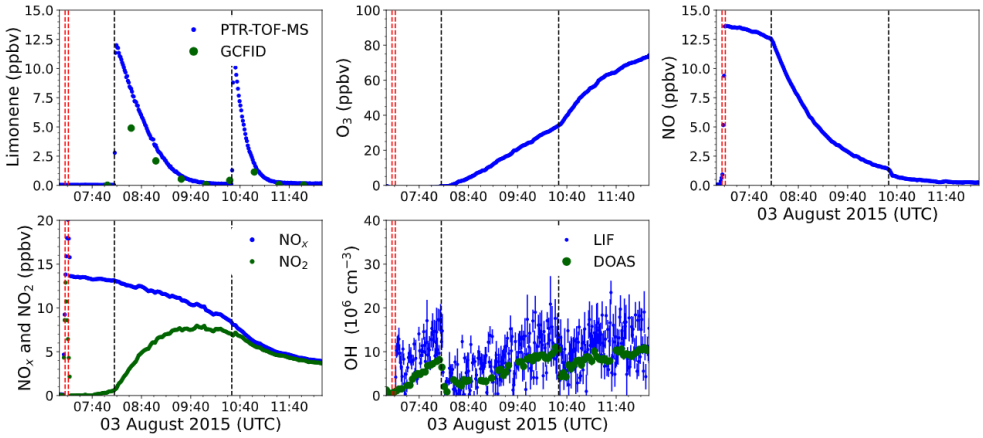

Figure 2-7. Overview of the radicals and trace gas measurements of the limonene photooxidation experiments with high NO mixing ratios. The black lines indicate when limonene was injected into the chamber. The leftmost red line indicates the injection of NO into the chamber; the second leftmost red line indicates the opening of chamber roof.

2.6 Plant emissions oxidation experiments conducted with the SAPHIR-PLUS and the SAPHIR chamber

Sweet chestnut trees of around 1 year old were used in the experiments investigating the emissions of trees. The trees were first placed outside under natural conditions with automatic irrigation for several months before the experiment. Four months before the start of the experiment, six trees were transferred into the SAPHIR-PLUS chamber for acclimating to the conditions inside (Fig. 2-8). To induce an early leaf emergence of the trees, the temperature inside the SAPHIR-PLUS chamber was maintained at around 25 °C. The trees were trimmed before being transferred into the SAPHIR-PLUS chamber.

In total five experiments were conducted in June and July 2022. For each experiment, the valve connecting SAPHIR-PLUS and the SAPHIR chamber was opened to transfer of VOCs into the dark clean SAPHIR chamber. The transfer process took about 1 to 2 days until the VOC concentration in the SAPHIR chamber were high enough, which was determined from OH reactivity measurements in the SAPHIR chamber. The OH reactivity of plant emissions that could be achieved was very low (~2.5 s^{-1}), when the SAPHIR-PLUS chamber was kept at ambient temperature (~25 °C). As emissions of monoterpenes from plants are known to increase with high temperature (Guenther et al., 1991), VOCs emissions were induced by increasing the temperature of SAPHIR-PLUS to around 30 °C to 35 °C. This was achieved by steadily ramping up the temperature in the SAPHIR-PLUS chamber two days before the transfer of VOCs. The maximum OH reactivity of the plant emissions in the SAPHIR chamber for a high temperature of the SAPHIR-PLUS chamber was 9 s^{-1} to 17 s^{-1}. The valve connecting the SAPHIR-PLUS and SAPHIR chamber was closed 1 hour before the start of the oxidation of plant emissions. The temperature of the SAPHIR-PLUS chamber was then gradually lowered to ambient levels (~25 °C) after the valve was closed to prevent prolonged heat stress on the plant that may affect the emission in the future (e.g., Kleist et al., 2012).

Three photooxidation and one ozonolysis experiments were performed (Table 2-2). Photooxidation experiments (04, 12, and 18 July 2022) were conducted with the opened chamber roof. In the experiment on 12 July 2022, about 10 ppbv of O_3 was injected 5 minutes after the opening of chamber roof to reduce the NO concentrations in the chamber. In the ozonolysis experiment, about 10 ppbv O_3 was injected into the dark chamber to initiate oxidation.

Concentrations of VOCs species were measured by GC-FID and PTR-TOF-MS in the SAPHIR chamber before and during the oxidation experiments to identify VOCs that were emitted from plants and produced during the oxidation of the emitted VOCs. The transfer efficiency of typical plant-emitted BVOCs from the SAPHIR-PLUS to the SAPHIR chamber was characterized in Hohaus et al. (2016) for different conditions. On average, only around 20 % of the VOC was lost during the transfer process, and no significant differences among various VOCs were observed. This indicates that the distribution of VOCs species measured in the SAPHIR chamber accurately represents the emissions of the plants.

Figure 2-8. Sweet chestnut trees were placed inside the SAPHIR-PLUS chamber.

Table 2-2. Experimental conditions of the plant emissions oxidation experiments. Values of $T_{SAPHIR\text{-}PLUS}$ were the mean temperature in the SAPHIR-PLUS chamber during the transfer of VOCs from SAPHIR-PLUS to the SAPHIR chamber; values of k_{OH_SAPHIR} were the maximum OH reactivity reached in the SAPHIR chamber contributed from the plant emissions; values of O_{3_SAPHIR}, NO_{SAPHIR} and OH_{SAPHIR} were the mean concentrations during the oxidation of the main plant emissions, which were derived from the time when the fastest decrease in OH reactivity was observed.

Date	$T_{SAPHIR\text{-}PLUS}$(°C)	k_{OH_SAPHIR} (s^{-1})	Injected O_3 (ppbv)	O_{3_SAPHIR} (ppbv)	NO_{SAPHIR} (ppbv)	OH_{SAPHIR} (10^6 cm^{-3})
29 June 2022[a]	ambient	2.5	45	/	/	/
04 July 2022	30	13	/	5	0.6	10
12 July 2022	31	17	10	15	0.4	10
18 July 2022	28	11	/	< 5	1.0	15
25 July 2022[b]	31	9	10	10	0	< 1

[a]Concentrations of OH-reactive VOCs were to low to be analyzed [b]Dark experiment

3. Methods for analyzing SAPHIR experiments in the SAPHIR chamber

3.1 Determination of the reaction rate coefficients of the oxidation of monoterpenes

This section describes the methods that were used to determine the reaction rate coefficients of the oxidation of monoterpene by OH radicals (k_{VOC+OH}) and O_3 (k_{VOC+O3}). Methods were developed and applied for the investigation of the reaction rate coefficients of the oxidation of sabinene, because only a few experimental data is available (Atkinson et al., 1990b). For the reaction rate coefficients of the oxidation of limonene, IUPAC has already proposed recommended reaction rate coefficients based on numerous experimental data (https://iupac.aeris-data.fr/, last access: 14 September 2023). Therefore, the reaction rate coefficients of the oxidation of limonene are not determined in this study. However, the method can be applied for investigating the reaction rate coefficient of OH- and O_3-oxidation for other VOCs.

3.1.1 Reaction rate coefficient of the ozonolysis reaction of sabinene kSAB+O3 in chamber experiments

In this section, the method to determine the reaction rate coefficient of the ozonolysis reaction of sabinene is presented. This method can also be generalized to other VOCs ozonolysis experiment performed in the SAPHIR chamber (Section 2.5, Fig. 2.4), where the VOC is oxidized by O_3 in the presence of an OH scavenger.

The loss rate of sabinene during an oxidation experiment in the SAPHIR chamber can be described by the differential equation:

$$\frac{d[\mathrm{SAB}]}{dt} = -[\mathrm{SAB}](k_{\mathrm{SAB+O_3}}[\mathrm{O_3}] + k_{\mathrm{SAB+OH}}[\mathrm{OH}] + k_{\mathrm{dil}}) \qquad \text{Equation 3-1}$$

where k_{SAB+OH} is the reaction rate coefficient of the photooxidation of sabinene; and k_{dil} is the dilution rate coefficient of the chamber determined from the flow rate of the replenish air. An OH scavenger was added to the chamber air around halfway of the ozonolysis experiments and consumed more than 95 % of the OH radicals (Section 2.5, Fig. 2.4). In this case, Equation 3-1 can be simplified to

$$\frac{d[\mathrm{SAB}]}{dt} = -[\mathrm{SAB}](k_{\mathrm{SAB+O_3}}[\mathrm{O_3}] + k_{\mathrm{dil}}) \qquad \text{Equation 3-2}$$

By solving the differential equation Equation 3-2, the reaction rate coefficients k_{SAB+O3} can calculated from the integrated loss of sabinene to O_3 and dilution within the time interval t' = 0 to t' = t:

$$\ln\frac{[\mathrm{SAB}]_0}{[\mathrm{SAB}]_t} = k_{\mathrm{SAB+O_3}}\int_0^t [\mathrm{O_3}]_{t'}dt' + \int_0^t k_{\mathrm{dil}}dt' \qquad \text{Equation 3-3}$$

$$k_{\mathrm{SAB+O_3}} = \frac{\ln\frac{[\mathrm{SAB}]_0}{[\mathrm{SAB}]_t} - \int_0^t k_{\mathrm{dil}}dt'}{\int_0^t [\mathrm{O_3}]_{t'}dt'} \qquad \text{Equation 3-4}$$

The uncertainty of the reaction rate coefficient k_{SAB+O3} determined with this method is about 25 %, which is associated with the precision of the sabinene concentrations measurements (10 %), the accuracy of the O_3 measurements (5 %), and the choice of the time interval for the calculation. The error from the accumulated dilution loss is insignificant as less than 5 % of sabinene was lost by dilution. The value of k_{SAB+O3} in Equation 3-4 depends on the time interval of integration. The integration starts at the time when the sabinene concentration reached its maximum for each injection of sabinene until the end of the experiment or the next sabinene injection, which is about 1 hour to 2 hours after the injections of sabinene. The value of rate coefficient k_{SAB+O3} is then determined from the mean value of k_{SAB+O3} calculated from every integration time step.

3.1.2 Determination of the temperature-dependency of the reaction rate coefficient of the photooxidation reaction in OH reactivity measurements

In this section, the setup and the method to determine the temperature dependence reaction rate constant of the OH-oxidation of sabinene (k_{SAB+OH}) at temperatures between 284 K and 340 K with OH reactivity measurements are presented. The principle of the OH reactivity measurement with laser flash-photolysis laser-induced fluorescence can be referred to the description in Section 2.4.2. Again, this method can be generalized to other VOCs.

First, a gas canister containing a mixture of sabinene in synthetic air was prepared by evaporating liquid sabinene in an evacuated SilcoNert coated canister (Roth Chemicals, GC grade, purity > 98 %). The sabinene vapor was then mixed with pure synthetic air prepared from ultra-pure liquid nitrogen and oxygen (79 % N_2, 21 % O_2, Linde, purity > 99.9999 %) resulting in a sabinene mixing ratio of 6 ppmv. The concentration of sabinene was determined with the total organic carbon (TOC) method, in which sabinene was first flowed through a pre-oven at 760 °C (1033 K) and then over a palladium catalyst at 500 °C (773 K). Sabinene was completely oxidized by the palladium catalyst and the concentration of the carbon dioxide produced from the oxidation was measured with a cavity ring-down spectrometer (CRDS, Picarro). Assuming that all carbon stems from sabinene, its concentration in the canister can be calculated from the measured CO_2 concentration.

In the OH reactivity instrument, a flow of 10 sccm sabinene was mixed with 20,000 sccm of humidified synthetic air with water mixing ratio of about 1.0 % together with O_3. The temperature of the flow tube is controlled by circulating water which temperature can be changed within a range of 10 °C to 70 °C (283 K to 343 K). The temperature is monitored with two PT100 temperature sensors. All flows were controlled by calibrated mass flow controllers. The sabinene mixing ratio in the flow was circa 5 ppbv. The O_3 concentration in the flow tube was 22 ppbv measured by an O_3 analyzer.

In total, three experiments were performed to measure the rate coefficients of the reaction of sabinene and OH (k_{SAB+OH}) at seven different temperatures between 10 °C to 70 °C (283 K to 343 K). Two batches (A and B) of sabinene gas mixtures were measured, with batch A being measured twice. After reaching a stable temperature, the OH reactivity of the air without sabinene (zero reactivity) was first measured for about 30 minutes, followed by the measurement of air with sabinene for another 40 minutes. The

procedure was then repeated at different temperatures. The OH reactivity of air with sabinene was subtracted by its corresponding zero reactivity ranging from 2 s^{-1} to 3 s^{-1}. The rate coefficient of the OH reaction was calculated by using the sabinene concentration in the canister ($[SAB]_0$) and the dilution factor f_{dil} determined from the flow rates:

$$k_{SAB+OH} = k_{OH,SAB} \cdot ([SAB]_0 \cdot f_{dil})^{-1} \quad \text{Equation 3-5}$$

The determination of the sabinene concentration in the canister with the TOC method is the predominant contributor to the uncertainty of the calculated reaction rate coefficients, resulting in uncertainties of about 2.5 % to 5.0 %. The loss of sabinene to O_3 can be neglected (0.005 % at 293 °C) due to low ozone concentration and the short residence time of less than two seconds in the flow tube. The temperature dependence of the reaction rate coefficient k_{SAB+OH} can be expressed by the Arrhenius equation:

$$k_{SAB+OH}(T) = A \cdot \exp\left(-\frac{E_A}{RT}\right) \quad \text{Equation 3-6}$$

where A is a pre-exponential factor, E_A is the activation energy, T is the temperature and R is the universal gas constant. The temperature dependence coefficient $-E_A/R$ is determined by a regression analysis of the logarithm of the reaction rate coefficient k_{SAB+OH} as a function of the inverse temperature.

3.1.3 Determination of the reaction rate coefficient of the photooxidation reaction k_{VOC+OH} in chamber experiments

The reaction rate coefficient of the oxidation reaction of sabinene by OH radicals can also be determined from the chamber experiments. This was done by conducting model simulations using a simplified chemical model as described in Hantschke et al. (2021).

The rate coefficient k_{SAB+OH} was determined by minimizing the root-mean-square error between sabinene concentrations measured by the PTR-TOF-MS instrument. The simplified model includes the chemical loss of sabinene by the reactions with OH and O_3, and by dilution. OH and O_3 concentrations were constrained to measurements. No further other secondary chemistry was included. The rate coefficient k_{SAB+O3} implemented in the model is adopted from literature value determined in room temperature (8.3×10^{-17} cm^3 s^{-1}, Cox et al., 2020), where the temperature is similar to the photooxidation experiments in SAPHIR.

Model simulations were only conducted for experiments with medium NO mixing ratio (Section 2.4), because the contribution of the OH reaction to the total loss of sabinene was more than 90 % in these experiments, such that the loss of sabinene to O_3 can be neglected. A value of the reaction rate coefficient k_{SAB+OH} was obtained for each injection of sabinene in the experiments with medium NO mixing ratio and each available OH instrument. The mean and standard deviation of the rate coefficient are then calculated from every injection. Since the chamber temperature varied from 20 °C to 35 °C (293 K to 308 K) between different photooxidation experiments with medium NO mixing ratios, the value of the reaction rate coefficient k_{SAB+OH} with this method could only represent the rate coefficient at near room temperature. Therefore, the reaction rate coefficient k_{SAB+OH} determined from the chamber experiment was only used to validate the value determined from the laboratory experiments using OH reactivity measurements.

3.2 Calculation of product yields

3.2.1 Calculation of the VOCs yield

Product yield of VOCs from the oxidation of monoterpenes can be calculated from the chamber experiments if they are measured by PTR-TOF-MS. The calculation of the product yield of VOCs species followed the method adopted in Kaminski et al. (2017) and Rolletter et al. (2019), in which the measured concentrations of organic products are corrected for their production from chamber emissions and loss due to dilution, photolysis, and chemical loss in their reaction with OH. Using product species *x* as an example, the loss rate can be expressed as:

$$x_{\mathrm{loss}} = -(k_{dil} + k_{x+\mathrm{OH}}[\mathrm{OH}] + j_x)[x] \qquad \text{Equation 3-7}$$

where [*x*] is the concentration of the product species; k_{dil} is the dilution constant measured during the experiment; $k_{x+\mathrm{OH}}$ is the reaction rate coefficient of the reaction between species *x* with OH; j_x is the photolysis rate coefficient for species *x*. If available, values of reaction rate coefficient $k_{x+\mathrm{OH}}$ are taken from IUPAC recommendations (e.g., HCHO and acetone). For species that do not have a recommended $k_{x+\mathrm{OH}}$ value by IUPAC, literature values are used instead (e.g., sabinaketone from the oxidation of sabinene). Values of photolysis rate constant j_x were measured for HCHO (j_{HCHO}) and acetone (j_{acetone}) in the experiments. For product species that do not have a measured photolysis rate constant, it is assumed their photolysis rate constants are similar to j_{HCHO} or j_{acetone}, which depends on the functional groups present in that species.

For the determination of HCHO and acetone yields, their concentrations are further corrected by their production rates from the chamber source (Q_x) that are determined by matching the increase of HCHO and acetone concentrations during the zero-air phase (Section 2.3). For species that are not produced from the chamber, the value of Q_x is zero.

The corrected concentration of product species ($[x]_{\mathrm{corr}}$), which is the concentration of the target species produced solely by the oxidation of monoterpenes, is then iteratively calculated using the following formula:

$$[x]_{\mathrm{corr}_{t+1}} = [x]_t + (\mathrm{x}_{\mathrm{loss}_t} - Q_{x_t})\Delta t \qquad \text{Equation 3-8}$$

The yield of product species can be calculated by comparing $[x]_{\mathrm{corr}}$ to the amount of reacted monoterpene. The amount of reacted monoterpene ($[\mathrm{terpene}]_{\mathrm{reacted}}$) can be calculated with the following equation:

$$[\mathrm{terpene}]_{\mathrm{reacted}_{t'}} = \int_{t=0}^{t=t'} ([\mathrm{terpene}]_t \cdot (k_{\mathrm{terpene+OH}}[\mathrm{OH}]_t + k_{\mathrm{terpene+O_3}}[\mathrm{O_3}]_t))\, dt \qquad \text{Equation 3-9}$$

where $[\mathrm{terpene}]_{\mathrm{reacted\_}t'}$ is the total amount of reacted terpene at time *t'*.

3.2.2 Calculation of the organic nitrate yield

The calculation of total organic nitrate yield of the photooxidation of monoterpenes and other VOCs requires measurements of NO, NO_2, and HONO mixing ratios. The method follows the description in Tan et al. (2021) and Hantschke et al. (2021), which is based on the difference between the total nitrogen production in the chamber and the concentrations of nitrogen species except organic nitrates.

Figure 3-1 illustrates the nitrogen chemistry considered in the calculation of the organic nitrate yield of the photooxidation of VOC. The total production of nitrogen oxides from the chamber can be calculated from the well-defined source strength of HONO (Q(HONO)), since HONO is the only source of the reactive nitrogen in the chamber. HONO produced from the chamber is photolyzed by sunlight to form OH radicals and NO. Under typical conditions, the lifetime of HONO due to photolysis is about 30 minutes. As HONO can be reformed by the reaction in NO with OH radicals, a photostationary state between OH, NO, and HONO is reached within several minutes. If there is a small change in the intensity of radiation that affects the chamber source strength Q(HONO) and photolysis frequency j_{HONO}, concentrations rapidly re-equilibrate in the photostationary state, the production of HONO from the chamber emission and the reaction of OH and NO is balanced by the loss of HONO from photolysis. The source strength Q(HONO) can then be calculated from measured HONO, OH, and NO concentrations, as well as the measured photolysis rate j_{HONO}:

$$\frac{d[\mathrm{HONO}]}{dt} = Q(\mathrm{HONO}) - j_{\mathrm{HONO}}[\mathrm{HONO}] + k_{\mathrm{OH+NO}}[\mathrm{OH}][\mathrm{NO}] \approx 0 \qquad \text{Equation 3-10}$$

$$Q(\mathrm{HONO}) = j_{\mathrm{HONO}}[\mathrm{HONO}] - k_{\mathrm{OH+NO}}[\mathrm{OH}][\mathrm{NO}] \qquad \text{Equation 3-11}$$

The concentration of NO_y (=NO_2 + NO + HONO) is the total reactive nitrogen accumulated over the course of the experiment after taking account into the accumulated loss of NO_y. Loss processes of NO_y include dilutions, the production of nitric acid (HNO_3) from the reaction in NO_2 and OH radicals, and the production of organic nitrates ($RONO_2$) from the reaction of NO with RO_2 radicals. It is assumed that nitric acid and organic nitrates do not photolyze back to NO_y. In addition, the calculation does not consider the potential production of peroxyacetyl nitrates (PANs) from the reaction of acetylperoxy radicals and NO_2. The loss rate of NO_y from dilution ($L_{NOy,dil.}$) can be calculated from the dilution rate constant (k_{dil}) in the chamber and the measured NO_y concentration:

$$L_{\mathrm{NO_y,dil.}} = k_{\mathrm{dil}}([\mathrm{NO_2}] + [\mathrm{NO}] + [\mathrm{HONO}]) \qquad \text{Equation 3-12}$$

Typical values of k_{dil} are about 10^{-6} s^{-1}, which can be calculated from the replenishment flow rate. The production rate of nitric acid is calculated from the measured OH and NO_2 concentrations. By considering the accumulated productions and losses of NO_y, the concentration of NO_y can be described as follows:

$$[\mathrm{NO_y}](t) = \int_0^t (Q(\mathrm{HONO})(t) - k_{\mathrm{OH+NO_2}}[\mathrm{OH}](t)[\mathrm{NO_2}](t) - L_{\mathrm{NO_y,dil.}}(t))dt - [\mathrm{RONO_2}](t) \qquad \text{Equation 3-13}$$

By rearranging Equation 3-13, the concentration of total organic nitrates is the accumulated production of nitrogen subtracted by the accumulated loss of from dilution, the production of nitric acid, and the current concentration of NO_y:

$$[\mathrm{RONO_2}](t) = \int_0^t (Q(\mathrm{HONO})(t) - k_{\mathrm{OH+NO_2}}[\mathrm{OH}](t)[\mathrm{NO_2}](t) - L_{\mathrm{NO_y,dil.}}(t))dt - [\mathrm{NO_y}](t) \qquad \text{Equation 3-14}$$

The concentrations of total organic nitrate can also be calculated from the amount of RO_2 derived from the OH-oxidation of VOC that reacts with NO having a nitrate yield ϕ_{VOC}.

$$[\mathrm{RONO_2}](t) = \phi_{\mathrm{VOC}} \int_0^t (\mathrm{RO_{2,VOC+OH}}(t) \times [\mathrm{NO}](t) \times k_{\mathrm{RO2+NO}})dt \qquad \text{Equation 3-15}$$

The concentration of RO_2 derived from the oxidation of OH can be estimated from the ratio of OH reactivity contributed by limonene to the measured total OH reactivity (k_{OH}) minus the contributions from inorganic species such as NO_x and O_3 ($k_{OH,inorg}$), as well as and HCHO ($k_{OH,HCHO}$). This is justified because the oxidation of an organic species by an OH radical except HCHO, leads to the production of a RO_2 radical.

$$\mathrm{RO_{2,VOC}} = \mathrm{RO_2} \frac{k_{\mathrm{OH,VOC}}}{k_{\mathrm{OH}} - k_{\mathrm{OH,HCHO}} - k_{\mathrm{OH,inorg}}} \qquad \text{Equation 3-16}$$

RO_2 radicals could be also produced from the ozonolysis of the target VOC, if it contains a C=C double bond. However, their concentrations cannot be easily estimated like RO_2 derived from the OH-oxidation using Equation 3-16. Therefore, this analysis is only applicable for experiments with medium NO mixing ratio, where limonene predominantly (> 90%) reacted with OH.

The total organic nitrate yield can be determined from the linear regression using Equation 3-14 and Equation 3-15. The uncertainty of organic nitrates concentrations (Equation 3-14) is about 21 %, which is mainly due to the uncertainty of the HONO photolysis rate used to calculate the chamber source of HONO (Q(HONO)) from Equation 3-11. The uncertainty of the organic nitrate concentration [$RONO_2$] in Equation 3-15 is about 35 %, which is due to the accuracies of the reaction rate coefficient k_{RO2+NO} (30 %), measurements of the NO concentration (5 %) and the calculated of $RO_{2,VOC+OH}$ (17 % for limonene, Equation 3-16). It should be noted that the calculation does not take account into the potential production of peroxyacyl nitrates (PANs) from the reaction in acyl peroxy radicals with NO_2, which may lead to an overestimation of the determined organic nitrate yield. Acyl peroxy radicals are produced from the O_2-addition of the acyl radicals, which are generally produced from secondary chemistry such as the aldehydic H-abstraction by OH radicals and the dissociation of an alkoxy radical with an α-oxo function group. Therefore, it is expected the production of acyl radicals only become more prominent at the later stage of a VOC photooxidation experiment when the secondary chemistry gain importance, or when VOC is mainly oxidized by O_3 that yields aldehyde and thereby potentially acyl radicals.

For the determination of nitrate yield of RO_2 derived from limonene oxidation, analysis was only conducted with photooxidation experiments with medium NO concentrations that have low O_3 concentrations. The time period of the analysis is also limited to the time when limonene was presence to reduce the potential impacts of secondary chemistry.

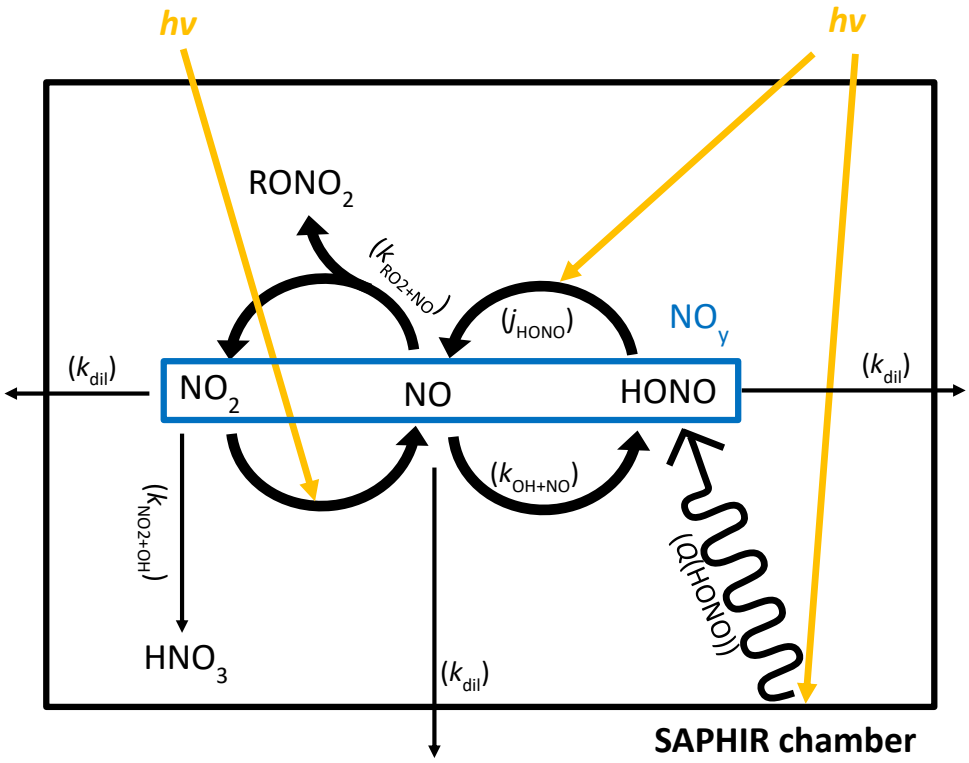

Figure 3-1. Nitrogen chemistry considered in the calculation of the total organic nitrate yield during a photooxidation experiment in SAPHIR. The rate coefficients of the processes are enclosed in parentheses.

3.2.3 Calculation of the OH yield from the ozonolysis reaction

The OH yield of the ozonolysis of sabinene is determined in this study using measurements in the ozonolysis experiments. The method for calculating the OH yield of the ozonolysis reaction can also be applied to limonene and other VOCs as well. Here, the description below is taking sabinene as an example.

The calculation of the OH yield of the sabinene ozonolysis reaction is based on the difference in loss rates of sabinene in the ozonolysis experiment with and without an OH scavenger. The loss rate constant of sabinene in the presence of an OH scavenger gives the ozonolysis rate coefficient (k_{SAB+O3}, Section 3.1.1). Without an OH scavenger, the differential equation Equation 3-1 is solved but the O_3 concentration and the dilution rate are treated as a constant instead of time-dependent variables:

$$\frac{d[\mathrm{SAB}]}{dt} = -[\mathrm{SAB}](k_{\mathrm{SAB+O3}}\langle[\mathrm{O_3}]\rangle_t + k_{\mathrm{SAB+OH}}\langle[\mathrm{OH}]\rangle_t + \langle k_{\mathrm{dil}}\rangle_t) \qquad \text{Equation 3-17}$$

where $\langle[x]\rangle$ are the mean value of variable x within the selected time interval. To calculate the OH yield of the ozonolysis of sabinene, the OH concentration is calculated from the balance of the OH production rate (P_{OH}) and its destruction rate that includes the OH reactivity (k_{OH}). In the ozonolysis experiment, OH radicals were mainly produced from the reaction of HO_2 with O_3 and the from the ozonolysis reaction. For the expression of OH reactivity, it is simplified to only consider the contribution from sabinene, as contributions from species other than sabinene (O_3, sabinaketone, HCHO, acetone etc.) to the total OH reactivity were less than 10 % until half of the injected sabinene reacted away. Overall, the OH concentration can be expressed as

$$[\mathrm{OH}] = \frac{P_{\mathrm{OH}}}{k_{\mathrm{OH}}} \approx \frac{k_{\mathrm{HO2+O3}}[\mathrm{O_3}][\mathrm{HO_2}] + k_{\mathrm{SAB+O3}}[\mathrm{O_3}][\mathrm{SAB}]\gamma_{\mathrm{SAB}}}{k_{\mathrm{SAB+OH}}[\mathrm{SAB}]} \qquad \text{Equation 3-18}$$

where γ_{SAB} is the OH yield of the sabinene ozonolysis reaction. To reduce the uncertainty associate with the assumptions in Equation 3-18, the time interval selected for the calculation of OH yield is shorter (30 minutes to 1 hour after the injection of sabinene) than that for the calculation of reaction rate coefficient k_{SAB+O3} (1 hour to 2 hours after the injection).

With a short time interval selected for the calculation of the OH yield, the whole calculation can be further simplified by replacing the integrated loss of sabinene to O_3, and dilution in Equation 3-3 with mean O_3 concentrations and dilution rate, respectively. This is because the uncertainty associated the variation of O_3 concentration and dilution reduce when the selected time interval for analysis is shorter. The loss rate of sabinene can be expressed as:

$$\ln(\frac{[\mathrm{SAB}]_0}{[\mathrm{SAB}]_t}) + a = k_{\mathrm{loss}}t = (k_{\mathrm{SAB+O3}}\langle[\mathrm{O_3}]\rangle_t + k_{\mathrm{SAB+OH}}\langle[\mathrm{OH}]\rangle_t + \langle k_{\mathrm{dil}}\rangle_t)\, t \qquad \text{Equation 3-19}$$

where k_{loss} is the regression coefficient of the fitted exponential decay of the measured sabinene concentrations; a is the regression intercept. Using the regression method for the calculation of OH yield is more robust than calculating the integrated loss of sabinene, as it is less affected by the choice of time interval for calculation.

Combining Equation 3-18 and Equation 3-19, the expression of the loss rate constant k_{loss} and the OH yield γ_{SAB} during the ozonolysis experiment without an OH scavenger becomes:

$$k_{\mathrm{loss}}\ (\text{without CO}) = k_{\mathrm{SAB+O3}}\langle[\mathrm{O_3}]\rangle_t + \frac{k_{\mathrm{HO2+O3}}[\mathrm{O_3}][\mathrm{HO_2}]+k_{\mathrm{SAB+O_3}}[\mathrm{O_3}][\mathrm{SAB}]\gamma_{\mathrm{SAB}}}{[\mathrm{SAB}]} + \langle k_{\mathrm{dil}}\rangle_t \quad \text{Equation 3-20}$$

$$\frac{k_{\mathrm{loss}}-\langle k_{\mathrm{dil}}\rangle_t-\frac{k_{\mathrm{HO2+O3}}[\mathrm{O_3}][\mathrm{HO_2}]}{[\mathrm{SAB}]}}{\langle[\mathrm{O_3}]\rangle_t} = k_{\mathrm{SAB+O_3}}(1+\gamma_{\mathrm{SAB}}) \quad \text{Equation 3-21}$$

where k_{SAB+O3} is the ozonolysis rate coefficient determined from the ozonolysis experiment after the OH scavenger was added (Equation 3-4), assuming k_{SAB+O3} did not change before and after the injection of the OH scavenger. The uncertainty of the OH yield of the ozonolysis of sabinene γ_{SAB}, which depends on the uncertainty of k_{SAB+O3}, could be as high as 50 % as the loss of sabinene to OH radicals is less important than that to O_3. It is expected that the relative uncertainty of the OH yield of the ozonolysis of a VOC species (γ_{VOC}) could be reduced, if the value of γ_{VOC} is high.

It is worth noting that potential systematic errors of about -20 % are not considered in the calculation, which arises from the assumption that the entire OH reactivity k_{OH} results from only sabinene (Equation 3-18), and from the temperature difference of 2 °C to 4 °C between the ozonolysis experiments with and without an OH scavenger caused by the gradual warming of the chamber during daytime. The value of the ozonolysis reaction rate coefficient k_{SAB+O3} could be lower by 10 % to 15 % at a temperature at 276 K than at temperature of 280 K. This is estimated from the temperature dependence of ozonolysis rate coefficients of structurally similar methylpropene and β-pinene, for which ozonolysis temperature dependent reaction rate coefficients are reported in Cox et al. (2020).

3.3 Model calculations

The limonene oxidation experiments were analyzed by comparing measurements with results from model calculations with the limonene oxidation mechanism from the Master Chemical Mechanism version 3.3.1 (MCM, http://chmlin9.leeds.ac.uk/MCM/, last access: 30 June 2023). MCM is a semi-explicit chemical mechanism that is constructed based on a defined protocol described in Jenkin et al. (1997). It includes the chemistry of four types of initialization of oxidation reaction (photolysis, and the oxidation by OH, O_3, and NO_3) for precursor VOCs and closed-shell products, as well as the chemistry of intermediates species including alkoxy radicals (RO), peroxy radicals (RO_2), excited Criegee intermediates, and stabilized Criegee intermediates. The kinetic parameters of the reactions are implemented based on IUPAC recommendation and structure activity relationship (SARs) (Jenkin et al., 1997).

The model used in the calculation is a zero-dimensional box model that calculates time series of trace gas concentrations by numerically solving the differential equations of the chemical reactions. In addition to the MCM mechanism, production of chamber sources species such as HONO, NO_2, HCHO, and acetone are included in the simulations.

Temperature, humidity, pressure, and photolysis frequencies are constrained in the model calculations with measurements in all simulation model runs. The production rates of chamber sources are optimized for each experiment by scaling the parameterization to match the observed concentrations of chamber source species during the zero-air phase. It is assumed that the parameterization can be extrapolated for the remaining of the experiment (Section 2.2). A background OH reactivity of about 1 s^{-1} to 2 s^{-1} is observed in the clean illuminated chamber due to the presence of unmeasured chemical species emitted from the chamber Teflon film. To describe the effect of these OH reactants, an artificial OH reactant that has the same chemical properties as CO is implemented in the model. The amount of this artificial reactant is adjusted to match measured the background OH reactivity during the zero-air phase in each experiment. It is assumed the background OH reactivity did not change throughout the experiment.

To estimate the importance of different loss pathways for RO_2 radicals through bi-molecular reactions in the experiments with different conditions, the RO_2 loss rate constant to bi-molecular reactions (k_{RO2}) can be calculated from the following expression:

$$k_{\mathrm{RO_2}} = k_{\mathrm{RO_2+NO}}[\mathrm{NO}] + k_{\mathrm{RO_2+HO_2}}[\mathrm{HO_2}] + k_{\mathrm{RO_2+RO_2}}[\mathrm{RO_2}] \qquad \text{Equation 3-22}$$

where k_{RO2+NO} (9×10^{-12} cm^3 s^{-1}), $k_{RO2+HO2}$ (2×10^{-11} cm^3 s^{-1}), and $k_{RO2+RO2}$ (1×10^{-12} cm^3 s^{-1}) are the reaction rate constants for the reaction of RO_2 derived from the OH reaction of limonene (C_{10}-RO_2) with NO, HO_2, and other RO_2 at 298 K, respectively. The values are adopted from the structure-activity relationship (SAR) described in Jenkin et al. (2019). The value of reaction rate constant $k_{RO2+RO2}$ is the upper limit of the self-reaction rates of C_{10}-RO_2 derived in the SAR.

Concerning the analysis of the experiments with limonene, four simulation model runs are performed for each experiment. In all model runs, physical parameters including temperature, pressure, photolysis frequencies, and the dilution rate of trace gases due to the replenishment flow are constrained to observations. If available, HONO concentrations are prescribed as measured to constrain the production from the chamber. In addition, ozone concentrations in the model are constrained to ensure that shortcomings of the model to predict ozone do not complicate the interpretation by an inappropriate fraction of limonene reacting with ozone. Time series of NO and NO_2 concentrations are constrained to observations in the model runs except for the fourth set of simulations to avoid potential impacts of shortcomings of the model to describe these species.

The four model runs include:

- reference model runs (Section 4.3.2), in which radical concentrations and OH reactivity were not constrained to measurements;
- constrained model runs (Section 4.3.2), in which HO_2 radical concentrations were constrained to measured values and the OH reactivity was adjusted to match the measurement; and
- optimized model runs (Section 4.3.6), in which additional reaction pathways were implemented in the model to test if they can improve agreement between simulation and measurements for radical concentrations and the OH reactivity; and

- NO_x model runs (Section 4.3.5), in which NO and NO_2 concentrations were not constrained to measurements for investigating the fate of nitrogen oxides. Radical concentrations and the OH reactivity were free parameters in the model. The nitrate yield of the RO radicals from the oxidation of limonene in the MCM model is updated from 22 % in the MCM model to 34 % determined in this experiment.

The purpose of the constrained model runs is to test whether there is a significant, unaccounted OH source that is not implemented in the MCM. This can be done by evaluating the modelled OH concentrations, after constraining the reaction rate of all known OH-producing reactions and matching the OH destruction rate to measurements. The former can be essentially done by constraining the HO_2 concentration to measurements and thereby the reaction rate of the reaction HO_2+NO, which is the main OH source during the photooxidation of limonene. However, the OH destruction rate cannot be constrained simply by forcing the modelled OH reactivity to be the measurements, because it is calculated from the concentration of all OH reactants.

From the simulation results of reference model runs, the OH reactivity from oxidation products were all overestimated by the model (Section 4.3.2). Potential reasons include wall loss reactions of low-volatility compounds such as organic nitrates and peroxides, uncertainties from the reactivity of products, intermediates that are mostly derived using structure–activity relationship (SAR) in the model (Jenkin et al., 1997; Saunders et al., 2003), and chemical loss due to reactions that are not included in the MCM (e.g., isomerization reactions). Therefore, OH reactivities in the constrained model runs are reduced by assuming organic nitrates and peroxides derived from limonene oxidation undergo a first-order loss process.

The additional loss rate for organic nitrates is estimated from the decaying signal at the corresponding mass to charge ratio of the least oxidized C_{10} nitrate species ($C_{10}H_{17}NO_6$) observed by the chemical ionization mass spectrometry (CIMS) instrument after the chamber roof was closed in the experiment with high NO concentrations. The lifetime of the least oxidized species C_{10} nitrate is used to estimate the loss rate, as the only C_{10} nitrate species from limonene oxidation that the MCM includes is $C_{10}H_{17}NO_4$. The loss rate constant is equivalent to a lifetime of about 2 h (Fig. 3-2, Zhao et al., 2018), which is comparable to the chemical loss rate in the reaction with OH for conditions of these experiments (chemical lifetime of 0.5 to 4 h). The specific reason for the additional loss of nitrates could not be identified but might be due to wall loss or due to loss by hydrolysis reactions in the humidified air, similar to findings in an isoprene rich forest (Romer et al., 2016).

Organic peroxides could not be detected by the CIMS instrument, and hence the additional loss rate is adjusted such that the simulated OH reactivity agrees with measurements in the experiments with low and medium NO when there should have been significant production of organic peroxides. This requires a lifetime of 10 min, much shorter than the lifetime on the order of hours under typical atmospheric conditions or those in the current experiments.

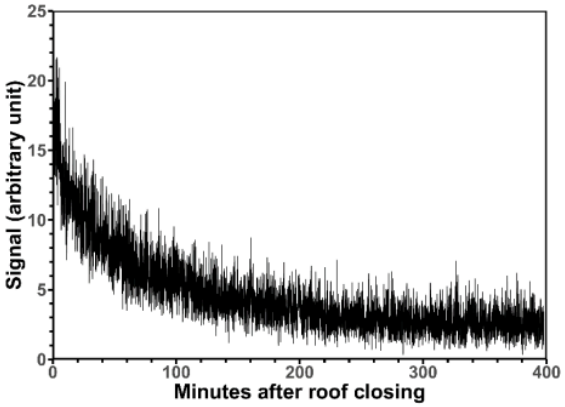

Figure 3-2. Nitrate ion CIMS signal for the compounds $C_{10}H_{17}NO_6$ during a limonene photooxidation experiment at high NO mixing ratios of 10 ppbv (Zhao et al., 2018). The rate constant of the signal is 8.5×10^{-3} s^{-1}.

3.4 Analysis of the chemical budget of radicals

3.4.1 Calculation of the chemical budget of OH radicals

The chemical budget of OH radicals during the oxidation of monoterpenes was calculated using the measurements in the chamber experiments. Since the lifetimes of the radical species in a typical SAPHIR experiment are very short (OH: < 1 s, HO_2 and RO_2: 2 s to 100 s), production rates of the radical species must equal their destruction rates on the same scale of the measurement time resolution. By considering radical production and destruction pathways that are typically included in atmospheric chemistry models, insights can be provided into if there are missing radical production pathways for example from fast RO_2-isomerization reactions (e.g., Fuchs et al., 2013; Novelli et al., 2020).

The destruction rate of OH radicals was calculated from the product of OH reactivity and OH concentration measurements (Hofzumahaus et al., 2009). In experiments with OH measurements by both DOAS and LIF, measured OH concentrations by DOAS were used for the calculation of the destruction rate of OH radicals as measurements by DOAS do not require calibration. OH concentrations measured by LIF were used for the calculation of the destruction of OH radicals in the ozonolysis experiments, due to the lower 1σ precision value of the LIF measurements and low OH concentrations in the ozonolysis experiments. The uncertainty of the OH destruction rate is about 16 %, which is calculated by error propagation of the measurement uncertainties.

Reactions producing OH radicals that were considered in the chemical budget analysis in this work are summarizes in Table 3-1, which include the photolysis of HONO and O_3, the reactions of HO_2 with NO and O_3, as well as the ozonolysis reaction of monoterpenes. Uncertainties of the production rates of OH radicals from these reactions are calculated from uncertainties of measurements and reaction rate coefficients (Atkinson et al., 2004; Cox et al., 2020).

Table 3-1. List of the reactions producing OH radicals considered in the analysis of chemical budget of radicals. Unless specified, reaction rate coefficient are given for room temperature of 298 K and 1 atm pressure.

Reaction	k	1σ uncertainty[b] (%)	Reference
HONO + $h\nu$ → OH + NO	j_{HONO}	35[c] 21[d]	Measured
O_3 + $h\nu$ → $O(^1D)$ + O_2	ϕ_{OH}[a], j_{O3}	19	Measured
HO_2 + NO → OH + NO_2	8.8×10^{-12} cm^3 s^{-1}	26	Atkinson et al. (2004)
HO_2 + O_3 → OH + $2O_2$	2.0×10^{-15} cm^3 s^{-1}	28	Atkinson et al. (2004)
Sabinene + O_3 → 0.26OH + 0.26RO_2	8.3×10^{-17} cm^3 s^{-1} (298 K)	105	Cox et al. (2020)
	3.7×10^{-17} cm^3 s^{-1} (278 K)	105	This study
Limonene + O_3 → 0.66OH + 0.66RO_2	2.1×10^{-16} cm^3 s^{-1}	25	Cox et al. (2020)
β-ocimene + O_3 → 0.55OH + 0.55RO_2	5.1×10^{-16} cm^3 s^{-1}	50	Cox et al. (2020)

[a]Yield of OH radicals of the photolysis of the photolysis of O_3 [b]Total 1σ uncertainty of the reaction: including uncertainties from measurements and reaction rate coefficients. [c]Experiments without HONO measurements, HONO concentration is estimated based on OH, NO, and j_{HONO} measurements during the zero-air phase with an uncertainty of 30 %. [d]Experiments with HONO measurements

3.4.2 Calculation of the chemical budget of RO_2 radicals derived from the oxidation of monoterpenes

The chemical budget of the RO_2 radicals can also be calculated similar to that for OH radicals. Due to short lifetime of RO_2 radicals during the experiments (1 s to 100 s, e.g., Section 4.3.2 and Section 5.2), the production and destruction rates of RO_2 radicals must be balanced within the time scale of several minutes. By comparing the production and destruction rates of RO_2, insights can be provided if loss or production processes of RO_2 radicals are missing.

The chemical budget analysis of RO_2 radicals is only calculated for the first-generation RO_2 radicals produced from the oxidation of monoterpenes (C_{10}-RO_2), as no speciated RO_2 radicals were available in the experiment. Instead of using RO_2 measurements, the concentrations of first-generation RO_2 radicals is calculated from their production rate using the known reaction rate coefficient and measurements of the VOC, O3, and OH radicals. The reaction rate coefficients of the bimolecular reaction loss of C_{10}-RO_2 can be taking from the structure activity relationships (Jenkins et al. 2019). To reduce the interference of other RO_2 species on the calculation of the chemical budget of C_{10}-RO_2, only measurements during the first 30 minutes after the first monoterpene injection are used for the analysis, so that the additional RO_2 production from the subsequent oxidation of organic products is minimized. The calculation starts with the rate loss constant of C_{10}-RO_2 to bi-molecular reaction (k_{RO2}), like in Equation 3-22 in Section 3.3.

$$k_{\mathrm{RO_2}} = \left(k_{\mathrm{RO_2+NO}}[\mathrm{NO}] + k_{\mathrm{RO_2+HO_2}}[\mathrm{HO_2}] + k_{\mathrm{RO_2+RO_2}}[\mathrm{RO_2}]\right) \quad \text{Equation 3-23}$$

The additional loss rate constant (k_{add}) required to balance production (P_{RO2}) and destruction (L_{RO2}) rates of C_{10}-RO_2 can be calculated as

$$L_{\mathrm{RO_2}} = [\mathrm{RO_2}]\left(k_{\mathrm{RO_2}} + k_{\mathrm{add}}\right) = k_{\mathrm{VOC+OH}}[\mathrm{VOC}][\mathrm{OH}] + k_{\mathrm{VOC+O_3}}[\mathrm{VOC}][\mathrm{O_3}]\gamma_{\mathrm{VOC}} = P_{\mathrm{RO_2}} \quad \text{Equation 3-24}$$

$$k_{\mathrm{add}} = \frac{P_{\mathrm{RO_2}}}{[\mathrm{RO_2}]} - k_{\mathrm{RO_2}} \quad \text{Equation 3-25}$$

where γ_{VOC} is the OH yield of the ozonolysis reaction of the VOCs (0.66 for limonene, Cox et al. 2020; 0.26 for sabinene, this study). It is assumed that the yield of C_{10}-RO_2 in the ozonolysis reactions of monoterpene is the same as the yield of OH radicals.

4. Investigation of the oxidation mechanism of limonene by OH radicals and O_3 in simulation chamber experiments

The majority of the content of this chapter was published in the peer-reviewed article "Investigation of the limonene photooxidation by OH at different NO concentrations in the atmospheric simulation chamber SAPHIR" (doi: https://doi.org/10.5194/acp-22-8497-2022) in the journal *Atmospheric Chemistry and Physics* by this author. Parts of the text and figures in this chapter are adapted from the open-access publication (Pang et al., 2022), under the CC BY 4.0 license (https://creativecommons.org/licenses/by/4.0).

4.1 Oxidation mechanisms of limonene

4.1.1 Oxidation mechanism of limonene in the Master Chemical Mechanism

The mechanism of the oxidation of limonene that is used in this study is adopted from the Master Chemical Mechanism (MCM). MCM is a near-explicit chemical mechanism describing the degradation of volatile organic compounds (VOCs) in the atmosphere.

Figure 4-1 illustrates the major reaction pathways of the oxidation of limonene by OH radicals relevant for the interpretation of experiments in this work. Reactions up to the second-generation closed-shell product, and the pathways of the ozonolysis reaction up to the first-generation closed-shell products are shown.

The OH oxidation of limonene leads to the production of two first-generation close-shell product limononaldehyde (LIMAL) and limona ketone (LIMKET). LIMAL is produced from the oxidation of the exocyclic C=C double bond whereas LIMKET is produced from the oxidation of the exterior C=C double bond. The second C=C double bond of LIMAL and LIMKET is then subsequently oxidized by another OH radicals that results in the second-generation product LMLKET.

Regarding the ozonolysis of limonene, the MCM only considers the addition of O_3 to the endocyclic C=C double bond which is much faster than that to the exterior terminal C=C double bond. The reaction on the exocyclic C=C double bond with O_3 yields two Criegee intermediates LIMOOA and LIMOOB. The Criegee intermediates undergo a series of radical reaction and yield first-generation oxidation products.

Apart from the C_9 and C_{10} close-shell products, HCHO is one of the major products of the oxidation of limonene by OH radicals and O_3. HCHO is produced from the oxidation of the exterior terminal double bond. In general, the oxidation rate constants of C=C double bonds increased with the number of alkyl-substituents via inductive effects (McGillen et al., 2007). Therefore, the oxidation of the di-substituted exterior double bond is slower than that of the tri-substituted endocyclic double bond, which resulted in a low HCHO yield in the OH- and O_3-oxidation of limonene. About 30 % of the OH-oxidation occurs at the exterior double bond (Peeters et al., 2007), and about 10 % of the ozonolysis reaction occurs at the exterior double bond (Wang and Wang, 2021).

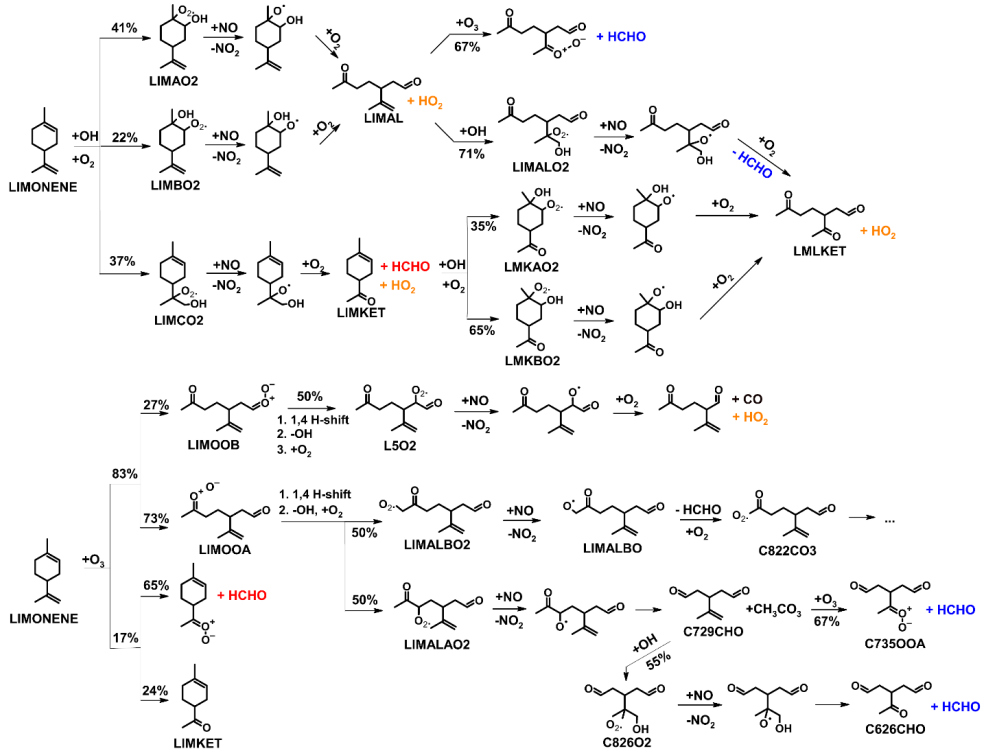

Figure 4-1. Simplified mechanism of the limonene oxidation by OH radical and O_3. All of the photooxidation mechanism and majority of the ozonolysis mechanism are adopted from MCM v 3.3.1. The branching ratios of the O_3 addition at the external C=C double bond are adopted from Wang and Wang (2021). The decomposition of LIMOOB to L5O2 is adopted from Chen et al. (2021). For simplicity the stereo-specificity of the intermediates, RO_2 reactions with HO_2 and other RO_2, as well as the formation of organic nitrates are not shown here. Production of HCHO from the first oxidation step of limonene is labeled in red; HCHO production from the second oxidation step is labeled in blue; production of a HO_2 radical is labeled in orange. The production of HCHO from the decomposition of LIMALBO is not classified, as it is not produced from the oxidation of the terminal C=C double bond.

4.1.2 Unimolecular reaction pathways for RO_2 derived from limonene oxidation

The limonene oxidation mechanism in the MCM model was implemented in MCM version 3.3.1, which was published in year 2015 (Jenkin et al., 2015). Since then there has been no significant modifications. The MCM does not consider any unimolecular reaction for the RO_2 produced from the oxidation of limonene. Recently, Møller et al. (2020) and Chen et al. (2021) proposed unimolecular reaction pathways for the first-generation RO_2 derived from the oxidation of limonene by OH (Fig. 4-2) and O_3 (Fig. 4-3), respectively. In their studies, they computed the rate constants of the possible unimolecular pathways (e.g., cyclization, H-abstraction). Due to the presence of a second C=C double bond, competitive unimolecular reactions (k > 1 s^{-1}) could be possible even for conditions with high NO concentrations (Møller et al., 2020).

Regarding the oxidation of limonene by OH radicals (Fig. 4-2), the OH-addition on the endocyclic C=C double bonds result in two RO_2 radicals, LIMAO2 and LIMBO2. Both RO_2 do not undergo competitive unimolecular reactions that are competitive under typical atmospheric condition. Potential unimolecular reactions have reaction rate constants of less than 10^{-3} s^{-1}, which is equivalent to the rate loss constant of RO_2 to the reaction with NO in the presence of less than 5 pptv NO. This is due to the steric factor from the six-member ring and surrounding substituents for secondary (LIMBO2) and tertiary (LIMAO2) peroxy radicals that prevents the peroxy radicals reaching the exterior C=C double bond (Møller et al. 2020). The OH-addition that takes place at the exterior C=C double bond of limonene yields tertiary peroxy radical LIMCO2. LIMCO2 can undergo competitive unimolecular reactions at rate ranging from 0.2 s^{-1} to 4.0 s^{-1} (equivalent to the rate loss constant of RO_2 to NO with a NO mixing ratio of 0.9 ppbv to 18 ppbv). The fastest unimolecular reactions are cyclization and allylic-H shift reaction, which are only possible in the presence of the second C=C double bond like in limonene (Møller et al., 2020).

The RO_2 radicals yielded from the ozonolysis reaction of limonene can undergo even faster unimolecular reactions than RO_2 from the OH-oxidation. This is due to the loss of steric hinderance from the six-member ring moiety from the ring-opening ozonolysis reaction, as well as due to the enhancement of the reaction rate in the presence of carbonyl groups inserted during the ozonolysis reaction. Taking the three RO_2 radicals (LIMALAO2, LIMALBO2, L5O2) produced from the ozonolysis reaction of the endocyclic cyclic C=C double bond for example, reaction rate constants of these unimolecular reactions range from 0.5 s^{-1} to 230 s^{-1} (Chen et al., 2021), which are equivalent to the rate loss constant of RO_2 radicals to NO with mixing ratios from 2 ppbv to 1000 ppbv. Fastest unimolecular reactions of these RO_2 radicals are cyclization, allylic-H shift, and aldehydic H-shift reactions, which are fast in the presence of a second C=C double bond or an aldehyde function group. Chen et al. (2021) did not investigate potential unimolecular reaction rate constants of products formed from the first unimolecular reactions, but it can be expected that unimolecular reactions of the products are also very competitive as RO_2 formed from their oxidation still contain either the C=C double bond or the aldehyde group.

With the findings from Møller et al. (2020) and Chen et al. (2021), it can be expected that the fast unimolecular reaction chemistry of the RO_2 radicals produced from the oxidation of limonene would be very different from the bi-molecular reactions chemistry implemented in the MCM model. Therefore, the results from Møller et al. (2020) and Chen et al. (2021) are used to explain the discrepancies observed between model simulations with the MCM and measurements (Section 4.4.1).

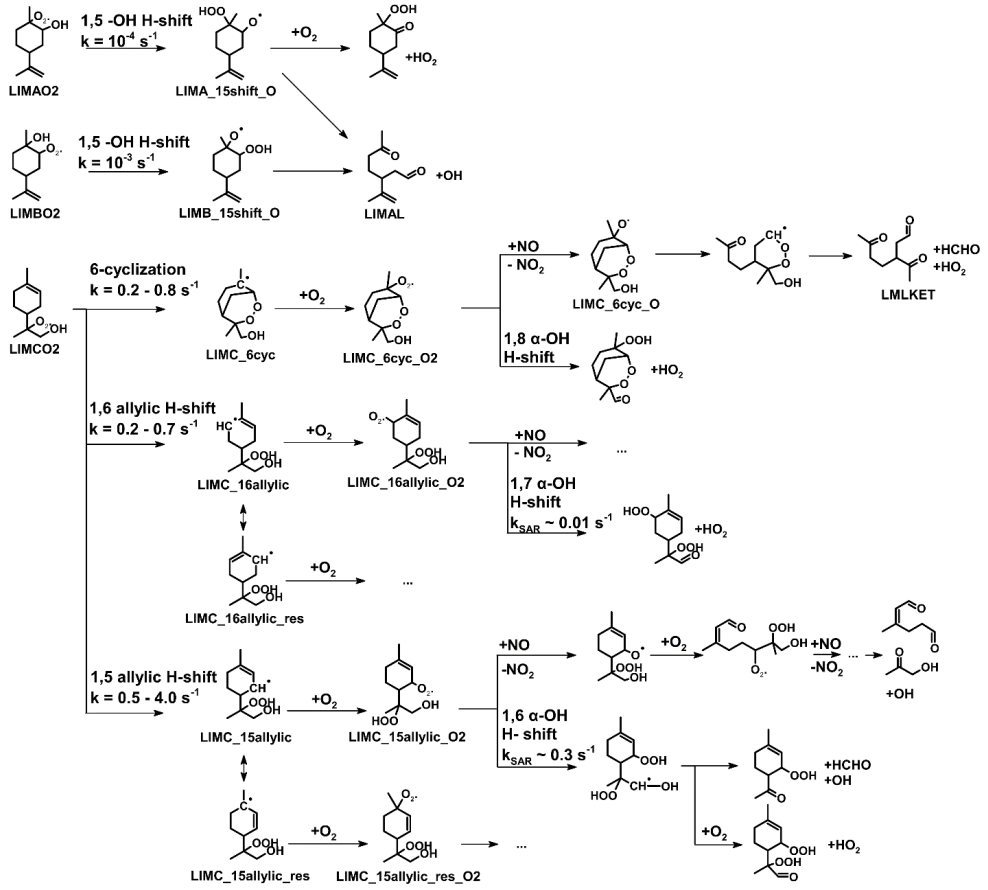

Figure 4-2. Mechanism of the unimolecular reaction pathways for the for the first-generation RO_2 produced from the oxidation of limonene by OH radicals proposed by Møller et al. 2020. Only the most competitive reactions ($k > 0.1\ s^{-1}$) are shown. For stereoisomers, the range of reaction rate constants are given.

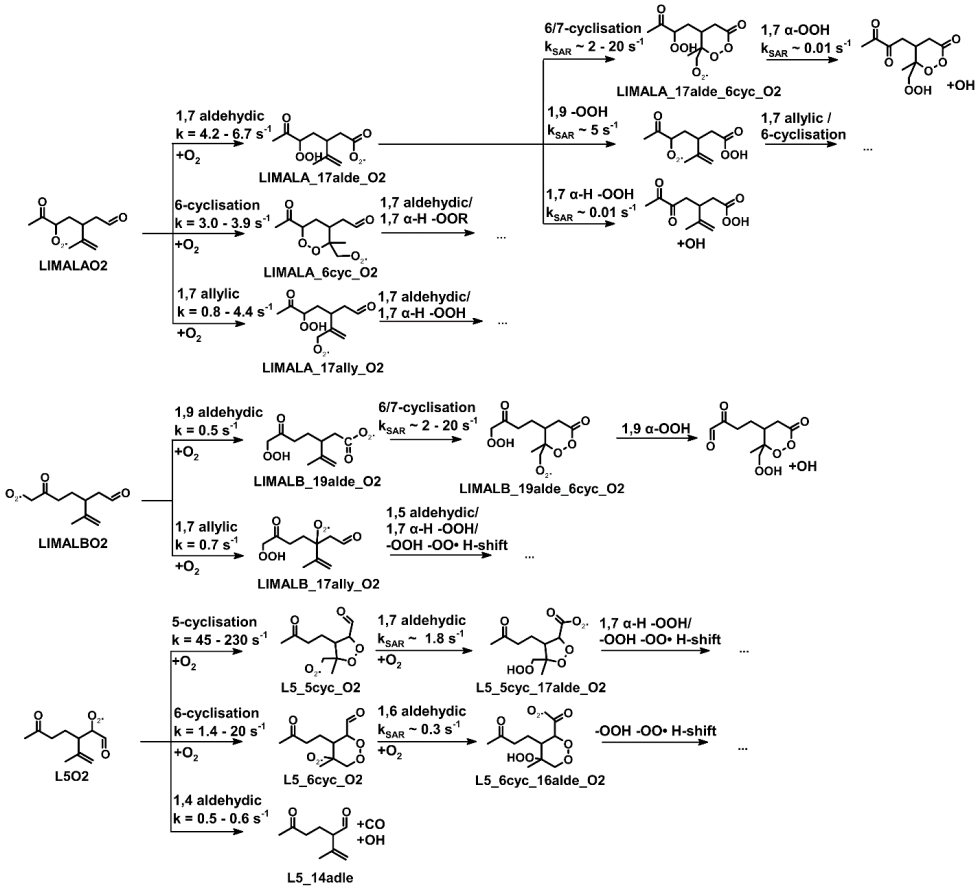

Figure 4-3. Mechanism of the unimolecular reaction pathways for the for the first-generation RO_2 produced from the ozonolysis of limonene proposed by Chen et al. 2021. Only the most competitive reactions ($k > 0.1\ s^{-1}$). The range of values are reaction rate constants for stereoisomers.

4.2 Overviews of limonene oxidation experiments

To investigate the oxidation of limonene at atmospherically relevant conditions, in total 7 experiments were conducted under NO mixing ratios from zero to 10 ppbv. The experiments can be divided into four conditions (ozonolysis, and photooxidation at low, medium, and high NO mixing ratios) and their general descriptions can be referred to Section 2.5. Experimental conditions of the 7 experiments are summarized in Table 4-1. The list of instruments used in the study of limonene are in Table 2-1. Measurements of radicals and OH reactivity with the LIF instrument; measurements of NO and NO_2 with chemiluminescence; measurements of O_3 with UV absorption, and measurements of photolysis frequencies calculated from actinic flux measurement from a spectroradiometer were available in all experiments for the study of limonene. The availability of the other instruments is listed in Table 4-2. Figure 4-4 to 4-10 show the relevant measurements of trace gas and radical concentrations of all the limonene oxidation experiments used for the analysis in this study. The photooxidation experiment with low NO mixing ratios on 13 June 2015 was performed with slightly differences. In addition to the O_a injection at the beginning of the experiment, about 800 ppbv of CO and 40 ppmv of CH_4 were injected before the injection of limonene, so that the increased in HO_2 and RO_2 concentrations from the injection of CO and CH_4 could be used as a reference for monitoring the measurement sensitivities of radicals (Fig. 4-6).

Table 4-1. Experimental conditions during the time period when the radical budget of limonene oxidation experiments is analyzed. k_{RO2} is the sum of the total loss rate RO_2 due to bimolecular with NO, HO_2, and other RO_2 calculated from measured concentrations. Average values are given except for limonene concentrations, for which maximum concentrations after the injection are given.

Experiment	NO (ppbv)	HO_2 (10^8 cm^{-3})	k_{RO2} (s^{-1})	OH (10^6 cm^{-3})	O_3 (ppbv)	Limonene (ppbv)	Date	Figure
Ozonolysis	0	4.0	0.10	< 1	55	4	05 Jun 2020	Fig. 4-4
Low NO	0.08	5.5	0.25	3	45	3	01 Sep 2012	Fig. 4-5
	0.10	10	0.04	3	105	4	13 Jun 2015	Fig. 4-6
	0.13	5.0	0.35	7.5	60	2.3	04 Jul 2019	Fig. 4-7
Medium NO	0.20	3	0.05	2	5	4	08 Aug 2012	Fig. 4-8
	0.30	4	0.07	4	5	4	10 Aug 2012	Fig. 4-9
High NO	0.7	11	0.15	8	45	10	03 Aug 2015	Fig. 4-10

Table 4-2. Measurements availability during the oxidation experiments of limonene. Available measurements are indicated with a tick symbol.

Date	Instrument (Measured species)					
	DOAS (OH, HCHO)	PTR-TOF-MS (VOCs)	GC-FID (VOCs)	CRDS (HCHO)	Hantzsch (HCHO)	LOPAP (HONO)
05 Jun 2020	✓	✓	✓	✓		
01 Sep 2012		✓	✓		✓	✓
13 Jun 2015	✓	✓	✓			✓
04 Jul 2019		✓		✓	✓	
08 Aug 2012		✓	✓		✓	✓
10 Aug 2012		✓	✓		✓	✓
03 Aug 2015	✓	✓	✓		✓	

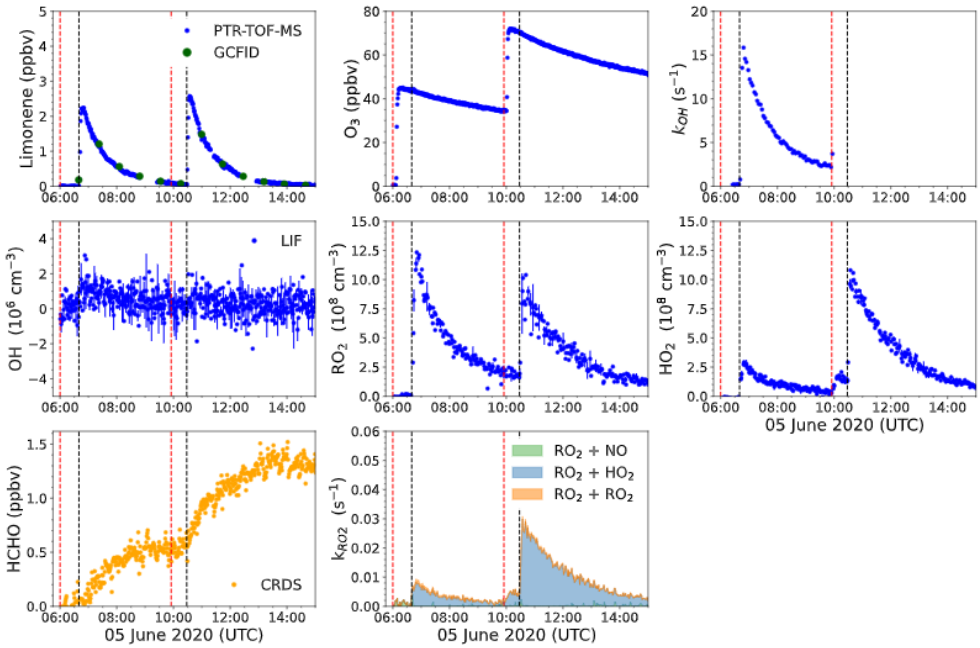

Figure 4-4. Overviews of the measured radicals and trace gas concentrations used in the analysis of the limonene ozonolysis experiment on 05 June 2020. The left red line indicates when O_3 was injected; the middle red line indicates when CO and O_3 was injected; the black lines indicate when limonene was injected into the chamber. After the injection of CO, the OH reactivity was too high to be measured (about 500 s^{-1}).

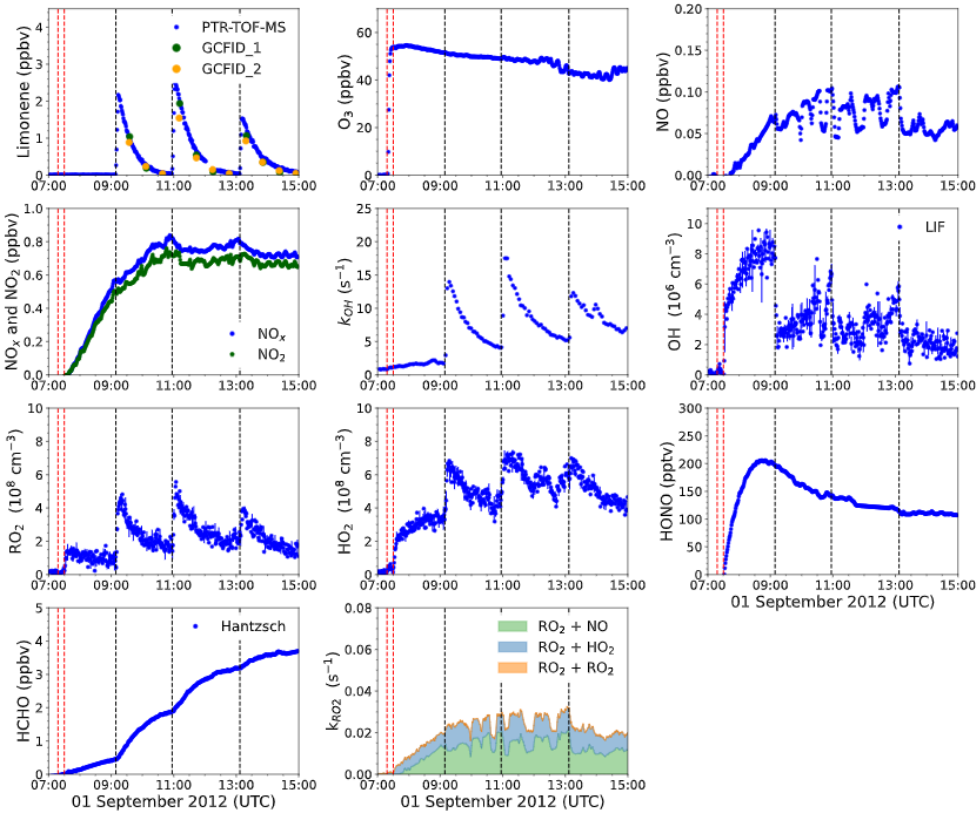

Figure 4-5. Overviews of the measured radicals and trace gas concentrations used in the analysis of the limonene photooxidation experiment with low NO mixing ratios on 01 September 2012. The leftmost red line indicates when O_3 was injected; the second-leftmost red line indicates when the chamber roof was opened; the black lines indicate when limonene was injected into the chamber.

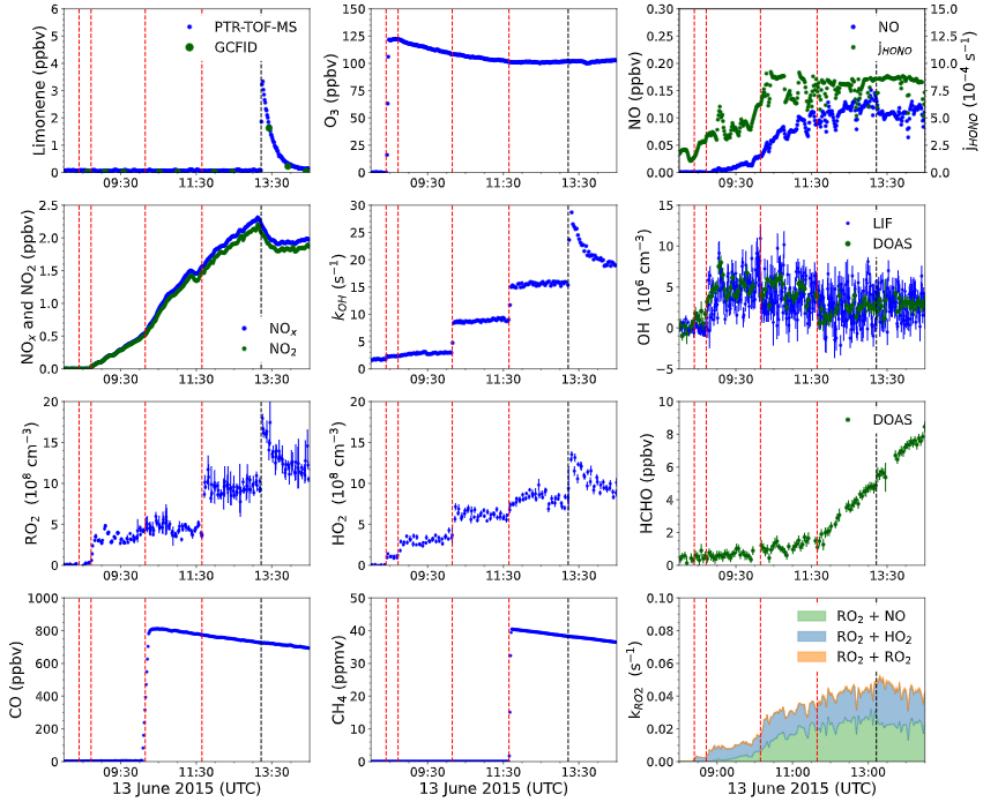

Figure 4-6. Overviews of the measured radicals and trace gas concentrations used in the analysis of the limonene photooxidation experiment with low NO mixing ratios on 13 June 2015. Form the leftmost red line to the rightmost red line, they indicate the injection of O_3, the opening of chamber roof, the injection of CO, and the injection of CH_4. The black line indicates when limonene was injected into the chamber.

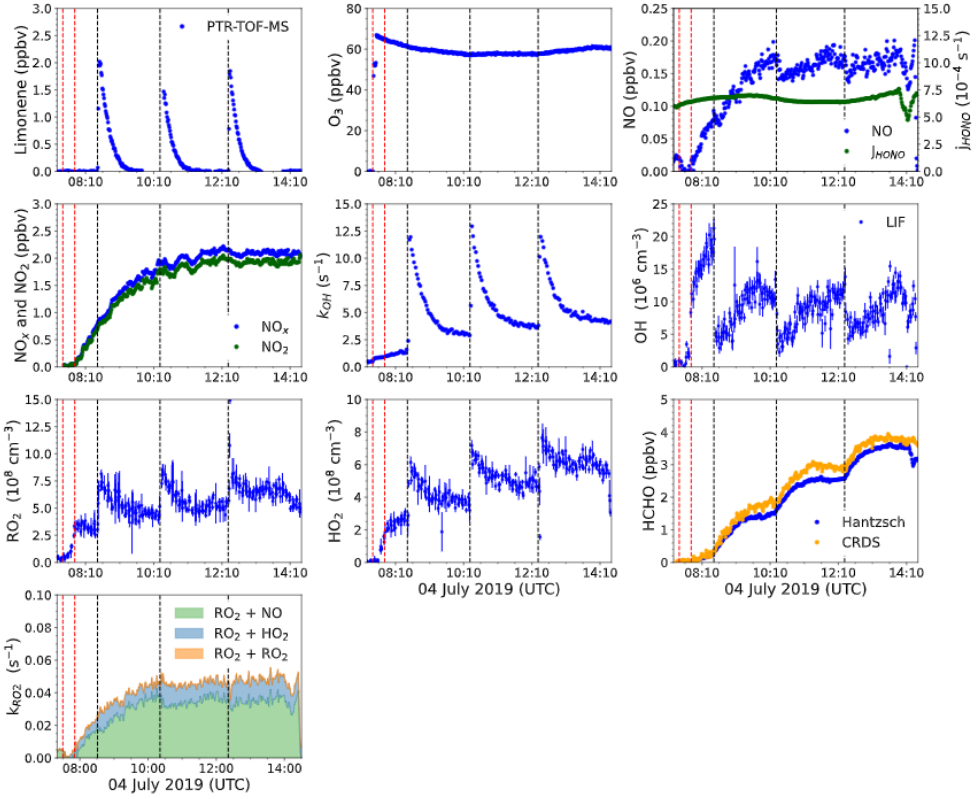

Figure 4-7. Overviews of the measured radicals and trace gas concentrations used in the analysis of the limonene photooxidation experiment with low NO mixing ratios on 04 July 2019. The leftmost red line indicates when O_3 was injected; the second-leftmost red line indicates when the chamber roof was opened; the black lines indicate when limonene was injected into the chamber.

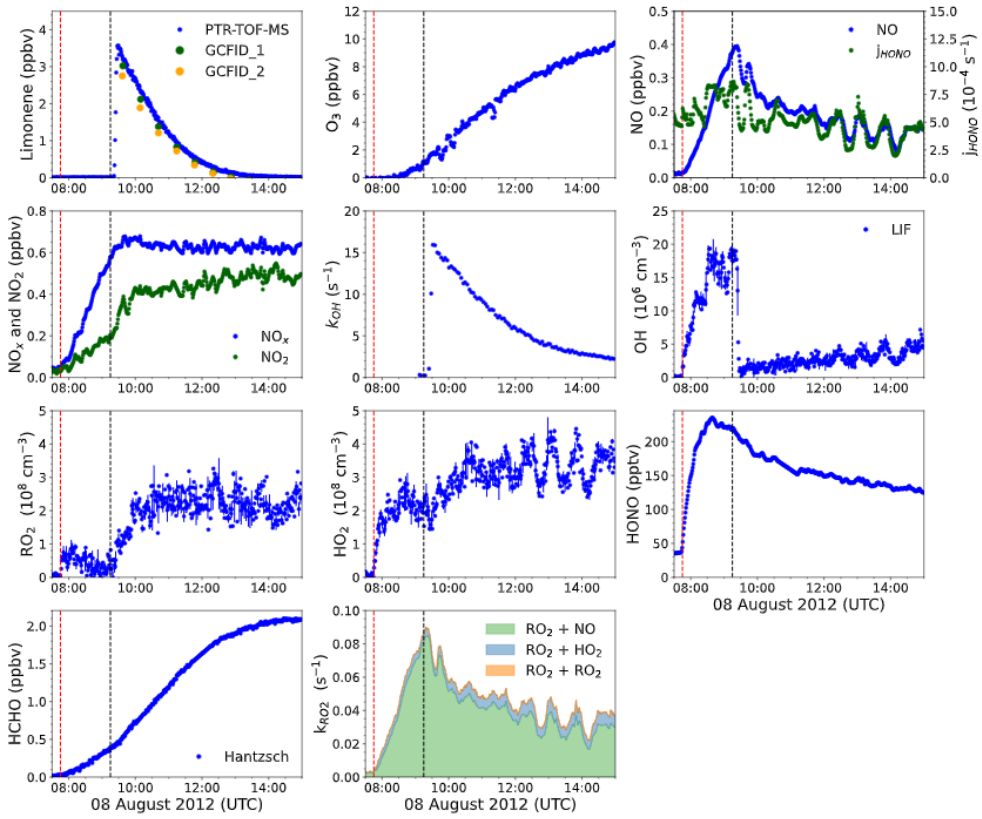

Figure 4-8. Overviews of the measured radicals and trace gas concentrations used in the analysis of the limonene photooxidation experiment with medium NO mixing ratios on 08 August 2012. The red line indicates when O_3 was injected; the black lines indicate when limonene was injected into the chamber.

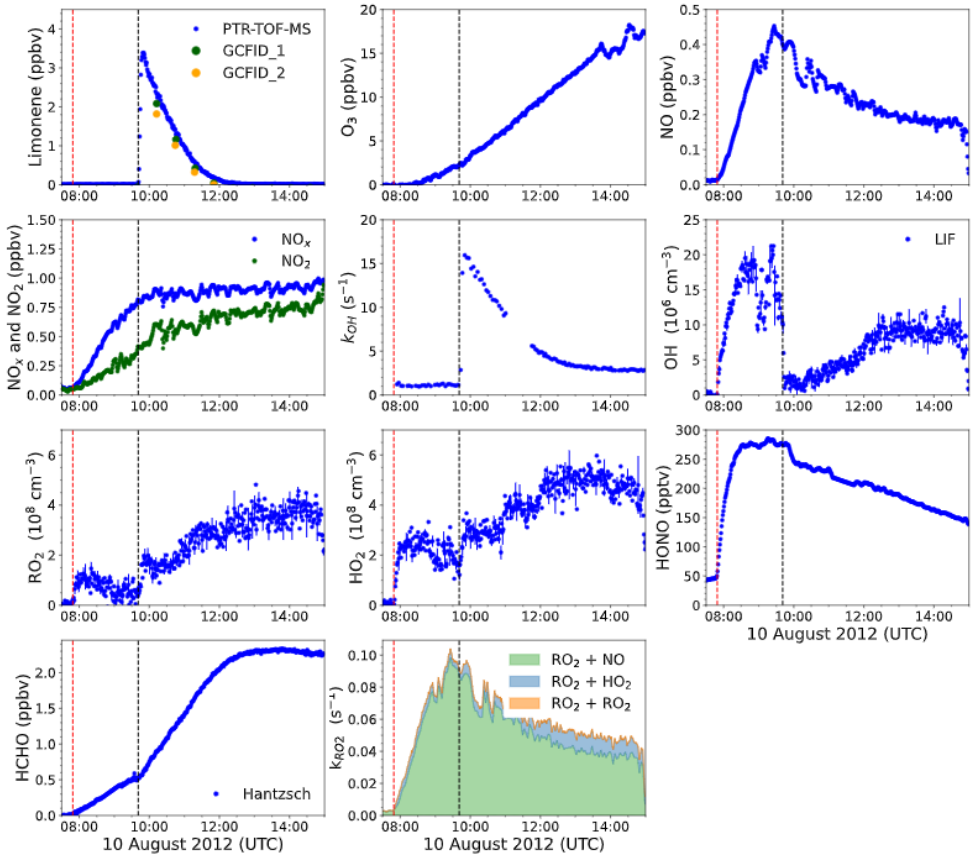

Figure 4-9. Overviews of the measured radicals and trace gas concentrations used in the analysis of the limonene photooxidation experiment with medium NO mixing ratios on 10 August 2012. The red line indicates when O_3 was injected; the black lines indicate when limonene was injected into the chamber.

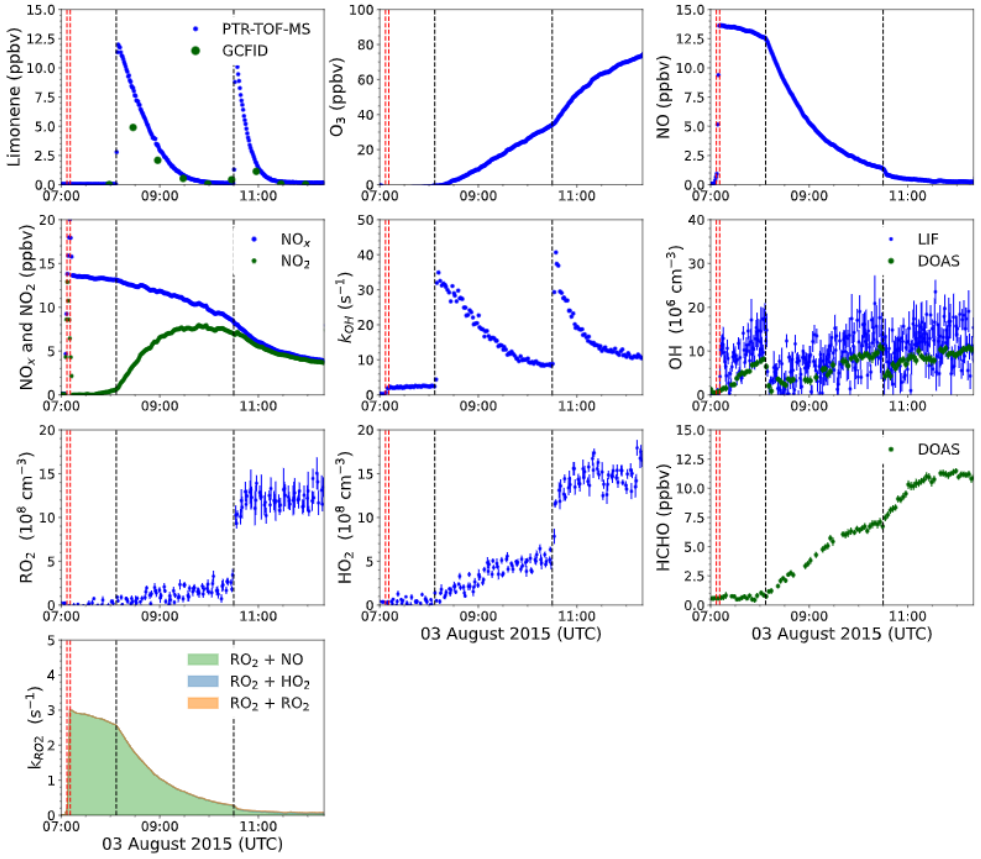

Figure 4-10. Overviews of the measured radicals and trace gas concentrations used in the analysis of the limonene photooxidation experiment with high NO mixing ratios on 03 August 2015. The red lines indicates when O_3 and NO were injected; the black lines indicate when limonene was injected into the chamber. The measurements during the first limonene injection were used for the calculation of HCHO yield due to the less interference on the production of HCHO from subsequent oxidation of secondary products (Section 4.3.1). The measurements during the second limonene injection were used for the comparison with model calculations and the calculation of radicals chemical budgets (Section 4.3.2).

4.3 Results

4.3.1 Yield of product species from the oxidation of limonene

HCHO is one of the main oxidation products of the oxidation of limonene. The calculation of HCHO yield from the oxidation of limonene is based on the method presented in Section 3.1.1.

For the evaluation of the HCHO yield, only measurements from the first limonene injection of each experiment are used, because further oxidation on the exterior C=C double bond yield secondary HCHO formation. The HCHO yield calculated for the second limonene injection onward would be interfered by secondary HCHO productions contributed from the first limonene injection (Fig. 4-1). This is demonstrated by the rapid increase in HCHO production when 80 % of limonene had reacted away after a roughly linear increase in HCHO production (Fig. 4-11). The rapid increase in HCHO production occurred when about 40 % of limonene was consumed. Therefore, only measurements when less than 40 % of limonene was consumed are used to calculate the HCHO yield, which results in values of (12 ± 3) %, (13 ± 3) %, and (32 ± 5) % for the OH oxidation experiments with low, medium, and high NO mixing ratios, respectively (Fig. 4-11). At later times of experiment, when all limonene reacted away, the HCHO yield increases to values of 40 % to 90 %. HCHO yields remain 100 % in all experiments, which is consistent with the production of HCHO from the oxidation of the exterior C=C bond in limonene only within the short time scale of hours in the experiments.

HCHO is produced from the dissociation of the alkoxy radical derived from the OH-addition reaction on the exterior C=C double bond. Therefore, the HCHO yield can be connected to the branching ratio of the OH-addition at the exterior C=C double bond, which is 37 % with an uncertainty of 15 % based on the SAR in Peeters et al. (2007). With the assumptions of all RO_2 produced from the OH-oxidation of the exterior C=C double bond (LIMCO2, Fig. 4-1) reacted with NO, and about 18 % (Jenkin et al., 2019) to 34 % (this study) of RO_2 derived from the OH-oxidation of limonene form organic nitrates, the expected HCHO yield of the OH-oxidation of limonene is about (28 ± 7) %.

In the experiment with high NO mixing ratios, RO_2 radicals exclusively reacted with NO (Fig. 4-10) and HCHO was expected to be produced from the dissociation of alkoxy radicals. Experimental yield value of (32 ± 5) % is consistent with the yield expected from the SAR of (28 ± 7) %. In experiments with medium NO mixing ratio and low NO mixing ratio, only about 85 % and 65 % of RO_2 reacts with NO (Fig. 4-5, Fig. 4-7 to 4-9), respectively. Accounting for the fraction of RO_2 which does not react with NO, the expected HCHO yields calculated from the SAR for experiments with low NO mixing ratio and medium NO mixing ratio are (18 ± 5) % and (24 ± 6) %, respectively. In both cases, values are higher than values determined from measured HCHO concentrations of around (13 ± 3) % in the experiments.

Table 4-3 summarizes the HCHO yield determined in this study and experimentally determined yields reported in literature. Values reported in literature ranged from 36 % to 43 % (Larsen et al., 2001; Lee et al., 2006). In these studies, experiments were conducted at much higher NO mixing ratios than experiments in this work. The high NO mixing ratio increases the turnover rate of RO_2 and it is not clear whether the secondary production of HCHO from the oxidation of primary products is taken account in the calculations of yield reported in literature (Fig. 4-1). This may explain the high HCHO yields determined in their studies. In the study conducted by Librando and Tringali (2005), HCHO yields were determined to

be 27 % and 92 % in experiments in the absence of NO and at high limonene concentrations of 13 ppmv and 2 ppmv, respectively. The large differences in the HCHO yields at different limonene concentrations could not be resolved. Results from their experiments may not be comparable to results derived in this work, because the chemical fate of RO_2 radicals in that study was likely dominated by RO_2+RO_2 reactions, which were less important at ambient conditions like in the experiments in this work.

The HCHO yield calculated from the ozonolysis experiment in the presence of an OH scavenger is (10 ± 1) %. The low HCHO yield of 10 % is consistent with the fact that O_3-addition on the exterior C=C double bond is the minor pathway of the reaction with a theoretical branching ratio of 13 % (Wang and Wang, 2021). The HCHO yield determined in this study agrees with laboratory studies. Grosjean et al. (1993) also determined a HCHO yield of 10 % in experiments conducted at high limonene concentration of 1.2 ppmv in the presence of an OH scavenger. Gong et al. (2018) determined a HCHO yields of 5 % to 11 % and 11 % to 27 % in two sets of experiments with different concentration ratios of limonene to O_3. The set of experiments resulting in a HCHO yield of 5 % to 11 % was performed with a limonene to O_3 ratio of about 1:2. The yield and experimental conditions were similar to conditions of experiments in this study. The group of experiments resulting in a HCHO yield of 11 % to 27 % was performed with a limonene to O_3 concentration ratio of 1:100. The high ratio of O_3 to limonene concentration likely led to an enhancement of secondary HCHO production through a second ozonolysis reaction of the exterior C=C double bond of the primary ozonolysis products (Fig 4-1). This would explain the high HCHO yield determined in these experiments.

The total organic nitrate yield of the photooxidation of limonene is determined with the method presented in Section 3.2.2. The calculation with the measurements from the photooxidation experiments with medium NO mixing ratios resulted in a value of (34 ± 5) % (Fig. 4-12a and Table 4-3) The nitrogen budget analysis in Fig. 4-12b shows that the accumulation production of nitrogen from the chamber (Σ(*Q*(HONO))) since the injection of limonene, was about the same as the amount of NO_y and nitric acid presented in the chamber when all limonene was consumed at around 13:00 hour (Fig. 4-8 and Fig. 4-12b). This suggests a significant fraction of nitrogen in the chamber presented in the form of organic nitrates.

The precision (~15 %) of the nitrate yield is determined by the precision of the measurements with linear error propagation and the nitrate yields determined from the two experiments. The uncertainty of the nitrate yield is about 30 %, which is mainly attributed to the accuracies of the reaction rate constants k_{RO2+NO} (~30 %) and the measurements of HONO (10 %) and j_{HONO} (18 %). This value is higher than values of 19 % (Jenkin et al., 2019) to 28 % (Arey et al., 2001; Leungsakul et al., 2005) determined using SAR. The yield determined in this study agrees with the value of (36 ± 6) % reported by Rollins et al. (2010), who determined the nitrogen content of the aerosols produced from the photooxidation of limonene under a high NO mixing ratio (500 ppbv).

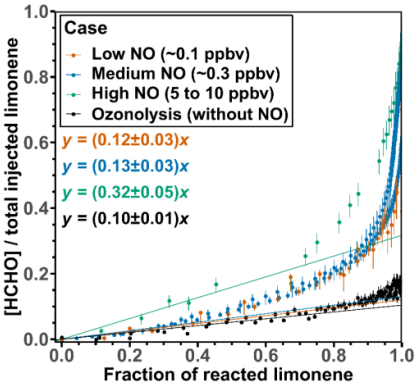

Figure 4-11. The regression between the HCHO concentrations divided by the injected limonene against the fraction of reacted limonene for the first limonene injection for each experiment. The regression includes data points up to 40 % of the fraction of reacted limonene.

Table 4-3. Product yields from the oxidation of limonene by OH radicals and O_3 determined in this work and reported values from literature. Maximum values for limonene, O_3 and NO concentrations in the experiments are listed.

Limonene + OH	HCHO yield (%)	Organic nitrates (%)	Limonene (ppbv)	NO (ppbv)
Larsen et al. (2001)	36 ± 5	/	1000	1000
Librando and Tringali (2005)	27 – 92	/	2100 – 13200	0
Lee et al. (2006)	43 ± 5	/	120	132[b]
Rollins et al. (2010)	/	36 ± 6[a]	< 100	500
This work	12 ± 3	/	3.5	0.05 – 0.15
	13 ± 3	34 ± 5	3.5	0.3
	32 ± 5	/	10	3 – 10
Limonene + O_3	HCHO yield (%)	Limonene (ppbv)	NO (ppbv)	OH scavenger
Grosjean et al. (1993)	10	1200	70 – 100	Yes[c]
Gong et al. (2018)	7 – 11	280	500	No
	5 – 8	280	500	Yes[d]
	13 – 27	183	19000	No
	11 – 23	183	19000	Yes[d]
This work	10 ± 1	4	50	No
	11 ± 1	4	80	Yes[e]

[a]Yield determined from aerosols. [b]Given as NO_x concentrations. [c]200 ppmv cyclohexane. [d]400 ppmv of 2-butanol or cyclohexane. [e]60 ppmv of CO.

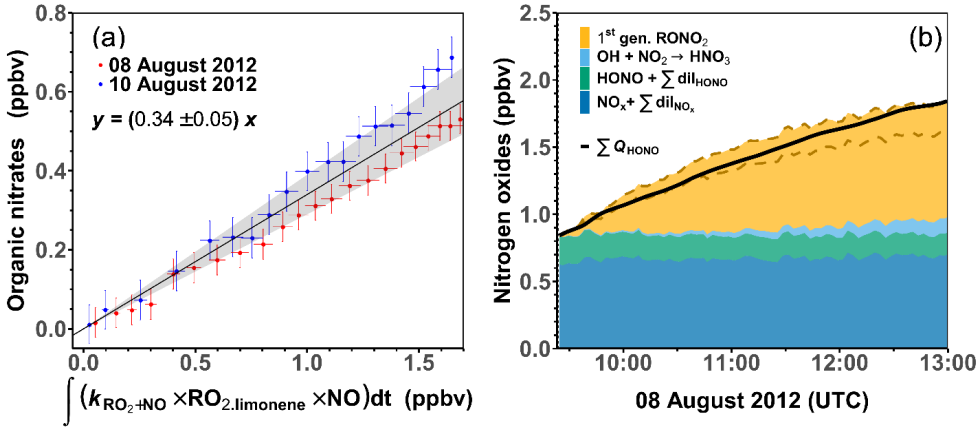

Figure 4-12. (a) Regression between calculated organic nitrate mixing ratio and integrated turnover rate of the reaction of limonene-derived RO_2 and NO. The regression only includes data when less than 60 % of the limonene from the first injection reacted away. (b) Concentrations of nitrogen oxide species after the first limonene injection in the experiment with medium NO on 8 August 2012 compared to the total production of HONO from the chamber source. The organic nitrate contribution is calculated using a nitrate yield of (34 ± 5) % for the reaction of limonene RO_2 with NO; the uncertainty range is enclosed by the two dashed lines.

4.3.2 Evaluating the radical chemistry of limonene oxidation in model simulations

To evaluate the ability of the MCM model of reproducing the measured radical concentrations, two sets of simulations (reference model run and constrained model run, Section 3.3) were conducted for experiments with experimental conditions. Here, only one experiment from each group of NO mixing ratios is analyzed here. Modelling comparison for experiments that are not included in this section could be found in the xlementary material Section 4 (Fig. S4-1 to Fig. S4-3).

Figure 4-13 shows the experimental conditions and the simulations of the experiment with medium NO mixing ratio on 08 Aug 2012. The experiment had a low O_3 concentrations of below 10 ppbv that over 90 % of limonene reacted with OH radicals. The NO concentrations were moderately high with values of about 0.3 ppbv. The OH concentration was around $(1 – 5) \times 10^6$ cm^{-3} and it increased as more limonene was consumed over the course of experiment; the concentration of HO_2 was about $(2 – 4) \times 10^8$ cm^{-3}; and the RO_2 concentration ranged from $(1 – 3) \times 10^8$ cm^{-3}. Over 85 % of the RO_2 radicals was lost to the reaction with NO. The chemical lifetime of RO_2 radicals was about 10 s to 40 s, if only the loss to bi-molecular reactions is considered.

In the reference model run, the OH reactivity is overestimated by about 5 s^{-1} at the end of the experiment after four hours of reaction, equivalent to 33 % of the initial OH reactivity right after the injection of limonene. Apart from limonene, contributors to the OH reactivity included aldehydes and ketones from oxidation products (70 %), organic peroxides (15 %), and organic nitrate (15 %), suggesting the model is likely overestimating the OH reactivity from closed-shell oxidation products. The modelled HO_2 concentration is underestimated by 10 % to 30 % and thereby underestimating the OH concentration due to the slower OH production rate from the reaction in HO_2 with NO. Despite the low OH concentration in the reference model and thereby the low reaction rate of limonene, the modelled RO_2 concentration is overestimated by 20 % to 40 %.

In the constrained model run, the modelled OH concentration shows a very good agreement with the measurement, which is also supported by the better simulation of the decaying limonene concentration than the reference model run. This suggests that the model can reproduce the OH concentration, if the OH destruction rate (i.e., OH reactivity) and the OH production rate from OH recycling (i.e., from the HO_2 + NO reaction) are also well-reproduced. Due to the higher OH concentration than in the reference run, the discrepancy between the modelled RO_2 concentration and measured values further increases to +(50 – 100) %.

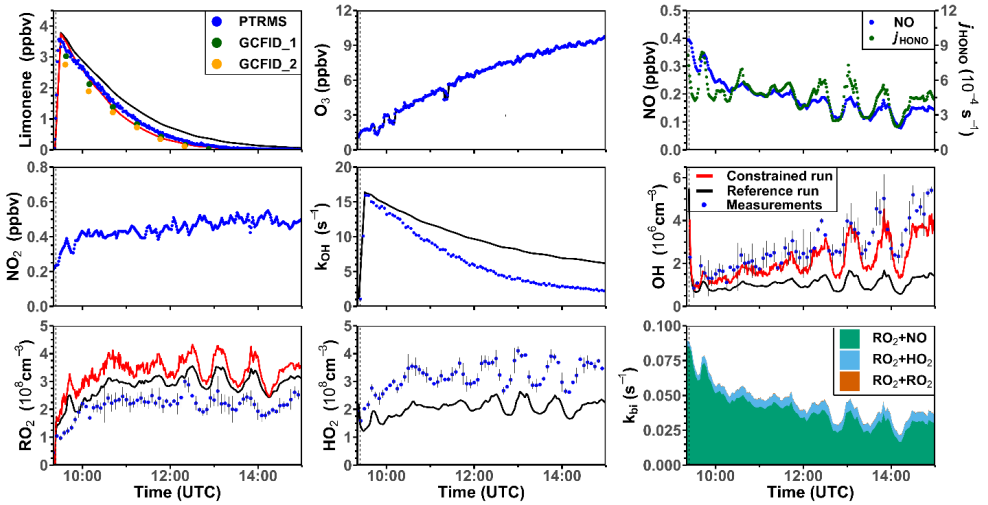

Figure 4-13. Modelled and measured radical concentrations and OH reactivity of the photooxidation experiment with medium NO mixing ratios on 08 August 2012. The vertical dotted line indicates the time when limonene was injected into the chamber.

Figure 4-14 shows the experiment conditions and the simulation results of the experiment with high NO mixing ratio on 03 Aug 2015. Only the part of the experiment after the second limonene injection is shown, as the measurements of radicals failed during the first part of the experiment. The O_3 concentration at the start of the second limonene injection was 35 ppbv, which was due to the production from the oxidation of limonene from the previous injection. O_3 at this concentration contributes about 30 % to the chemical loss of limonene during the experiment. The NO concentration was about 0.3 ppbv to 1.5 ppbv, which results in a short RO_2 lifetime of 3 s to 10 s, if only the loss to bi-molecular reactions is considered. More than 70 % of the RO_2 reacted with NO and the rest reacted with HO_2. The radicals concentrations were in general higher than in other experiments, as a higher concentration (10 ppbv) of limonene was injected in this experiment. The OH concentration was about $(5 – 15) \times 10^8$ cm^{-3} and measurements by LIF and DOAS instruments. Measurements of both instruments agree. The concentrations of RO_2 and HO_2 radicals were about 1×10^9 cm^{-3} throughout the experiment.

Similar to the experiment with medium NO mixing ratio, the OH reactivity modelled in the reference run is overestimated by about 10 s^{-1} (equivalent to 33 % of the initial OH reactivity of the injected limonene) after limonene was consumed 90 minutes after its injection. Modelled HO_2 concentrations are underestimated the measurements by 50 % to 70 % and thereby underestimating the modelled OH concentrations. The underestimation of modelled OH concentrations leads to a slower than measured decay of the modelled limonene concentration. In the constrained model run, modelled OH concentrations agree better with measured values when the OH reactivity and HO_2 concentrations match

the measurements. However, RO_2 concentrations are overestimated by the model by 30 % during the first hour of oxidation even though modelled OH concentrations are still slightly lower than measurements.

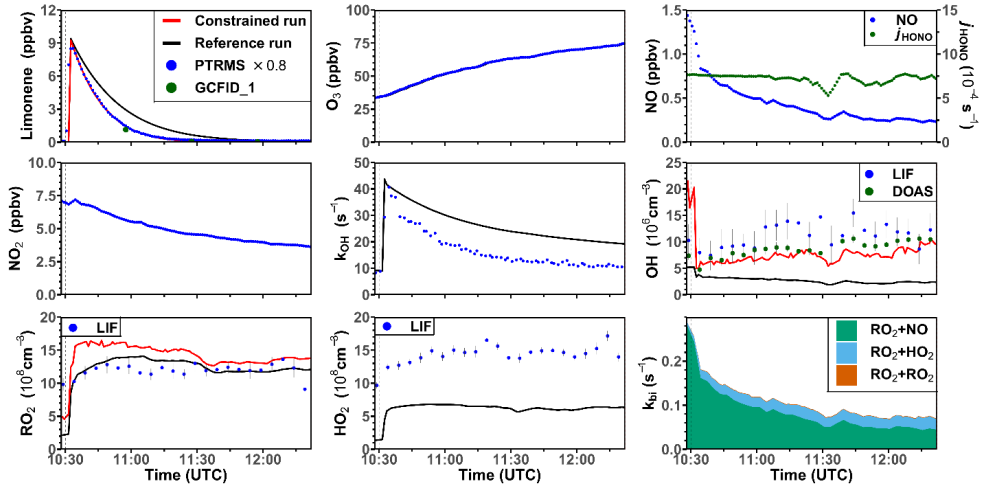

Figure 4-14. Modelled and measured radical concentrations and OH reactivity of the photooxidation experiment with high NO mixing ratios on 03 August 2015. The vertical dotted line indicates the time when limonene was injected into the chamber.

Figure 4-15 shows the experimental conditions and model results of the experiment with low NO mixing ratios on 01 Sep 2012. About 50 ppbv of O_3 was injected into the chamber before the experiment, so that NO concentrations are suppressed to below 0.1 ppbv. About 30 % to 40 % of limonene reacted with O_3. At such low NO concentration, the lifetime of RO_2 increases to about 50 s if only losses to bi-molecular reactions are considered. Only about 50 % to 60 % of the RO_2 radicals reacted with NO and the remaining part reacted with HO_2. The OH concentration was around $(2 – 6) \times 10^6$ cm^{-3} and it increased as the OH reactivity became lower; the concentration of HO_2 was about $(4 – 7) \times 10^8$ cm^{-3}; and the RO_2 concentration ranged from $(2 – 5) \times 10^8$ cm^{-3}.

In the reference run simulation, modelled OH reactivity is overestimated by 5 s^{-1} (33 % of the initial OH reactivity from the injected limonene) when all limonene is consumed similar as in the experiments with medium and high NO mixing ratios. The model underestimates the measured HO_2 concentrations by 20 % to 50 %, in particularly the increase of HO_2 right after each injection of limonene is not well captured by the model. The model underestimates the measured OH concentration by at least 50 %. The largest discrepancy between model results and measurements is observed for the RO_2 concentration, as the model overestimates the measurements by 500 % to 700 %. The high modelled RO_2 concentration in the

reference model run partially explain the underestimation of the HO_2 concentrations, because HO_2 radical are quickly consumed in the reaction with RO_2 radicals.

In the constrained model run, the agreement between the modelled and measured OH concentrations improves, but the modeled concentration is still lower than the measured values. However, the good agreement between time series of modelled and measured limonene concentrations suggests that the OH measurements by the LIF instruments could be slightly higher than the true OH concentration. The modelled RO_2 concentrations are also greatly overestimated in the constrained model run by 300 % to 500 % when HO_2 concentrations are constrained.

There are studies reported that measurements of HO_2 and RO_2 by the LIF instrument can be interfered by a fast conversion of RO_2 to HO_2 radicals for some of the VOC species (reference), which can lead to high measured HO_2 concentrations and low RO_2 concentrations. The maximum interference on the measurements of RO_2 and HO_2 radicals were about 20 %, based on the configuration of the LIF instrument in this study (Chandrakiran master thesis). Therefore, interferences on the radicals measurements by the LIF instrument cannot fully explain the large discrepancy between the modelled and measured RO2 concentrations. This suggests there could be some rapid loss pathways for RO_2 radicals are not included in the current MCM model.

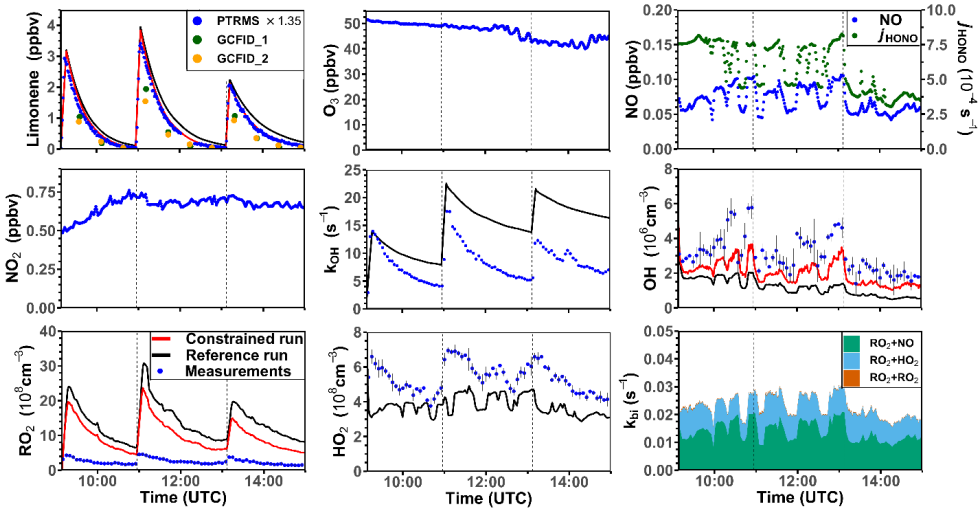

Figure 4-15. Modelled and measured radical concentrations and OH reactivity of the photooxidation experiment with low NO mixing ratios on 01 September 2012. The vertical dotted lines indicate the time when limonene was injected into the chamber.

The RO_2 concentration right after the injection was about 1×10^9 cm^{-3} and decreased while limonene reacted away; the HO_2 concentration was about 3×10^8 cm^{-3}; and the maximum OH concentrations was about 1×10^6 cm^{-3} that is three-times higher than the 1σ-precision of the measurements, suggesting that there was a significant production of OH radicals from the ozonolysis reaction of limonene. Due to the absence of NO in this experiment that was performed in the dark chamber, the lifetime of RO_2 radicals was long with 100 s right after the injection of limonene, because RO_2 radicals could only react with other RO_2 and HO_2 radicals. Over 90% of the RO_2 radicals were lost through the reaction with HO_2 radicals and the remaining 10 % reacted with other RO_2 radicals. During the second part of the experiment, after 100 ppmv of CO as OH scavenger was injected into the chamber at 10:00 UTC, the HO_2 concentration increased due to the reaction of CO with OH radicals. When limonene was injected again in the presence of the OH scavenger, the RO_2 and HO_2 concentrations were around 1×10^9 cm^{-3}. The lifetime of RO_2 was about 50 s and most of the radicals reacted with HO_2, when only losses to bi-molecular reactions are considered.

In the reference model run simulation, the model overestimates the OH reactivity by 5 s^{-1} similar to other experiments. The HO_2 concentration in the model underestimated by 90 %. This can be explained as HO_2 is mostly produced from the reaction of O_3 with OH in the model when NO is absent. Modelled RO_2 concentration are greatly overestimated by 300 % to 600 %, similar to experiments with low NO mixing ratios.

In the constrained run simulation, the modelled RO_2 concentration overestimated by 200 % when there was no OH scavenger present, but a good agreement is found when the OH scavenger was present. Modelled OH concentrations are similar as in the reference model run. Values are only slightly higher due to the lower OH reactivity.

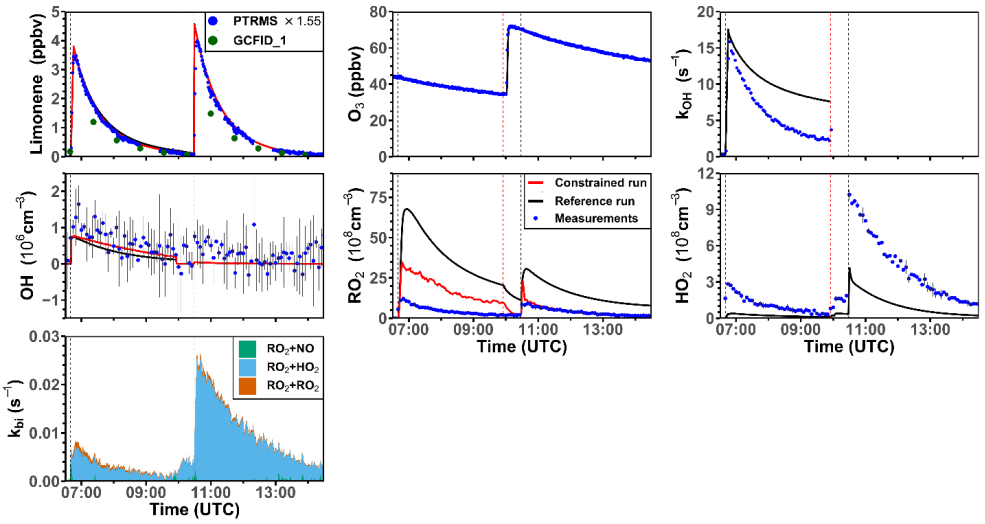

Figure 4-16. Modelled and measured radical concentrations and OH reactivity of the ozonolysis on 05 June 2020. The black vertical dotted lines indicate the time when limonene was injected into the chamber. The red vertical dotted line indicates when 100 ppmv CO was injected into the chamber.

Based on the comparisons between model simulations and measurements for experiments with different NO mixing ratios, several general observations can be made in all experiments:

- The model overestimates the OH reactivity after several hours of reaction in all experiments by about 33 % of the initial OH reactivity from the injected limonene., This partly explains of the low modelled OH concentrations, because the OH loss rate is too high in the model.
- The model underestimates the HO_2 concentrations in all experiments, particularly in experiments with low NO mixing ratios. As a consequence, OH concentrations are underestimated by the model due to a too low OH production rate from the reaction of HO_2 with NO.
- When the HO_2 concentration in the model is constrained to measurements and the modelled OH reactivity matches the measurements, modelled OH concentrations are in good agreement with measurements and the consumption of limonene is well described in the model.
- The modelled RO_2 concentration depends on the performance of the model to reproduce measured OH and HO_2 concentrations. In the constrained model runs, when HO_2 is constrained and OH agrees well with measurements, modelled RO_2 concentrations are still higher than measurements especially when NO mixing ratios are low.

4.3.3 Chemical budgets of OH radicals during the oxidation of limonene

Chemical budgets of OH radicals during the oxidation of limonene are calculated using the method described in Section 3.4.1. The results for the ozonolysis experiment, and photooxidation experiments with different NO mixing ratios are shown in Fig. 4-17. Chemical budgets of experiments not included in this section can be referred to the supplementary material (Fig. S4-4).

The destruction and production rates of OH radicals in the experiments with medium (08 August 2012, Fig. 4-17a) and high NO mixing ratios (03 August 2015, Fig. 4-17c) were balanced within the uncertainties of measurements during the whole experiments. This is consistent with the overall good agreement between modeled and measured OH radical concentrations obtained for the constrained model run (Fig. 4-13 and 4-14). In the experiment with high NO mixing ratios, the total OH turnover rate was higher of over 20 ppbv h^{-1} compared to the other experiments. This is because the high limonene concentration (10 ppbv) in the experiment increased the destruction rate of OH radicals and the high NO concentration increased the production rate OH radicals from the reaction with HO_2.

In the experiment with low NO mixing ratios on 01 September 2012 (Fig. 4-17b), the OH production rate was 6 ppbv h^{-1} after the injection of limonene and about 33 % were contributed from the OH production from the limonene ozonolysis. The NO concentration varied over the course of the experiment, making OH regeneration from the reaction in HO_2 with NO an important OH source with a contribution of 15 % to 50 % to the total OH production in addition to OH production from the photolysis of HONO and O_3. About 1.0 ppbv h^{-1} (20 % to 33 %) of the OH destruction rate is not explained by these OH production processes, which is consistent with the underestimation of OH concentrations in the constrained model run compared to measured values (Fig. 4-15). However, the gap between the OH destruction rate and destruction rate is about 1 ppbv h^{-1} throughout the whole experiment and does not vary with the amount of limonene present in the chamber. This suggests that either the missing OH source is not related to the oxidation of limonene or it is due to measurement artifacts, for example, in the OH measurements, which would lead to an overestimation of the OH destruction rate. An artifact in the OH measurement would also be consistent with what is observed in the constrained model run, where the rapid decrease in the modeled limonene concentration suggests that the measured OH is too high in this experiment (Fig. 4-15).

In the ozonolysis experiment, prior to the addition of CO as an OH scavenger (Fig. 4-17d), OH was only produced by the ozonolysis of limonene. The total OH production rate was about 2 to 3 ppbv h^{-1} at the beginning of the oxidation and gradually declined while limonene was being consumed. The total OH destruction rate is well-explained by the production from limonene ozonolysis, suggesting that OH production from further ozonolysis reactions of product species was not significant for conditions of this experiment.

In conclusion, the OH production rate from the major OH sources included in Table 3.1 is balanced by the OH destruction rate within the 25 % uncertainty of the calculation in the ozonolysis experiment and the photooxidation experiments with medium and high NO mixing ratios. In the experiments with low NO concentrations, imbalances of 20 % to 33 % are observed, indicating that additional OH production processes with rates of 1.0 ppbv h^{-1} would be required to explain the observed destruction rate, but there are indications that this could be due to a measurement artifact in the OH measurements.

In all the experiments, the OH production rates are lower than OH destruction rates at later times of the experiments, when secondary chemistry becomes important. However, differences are similar to the uncertainty of the calculations. These discrepancies may indicate that additional OH could be produced from unaccounted reactions of oxidation products, for example, from the photolysis of organic peroxides in the photooxidation experiments (Badali et al., 2015).

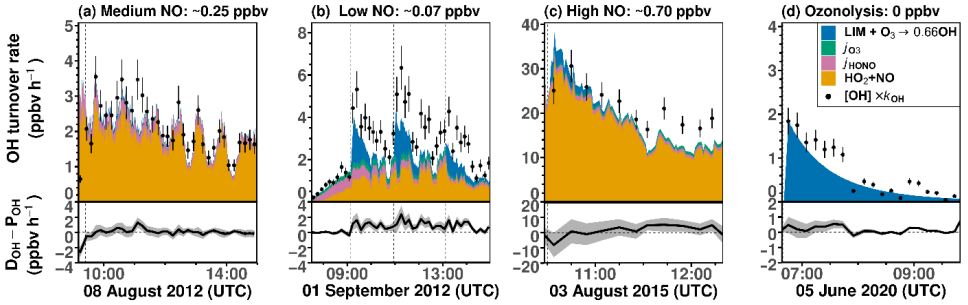

Figure 4-17. The upper panels are the ten-minute average values of the total OH destruction rate (D_{OH}, black dots) and major OH sources (P_{OH}, colored-shaded area) during the oxidation of limonene with (a) medium NO mixing ratios, (b) low NO mixing ratios, (c) high NO mixing ratios, and (d) zero NO mixing ratio (ozonolysis experiment). The production of OH radicals from the reaction in O_3 with HO_2 is not included, because the contribution to the total OH production was negligible (< 0.01 ppbv h^{-1}) for conditions of the experiments. The bottom panels are the difference between the OH destruction rate and the total OH production rate. The grey shaded area gives the uncertainties of the difference between the destruction and production rate of OH radicals.

4.3.4 Chemical budgets of first-generation RO_2 radicals from the oxidation of limonene

The discrepancies between measured and simulated RO_2 radical concentrations are much higher (up to a factor of 2) in the ozonolysis experiment and the photooxidation experiments with low NO mixing ratios, compared to the experiments with medium or high NO mixing ratios. An analysis of the composition of the RO_2 concentrations using model results from the constrained model run (Section 2.4) shows that the concentrations of RO_2 radicals produced in the initial reaction of limonene with OH and O_3 already exceed the measured total RO_2 concentrations (Fig. 4-18). Model–measurement percentage differences are at least a factor of 2 higher than the accuracy of the measured RO_2 concentration (~25 %). Therefore, the discrepancy suggests that additional loss pathways for RO_2 have to be included in the model. To examine the magnitude of the additional RO_2 loss rate, a chemical budget analysis for RO_2 radicals derived from the oxidation of limonene (C_{10}-RO_2) is performed with the method described in Section 3.4.2, in which the production rate of C_{10}-RO_2 is compared to the loss rate of C_{10}-RO_2 and the additional loss rate constant of C_{10}-RO_2 (k_{add}) required to balance the chemical budget is calculated. Table 4-4 summarizes the calculation results.

The values of the additional loss rate constant, k_{add}, range from 0.01 to 0.06 s^{-1} in different experiments but are similar to the high relative uncertainty of at least 50 %. The large relative uncertainty is caused by the small differences between production and destruction rates, which also increase with increasing RO_2 and NO concentrations (and thereby k_{RO2}). The relative uncertainties of the additional loss are less than 100 % in only three experiments, which include the ozonolysis experiment (5 June 2020) and the experiments with low (1 September 2012) and medium NO concentrations (8 August 2012). In the ozonolysis experiment, the additional RO_2 loss is lower by a factor of 4 than in the other two experiments. The large difference in k_{add} could be attributed to the different RO_2 species that are formed from the photooxidation reaction and the ozonolysis reaction. RO_2 formed from the photooxidation reaction has retained its six-member ring moiety, whereas the majority of RO_2 formed from the ozonolysis reaction is acyclic. In addition, the lower temperature during the ozonolysis experiment (286 K) than the photooxidation experiments (300 – 310 K) could lead to a slower additional loss pathway.

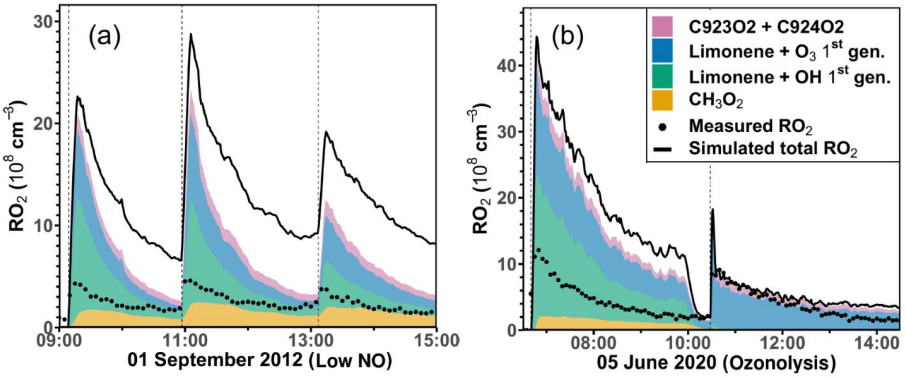

Figure 4-18. The total RO_2 radical concentrations and their specifications (shaded area) from model calculation compared to the measured values (black dots) for (a) the experiments with low NO mixing ratios and (b) the ozonolysis experiment. Methylperoxy radicals (CH_3O_2) are produced from the oxidation of HCHO. RO_2 radicals produced from in the initial reactions of limonene with OH or O_3 are summed. C923O2 and C924O2 are RO_2 radicals produced from the further oxidation of the first-generation oxidation products. Name are taken from the MCM model.

Table 4-4. Additional removal rate constants (k_{add}) that are required to balance the RO_2 production (P_{RO2}) and destruction rates in the different experiments together with conditions of the experiments such as the percentage of limonene that reacted with OH (LIM + OH) or O3 (LIM + O_3). Only data from 30 min after the first limonene injection are analyzed.

Experiment	LIM+OH (%)	LIM+O3 (%)	NO (ppbv)	P_{RO2} (10^7 cm^{-3} s^{-1})	RO_2 (10^8 cm^{-3})	k_{RO2} (10^{-2} s^{-1})	k_{add} (10^{-2} s^{-1})
Ozonolysis (05 Jun 2020)	49	51	< 0.01	2.3 ± 0.6	10.0 ± 1.4	0.9 ± 0.3	1.4 ± 0.7
Low NO (01 Sep 2012)	59	41	0.07	2.8 ± 0.8	3.5 ± 0.5	2.5 ± 0.7	5.6 ± 2.7
Low NO (04 Jul 2019)	72	28	0.09	3.1 ± 0.9	6.4 ± 1.0	3.1 ± 0.9	1.7 ± 1.7
Medium NO (08 Aug 2012)	97	3	0.29	1.7 ± 0.5	1.4 ± 0.2	6.9 ± 2.1	5.2 ± 3.5
Medium NO (10 Aug 2012)	95	5	0.35	1.8 ± 0.5	1.6 ± 0.2	8.2 ± 2.7	3.3 ± 4.2

4.3.5 Evaluating the nitrogen chemistry of limonene oxidation in model simulations

In the reference model run and constrain model run (Section 4.3.2), NO and NO_2 concentrations are constrained to measured values. If these are not constrained, NO_x is underestimated at the beginning of the experiments, but values are overestimated at the end (Fig. 4-19). The discrepancy at the beginning can be mainly attributed to the overestimation of modeled RO_2 concentration, which leads to an overestimation of the formation of organic nitrates that act as sinks for NO_x on the timescale of the experiments. To illustrate the impact of RO_2 concentrations on the modeled NOx concentrations, two model runs are compared: one with modeled RO_2 concentrations without modification of the RO_2 chemistry except the nitrates yield (reference model); and the second with modeled RO_2 concentrations adjusted to match the measurements.RO_2 concentrations are adjusted by applying an additional loss with a fixed rate constant for all six first-generation RO_2 derived from -OH and -O_3 oxidation (Fig. 4-1). The additional loss rate constant for RO_2 is around 0.01 to 0.06 s^{-1}, similar to the loss rate constant derived in the analysis of the chemical budget for C_{10}-RO_2 (k_{add}, Section 4.3.4). It should be noted that only data within 1 h after the first limonene injection are evaluated, as secondary chemistry is absent for the RO_2 that is lost additionally in this model.

Figure 4-19 shows the modeled NO and NO_x concentrations for the two model runs. The modelled NO and NO_x for other experiments are shown in Fig. S4-5. In the experiment with medium NO mixing ratios on 8 August 2012, RO_2 radical concentrations are overestimated by about 50 % to 100 % in the reference model and modeled NO, and NO_x concentrations are 25 % lower than measurements. With an additional RO_2 loss rate constant of 0.05 s^{-1}, the fraction of RO_2 that reacts with NO reduces from 80 % to 90 % in the reference model to 45 % to 60 % in the model with adjusted model. Therefore, the loss of NO_x by the formation of organic nitrates is also reduced, so that the model-measurement agreement for NO and NO_x improves for the first 2 h of the experiments.

Both model runs overestimate the NO_x and NO concentrations when all limonene reacted away after 13:00 UTC. The measured NO_x concentration remains stable at around 0.6 ppbv throughout the whole experiment after the injection of limonene. However, NO_x concentrations increase at a rate of about 0.15 ppbv h^{-1} in the reference model. The increase is reduced to less than 0.05 ppbv h^{-1} in the model run with the additional RO_2 loss during the last 2 h of the experiment. The production of NO_x in the model at later times of the experiment can be explained by the production of NO_2 from the photolysis of the first-generation organic nitrates and their oxidation by OH. These effects are more important in the reference model run when the modeled first-generation organic nitrates are high. To reconcile the difference in NO_x concentrations between the model and measurements, a stronger nitrogen sink is required in the model. This may also suggest that the model underestimates the organic nitrate formation from the reaction of NO with RO_2 from the oxidation of product species. Another explanation would be that the lifetime of limonene-derived organic nitrates from OH oxidation is too short in the model.

In the experiment with low NO concentrations on 1 September 2012, the fraction of RO_2 that reacts with NO reduces from about 50% to 16% if an additional RO_2 loss with a rate constant of 0.06 s-1 (Table 5) is applied. In this experiment, a large fraction of NO_x in the model is lost due to the formation of PAN or PAN-like species from acyl peroxy radicals (e.g., CH3CO3 and C822CO3) that are formed in the radical

chain reaction of the ozonolysis reaction of limonene (Fig. 1). The additional loss of the initially formed RO_2 species competes with the reaction with NO_2, and therefore the formation of PAN reduces if the additional loss is applied. This effect of reduced NO_x loss in the ozonolysis reaction adds to the effect for a reduced organic nitrate formation discussed for the experiment on 8 September 2012 at medium NO mixing ratios.

Although the reduced NO_x loss significantly improves the model–measurement agreement for the first part of the experiments if an additional RO_2 loss process is included in the model, NO_x concentrations are overestimated by this model at later times, when the chemistry of product species gains in importance. This could be due to neglecting the impact of the subsequent chemistry of the additional RO_2 loss reactions on nitrogen oxide concentrations. The chemistry of nitrogen oxide species in the experiment with low NO concentrations is more complex compared to the experiment with medium NO as a significant fraction of RO_2 radicals is produced by the ozonolysis of limonene in addition to the reaction with OH. Further investigation will be required to specifically clarify the impact of the formation of PAN and PAN-like species from the ozonolysis of limonene (Fig. 4-1). To the best of our knowledge, there is no experimental study investigating PAN formation from the oxidation of limonene.

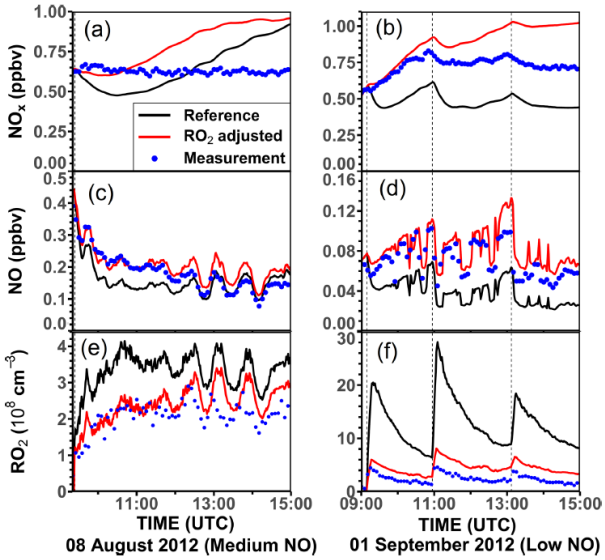

Figure 4-19. Simulation of NO_x (a, b) and NO (c, d) concentrations at different RO_2 concentrations (e, f) in experiments with medium NO mixing ratios (left panels) and low NO mixing ratios (right panels).

4.3.6 Optimizing the simulation of radical concentrations and OH reactivity in model simulations

From the investigation of radicals chemistry during the oxidation of limonene, it can be concluded the OH reactivity, RO_2, and HO_2 concentrations cannot be correctly reproduced by the MCM mechanism, whereas the OH concentration can be correctly reproduced when the OH reactivity and the HO_2 concentrations are constrained. The calculation of the chemical budget of C_{10}-RO_2 and the model simulations of nitrogen chemistry also hint the RO_2 concentrations are too high in the model. Therefore, additional reactions are implemented into the MCM model to optimize the simulation of HO_2 and RO_2 concentrations. The implementation of the additional reactions follows the method used in Hofzumahaus et al. (2009).

$$\mathrm{RO_2} + (X) \longrightarrow \text{products} + \mathrm{HO_2} \qquad \text{Reaction 4-1}$$

$$\mathrm{RO_2} + (X) \longrightarrow \text{products} + \mathrm{OH} \qquad \text{Reaction 4-2}$$

where RO_2 is the peroxy radicals distinguished from their production in the reaction of limonene with either OH (limOH–RO_2; i.e., LIMAO2, LIMBO2, and LIMCO2, Figure 4-1) or O_3 (limO_3–RO_2; i.e., LIMALAO2, LIMALBO2, and L5O2, Figure 4-1), because these peroxy radicals are structurally similar to peroxy radicals from the OH reaction with a β-OH moiety of a six-carbon ring and limO_3–RO_2 being acyclic peroxy radicals with a β-oxo, an aldehyde, and an isopropenyl group. Therefore, it is assumed that they have similar reaction pathways. These reactions could involve an unknown reaction partner *X*, or could be unimolecular reactions.

Reaction rate constants for Reaction 4-1 (k_1) and Reaction 4-2 (k_2) are implemented as pseudo-first-order reaction rate constants. RO_2 radicals within the same group (limOH–RO_2 or limO_3–RO_2) is assumed to have the same rate constants. Reaction 4-1 would lead to HO_2 production, and Reaction Reaction 4-2 would lead to OH production. In the optimized model runs, the reaction rate constants are optimized to minimize the model–measurement discrepancies for OH, HO_2, RO_2 concentrations and OH reactivity. The sum of k_1 and k_2 must be within the range of the additional RO_2 loss rate constant k_{add} (Section 4.3.4, Table 4-4). A missing HO_2 source is found in the reference model for all the experiments (Figs. 4– 7). Assuming that the loss rate of the HO_2 radical, which mainly reacts with NO, is correctly accounted for, an additional RO_2 to HO_2 conversion (Reaction 4-1) is needed to bring measurement and model results into agreement. In contrast, missing OH is only found in the experiments with low NO, as evident from the analysis of the chemical budget of OH radicals (Figure 4-15). These observations indicate that additional RO_2 to OH conversion (Reaction 4-2) can only be competitive with other bimolecular reactions for NO mixing ratios of less than 0.05 ppbv, which is equivalent to a loss rate constant of $k < 10^{-2}$ s^{-1}.

The model–measurement agreement of radical concentrations is first optimized based on the second half of the ozonolysis experiment, when CO was added as an OH scavenger. In this case, only limO_3–RO_2 is present, but the conversion to either HO_2 (Reaction 4-1) or OH (Reaction 4-2) cannot be distinguished, because OH rapidly converts to HO_2. To achieve agreement between modeled and measured HO_2 concentrations during this part of the ozonolysis experiment, the sum of the additional loss rate constants (k_1 + k_2) would need to be (0.017±0.008) s^{-1}. The uncertainty is mainly due to the uncertainty in the measurement of HO_2 concentrations of about 20 %. The upper limit for the rate constant k_2 for the loss of

$limO_3$–RO_2 can be estimated from the first part of the ozonolysis experiment, when no OH scavenger was present. Since 80 % to 100 % of the observed OH production can already be explained by OH production from the limonene ozonolysis reaction (Figure 4-17d), the rate constant of k_2 for $limO_3$-RO_2 would need to be less than 0.004 s^{-1}. This implies that the rate constant k_2 for limOH-RO_2 is also less than 0.004 s^{-1}, as about 40 % of limonene is oxidized by OH in the ozonolysis experiment without an OH scavenger.

The implementation of Reaction 4-1 for $limO_3$–RO_2 for additional HO_2 production cannot significantly improve the model–measurement discrepancies of HO_2 concentrations in the experiments, when limonene is predominantly oxidized by OH. Also in the ozonolysis experiment, HO_2 concentrations are still underestimated by about 40 % during the part of the experiment without an OH scavenger. Hence, the reaction rate constant k_1 for an additional loss of limOH–RO_2 is also optimized to match the measured HO_2 concentrations.

Optimization of the reaction rate constant k_1 for the additional loss of limOH-RO_2 for individual experiments results in values that differ by 1 order of magnitude. For instance, the optimum rate constant is (0.006±0.003) s^{-1} in the ozonolysis experiment without an OH scavenger, but it is (0.05±0.03) s^{-1} in the experiment with medium NO concentrations on 08 August 2012. These optimized rate constants are consistent with the values of the loss rate constant k_{add} (Table 4-4), with the rate required in the ozonolysis experiment having a slower rate and the rate required in the experiment with medium NO concentrations having a faster rate. The exact reason for such large differences is not clear but could be related to the higher temperature (16°C – 27 °C) in the photooxidation experiments, when the chamber air was exposed to sunlight. The average value of the rate constant for the conversion from RO_2 to HO_2 for the experiments in this work is 0.03 s^{-1}. This value is applied to all optimized model runs in the following to illustrate its impacts on modeled RO_2 and HO_2 concentrations and OH reactivity (Figure 4-21 to Figure 4-23).

A summary of all reactions included for the optimized model run is available in Table 4-5. Figure 4-20 shows the increase in the OH production rate in the optimized model runs that include the conversion of limO3-RO_2 to OH at a rate constant of 0.003 s^{-1}. The total OH production rate increases by about 0.2 ppbv h^{-1} in both experiments, corresponding to 5 % to 10 % increases. This reduces the imbalance between OH production and destruction rates in the experiment with low NO by about 20 % without significantly impacting the balance in the ozonolysis experiment. This demonstrates that the additional OH production from the conversion of limOH–RO_2 and $limO_3$–RO_2 to OH is not sufficient to fully close the gap between OH production and destruction rates in the experiment with low NO, for which the discrepancy is largest among all experiments in this work.

Figure 4-21 to 4-23 and Fig. S4-6 to S4-8 show the radical concentrations and OH reactivity obtained in the reference and optimized model runs. In the optimized model run, the model-measurement agreement for RO_2 and HO_2 concentrations improves compared to the reference model run, as can be expected from the adjustment of the reaction rate constant. In the experiment with low NO concentrations, however, an optimal agreement of both RO_2 and HO_2 concentrations cannot be simultaneously achieved.

Table 4-5. Additional reactions implemented in the MCM model to optimize the simulation of radical concentrations and OH reactivity.

Reaction	Reaction rate constant (s^{-1})	Comment
LIMALAO2 → OH LIMALBO2 → HO_2 L5O2 → HO_2	0.003	Illustrate the impact of the additional OH source on the OH budget in the ozonolysis experiment, when there is no OH scavenger.
LIMALAO2 → HO_2 LIMALBO2 → HO_2 L5O2 → HO_2	0.014	Derived from the optimization of HO2 model-measurement agreement in the ozonolysis experiment when there is an OH scavenger, assuming k_2 for $limO_3$-RO_2 is 0.003 s^{-1}.
LIMAO2 → HO_2 LIMBO2 → HO_2 LIMCO2 → HO_2	0.030	Optimized based on the HO_2 model-measurement agreement in the experiments with low NO and medium NO, and the ozonolysis experiment when OH scavenger is absence. 0.030 s^{-1} is the mean value of the optimized values that span one order of magnitude.

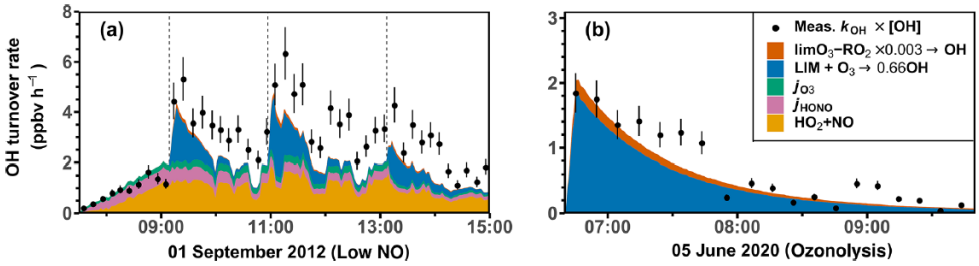

Figure 4-20. Measured 10-min mean total OH destruction rate compared to the OH production rate from the main measured OH sources for (a) the experiment with low NO concentration on 1 September 2012 and (b) the ozonolysis experiment on 5 June 2020 for the optimized model run that includes additional OH production from the reaction of RO_2 from limonene ozonolysis and HO_2 (Reaction 4-2).

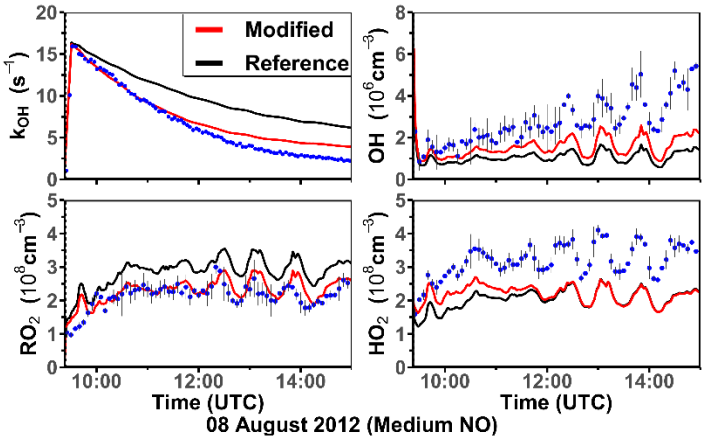

Figure 4-21. Comparison of the modelled OH reactivity k_{OH}, OH, HO_2, RO_2 radical concentrations in the photooxidation experiment with medium NO mixing ratio on 08 Aug 2012 using the MCM model (reference model) and the model with additional reaction pathways from Table 4-5 implemented (modified model).

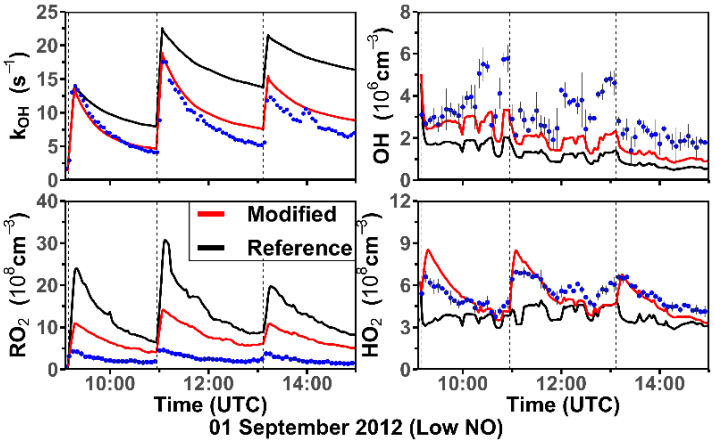

Figure 4-22. Comparison of the modelled OH reactivity k_{OH}, OH, HO_2, RO_2 radical concentrations in the photooxidation experiment with low NO mixing ratio on 01 Sep 2012 using the MCM model (reference model) and the model with additional reaction pathways from Table 4-5 implemented (modified model).

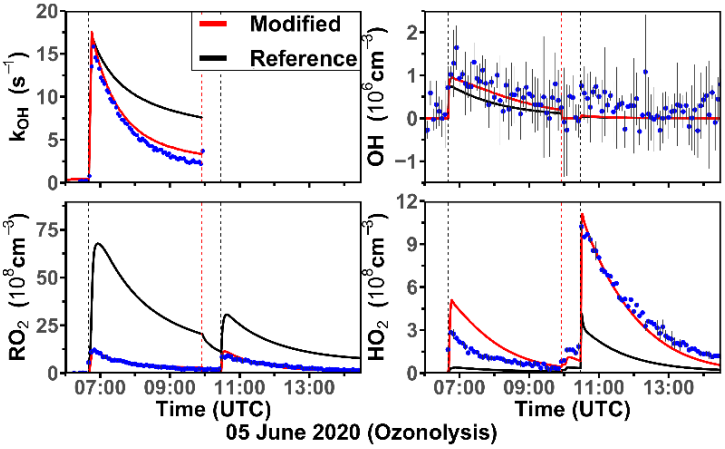

Figure 4-23. Comparison of the modelled OH reactivity k_{OH}, OH, HO_2, RO_2 radical concentrations in the ozonolysis experiment on 05 Jun 2012 using the MCM model (reference model) and the model with additional reaction pathways from Table 4-5 implemented (modified model).

4.4 Discussions

In this section, possibilities of the underlying chemistry of the additional loss of RO_2 and the additional production of HO_2 from Reaction 4-1 are discussed. The small additional OH source from the conversion from RO_2 with a reaction rate constant of 0.003 s^{-1} is not discussed here (Reaction 4-2), as its contribution on the chemical budget of OH radicals are small (Fig. 4-20).

4.4.1 RO_2 loss and HO_2 production from RO_2 isomerization reactions

HO_2 radicals can be produced from the isomerization reaction of RO_2 radicals for example in the isomerization reaction of RO_2 radicals derived from isoprene photooxidation (Peeters et al. 2014).

The possibility of the conversion from RO_2 to HO_2 by isomerization is investigated using the isomerization pathways calculated for RO_2 derived from limonene oxidation and SARs (Fig. 4-2 and 4-3; Vereecken and Peeters, 2009; Møller et al., 2020; Vereecken and Nozière, 2020; Chen et al., 2021; Vereecken et al., 2021).

For radicals produced from the photooxidation of limonene, RO_2 radicals LIMAO2 and LIMBO2 can undergo a slow ($k < 10^{-3}$ s^{-1}) -OH H-shift reaction that is 1 order of magnitude slower than the rate of the RO_2-to-HO_2 conversion applied in the sensitivity run (Fig. 4-2). In addition, the production of HO_2 through the H-abstraction by O_2 of the alkoxy radical LIMA_15shift_O is not as favorable as the ring-cleavage alkoxy dissociation that eventually produces an OH radical (Vereecken and Peeters, 2009). Therefore, even with the potential production of HO_2 through the isomerization of RO_2 derived from the isomerization of LIMCO2 (e.g., 1,8 α-OH H-shift of LIMC_6cyc_O2), the production of HO_2 is limited by the 37% yield of LIMCO2 from the oxidation of limonene by OH. In addition, the rate constants of the H-shift reaction for the intermediate radicals derived from LIMCO2 (e.g., LIMC_6cyc_O2, LIMC_ 16allylic_O2, LIMC_15allylic_O2) have a high uncertainty, as it is assumed that the SARs for acyclic compounds can be applied for cyclic RO_2. For these reasons, isomerization reactions for limOH–RO_2 are unlikely the reason for the additional HO_2 production and RO_2 loss required to match observed radical concentration measurements.

For radicals produced from the ozonolysis of limonene, reaction rate constants of the first two of the isomerization reaction are about 1 to 2 orders of magnitude faster than the RO_2-to-HO_2 conversion rate used in the optimized run (Fig. 4-3). One of the possible RO_2 loss mechanisms through the isomerization reaction is an α-OOH H-abstraction reaction. Although the value of the rate constant of the α-OOH H-abstraction reaction derived from SAR is of the same magnitude (~10^{-2} s^{-1}) as the RO_2-to-HO_2 conversion rate constant applied in the optmized run, abstraction of the hydrogen with an α-OOH group would lead to the production of an OH radical rather than a HO_2 radical. Therefore, isomerization reactions of limO_3–RO_2 can also not explain the missing RO_2-to-HO_2 conversion resulting from observations in the experiments in this work.

4.4.2 RO_2 loss from the RO_2 recombination reaction

Apart from isomerization, HO_2 could also be produced from the dissociation of alkoxy radicals derived from RO_2 from the reaction of limonene with OH. Alkoxy radicals could be produced from the recombination reaction of RO_2 radicals in addition to the reaction of RO_2 with NO.

$RO_2 + R'O_2 \longrightarrow RO + R'O + O_2$ Reaction 4-3

$RO_2 + R'O_2 \longrightarrow ROH + R'(=O) + O_2$ Reaction 4-4

$RO_2 + R'O_2 \longrightarrow R(=O) + R'OH + O_2$ Reaction 4-5

$RO_2 + R'O_2 \longrightarrow ROOR + O_2$ Reaction 4-6

The current knowledge about the branching ratio of Reaction 4-3 to Reaction 4-6, as well as the reaction rate constants of RO_2 self- or cross-reaction is limited, especially for complex RO_2 derived from monoterpenes. There are no specific investigations for RO_2 from limonene. Reaction rate constants implemented in the MCM model are based on estimated cross-reaction rates between RO_2 and methyl peroxy radicals (CH_3O_2) (Jenkin et al., 1997, 2019). The reaction rate constants of the RO_2 recombination reactions, $k_{RO2+RO2}$, for limonene-derived radicals are between 10^{-12} and 10^{-13} cm^3 s^{-1} in the MCM, consistent with results for RO_2 from methyl cyclohexene, which contain a trisubstituted endocyclic double bond like limonene (Boyd et al., 2003).

However, the reaction rate constant $k_{RO2+RO2}$ could be higher if the cross-reaction partners are other large limonene-derived radicals rather than CH_3O_2. For example, Berndt et al. (2018) investigated the self-reaction rate constants for RO_2 derived from the reaction of α-pinene with OH after they undergo two steps of unimolecular reactions (i.e., $C_{10}H_{16}OH(O_2)_2$-O_2). They found that values range between 1-4×10^{-11} cm^3 s^{-1} in this case. However, it should be noted that these reaction rate constants are derived from the production rate of peroxide products (ROOR, Reaction 4-6) rather than the loss rate of RO_2.

Using the values of the reaction rate constants $k_{RO2+RO2}$ for RO_2 from limonene oxidation from the MCM, the upper limit of the RO_2 loss rate constant due to the reactions with other RO_2 is about 10^{-3} s^{-1} in the ozonolysis experiment and experiments with low NO mixing ratios, and 2×10^{-4} s^{-1} in the experiments with medium NO mixing ratios. From the additional loss rate constant (10^{-2} s^{-1}; Table 4-4) determined from the chemical budget analysis for C_{10}-RO_2, the value of the reaction rate constant for the RO_2+RO_2 reaction that would be required to explain the observations ($k'_{RO2+RO2}$) can be calculated. This results in values of $k'_{RO2+RO2}$ that are about 3×10^{-10}, 1×10^{-11}, and 3×10^{-11} cm^3 s^{-1} in the medium-NO, low-NO, and ozonolysis experiments, respectively. The uncertainties of the rate constants are about 50 % to 60 %, which are derived from the error propagation of RO^2 concentrations and optimal rate constants in the optimized model run (Table 4-5). It should be noted that these values are collective loss rate constants of all first-generation RO_2 species from limonene oxidation before the formation of closed-shell products, including highly oxidized RO_2 produced from potential auto-oxidation reactions.

The values of the reaction rate constant $k'_{RO2+RO2}$ found in the low-NO experiment and ozonolysis experiment are on the same order of magnitude (10^{-11} to 10^{-10} cm^3 s^{-1}) as values reported by Berndt et al.

(2018) for RO_2 from α-pinene oxidation. Berndt et al. (2018) also showed that the reaction rate constant for the self-reaction of RO_2 increases when the RO_2 becomes more oxidized. This hints that the importance of RO_2 recombination reactions for RO_2 derived from limonene oxidation could be higher than previously thought because of the rapid isomerization reaction of these radicals (Møller et al. (2020) and Chen et al. (2021); Fig. 4-2 and 4-3).

In the experiment with low NO concentrations, the additional loss rate constant for RO_2 radicals that is required to explain measured RO_2 concentrations (k ~ 0.06 s^{-1}, Table 4-4) is higher than the rate constant of the additional RO_2-to-HO_2 conversion required to explain measured HO_2 concentration (k ~ 0.006 to 0.02 s^{-1}). This would be consistent with a faster reaction rate constant for the RO_2+RO_2 reaction, because only a fraction of the RO_2+RO_2 reaction would lead to the formation of alkoxy and therefore HO_2 radicals (Reaction 4-3 to Reaction 4-6).

However, it would be unclear why the reaction constant $k'_{RO2+RO2}$ required in the experiment with a medium NO mixing ratio would be higher compared to the other experiments. It is also worth noting that the decomposition of alkoxy radicals produced from RO_2 from the ozonolysis of limonene leads to the production of peroxy radicals, which does not lead to the production of HO_2 in most of the RO_2–RO_2 reaction chain (Fig. 4-1). Therefore, the missing production of HO_2 in the ozonolysis experiment cannot be explained by a higher than previously thought reaction rate constant of the RO_2–RO_2 reaction.

5. Investigation of the oxidation mechanism of sabinene by OH radicals and O_3 in simulation chamber experiments

Most of the content of this chapter was published as peer-reviewed article "Atmospheric photooxidation and ozonolysis of sabinene: reaction rate coefficients, product yields, and chemical budget of radicals" (doi: https://doi.org/10.5194/acp-23-12631-2023) in the journal *Atmospheric Chemistry and Physics* by this author (Pang et al., 2023). Parts of the text and figures in this chapter are adapted from this open-access publication, under the CC BY 4.0 license (https://creativecommons.org/licenses/by/4.0).

5.1 Proposed mechanism of the oxidation of sabinene

There are fewer studies on the oxidation of sabinene compared to limonene as sabinene is less abundant in the atmosphere. An oxidation mechanism of sabinene is not implemented in the MCM and therefore evaluation of the oxidation of the sabinene is based on the few published mechanisms.

Oxidation mechanisms of sabinene by OH radicals were proposed by Carrasco et al. (2006) and Wang and Wang (2018). Carrasco et al. (2006) determined the product yield from oxidation experimentally and investigated the energy barrier of different reaction pathways for first-generation alkyl and alkoxy radicals with quantum chemical calculation. Wang and Wang (2018) conducted a more comprehensive theoretical study on the OH-oxidation of sabinene, where unimolecular reactions of RO_2 derived from the oxidation of sabinene were also investigated.

Figure 5-1 illustrates the oxidation mechanism proposed by Wang and Wang (2018). Similar to the oxidation of limonene, the OH-oxidation of sabinene could either start with the addition reaction on the C=C double bond or the abstraction of an H-atom. More than 90 % of the OH-oxidation proceeds through the OH-addition pathway (pathways (a) and (b) in Figure 5-1) and results in the production of two RO_2 species, SABINOHAO2 and SABINOHBO2. Due to the ring strain present in the bicyclic three-member ring, the alkyl radical formed from the OH-addition reaction through pathway (b) quickly isomerizes to release the ring strain with a yield of 99 % under typical atmospheric conditions. The isomerized alkyl radical subsequently reacts with O_2 to form RO_2 SABINOHBO2.

There are no competitive unimolecular reactions with rate constant exceeding 10^{-3} s^{-1} for the peroxy radical SABINOHAO2, therefore this RO_2 radical mainly loss in bi-molecular reactions for atmospheric conditions. The reaction of SABINOHAO2 with NO produces HCHO and sabinaketone, which are the major oxidation products of sabinene by OH radicals. In contrast, the peroxy radical SABINOHBO2 has a more competitive unimolecular reaction with a rate coefficient of 5 s^{-1} at room temperature. This value is equivalent to the loss rate of RO_2 in the presence of 22 ppbv of NO. The product of the unimolecular reaction subsequently reacts and isomerizes to form close-shell product with a chemical formula of

$C_{10}H_{16}O_5$. The competing bimolecular reaction with NO of SABINOHBO2 produces the major product acetone and a closed-shell product with the sum formular $C_7H_{10}O_2$.

The mechanism of the ozonolysis reaction was investigated with quantum chemical calculations by several studies (Zhao et al., 2010; Wang and Wang, 2017; Almatarneh et al., 2019). Studies conducted by Zhao et al. (2010) and Almatarneh et al. (2019) investigated the chemistry of O_3-addition and Criegee intermediates, whereas Wang and Wang (2017) also looked into the chemistry of species produced after Criegee intermediates and calculated the theoretical yield of major products based on the mechanism. Therefore, the mechanism proposed by Wang and Wang (2017) is used as a reference to evaluate the ozonolysis experiments of sabinene in this work.

Figure 5-2 shows the simplified ozonolysis mechanism of sabinene proposed by Wang and Wang (2017). The O_3 addition on the C=C double bond produces a carbonyl product and a Criegee intermediate. The production of C_9-Criegee intermediates (CI-1 and CI-2) that is accompanied by the production of HCHO (pathways (B) and (C)) is much more favorable than the production of the C_1-Criegee intermediate (CH_2OO) together with the C_9-cabonyl product sabinaketone (pathway (A)). It is expected that 83 % of the reaction proceeds through the pathways (B) and (C) and 17 % undergoes pathway (A). Criegee intermediates CI-1 and CI-2 produced from pathways (B) and (C) could then undergo unimolecular reaction or bi-molecular reactions. Although CI-1 and CI-2 have similar structure, they have different chemistry owning to the bicyclic ring. CI-1 proceeds with a 1,4-H-shift to a vinyl hydroperoxide (VHP) with a very fast rate coefficient (2700 s^{-1}), whereas CI-2 can only undergo a ring-closure reaction to dioxirane with a rate coefficient of 1 s^{-1}, or can be stabilized through the collision with air molecules to form a stabilized Criegee intermediate (sCI). The VHP from CI-1 dissociates and forms an OH radical and a β-oxoalkyl radical that reacts with O_2 to form a RO_2 radical. The dioxirane from CI-2 isomerizes and can form lactones. At room temperature and pressure, the majority (89 %) of CI-1 undergoes the fast unimolecular reaction forming a VHP whereas with only 11 % is stabilized. Only 22 % of CI-2 undergoes the slow unimolecular reaction forming dioxirane and 78 % of CI-2 is stabilized. The stabilized Criegee intermediates from both CI-1 and CI-2 can react bi-molecular reaction with for example water, CO, and NO, or undergo unimolecular reactions with pathways that are similar to that of Criegee intermediates. The reaction of sCI with water can produce an α-hydroxylalkyl hydroperoxide (AHAP, Figure 5-2), which can decompose into hydroperoxide and sabinaketone through catalyzation by water and organic acids.

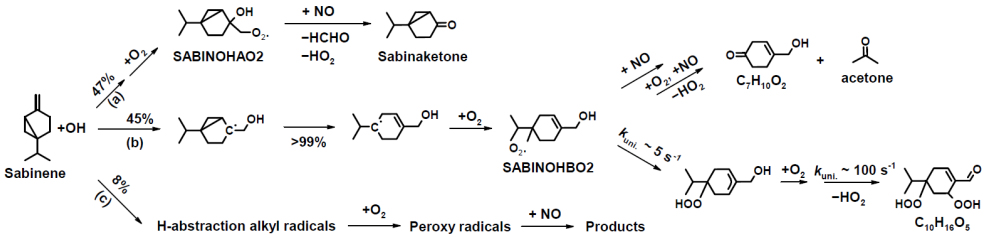

Figure 5-1. Simplified mechanism of the oxidation of sabinene by OH radical proposed by Wang and Wang (2018).

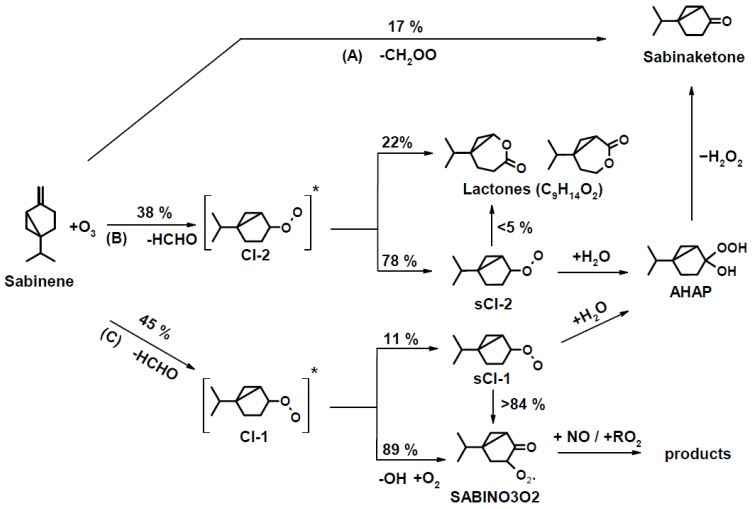

Figure 5-2. Simplified mechanism of the ozonolysis of sabinene proposed by Wang and Wang (2017).

5.2 Overview of sabinene oxidation experiments

In total seven experiments were conducted to investigate the oxidation of sabinene at different NO mixing ratios in the SAPHIR chamber. The experiments can be divided into three types with different conditions (ozonolysis, photooxidation at low, and medium NO mixing ratios) as described in Section 2.4. The experimental conditions of the experiments are summarized in Table 5-1. The complete list of instruments used in the study can be found in Table 2-1 (Chapter 2). Measurements of the OH reactivity with the LIF instrument; measurements of NO and NO_2 with chemiluminescence; measurements of O_3 with UV absorption; measurement of VOCs with PTR-TOF-MS; and measurements of photolysis frequencies with spectroradiometer were available in all experiments for the study of sabinene. The availability of the radical and formaldehyde is listed in Table 5-2. Figure 5-3 to 5-9 shows the relevant measurements of trace gases and radical concentrations of all sabinene oxidation experiments analyzed in this study.

Table 5-1. Experimental conditions during the time period when the sabinene oxidation experiments are analyzed. k_{RO2} is the sum of the total loss rate RO_2 due to bimolecular reactions with NO, HO_2, and other RO_2 calculated from measured concentrations. Average values are given except for limonene concentrations, for which maximum concentrations after the injection are given.

Type of experiment	Temperature (K)	NO (ppbv)	k_{RO2} (s^{-1})	OH (10^6 cm^{-3})	O_3 (ppbv)	Sabinene (ppbv)	Date	Figure
Ozonolysis	279	0	0.02	< 1	105	6	24 Jan 2022	Fig. 5-3
	277	0	0.02	< 1	220	6	25 Jan 2022	Fig. 5-4
Low NO	303	0.2	/[a]	6	75	4.5	08 Sep 2021 (1st injection)	Fig. 5-5
	303	0.25	0.07	3.5	70	8	30 Jun 2022	Fig. 5-6
	295	0.10	0.03	3.5	105	6	06 Jul 2022	Fig. 5-7
Medium NO	302	0.5	/[a]	5.0	15	3.5	06 Sep 2021	Fig. 5-8
	297	0.5	/[a]	4.5	10	4	08 Sep 2021 (2nd injection)	Fig. 5-5
	304	1.0	0.4	3.5	25	6	05 Jul 2022	Fig. 5-9

[a]Radical measurements by LIF were not available for experiments on 06 and 08 Sep 2021

Table 5-2. Availability of measurements for radicals and formaldehyde for the oxidation experiments of sabinene. Available measurements are indicated with a tick symbol.

Date	Instrument (Measured species)		
	DOAS (OH, HCHO)	LIF (OH, HO_2, RO_2)	CRDS (HCHO)
24 Jan 2022	✓	✓	✓
25 Jan 2022	✓	✓	✓
08 Sep 2021	✓		✓
30 Jun 2022	✓	✓	✓
06 Jul 2022		✓	
06 Sep 2021	✓		✓
05 Jul 2022	✓	✓	

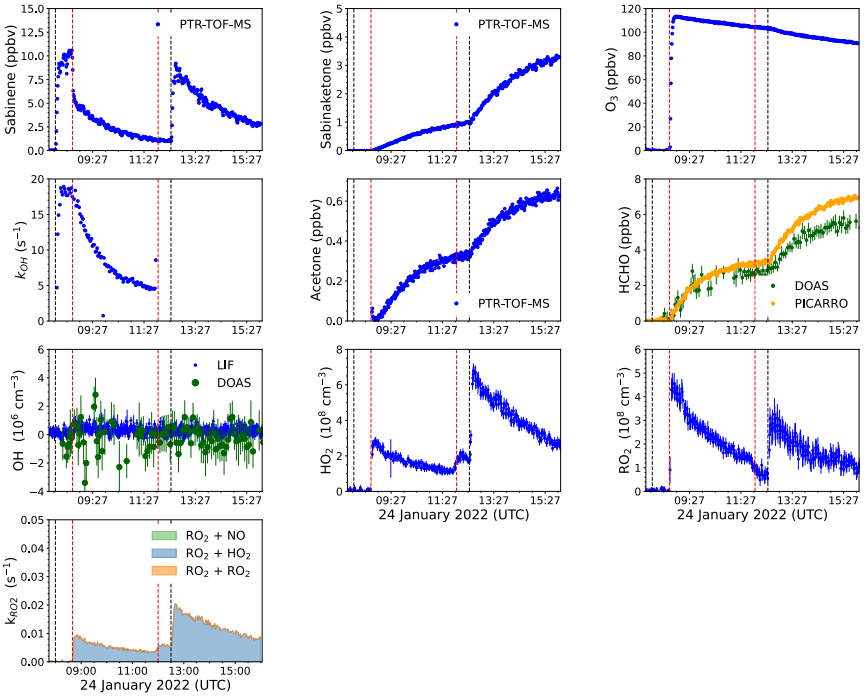

Figure 5-3. Overview of the measured radical and trace gas concentrations used in the analysis of the sabinene ozonolysis experiment on 24 January 2022. The leftmost red line indicates when O_3 was injected; the middle red line indicates when 100 ppmv of CO was injected; the black lines indicate when limonene was injected into the chamber. After the injection of CO, the OH reactivity was too high to be measured (about 500 s^{-1}).

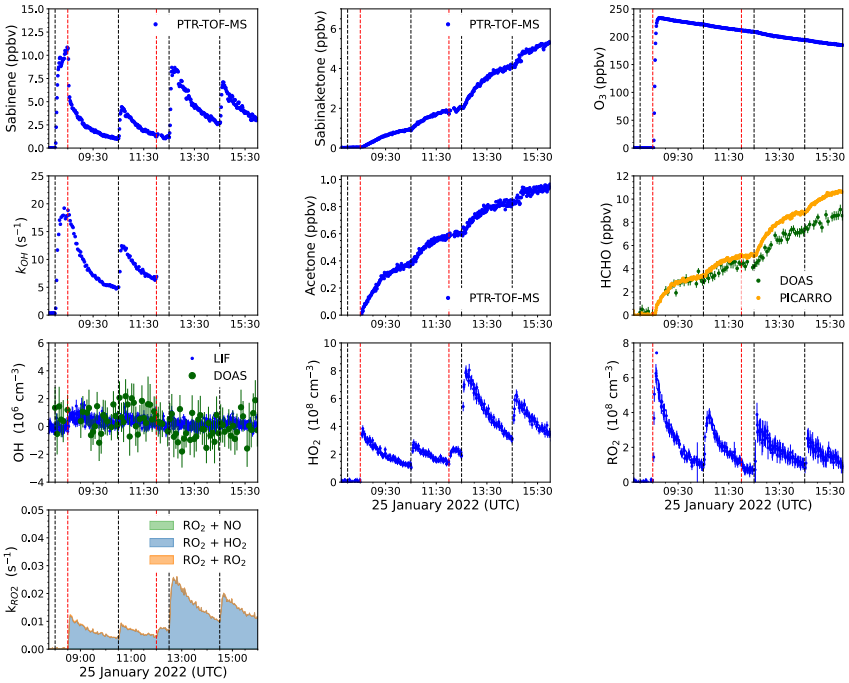

Figure 5-4. Overview of the measured radical and trace gas concentrations used in the analysis of the sabinene ozonolysis experiment on 25 January 2022. The leftmost red line indicates when O_3 was injected; the middle red line indicates when 100 ppmv CO was injected; the black lines indicate when limonene was injected into the chamber. After the injection of CO, the OH reactivity was too high to be measured (about 500 s^{-1}).

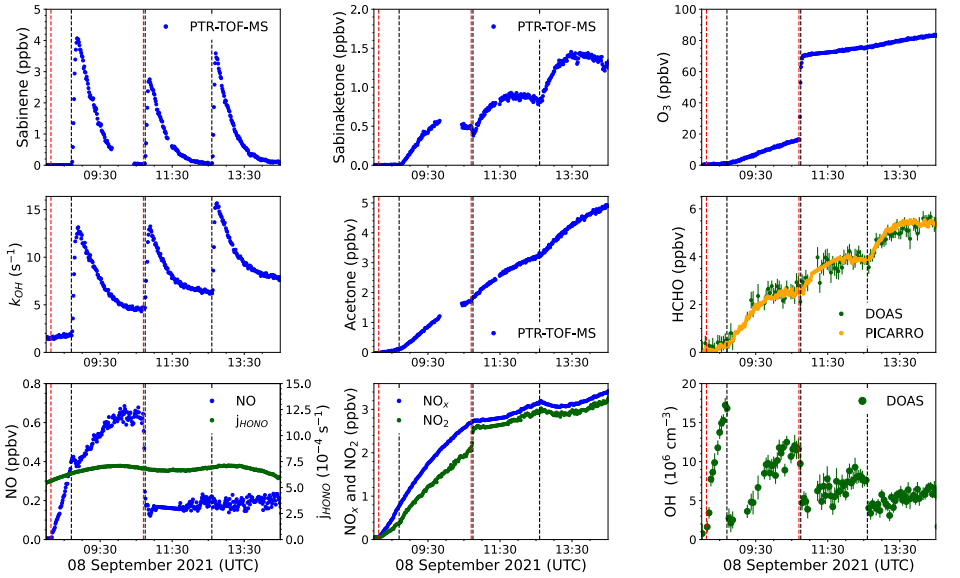

Figure 5-5. Overview of the measured radical and trace gas concentrations used in the analysis of the sabinene photooxidation experiment with low and medium NO mixing ratios on 08 September 2021. The leftmost red line indicates when the chamber roof was opened; the middle red line indicates when O_3 was injected; the black lines indicate when limonene was injected into the chamber.

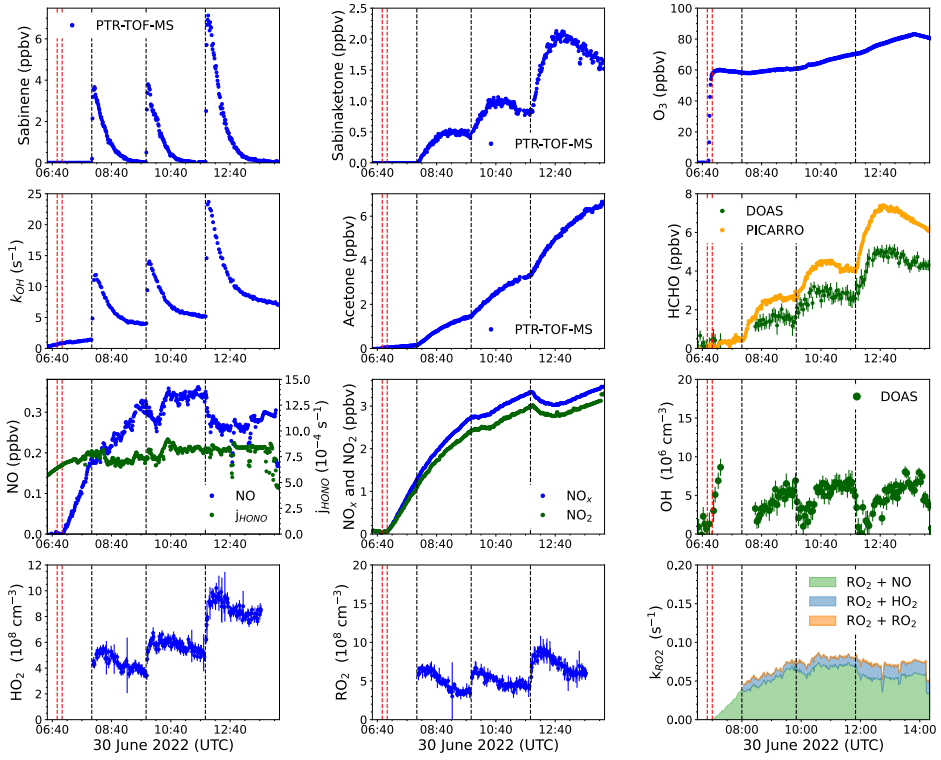

Figure 5-6. Overview of the measured radical and trace gas concentrations used in the analysis of the sabinene photooxidation experiment with low NO mixing ratios on 30 June 2022. The leftmost red line indicates when O_3 was injected; the second leftmost red line indicates when the chamber roof was opened; the black lines indicate when sabinene was injected into the chamber.

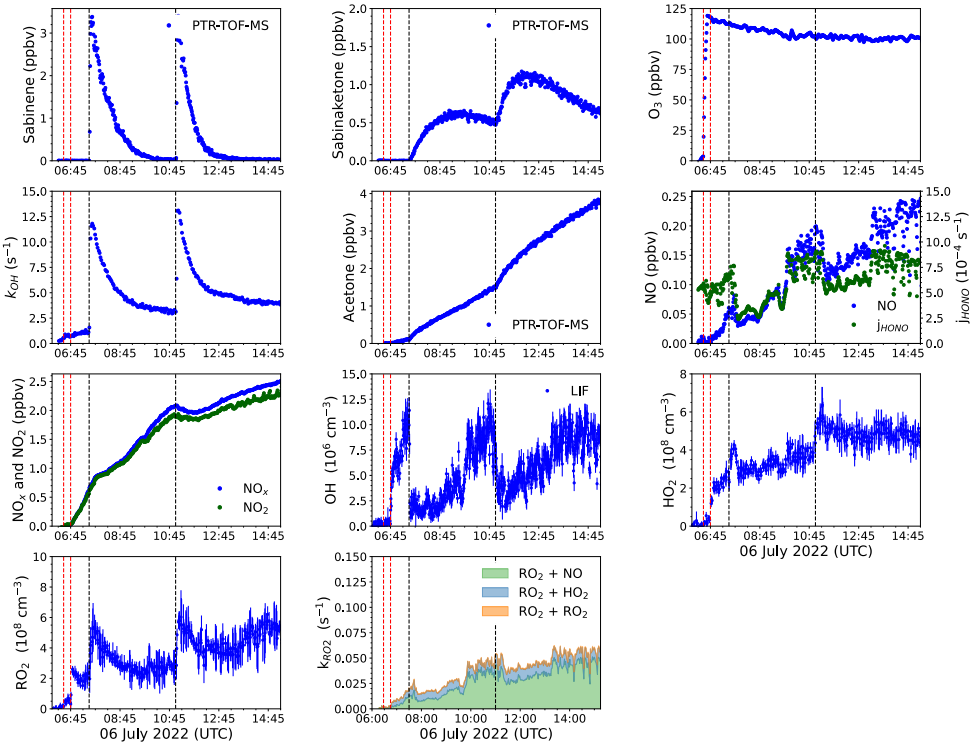

Figure 5-7. Overview of the measured radical and trace gas concentrations used in the analysis of the sabinene photooxidation experiment with low NO mixing ratios on 06 July 2021. The leftmost red line indicates when O_3 was injected; the second leftmost red line indicates when the chamber roof was opened; the black lines indicate when sabinene was injected into the chamber.

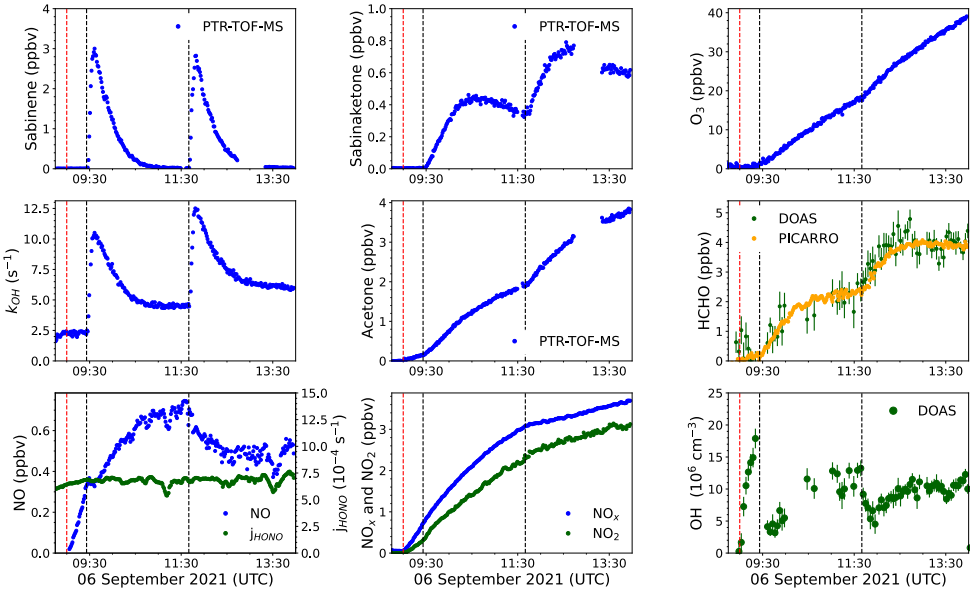

Figure 5-8. Overview of the measured radical and trace gas concentrations used in the analysis of the sabinene photooxidation experiment with medium NO mixing ratios on 06 September 2021. The leftmost red line indicates when the chamber roof was opened; the black lines indicate when sabinene was injected into the chamber.

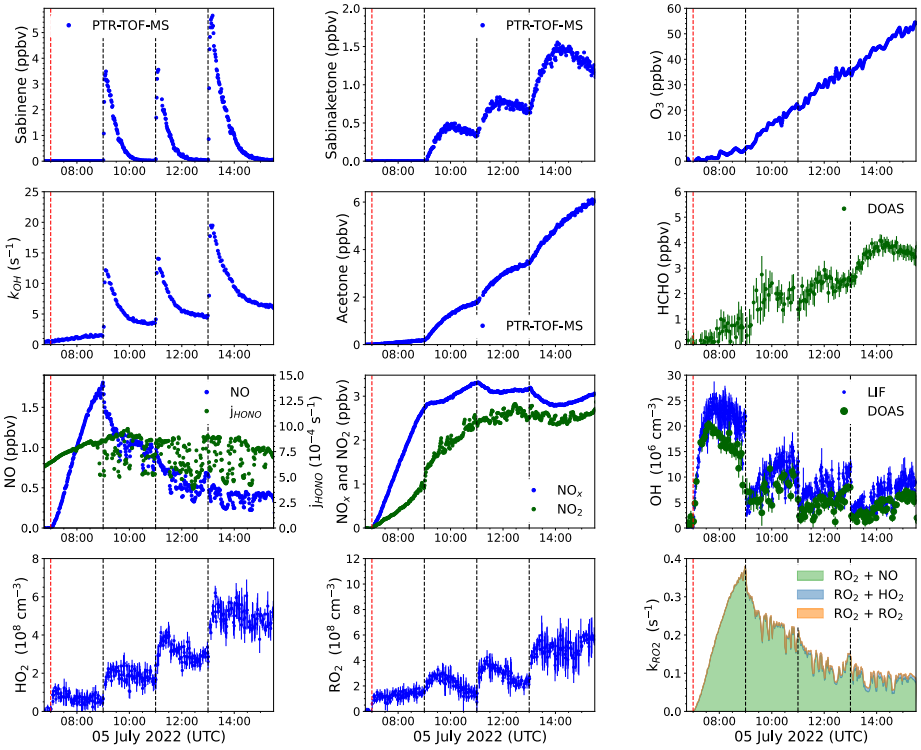

Figure 5-9. Overview of the measured radical and trace gas concentrations used in the analysis of the sabinene photooxidation experiment with medium NO mixing ratios on 05 July 2022. The leftmost red line indicates when the chamber roof was opened; the black lines indicate when sabinene was injected into the chamber.

5.3 Results of the analysis of sabinene oxidation experiments

5.3.1 Reaction rate coefficients of the oxidation of sabinene (k_{SAB+OH} and k_{SAB+O3}) determined in chamber experiments and in laboratory measurements

The average value of the ozonolysis reaction rate constant k_{SAB+O3} determined from the chamber experiments in this work is (3.4±0.8) × 10^{-17} cm^3 s^{-1}. This value is 58 % lower than values reported in literature (Table 5-3), in which the reaction rate coefficient k_{SAB+O3} was determined at room temperature ((296±2) K) using absolute and relative rate techniques (Atkinson et al., 1990a, b; Bernard et al., 2012). The lower value determined in this study could be due to the low temperature (278 K) in the chamber experiments. This is supported by the known temperature dependence of ozonolysis rate coefficients of structurally similar alkenes such as isobutene, β-pinene, and camphene, for which values decrease by about 25 % to 50 % with relative uncertainties of about 25 % (Cox et al., 2020).

SAR in Jenkin et al. (2020) gives values for the ozonolysis reaction rate coefficient of sabinene four to five times lower than values determined with laboratory studies in this work and reported in literature. Values are 1.4×10^{-17} and 9.3×10^{-18} cm^3 s^{-1} at 298 K and 278 K, respectively. Since all experimentally determined values are higher, it is likely that SAR underpredicts the rate coefficient k_{SAB+O3}. The large difference is likely related to the ring strain of the bicyclic ring. Species in that SAR with ozonolysis rate constants differing by more than a factor of three are mostly polycyclic compounds (e.g., camphene, α-copaene, and 3-carene) including sabinene. Since the SAR was constructed mostly with acyclic and monocyclic alkenes, it is likely that the impact of the ring strain on the ozonolysis rate constant for polycyclic species is not properly captured.

The Arrhenius expression of the reaction rate coefficient k_{SAB+OH} derived from laboratory OH reactivity measurements at temperatures between 284 K and 340 K at ambient pressure is

$k_{SAB+OH}(T) = (1.67\pm0.16)\times10^{-11}\times\exp((537\pm30)/T)$ cm^3 s^{-1}

The accuracy is 13 % to 15 % (Fig. 5-10), which is mainly due to the uncertainty of sabinene concentrations during the OH reactivity measurement. The value at room temperature of 298 K is (1.0±0.2)×10^{-10} cm^3 s^{-1}. This agrees with the value required to describe the consumption of sabinene in the chamber experiments of (1.4±0.5)×10^{-10} cm^3 s^{-1} (Fig. 5-11), as well as with the value of (1.17±0.05)×10^{-10} cm^3 s^{-1} determined in laboratory experiments (Atkinson et al., 1990b). The temperature-dependence coefficient of the rate coefficient k_{SAB+OH} of (537±30) K is similar to that of structurally similar β-pinene ((460±150) K) and isobutene ((505±200) K) (Mellouki et al., 2021).

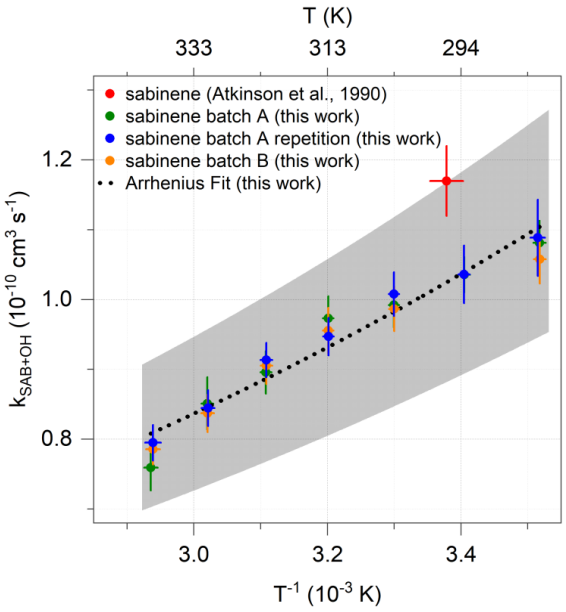

Figure 5-10. Values of k_{SAB+OH} determined in laboratory experiments using the OH reactivity instrument. The shaded area represents the uncertainty of the Arrhenius expression.

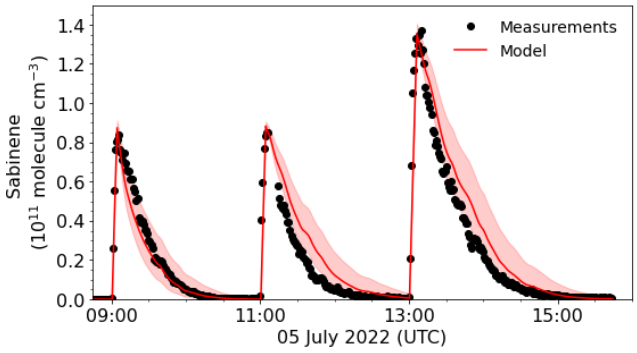

Figure 5-11. Modelled and measured sabinene concentrations in the photooxidation experiment with medium NO mixing ratios (05 July 2022) used for the determination of the OH reaction rate coefficient k_{SAB+OH}. The red line and shaded area represent the simulation results applying a value of the OH reaction rate coefficient of sabinene of k_{SAB+OH} = (1.4±0.5)×10^{-10} cm^3 s^{-1}.

Table 5-3. List of the reaction rate coefficients of the oxidation of sabinene by OH radicals and O_3 reported in literature and determined in this study.

	Reaction rate coefficient ($cm^3\ s^{-1}$)	Temperature (K)	Method	Reference
Sabinene + OH	$(1.17\pm0.05) \times 10^{-10}$	296±2	Relative rate	Atkinson et al. (1990b)
	6.08×10^{-11}	298	SAR	Jenkin et al. (2018)
	$(1.67\pm0.16) \times 10^{-11} \times \exp((537\pm30)/T)$	284 – 340	OH reactivity measurement	This study
Sabinene + O_3	$(8.1\pm0.8) \times 10^{-17}$	296±2	Absolute rate	Atkinson et al. (1990a)
	$(6.2\pm2.1) \times 10^{-17}$	297±2	Absolute rate	Bernard et al. (2012)
	$(8.8\pm1.0) \times 10^{-17}$	296±2	Relative rate	Atkinson et al. (1990b)
	1.4×10^{-17}	298	SAR	Jenkin et al. (2020)
	$(3.4\pm0.8) \times 10^{-17}$	278±2	Absolute rate	This work

5.3.2 Product yield of the oxidation of sabinene

Formaldehyde is one of the major products from the oxidation of sabinene by both oxidants, OH and O_3. The analysis of the photooxidation experiments results in a HCHO yield of (46±25) %. The uncertainty is due to the uncertainty of the HCHO chamber source, corrections for the loss of HCHO, and the calculation of the amount of reacted sabinene. There is no significant difference in the HCHO yields determined in the experiments with either medium or low NO mixing ratios (Fig. 5-12a), which can be expected as the majority of RO_2 radicals reacted with NO in both experiments (Fig. 5-6, Fig. 5-7, and Fig. 5-9). The HCHO yield reported in this study is higher than the yield of 25 % reported by Carrasco et al. (2006) (Table 5-4), who conducted experiments at a high concentration (~ 2 ppmv) of sabinene using either H_2O_2 or HONO photolysis as OH sources. The authors found similar HCHO yields in their experiments for different NO concentrations. Larsen et al. (2001) also performed experiments in the absence of NO and resulting in HCHO yield of (35±4) %. This value is lower than the yield found in this study but still agrees within the uncertainties.

The photooxidation of sabinene results in an acetone yield of (21±15) % in this study (Fig. 5-12b), when OH radicals predominantly reacted with sabinene. The uncertainty of the acetone yield is mainly due to the uncertainty in the chamber source, corrections for losses, and the calculation of the amount of reacted sabinene. The value is consistent with the yields in the studies by Carrasco et al. (2006) and Reissell et al. (1999) (Table 5-4). Reissell et al. (1999) performed photooxidation experiments at high initial NO concentrations (~10 ppmv) and with a high NO:sabinene concentration ratio (~10:1). In another study by Larsen et al. (2001), the acetone yield was lower than the values found in this study and studies conducted by Reissell et al. (1999) and Carrasco et al. (2006).

The yield of sabinaketone of the photooxidation of sabinene is (18±16) % (Fig. 5-12c). The large uncertainty of the calculation is due to the uncertainty of the measurement sensitivity of sabinaketone.

This value agrees well with literature values that range from 17 % to 24 % (Table 5-4). There is no significant dependence of the yield of sabinaketone from the OH oxidation of sabinene on the NO mixing ratio, which is also consistent with the findings in Carrasco et al. (2006).

The HCHO yield determined in the ozonolysis experiments is (48±15) %, when the OH oxidation was suppressed by the presence of an OH scavenger. This value is consistent with the yield of (52±9) % reported by Chiappini et al. (2006), who conducted ozonolysis experiments in the presence of an OH scavenger and with high concentrations (~ 1 ppmv) of sabinene and O_3.

The ozonolysis of sabinene produces a small amount of acetone compared to the photooxidation by OH. The low acetone yield of (5±2) % determined in this study agrees well with those reported by Reissell et al. (1999) and Chiappini et al. (2006) (Table 5-4).

The yield of sabinaketone from the ozonolysis of sabinene is (31±15) %. This value is lower than values reported in literature, which range between 35 % to 50 %, but still agrees within the combined uncertainties (Hakola et al., 1994; Yu et al., 1999; Chiappini et al., 2006; Table 5-4). The sabinaketone yield could increase with increasing humidity due to the reaction of the stabilized Criegee intermediates with water (Wang and Wang (2017), Figure 5-2) and a laboratory study on the nopinone yield from the ozonolysis of structurally similar β-pinene (Ma and Marston, 2008). However, the absolute humidity during the ozonolysis experiments in this study of 0.25 % was not much different or higher than the humidity in the experiments reported in literature (Table 5-4), so that it is unlikely that humidity explains the lower value in this work.

Table 5-4. Summary of the product yields from the oxidation of sabinene reported in literature and determined in experiments in this study.

	Acetone	HCHO	Sabinaketone	OH	Reference
Sabinene + OH	/	/	17 %	NA	Arey et al. (1990)
	/	/	(17±3) %	NA	Hakola et al. (1994)
	(19±3) %	/	/	NA	Reissell et al. (1999)
	(9±3) %	(35±4) %	(24±10) %	NA	Larsen et al. (2001)
	(25±5) %	(25±5) %	(22±6) % (no NO_x)	NA	Carrasco et al. (2006)
	(23±5) %	(25±6) %	(19±5) % (with NO_x)	NA	
	(21±15) %	(46±25) %	(18±16) %	NA	This work
Sabinene + O_3	(3±2) %	/	/	/	Reissell et al. (1999)
	/	/	(47±24) %[a]	/	Yu et al. (1999)
	/	/	(50±9) %[b]	/	Hakola et al. (1994)
	Detected	(52±9) %	(35±14) %[c]	/	Chiappini et al. (2006)
	/	/	/	(33±5) %	Aschmann et al. (2002)
	/	/	/	(26±13) %	Atkinson et al. (1992)
	(5±2) %	(48±15) %	(31±15) %[d]	(26±29) %	This work

NA: Not applicable [a]Experiments were performed at around 5 % relative humidity (Griffin et al., 1999) [b]The humidity is not mentioned [c]Experiments were performed with less than 300 ppm of water [d]Ozonolysis experiments were conducted at 0.25 % absolute humidity.

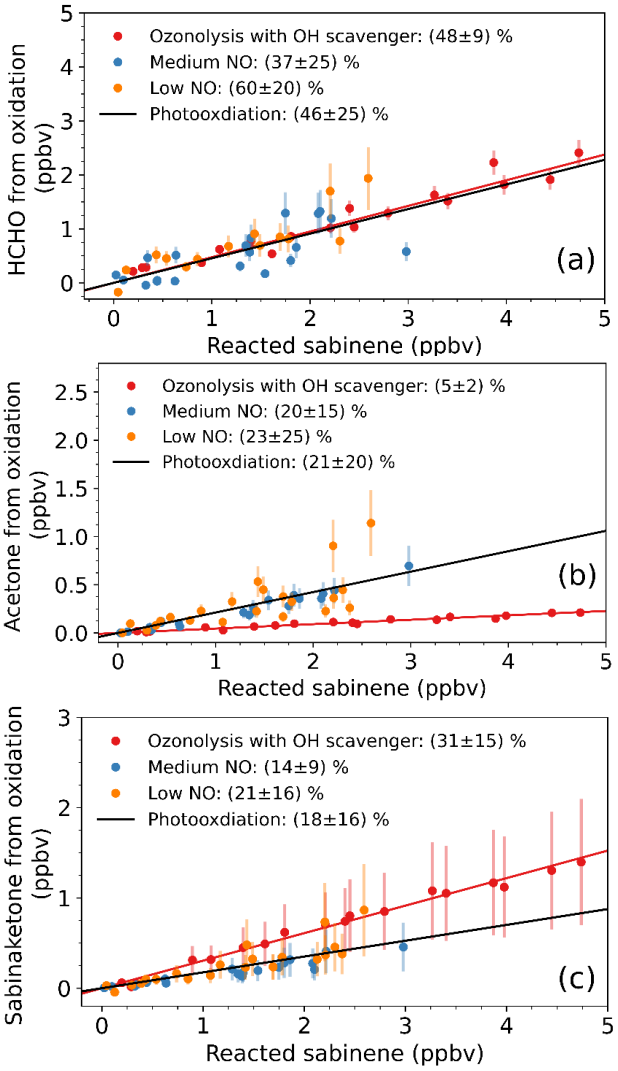

Figure 5-12. Determination of the yields of HCHO (a), acetone (b), and sabinaketone (c) from the reaction of sabinene with OH and O_3. 'Photooxidation' refers to the yields calculated from all data from the experiments with low NO and medium NO mixing ratios. For clarity, only data points from the time period, when 50 % of the injected sabinene was still present (3 ppbv to 4 ppbv) are shown.

5.3.3 Comparison between product yields determined in this study to the values expected from theoretical calculations

The product yields of the photooxidation of sabinene determined in this study can be compared to yields expected from the sabinene oxidation mechanisms by Wang and Wang (2017) and Wang and Wang (2018).

In the OH oxidation mechanism by Wang and Wang (2018), HCHO is only produced from the subsequent chemistry of the RO_2 radical SABINOHAO2 that results from one of the two OH-addition reactions of sabinene (Fig. 5-1). It is reasonable to expect that about 20 % to 35 % of RO_2 derived from the OH-oxidation of sabinene forms organic nitrates when they react with NO similar to peroxy radicals derived from other monoterpenes (e.g., Rollins et al., 2010), Therefore, the HCHO from the OH-oxidation of sabinene is expected to be 31 % to 38 % when considering the branching ratio of reaction pathway (a) stated in Wang and Wang (2018) and the organic nitrate yield. This agrees with the HCHO yield of (46±25) % (Table 5) determined in the photooxidation experiments.

The yield of acetone in the OH oxidation of sabinene expected from the mechanism by Wang and Wang (2018) is determined by the branching ratio of the OH-addition reaction producing the RO_2 radical SABINOHBO2 as well as by the fraction of SABINOHBO2 that undergoes an isomerization reaction or forms organic nitrates in the reaction with NO, from which eventually acetone is produced. For atmospheric conditions like in the experiments in this work, it is expected that more than 90 % of SABINOHBO2 undergoes the unimolecular reaction ($k_{uni} \sim 5\ s^{-1}$, Fig. 5-1) and less than 10 % undergoes bimolecular reactions ($k_{RO2} < 0.4\ s^{-1}$; Figure 5-6, Figure 5-7 and Fig. 5-9). Therefore, the acetone yield is expected to be only around 4 % (reaction path (b) in Fig. 5-1).

The experimentally determined acetone yield of (21±15) % is significantly higher than this value. To bring both values into agreement, the rate coefficient of the unimolecular reaction of SABINOHBO2 would need to be on the same order of magnitude as the loss rates constant of bimolecular RO_2 reactions in this study ($\sim 0.2\ s^{-1}$), so that about half of the RO_2 radical SABINOHBO2 undergoes bimolecular reactions (mainly with NO). The uncertainty of the unimolecular reaction rate coefficient of about 5 s^{-1} calculated in Wang and Wang (2018) has an uncertainty of about one order of magnitude. Therefore, the unimolecular reaction rate constant calculated by Wang and Wang (2018) agrees with the rate constant required to reach a good agreement of acetone yield, despite the large difference between the acetone yield determined in the experiments and the yield expected from the mechanism in Wang and Wang (2018).

It should be noted that acetone might be produced from pathways other than the reaction pathways of RO_2 radical SABINOHBO2 suggested in Wang and Wang (2018). This would be consistent with the observation that the acetone yield found in this study and in Carrasco et al. (2006) does not strongly depend on the NO concentration (Table 5-4), which would be expected, if acetone is produced from reaction pathways that do not without other competitions. For example, acetone might be produced from a very fast isomerization reaction so that bimolecular reactions cannot compete for typical atmospheric concentrations of partners like NO.

The sabinaketone yield of (18±16) % from the OH-oxidation of sabinene determined from the experiment is lower than the yield of 31 % to 38 % expected from the mechanism by Wang and Wang (2018) after

taking account into the branching ratio of reaction pathway (b) in Fig. 1 and the potential production of organic nitrates. The mechanism by Wang and Wang (2018) also suggests the production of sabinaketone comes together with the production of HCHO and thereby have the same yield. However, only the HCHO yield determined in this study agrees with the HCHO yield expected from the mechanism by Wang and Wang (2018). The large difference between the HCHO yield and sabinaketone yield in this study could be due to the large uncertainties of the yields.

Regarding the ozonolysis of sabinene, the HCHO yield determined in the experiments in this study and in the study by Chiappini et al. (2006) are about 35 % lower than the HCHO yield of 83 % expected from the mechanism by Wang and Wang (2017). In their mechanism, HCHO is directly formed as co-product of the two Criegee intermediates CI-1 and CI-2, so that the HCHO yield reflects the sum of the branching ratios for these reaction pathways (reactions (B) and (C), Fig. 5-2). The low HCHO yield in the experiments might therefore hint that the combined branching ratios of reaction pathways (B) and (C) in the mechanism by Wang and Wang (2017) in Fig. 5-2 are too high.

The production of acetone from the ozonolysis of sabinene is not discussed in Wang and Wang (2017). The small yield of (5±2) % determined in this work also suggests that only minor reaction pathways lead to the production of acetone. One feasible mechanism could be the breakage of the 3-membered ring in the Criegee intermediate CI-2 that yields a biradical BI-RAD (Fig. 5-13). A similar mechanism was proposed for the Criegee intermediates from the ozonolysis of β-pinene (Nguyen et al., 2009). The expected yield of the analogous biradical formed from the ozonolysis of β-pinene is 3 %, which explains the low acetone yield between 1 % to 7 % observed for β-pinene (Lee et al., 2006). If a similar reaction pathway applies for Criegee intermediate from sabinene, it can be expected that this is mainly relevant for the Criegee intermediate CI-2 because of the fast loss of the Criegee intermediate CI-1 in the fast H-migration reaction (Wang and Wang, 2017). Therefore, the small acetone yield might be explained by the breakage of the 3-membered ring of the Criegee intermediate CI-2.

The sabinaketone yield of (31±15) % determined from the ozonolysis experiments is lower than the value of 47 % expected from the calculations by Wang and Wang (2017). As discussed above in the comparison with values reported in literature, humidity could impact the sabinaketone yield, but the overall effect is expected to be small. Values reported in literature are in better agreement with the yield of 47% expected from the mechanism by Wang and Wang (2017). Therefore, the low value determined in the work is likely due to the high uncertainty in the sabinaketone measurements.

The OH yield from the ozonolysis reaction of sabinene of (26±29) % determined in the experiments is lower than the yield of 44 % expected from the mechanism in Wang and Wang (2017), but still within agreement due to the uncertainties in the values determined in the experiment and in the theoretical calculations. The OH yield expected from the mechanism is based on the fraction of the Criegee intermediate CI-1 that undergoes unimolecular decomposition forming an OH radical and an β-oxo alkyl radical (Fig. 5-2), which does not consider the potential OH production from the Criegee intermediate CH_2OO. It is expected that about 40 % to 50 % of CH_2OO is stabilized by collisions to form a stabilized Criegee intermediate and subsequently reacts with water at moderate humid conditions (Long et al., 2016; Nguyen et al., 2016; Pfeifle et al., 2018), and about 17 % of CH_2OO results in the production of an OH

radical (Atkinson et al., 2006). Therefore, the overall additional contribution to the OH yield of the ozonolysis of sabinene from the chemistry of CH_2OO is only about 3 %.

Regarding the production of OH radicals from the chemistry of the C_9-Criegee intermediates CI-1 and CI-2, the OH yield can be affected by the uncertainty of the yield of the stabilized Criegee intermediate sCI-1. Laboratory experiments quantifying the yield of the stabilized Criegee intermediate would partly help constraining the OH yield. However, to the best of our knowledge, there are no measurements of stabilized Criegee intermediates from the ozonolysis of sabinene.

The OH yield can also be affected by reactions that were not investigated by Wang and Wang (2017). For example, an OH radical may not be formed from the dissociation of the vinyl hydroperoxide. In the proposed mechanism by Barber et al. (2018) and Kuwata et al. (2018) (Fig. 5-14), the hydroxyl group that is partly dissociated from the hydroperoxide group can recombine with the β-oxo alkyl radical and form a 2-hydroxyketone, instead of a complete dissociation. With this additional mechanism, the expected OH yield from the ozonolysis of sabinene would be reduced. Further investigations of the relative importance of the recombination pathway are needed to quantify the potential impact.

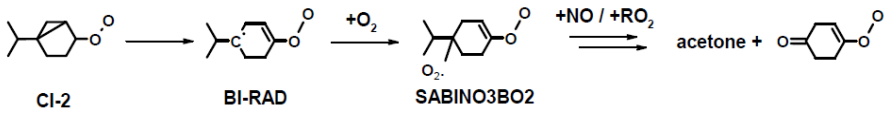

Figure 5-13. Possible reaction pathway of the Criegee intermediate CI-2 that could explain the small production of acetone from the ozonolysis of sabinene.

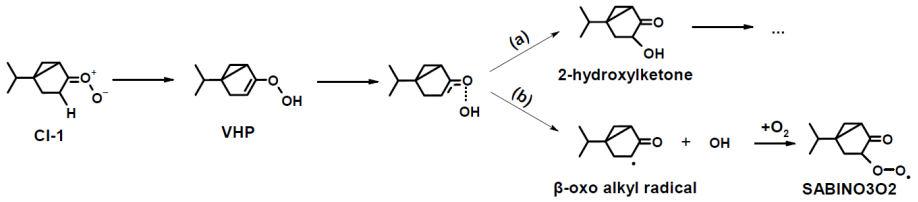

Figure 5-14. Possible pathways of the dissociation of the vinyl hydroperoxide (VHP) from CI-1 that lead to the production of (a) 2-hydroxylketone, and (b) an OH radical and a β-oxo alkyl radical.

5.3.4 Chemical budget of OH radicals during the oxidation of sabinene

The sum of OH radical production rates from different pathways needs to be balanced by the OH destruction rate. In the ozonolysis experiment (Fig. 5-15a), the production and destruction rates of OH were low with values of less than 1.5 ppbv h^{-1}. The OH concentration was close to the limit of detection of the instrument (< 10^6 cm^{-3}), so that the calculation of the loss rate has a high uncertainty. In the first hour of the experiment, about 65 % of the total OH production was from the ozonolysis reaction (0.75 ppbv h^{-1}) and the remaining part was from the reaction of HO_2 with O_3 (0.5 ppbv h^{-1}). The total production rate of OH was on average slightly higher (+0.2 ppbv h^{-1}) than the destruction rate. However, this discrepancy is within the uncertainty of the calculations, so that the chemical budget can be regarded as balanced by the considered OH production and destruction reactions.

In the photooxidation experiment with low NO mixing ratios (Fig. 5-15b), the production rate of OH ranged between 2 and 6 ppbv h^{-1}. A good agreement between the OH production and destruction rates can be seen during the zero-air phase, demonstrating that the analysis includes all important OH production pathways in the clean chamber before sabinene was injected.

After the injection of sabinene, the OH destruction rate increased due to the reaction with sabinene. The OH production rate concurrently increased due to the enhanced regeneration of OH from the reaction of HO_2 with NO and due to the production of OH from the ozonolysis of sabinene. For NO mixing ratios (0.05 ppbv to 0.15 ppbv) in this experiment, 20 % to 60 % of the OH was produced from the reaction of HO_2 with NO, and the remaining part was from the photolysis of HONO and O_3 and the reaction of HO_2 with O_3. The contribution of the ozonolysis of sabinene to the total OH production was maximum 10 % to 30 % right after both sabinene injections, but quickly decreased, while sabinene was being oxidized. Overall, the OH production rate was excellently balanced by the OH destruction rate in the experiments with low NO mixing ratios suggesting that there was no significant unaccounted OH sources for the conditions of these experiments.

In the photooxidation experiment with medium NO concentrations (Fig. 5-15c), the OH production and destruction rates were 4 ppbv to 10 ppbv h^{-1}, which were higher than values in the experiments with low NO. The high production rate is mainly due to a fast regeneration of OH in the reaction of HO_2 with NO contributing 70 % to 80 % to the total OH production rate. The production rate of OH was also well balanced by the OH destruction rate within the uncertainties of calculations.

In summary, the OH production and destruction rates in the oxidation experiments with sabinene were well balanced for all conditions experienced in this work. This suggests that there are no unaccounted OH production reactions in the photooxidation of sabinene, so that well known photolysis reactions and bi-molecular reactions are sufficient to be considered in the chemical budget of OH radicals This is consistent with the mechanism proposed by Wang and Wang (2017 and 2018).

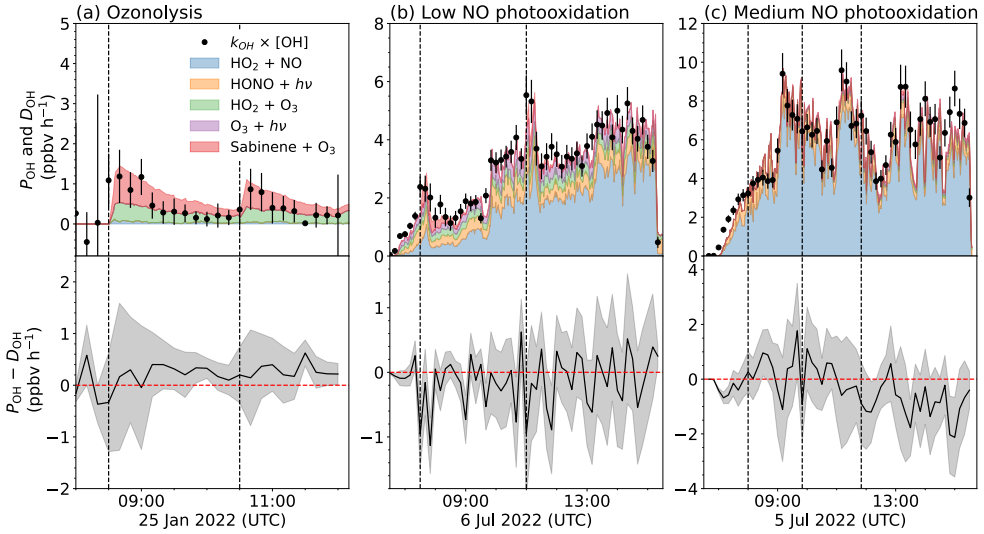

Figure 5-15. Overview of the production rate of OH (P_{OH}, colored areas) and the destruction rate of OH (D_{OH}, black dots) (top panel), as well as their differences (bottom panel) in (a) an ozonolysis experiment, (b) experiments with low NO, and (c) with medium NO mixing ratios. Grey shaded areas are the 1σ uncertainty of the difference between P_{OH} and D_{OH}.

6. Investigation of the oxidation of biogenic organic compounds from real plant emission

6.1 Emission of organic compounds from sweet chestnut (*Castanea sativa*)

6.1.1 Species emitted by sweet chestnut trees

In the first part of the plant chamber experiments, the emissions of sweet chestnut trees at different temperatures were analyzed. At an ambient temperature of around 22 °C to 26 °C in the SAPHIR-PLUS chamber, only a small amount of VOCs that are reactive toward OH radicals were emitted by the sweet chestnut trees as demonstrated by a low maximum OH reactivity (2.5 s^{-1}) reached in the SAPHIR chamber, after emissions were transferred into the SAPHIR chamber (Fig. S6-1). Organic compounds that contribute to the measured OH reactivity include acetaldehyde, methylglyoxal, acetone, hydroxyacetone, and a very low concentrations (< 100 pptv) of isoprene, α-pinene, and β-ocimene. VOCs that are not very reactive toward OH radicals were also observed, which include methanol and acetic acid having mixing ratios of about 0.5 ppbv to 1.0 ppbv in the SAPHIR chamber.

At an elevated temperature between 28 °C to 32 °C in the SAPHIR-PLUS chamber, VOCs were emitted at a higher rate as indicated by the maximum OH reactivity of 10 s^{-1} to 18 s^{-1} reached in the SAPHIR chamber (Fig. S6-1). The increase in OH reactivity was mainly due to the increase in the emission of trans-β-ocimene and cis-β-ocimene that were observed in GC measurements in the SAPHIR and SAPHIR-PLUS chambers. The sum of concentrations of both β-ocimene isomers reached 1 ppbv to 2 ppbv in both chambers (Fig. 6-1 and Fig. S6-2 to S6-4). The offline GC measurement in the SAPHIR-PLUS chamber gave consistent results with β-ocimene concentrations of up to 1.5 ppbv. In addition, a reactive alkene, p-mentha-1,5,8-triene (molecular formula: $C_{10}H_{14}$), with a maximum concentration of about 0.3 ppbv was observed by the offline GC instrument. The GC instrument in the SAPHIR chamber was not calibrated for p-mentha-1,5,8-triene and no strong signal other than β-ocimene was observed in the GC chromatogram. The PTR-TOF-MS instrument in the SAPHIR chamber detected the presence of p-mentha-1,5,8-triene, but the signal was too small to be quantified. The GC and the PTR-TOF-MS measurements suggest that p-mentha-1,5,8-triene had a very low concentration or was even absence in the SAPHIR chamber, which might be related to the loss of this VOC species when it was transferred to the SAPHIR chamber.

Apart from β-ocimene and p-mentha-1,5,8-triene, monoterpene species including sabinene, α-phellandrene, α-pinene, β-pinene and limonene were detected by the offline GC measurement in the SAPHIR-PLUS chamber at experiments with an elevated temperature, but their concentrations were one order of magnitude lower than that of β-ocimene. The emission of β-ocimene showed a dependence on the light intensity as evident by the decrease in concentration in the SAPHIR chamber when the lights in SAPHIR-PLUS were off. During this period, the decrease could be explained from the replenishing flow of synthetic air (Fig. 6-1 and Fig. S6-2 to S6-4). The dependency on light of the emission of monoterpenes by sweet chestnut trees suggests that significant part of the monoterpene emissions would be originated from *de novo* synthesis rather than pool emissions. *de novo* emission of terpenes is commonly found in

deciduous trees including sweet chestnuts, for which a storage structure of synthesized terpenes in leaves is not available (Loreto and Schnitzler, 2010).

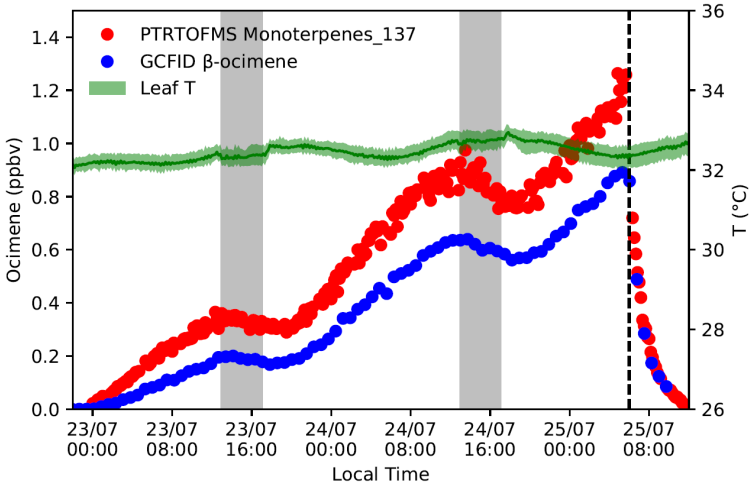

Figure 6-1. The mean leaf temperature measured in the SAPHIR-PLUS chamber and monoterpene concentrations measured by PTR-TOF-MS and β-ocimene concentrations measured by GC-FID in the SAPHIR chamber during the coupling phase between the SAPHIR-PLUS and the SAPHIR chambers. The green colored area indicates the maximum and minimum leaf air temperature among the four measurements at different plants. The grey shaded area indicates when the light in the SAPHIR-PLUS chamber was turned off. The dotted line indicates the decoupling of the two chambers followed by the start of the oxidation of VOCs.

6.1.2 Comparison of VOCs concentrations in the SAPHIR chamber measured by PTR-TOF-MS and GC instruments

Significant amounts of acetaldehyde, acetone, and β-ocimene were detected by both PTR-TOF-MS and GC instruments during the experiments. β-ocimene concentrations measured by the GC instrument were on average 23 % lower than measurements by the PTR-TOF-MS instrument (Fig. 6-2). The difference is within the combined uncertainties of both instruments. Uncertainties of PTR-TOF-MS measurements include the measurement sensitivity for β-ocimene, which is assumed to be the same as that for α-pinene, for which the instrument is regularly calibrated. All monoterpene species including β-ocimene appear on the same ion mass signal. Therefore, the presence of other monoterpene species could also explain the differences in the measurements by the two instruments. GC measurements in the SAPHIR-PLUS chamber suggest that the total concentration of monoterpene species other than β-ocimene was about 10 % of the measured β-ocimene concentrations, which can explain the difference in measured monoterpene and β-ocimene concentrations in the SAPHIR chamber.

Measurements of acetone show a large discrepancy between the two instruments, with the concentrations measured by PTR-TOF-MS being on average 43 % higher than measured by the GC instrument. The difference is larger than the combined uncertainties of 7 % (Table 2-1) found in the limonene oxidation experiments. The exact reason for the large difference in the plant emission experiments remains unclear.

Measurements of acetaldehyde also show a large discrepancy without a clear correlation between the two instruments. Such large differences can be caused by the calibration process of the online GC instrument, in which peak broadening and tailing, and thereby coelution with other species can occur for acetaldehyde. This may be explained by the fact that the temperature program run by the GC instrument is not optimized for the measurements of small VOCs that have a low boiling point. VOCs with low boiling points are prone to interferences from water present in the sample, as they are both vaporized at a similar time during the temperature ramp. The measurement of acetaldehyde by the PTR-TOF-MS instrument may also be subject to interference from the fragmentation of compounds such as oxygenated VOCs (Yuan et al., 2016; Coggon et al., 2023), especially in a complex chemical composition. For example, the ionization of ethanol (m/z: 47) can produce fragments occurring on the same ion mass signal (m/z: 45) that is typically assigned to acetaldehyde (Buhr et al., 2002). Therefore, the correlation of the acetaldehyde concentrations measured by the PTR-TOF-MS and GC-FID instruments might be weak in the plant emission experiments in this work.

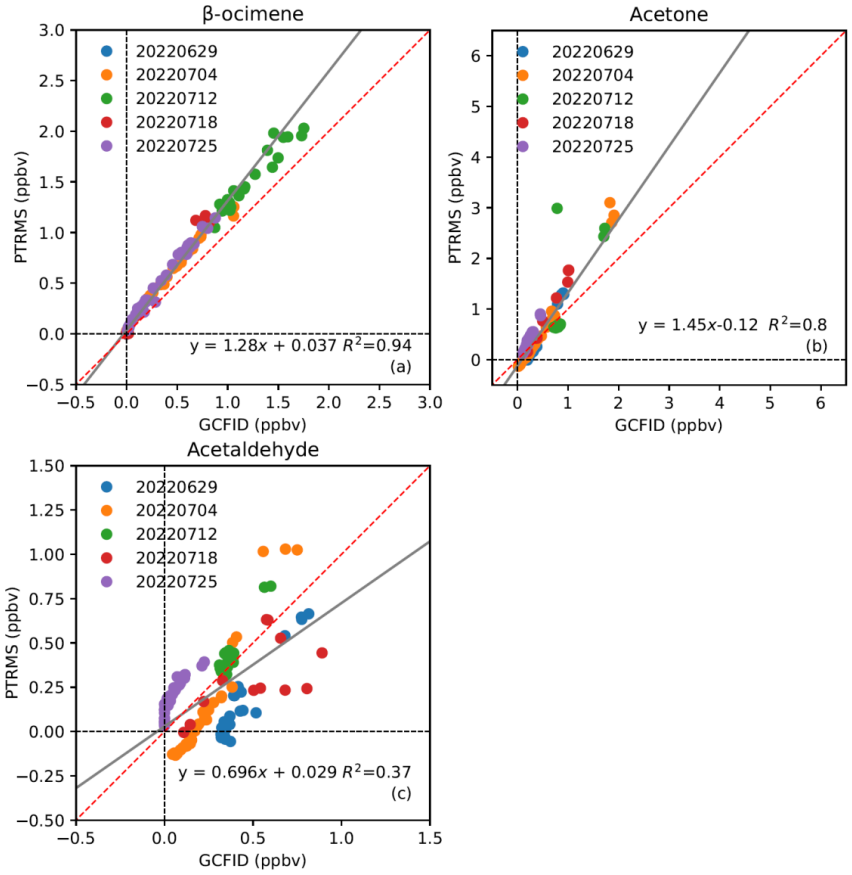

Figure 6-2. Comparison of the measurements of (a) β-ocimene, (b) acetone, (c) acetaldehyde in the SAPHIR chamber detected by PTR-TOF-MS and GC-FID instruments during the plant emission experiments. The grey line represents the regression result and the red dotted line represents the 1:1 line. Colors of the measurements distinguish between experiments on different days.

6.2 Oxidation of the BVOCs emitted by sweet chestnut trees

6.2.1 Comparison of measured total OH reactivity and OH reactivity calculated from measured BVOC concentrations

The OH reactivity measurement constrains the total amount of reactive species present in the SAPHIR chamber and contains information, if VOC measurements include all chemically relevant species. If the measured OH reactivity is higher than the OH reactivity calculated from the concentrations of single VOCs during the coupling of the two chambers, reactive VOCs species are missing in the measurements, whereas VOC concentrations are too high if the measured OH reactivity is lower than the calculated value.

The OH reactivity is calculated using the reaction rate constants of the reaction with OH radicals and the concentrations of the OH reactants:

$$k_{\mathrm{OH}} = \sum_i [x_i] k_{x_i+\mathrm{OH}} \qquad \text{Equation 6-1}$$

where k_{x+OH} is the reaction rate constant of the OH oxidation reaction taken from IUPAC (https://iupac.aeris-data.fr/en/home-english/, last access: 26 August 2023). Concentrations of the VOCs species measured by PTR-TOF-MS are eventually used for the calculation, as more oxidation product species were detected by this instrument and measurements have a higher time resolution than the GC measurements.

The OH reactivity calculated from VOCs concentrations measured by GC would be about 25 % lower than that of measured VOCs concentration measured by PTR-TOF-MS before the oxidation of VOCs (Fig. 6-2), when monoterpene species (β-ocimene) were the main contributor to the OH reactivity. Products species other than acetaldehyde and acetone from the oxidation of β-ocimene were not measured by GC. Therefore, it is expected that some species are missing in the calculation of the OH reactivity after the start of the oxidation of VOCs, if only the GC measurements are used.

The PTR-TOF-MS instrument was not calibrated for some product species from the oxidation of β-ocimene. The measurement sensitivities (s_x) were estimated based on the ratio of the reaction rate constants of the protonation reaction of the VOC (k_{x+H+}) to that of acetone ($k_{\mathrm{acetone+H+}}$) calculated from available literature values (Pagonis et al., 2019), as well as from the measurement sensitivity of acetone (s_{acetone}) which is determined in regular calibrations of the instrument.

$$s_x = s_{\mathrm{acetone}} \cdot \frac{k_{x+\mathrm{H}^+}}{k_{\mathrm{acetone+H}^+}} \qquad \text{Equation 6-2}$$

Figure 6-3 and 6-4 show the time series of measured OH reactivity and the OH reactivity calculated from measured concentrations of single species in the photooxidation experiment on 12 July 2022 and in the ozonolysis experiment on 25 July 2022. For the experiments on 04 July 2022 and 18 July 2022, the time series could be found in the Supplementary material (Fig. S6-5 and S6-6). It should be noted that isomers are measured collectively by the PTR-TOF-MS, but it is assumed that the ion mass signal at a specific m/z is only attributed to only one species. Ion mass signals were preferably assigned to expected oxidation products of β-ocimene, as β-ocimene was the major emitted species.

Before the initiation of the oxidation of VOCs, 95 % of the calculated OH reactivity is due to monoterpenes, most of which was β-ocimene. The difference between the measured and calculated OH reactivity is around 2 s^{-1} to 3 s^{-1} for the photooxidation experiment. A similar difference is also observed for the ozonolysis experiment. The small discrepancy before the oxidation can be explained by the uncertainty in the measurement sensitivity of the PTR-TOF-MS instrument for β-ocimene, which could be as high as 50 % (Sekimoto et al. 2017).

The difference in OH reactivity could also stem from missing contributions from the alkenes species p-mentha-1,5,8-triene, which was only observed by the offline GC measurements in the SAPHIR-PLUS chamber, but no strong mass signal was observed at the expected m/z from p-mentha-1,5,8-triene ($C_{10}H_{15}^+$) in the mass spectrum of the PTR-TOF-MS instrument.

Based on the concentration ratio of p-mentha-1,5,8-triene to β-ocimene measured in the SAPHIR-PLUS chamber by the offline GC instrument, its estimated contribution to the OH reactivity in the SAPHIR chamber could be between 2 s^{-1} to 7 s^{-1}, which is slightly larger than the missing OH reactivity before the oxidation phase of the experiment.

At the beginning of the photooxidation experiment (Fig. 6-3), β-ocimene exclusively reacted with OH radicals. The difference between the OH reactivity and the calculated OH reactivity increased to 5 s^{-1}, which could be related to the production of products which were not quantified by the PTR-TOF-MS instrument. The products could be species that still retain a C=C double bonds after the initial oxidation reaction. The measured OH reactivity dropped to 5 s^{-1} after most of the β-ocimene has been consumed within 60 minutes. The relatively stable OH reactivity at later times of the experiments suggests that both β-ocimene and reactive oxidation products (e.g., oxygenated alkenes), were already consumed after 60 minutes. The contributions of ketones including acetone and hydroxyacetone to the OH reactivity were low, as their concentrations were low and they are not very reactive towards OH radicals ($k < 10^{-11}$ cm^3 s^{-1}). Methyl vinyl ketone (MVK), which has a C=C double bond, is produced from the photooxidation of β-ocimene and quickly reacts with the OH radical leading to a small contribution to the OH reactivity at the beginning of the oxidation phase of the experiment.

During the photooxidation experiments, NO_x was produced from the photolysis of HONO and O_3 was produced from the oxidation of VOCs. They contributed about 1.5 s^{-1} to the OH reactivity. Aldehydes produced from chamber sources (formaldehyde) and from the oxidation of β-ocimene (acetaldehyde, methylglyoxal) contributed about 1 s^{-1} to the OH reactivity. About 1 s^{-1} to 2 s^{-1} (30 % – 50 %) of the measured OH reactivity during the oxidation phase of the experiment could not be assigned to any measured chemical species. The remaining gap might be explained by the uncertainty in the measurement sensitivity of the PTR-TOF-MS instrument for oxidation products especially for MVK and methylglyoxal.

At the beginning of the ozonolysis experiment, β-ocimene reacted with 10 ppbv of O_3 and with OH radicals produced from the ozonolysis of β-ocimene. About half of the β-ocimene reacted with OH radicals and the other half reacted with O_3. Ketones (MVK, acetone, hydroxyacetone) were produced during the oxidation of β-ocimene, but only aldehydes and β-ocimene contributed a non-negligible amount to the OH reactivity.

About 4 s^{-1} of the OH reactivity (80 % of the measured value) is missing from the calculations in the ozonolysis experiment, which could be related to missing measurements of secondary products from the ozonolysis of β-ocimene. A study by (Reissell et al., 2002) showed that the ozonolysis of β-ocimene produced 4-methyl-hexa-3,5-dienal ($C_7H_{11}O$) with a yield of 33 %. This molecule is an aldehyde with two conjugated C=C double bonds and therefore it is expected to be reactive towards OH radicals. The PTR-TOF-MS also detected an ion mass signal at the respective mass $[C_7H_{11}OH]^+$ (m/z: 112), but the signal was not high enough to give quantitative measurements. Presumably concentrations of 4-methyl-hexa-3,5-dienal were low in the experiments as it is rapidly lost in the reactions with OH and O_3.

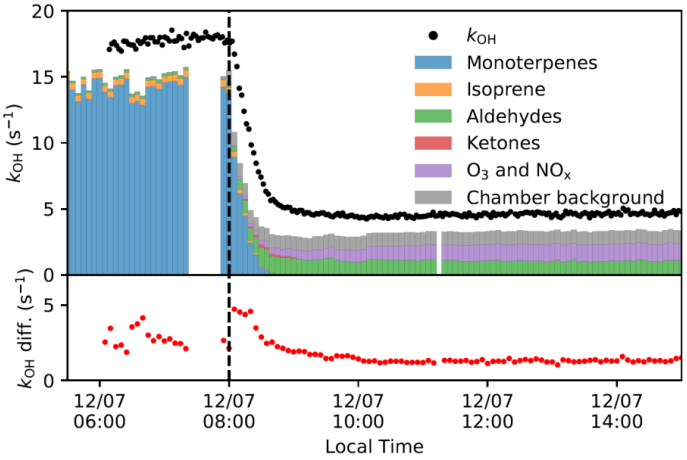

Figure 6-3. Comparison of the measured OH reactivity (black dots) and calculated OH reactivity using PTR-TOF-MS measurements of single reactants (top panel, and their differences (bottom panel) for the photooxidation experiment on 12 July 2022. The vertical dashed line indicates the time when the chamber roof was opened, which initiated the photooxidation of VOCs. The constant contribution from "chamber background" of 1 s^{-1} refers to the background OH reactivity expected to be present in the illuminated chamber. The value of 1 s^{-1} is taken from other VOC photooxidation experiments conducted within the time period of the plant emission experiments.

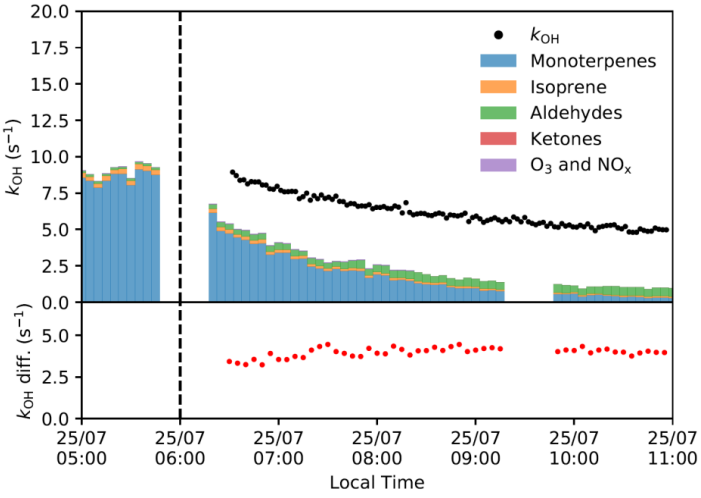

Figure 6-4. Comparison of the measured OH reactivity and the calculated OH reactivity from the PTR-TOF-MS measurements of single reactants (top panel), and their differences (bottom panel) for the ozonolysis experiment on 25 July 2022. The vertical dotted line indicates the time when O_3 was injected.

6.2.2 Chemical budget of OH radicals during the oxidation of VOCs from plant emissions

The chemical budget of OH radicals during the oxidation of plant emissions is calculated for the photooxidation experiments on 04, 12, and 18 July 2023 using the method described in Section 3.4.1. Measurements of HONO concentrations and a zero-air phase for determining the production rate of HONO were not available in the plant emission oxidation experiments. To estimate the HONO concentration in the chamber, it is assuming the scaling factor of the production rate of HONO (Section 2.3) is the same as those determined from other single VOC photooxidation experiments conducted during July 2022, when the plant emission experiments were also performed. A chemical box model with only chamber chemistry was then run using the HONO production rate scaling factor and measured OH concentrations and photolysis rates to calculate the HONO concentration in the chamber. Sensitivity model runs of the HONO production rate scaling factor suggests the uncertainty of the HONO concentration is about 50 %.

Figure 6-5 shows the chemical budgets of OH radicals during the plant emission photooxidation experiments on 12 and 18 July 2023. The production and destruction rates of OH radicals are balanced within the measurement uncertainties at the time when β-ocimene was completely consumed. When β-ocimene was present, the production rate of OH radicals was about (2.0±1.5) ppbv h^{-1} less than the destruction rate. This suggests that there was a small additional OH source present that is not included in the calculations during the oxidation phase of the experiment. However, differences are small and close to the uncertainty of the calculations.

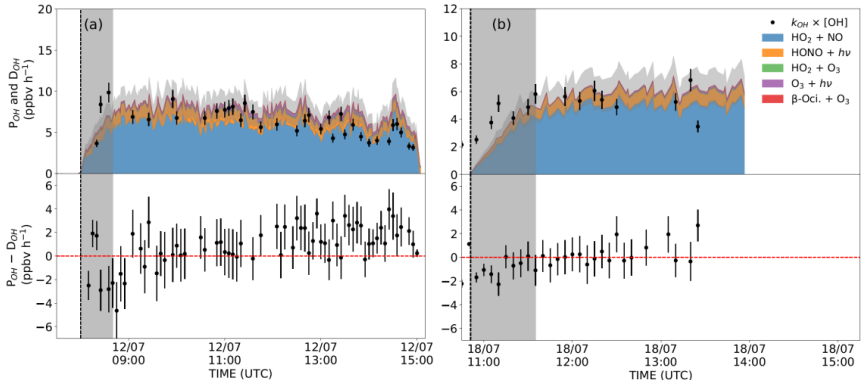

Figure 6-5. The chemical budget of OH radicals during the two plant emissions photooxidation experiment on 12 and 18 July 2023. OH radical destruction rates (D_{OH}) calculated from the OH reactivity and concentration, and the OH radical production rate (P_{OH}, colored areas) are shown in the upper panels. The light grey area represents the uncertainty of the calculation of the production rate P_{OH}; the dark grey area represents the time when the monoterpene (β-ocimene) concentration was higher than 0.01 ppbv, so that this was the dominant OH reactant; the vertical dashed line represents the start of the oxidation of VOCs. In the bottom panels, the difference between P_{OH} and D_{OH} is shown.

6.3 Discussion of the experiments with real plant emissions

6.3.1 Emitted organic compounds of sweet chestnut reported in literature

Emissions from sweet chestnut were investigated by Aydin et al. (2014), who measured emissions from emissions from mature trees with ages between 20 years and 40 years in the field. It was found that monoterpenes were the dominant emission by mass (> 95 %), followed by a small amount of sesquiterpenes and isoprene. Among the monoterpene emissions, 65 % was sabinene and 13 % was trans-β-ocimene.

Emissions of sweet chestnut trees were also measured by Lüpke et al. (2017). The measurements were conducted in a controlled environment in a plant chamber enclosing 2-year-old sweet chestnut trees. Emissions from 20 trees were sampled and three groups of emission spectra were identified: 1) emissions that were dominated by β-ocimene; 2) emissions that were dominated by α-pinene and β-pinene; and 3) emissions without a dominant monoterpene species.

Emission of β-ocimene was measured in all three studies, but it was only a minor emission source in the study by Aydin et al. (2014). One explanation might be the difference in the tree ages and phenology causing the difference in the emissions (e.g, Lim et al., 2011 and Wiß et al., 2017).

Table 6-1. Reported VOCs (C_{10} species) emissions of sweet chestnut trees.

Reference	Main emissions (Relative emission)
This study[a]	- β-ocimene (60 – 90 %) - p−mentha−1,5,8−triene (< 30 %) - p-cyemene, sabinene, α-phellandrene, limonene, α- and β-pinene (< 5 % each)
Lüpke et al. (2017)[b]	- β-ocimene (50 – 75 %) - α-, β-, γ-terpinene (30 % combined), p−cymene (15 %) and α−thujene (15 %) - α- and β-pinene (50 % combined)
Aydin et al. (2014)	- sabinene (65 %) - trans-β-ocimene (13 %)

[a]Offline GC measurement in the SAPHIR-PLUS chamber. Relative emission rates are estimated from the concentrations measured in the SAPHIR-PLUS chamber. [b]Three groups of main emissions were found.

6.3.2 Photooxidation chemistry of β-ocimene

β-ocimene consists of three C=C double bonds which include an isobutenyl moiety and an isoprenyl moiety (Fig. 6-6, Fig. 6-7, and Fig. 6-8). The structure of β-ocimene is very similar to that of myrcene with the only difference being the position of the isoprenyl moiety. The chemical budget of OH radicals during the photooxidation of isoprene (Fuchs et al., 2013; Novelli et al., 2020) and myrcene (Tan et al., 2021) were investigated in the SAPHIR chamber, therefore results of these studies can be compared to the results of the photooxidation of β-ocimene in this work.

In Fuchs et al. (2013) and Novelli et al. (2020), it is shown that there is a missing source for OH radicals during the photooxidation of isoprene when NO concentrations are low (< 0.5 ppbv), if only the OH-recycling reaction from the reaction of HO_2 with NO is considered. Additional OH radicals can be produced without the presence of NO through the photolysis of products from the isomerization reaction (1,6 H-shift) of one of the RO_2 isomers derived from the photooxidation of isoprene (Fig. 6-6). The photooxidation of isoprene starts with the OH addition on the terminal carbon that yields a conjugated alkyl radical. Depending on the position of the O_2 addition reaction, the alkyl radical reacts with O_2 and form either a δ-OH allylperoxy radical or a β-OH peroxy radicals. If the allylperoxy radical has a Z-configuration, it can additionally additionally undergo a fast 1,6 H-shift reaction (Peeters et al., 2014).

In the photooxidation of myrcene, about 48 % of the OH-addition reaction occurs on the non-conjugated C=C double bond and 52 % of reaction occurs on the conjugated C=C double bond (Fig. 6-7, Peeters et al., 2007). Similar to isoprene, some of the alkyl radicals produced from the OH-addition on the conjugated C=C double bond yields a Z-δ-hydroxylallylperoxy radical (Z-δ-OH-RO_2) after the reaction with O_2. The Z-δ-OH-RO_2 can then undergo 1,6 H-shift like the analogous RO_2 of isoprene. However, the analysis of the chemical budget for OH radicals in Tan et al., 2021 suggests that a good agreement between OH production and destruction rates was already achieved without an additional OH source from isomerization reactions for NO mixing ratios as low as 0.06 ppbv. One possibility is that the non-conjugated C=C double bond in the Z-δ-OH-RO_2 radicals allows for an alternative, competitive isomerization reaction pathway. Using the SAR in Vereecken et al. (2021), the Z-δ-OH-RO_2 radical could undergo a 7-cyclization reaction with a rate constant of about 4 s^{-1}, which is one order of magnitude faster than the abstraction of the α-H atom of the hydroxyl group (1,6 H-shift) similar to that of isoprene. The presence of the isolated C=C double bond also allows the Z-δ-OH-RO_2 radical to undergo a 1,6 H-shift reaction of the allylic H atom, which has an expected rate constant of 0.7 s^{-1} (Vereecken and Nozière, 2020). It is unclear whether an OH radical is eventually produced from the additional isomerization reaction pathways, but those additional pathways likely suppress the production of OH radicals through the 1,6 α-OH H-shift pathway that is known for the RO_2 radicals derived from isoprene.

It is expected that the chemistry of β-ocimene is similar to that of myrcene, with 41 % of OH-addition reaction occurring at the isolated C=C double bond and 44 % occurring at the conjugated C=C double bond on the terminal C atom that yields a conjugated alkyl radical. For alkyl radicals produced from the OH-addition on the terminal C atom of the conjugated C=C double bond, they can react with O_2 to form a δ-hydroxy allyl peroxy radical that is similar to the Z-δ-OH-RO_2 radical from myrcene. These peroxy radicals produced from the photooxidation of β-ocimene can also undergo fast isomerization due to the presence of the isolated C=C double bond. The cyclization rate constant for the analogous Z-δ-OH-RO_2 peroxy

radical from β-ocimene is estimated to be more than 100 s^{-1} (Vereecken et al., 2021), which is about 2 orders of magnitude faster than the cyclization reaction for peroxy radicals produced from myrcene photooxidation. This is because the position of the isolated C=C double bond in β-ocimene allows for the formation of 5- or 6-member ring, which is more sterically favorable compared to the formation of 7- or 8- member for the peroxy radicals from myrcene photooxidation. Products may not efficiently produce OH, explaining why no significant missing OH source is observed in the analysis of the chemical budget of OH radicals in the photooxidation of myrcene and β-ocimene.

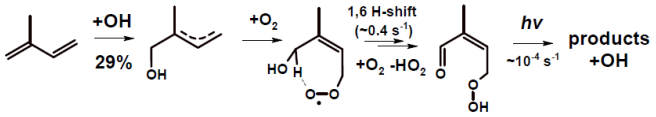

Figure 6-6. Simplified mechanism of the 1,6 H-shift isomerization reaction of one of the RO_2 radical derived from the photooxidation of isoprene that produces OH radicals from the subsequent chemistry of products. Only one of the pathways forming the δ-hydroxylallylperoxy radical is shown.

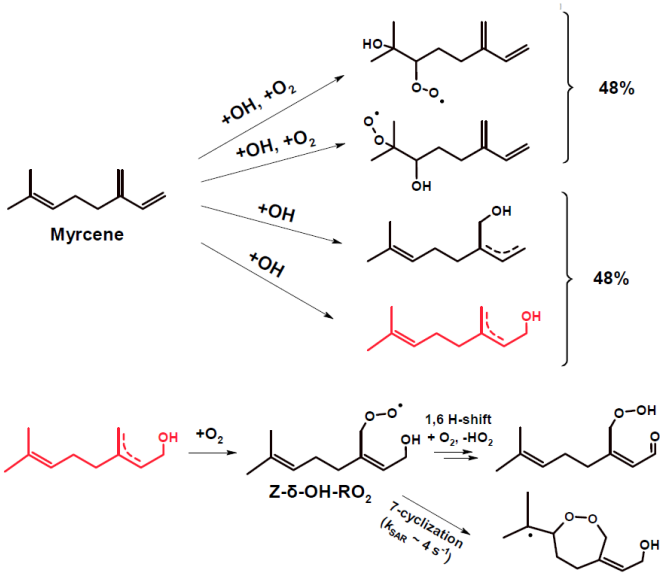

Figure 6-7. Production of RO_2 radicals in the reaction of myrcene with OH and subsequent isomerization reactions of one of the RO_2 radicals. For simplicity, some geometric isomers are not shown. The cyclization rate for the peroxy radical is estimated from the SAR in Vereecken et al. (2021). It should be noted that the impact of the β-γ C=C double bond (relative to the peroxy group) on the rate constant of the cyclization reaction is not taken into account in the SAR.

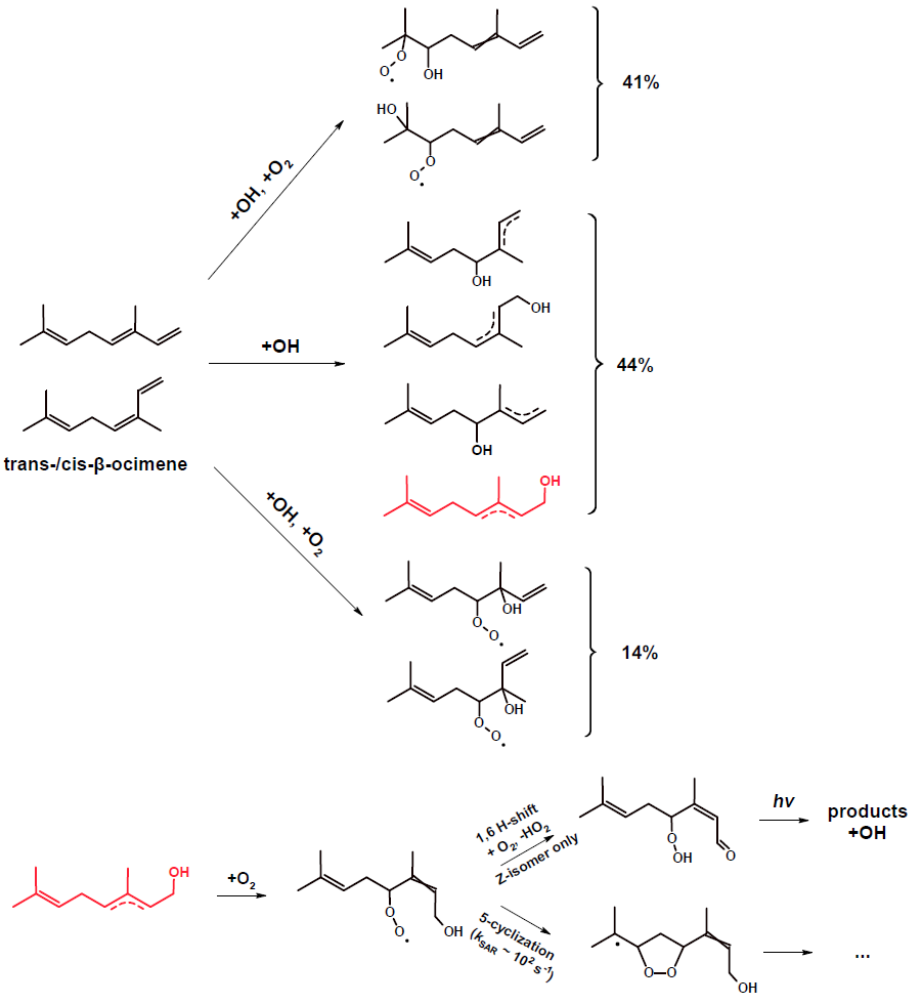

Figure 6-8. Production of RO_2 radicals in the OH reaction of β-ocimene and the subsquent isomerization reactions of one of the RO_2 radicals. For simplicity, some geometric isomers are not shown. The cyclization rate for the peroxy radical is estimated from the SAR in Vereecken et al. (2021).

7. Summary and Conclusions

In this work, the oxidation of two monoterpenes at atmospherically relevant NO levels was investigated in experiments conducted in the atmospheric simulation chamber SAPHIR chamber. Product yields and the chemical budget of OH radicals were the focus of this study, as they give information about the chemistry of the peroxy radicals produced from the oxidation impacting the subsequent production of secondary pollutants. In addition, temperature-dependence reaction coefficients were determined for the photooxidation of monoterpenes, for which only rate coefficients at room temperature were available. Furthermore, the oxidation of a VOC mixture emitted by plants was studied using the SAPHIR-PLUS chamber together with the SAPHIR chamber. The composition of the VOC mixture emitted at different temperatures was determined. The OH reactivity measurements in the SAPHIR chamber were compared with the OH reactivity calculated from VOC measurements before and after the oxidation of the VOCs emitted from plants. Similar to the experiments of the oxidation of a single monoterpene, the chemical budget of OH radicals during the oxidation of plant emissions was calculated.

7.1 Oxidation of limonene

The oxidation of limonene by OH radicals and O_3 was investigated over a range of at NO mixing ratios between 0 and 10 ppbv. The yield of HCHO of the oxidation of limonene was calculated, and it was found that the yield varied from 12 % to 32 % for experiments at different NO concentrations. The HCHO yield determined in this work is similar to that found in other studies only for the experiments conducted at high NO concentrations of 10 ppbv. The HCHO yield determined in experiments at low NO concentrations of less than 1 ppbv is about 15 %. This is less than the yield expected from the fraction of the peroxy radical (LIMCO2) which reacts with NO and thereby produces HCHO. To reconcile the difference in the HCHO yield, the relative loss of peroxy radical LIMCO2 from pathways other than the reaction with NO has to be increased when the NO concentrations are low. This could include an underestimated reaction rate constants of peroxy radicals LIMCO2 in reactions with HO_2 and other RO_2 radicals, or an unaccounted unimolecular reaction pathway for the peroxy radical LIMCO2 that does not lead to the production of HCHO.

The chemical budget of OH radicals was calculated by comparing the measured destruction rate of OH radicals and the measured production rate of OH radicals from well-known chemical reactions. This showed excellent agreement in all experiments at different NO concentrations within the measurement uncertainties, suggesting that well-understood chemical reactions such as photolysis of O_3, HONO, and the reaction in HO_2 and NO can explain the entire production of OH radicals in the oxidation of limonene.

The chemical budgets of first-generation RO_2 radicals from the oxidation of limonene (C_{10}-RO_2) were also investigated. Given that the production rate of C_{10}-RO_2 is well-constrained, the loss rate of C_{10}-RO_2 calculated based on the bimolecular reaction rate constants used in SAR (Jenkin et al., 2019) is too low to balance the destruction rate. To bring the loss rate of C_{10}-RO_2 to the production rate of C_{10}-RO_2, an

additional loss rate of $(1 – 5)\times10^{-2}$ s-1 for RO_2 is needed, which is on the same of magnitude as the loss rate of RO_2 to bimolecular reactions.

Measurements were compared to the model simulation using the semi-explicit chemical model Master Chemical Mechanism version 3.3.1 (MCM). With the standard MCM model, in which reaction rate constants for the reaction of RO_2 are mostly derived from SAR (e.g., Jenkin et al., 2019), the OH reactivity and RO_2 concentrations are overestimated, and HO_2 and OH concentrations are underestimated. Results show that the lower the NO concentration, the larger the differences are between modelled and measured HO_2 and RO_2 radical concentrations. The modelled OH reactivity was consistently higher than measurements at the end of the oxidation of limonene. The model-measurement difference was about 25 % of the equivalent OH reactivity from the initially injected limonene. This value was similar in all experiments with different NO levels. The modelled OH concentration agreed with the measurements, if the HO_2 concentration and the OH reactivity matched the measurements, which is consistent with the observed balance in the chemical budget of OH radicals.

A sensitivity test run was conducted to test how the modelled and measured OH reactivity and radical concentrations can be brought into agreement. This requires a direct conversion from C_{10}-RO_2 to HO_2 with a rate constant of about 3×10^{-2} s^{-1}, consistent with the results in the chemical budget analysis of C_{10}-RO_2. The implementation of the rapid loss of C_{10}-RO_2 also improves the model-measurement agreement of concentrations of NO and NO_2, as the lower RO_2 concentration reduces the consumption of NO.

Agreement between modelled and measured OH reactivity can be achieved, if the reactivity of organic products from the subsequent chemistry of C_{10}-RO_2 radicals are assumed to be very low. This is in contrast to the prediction of MCM mechanism, which assumes a fast OH oxidation reaction of product species due to the second C=C double bond in limonene.

The underlying mechanism of the additional loss for C_{10}-RO_2 could include unimolecular reactions of RO_2 derived from the oxidation of limonene by OH radicals (Møller et al., 2020) and O_3 (Chen et al., 2021), as well as a fast reaction rate constant of RO_2 self-reaction determined in experiments for highly oxygenated RO_2 radicals from unimolecular reactions by Berndt et al. (2018). C_{10}-RO_2 produced from the oxidation of limonene are expected to be quickly oxidized by isomerization reactions followed by the reaction with O_2 as suggested by Møller et al. (2020) and Chen et al. (2021). The isomerization reaction for C_{10}-RO_2 is very competitive even at very high NO mixing ratios of more than 10 ppbv. The highly oxidized C_{10}-RO_2 can then rapidly react with other highly oxidized RO_2 radicals, which is shown in Berndt et al. (2018) for α-pinene. However, this proposed pathway can only explain the enhanced RO_2 loss but not the enhanced HO_2 production observed in the experiments in this work. The underlying chemistry of the additional HO_2 source is still not clear. HO_2 could be produced from the self-reaction of RO_2 but the branching ratio of RO_2 self-reaction are not well-studied for large (≥ C_{10}) oxygenated RO_2.

7.2 Oxidation of sabinene

The oxidation of sabinene by OH radicals and O_3 was studied in chamber experiments at NO mixing ratios ranging from 0 to 1 ppbv. In addition, the temperature-dependence of the OH oxidation rate coefficient between 284 K and 340 K was determined by OH reactivity measurements in the laboratory.

The determined temperature-dependence of the rate coefficient is consistent with the only literature value at room temperature determined by Atkinson et al. (1990), as well as with the coefficient of temperature dependence of other structurally similar alkenes. This method of determining the temperature-dependence of rate coefficients with OH reactivity measurements could be applied to other VOCs, for which a temperature-dependence rate coefficient is not available.

Product yields and the chemical budget of OH radicals were calculated from the chamber experiment, and they were compared to results that would expect from the sabinene oxidation mechanisms proposed by Wang and Wang (2017 and 2018). The calculation of the chemical budget of OH radicals revealed that the production rate of OH radicals agreed with the destruction rate of OH radicals at different NO levels without the need of an additional OH source from for example isomerization reactions of RO_2 radicals similar to the results found for the oxidation of limonene. This finding is consistent with the sabinene photooxidation mechanism proposed by Wang and Wang (2018), in which isomerization reactions of RO_2 radicals do not produce OH radicals.

Product yields including HCHO, acetone, and sabinaketone agree with yields determined in previous experimental studies. When comparing the experimental yields to the yields expected from the mechanism proposed by Wang and Wang (2018) however, only the yields of HCHO and sabinaketone agree. The acetone yield, which depends on the competition between bimolecular reactions and unimolecular reactions of RO_2 radicals in Wang and Wang (2018), does not show a dependence on the NO concentrations in the experiments in this work. The calculation of the loss rate constant of RO_2 to bimolecular reactions suggests that the unimolecular reaction rate for RO_2 derived from theoretical calculation has to be one order of magnitude lower, so that the acetone yield expected from the mechanism agrees with the experimental results. An alternative explanation for the discrepancy between the expected and experimental yields could be that acetone is not produced from the two competing reaction pathways of the RO_2 radical as suggested by the mechanism. For instance, acetone could be instead produced from a fast unimolecular reaction, so that the bimolecular reaction with NO is not competitive. This could explain why the acetone yield does not depend on the NO concentration in this as well as in previous laboratory studies.

Product yields of HCHO, sabinaketone, and OH radicals from the ozonolysis of sabinene also agree with yields determined in previous laboratory studies and with the yields expected from the mechanism in Wang and Wang (2017). However, there is a tendency that values are lower and have a large uncertainty. Several questions remain open in this study, including a potential water-vapor-dependence of the product yield of sabinaketone, and the yield of the stabilized Criegee intermediates that could affect the OH yield.

7.3 Plant emissions and the investigation of their oxidation

The oxidation of VOCs emitted directly from sweet chestnut trees was investigated by coupling the SAPHIR-PLUS chamber and the SAPHIR chamber. The SAPHIR-PLUS chamber houses the canopy of trees in a controlled environment. Emitted VOCs were transferred into the dark SAPHIR chamber before the start of the experiment. Emissions from sweet chestnut trees were measured by offline GC-FID/MS measurements in the SAPHIR-PLUS chamber, as well as by online GC-FID/MS, PTR-TOF-MS, and OH reactivity in the SAPHIR chamber. Five experiments were conducted to characterize the emission of VOCs from sweet chestnut trees. The temperature of the SAPHIR-PLUS chamber was varied between 22 °C and 31 °C.

At an ambient temperature of 22 °C, measured OH reactivity reached in the SAPHIR chamber was low with a value of 2 s^{-1}, as a large fraction of the emitted VOCs such as methanol and acetic acid have a slow rate of photooxidation and the overall emission rate of the trees was rather low. The OH reactivity increased to 11 s^{-1} – 18 s^{-1} with increasing temperature in the SAPHIR-PLUS chamber, which was mainly due to an increase of the emission of monoterpenes. About 1 ppbv to 2 ppbv of monoterpenes were observed in the SAPHIR chamber at an elevated temperature of about 28 °C to 31 °C. The GC measurements in the SAPHIR chamber revealed that β-ocimene was the sole dominant species in the OH reactivity; the offline GC measurements in the SAPHIR-PLUS chamber in addition showed small amounts (< 10 % total compared to the concentration of β-ocimene) of other monoterpene species, as well as a notable amount (~30 % compared to the concentration of β-ocimene) of the reactive alkene p-mentha-1,5,8-triene. The budget of the OH reactivity was calculated for emissions at elevated temperature and showed that more than 85 % of the measured OH reactivity can be explained by β-ocimene. The missing OH reactivity of about 2.0 s^{-1} to 2.5 s^{-1} could be attributed to the uncertainty in the PTR-TOF-MS measurement of monoterpenes, as well as to the potential presence of p-mentha-1,5,8-triene that was not quantified by the PTR-TOF-MS instrument.

The emitted VOCs from sweet chestnut trees at elevated temperatures were oxidized in the SAPHIR chamber by OH radicals or by ozone. The budget of OH reactivity was calculated. In the photooxidation experiment, about 50 % to 70 % of the OH reactivity was explained by measured VOCs during the oxidation of β-ocimene. The contribution of OH reactivity was mainly from β-ocimene, followed by acetaldehyde and methylglyoxal that are expected to be produced from the oxidation of β-ocimene. The unexplained OH reactivity could be related to the measurement uncertainty of aldehydes in the PTR-TOF-MS instrument, and the other unmeasred secondary products.

In the ozonolysis experiment performed in the dark chamber, only about 20 % to 50 % of the OH reactivity was explained by measured VOCs. The OH reactivity was also mainly from β-ocimene and the small product species acetaldehyde (< C_4). The unexplained OH reactivity could be related to the missing secondary products 4-methyl-hexa-3,5-dienal ($C_7H_{11}O$) that has been reported as an important product of the ozonolysis of β-ocimene. However, no strong ion mas signal of that compound at the respective mass could be measured by the PTR-TOF-MS instrument.

The chemical budget of OH radicals was calculated for the plant emission photooxidation experiments like in the experiments with limonene and sabinene. A missing OH source of about (2.0±1.5) ppbv h^{-1}, 30 % of the total OH destruction rate, was found when β-ocimene was present in the chamber. This indicates that there might be additional OH production from the isomerization of peroxy radicals derived from the photooxidation of β-ocimene. However, this result is based on only few measurements due to the short chemical lifetime of β-ocimene of 30 minutes which was much shorter than for sabinene and limonene in the experiments with those species. Additional experiments at different NO levels are needed for a firm conclusion on whether additional OH radicals are produced from the isomerization of peroxy radicals derived from β-ocimene.

7.4 Outlook

In this work, the chemical budgets of OH radicals were calculated for the monoterpenes. The OH reactivity and OH concentration measurements constrain the OH destruction rate with a low uncertainty, which allows for a direct comparison of all the OH production reactions and an evaluation of whether there is a missing OH source during the oxidation of monoterpene.

The evaluation of the chemical budgets of HO_2 and RO_2 radicals are more challenging than that of OH radicals due to the larger number of reactions for which reactant concentrations need to be quantified. The chemistry of HO_2 radical was only evaluated in the limonene oxidation experiments using the simulation results from the MCM model, but not for sabinene and β-ocimene that are not included in the MCM. To evaluate the HO_2 chemistry from the oxidation of monoterpenes in the future, chemical models that include more monoterpene species such as generated by GECKO-A (Valorso et al., 2011) could be used.

The analysis of the chemical budget for first-generation RO_2 radicals greatly improves the understanding of the oxidation chemistry of monoterpenes as shown in the experiments with limonene in this work. The calculation of the well-constrained production rate of RO_2 is based on OH, O_3, and limonene concentration measurements. Loss rate of RO_2 radicals in bimolecular reactions can be calculated using reaction rate constants derived from SARs (Jenkins et al. 2019). However, the derived loss rate constants for monoterpene-derived radicals have large uncertainties as SARs are most often derived from the knowledge of rate constants for small radicals. To further improve our understanding on the chemical budget for RO_2 radicals especially for large RO_2 radicals, precise measurements of highly oxygenated closed-shell products are needed such as Luo et al. 2023 for the photooxidation of limonene. The knowledge of the chemistry of highly oxygenated RO_2 radicals would be vital for understanding the chemical budgets of radicals, especially for environments with low NO concentrations.

In this work, radical chemistry during the oxidation of plant emissions were for the first time studied using the controlled environment of the SAPHIR-PLUS chamber. The VOC composition obtained from the sweet chestnut emissions was relatively simple, comprising one dominant reactive monoterpene species (β-ocimene) together with several VOC species which are much less reactive. In the future, it would be worthwhile to investigate the radical chemistry during the oxidation of plant emissions with a more

complex VOC composition. Yu (2018) conducted plant emission oxidation experiments with a complex mixture that consist of isoprene, 5 monoterpene species, and 2 sesquiterpenes species by using other plant species. However, radical chemistry was not investigated in that study.

Apart from looking into the radical chemistry during the oxidation of a complex VOC mixture, the SAPHIR-PLUS chamber can be used to investigate the impacts of environmental stresses on the radical chemistry. Environmental stresses such as heat or drought stress, water stress can be applied by adjusting the temperature and irrigation, respectively. These stresses can alter the VOC composition and thereby affect the radical chemistry during its oxidation (Loreto and Schnitzler, 2010). Under climate change with an overall warmer climate, it can be expected that heat and drought stress will be more prevalent. The SAPHIR-PLUS and the SAPHIR chamber are useful tools for studying the radical chemistry of VOCs in the future.

References

Adachi, H. and Basco, N.: Kinetic spectroscopy study of the reaction of $C_2H_5O_2$ with NO, Chem. Phys. Lett., 64, 431–434, https://doi.org/10.1016/0009-2614(79)80215-8, 1979.

Alicke, B.: Impact of nitrous acid photolysis on the total hydroxyl radical budget during the Limitation of Oxidant Production/Pianura Padana Produzione di Ozono study in Milan, J. Geophys. Res., 107, 8196, https://doi.org/10.1029/2000JD000075, 2002.

Almatarneh, M. H., Elayan, I. A., Altarawneh, M., and Hollett, J. W.: A computational study of the ozonolysis of sabinene, Theor. Chem. Acc., 138, 30, https://doi.org/10.1007/s00214-019-2420-7, 2019.

Arey, J., Atkinson, R., and Aschmann, S. M.: Product study of the gas-phase reactions of monoterpenes with the OH radical in the presence of NO x, J. Geophys. Res. Atmospheres, 95, 18539–18546, https://doi.org/10.1029/JD095iD11p18539, 1990.

Arey, J., Aschmann, S. M., Kwok, E. S. C., and Atkinson, R.: Alkyl Nitrate, Hydroxyalkyl Nitrate, and Hydroxycarbonyl Formation from the NO_x–Air Photooxidations of C_5–C_8 *n*-Alkanes, J. Phys. Chem. A, 105, 1020–1027, https://doi.org/10.1021/jp003292z, 2001.

Aschmann, S. M., Arey, J., and Atkinson, R.: OH radical formation from the gas-phase reactions of O_3 with a series of terpenes, Atmos. Environ., 36, 4347–4355, https://doi.org/10.1016/S1352-2310(02)00355-2, 2002.

Atkinson, R., Aschmann, S. M., and Pitts, J. N.: Rate constants for the gas-phase reactions of the nitrate radical with a series of organic compounds at 296 .+-. 2 K, J. Phys. Chem., 92, 3454–3457, https://doi.org/10.1021/j100323a028, 1988.

Atkinson, R., Hasegawa, D., and Aschmann, S. M.: Rate constants for the gas-phase reactions of O_3 with a series of monoterpenes and related compounds at 296 ± 2 K: GAS-PHASE REACTIONS OF O_3, Int. J. Chem. Kinet., 22, 871–887, https://doi.org/10.1002/kin.550220807, 1990a.

Atkinson, R., Aschmann, S. M., and Arey, J.: Rate constants for the gas-phase reactions of OH and NO_3 radicals and O_3 with sabinene and camphene at 296±2 K, Atmospheric Environ. Part Gen. Top., 24, 2647–2654, https://doi.org/10.1016/0960-1686(90)90144-C, 1990b.

Atkinson, R., Aschmann, S. M., Arey, J., and Shorees, B.: Formation of OH radicals in the gas phase reactions of O_3 with a series of terpenes, J. Geophys. Res., 97, 6065, https://doi.org/10.1029/92JD00062, 1992.

Atkinson, R., Baulch, D. L., Cox, R. A., Crowley, J. N., Hampson, R. F., Hynes, R. G., Jenkin, M. E., Rossi, M. J., and Troe, J.: Evaluated kinetic and photochemical data for atmospheric chemistry: Volume I - gas phase reactions of O_x, HO_x, NO_x and SO_x species, Atmospheric Chem. Phys., 4, 1461–1738, https://doi.org/10.5194/acp-4-1461-2004, 2004.

Atkinson, R., Baulch, D. L., Cox, R. A., Crowley, J. N., Hampson, R. F., Hynes, R. G., Jenkin, M. E., Rossi, M. J., Troe, J., and IUPAC Subcommittee: Evaluated kinetic and photochemical data for atmospheric

chemistry: Volume II – gas phase reactions of organic species, Atmospheric Chem. Phys., 6, 3625–4055, https://doi.org/10.5194/acp-6-3625-2006, 2006.

Aydin, Y. M., Yaman, B., Koca, H., Dasdemir, O., Kara, M., Altiok, H., Dumanoglu, Y., Bayram, A., Tolunay, D., Odabasi, M., and Elbir, T.: Biogenic volatile organic compound (BVOC) emissions from forested areas in Turkey: Determination of specific emission rates for thirty-one tree species, Sci. Total Environ., 490, 239–253, https://doi.org/10.1016/j.scitotenv.2014.04.132, 2014.

Ayers, G. P., Penkett, S. A., Gillett, R. W., Bandy, B., Galbally, I. E., Meyer, C. P., Elsworth, C. M., Bentley, S. T., and Forgan, B. W.: Evidence for photochemical control of ozone concentrations in unpolluted marine air, Nature, 360, 446–449, https://doi.org/10.1038/360446a0, 1992.

Badali, K. M., Zhou, S., Aljawhary, D., Antiñolo, M., Chen, W. J., Lok, A., Mungall, E., Wong, J. P. S., Zhao, R., and Abbatt, J. P. D.: Formation of hydroxyl radicals from photolysis of secondary organic aerosol material, Atmospheric Chem. Phys., 15, 7831–7840, https://doi.org/10.5194/acp-15-7831-2015, 2015.

Bai, J., Guenther, A., Turnipseed, A., Duhl, T., and Greenberg, J.: Seasonal and interannual variations in whole-ecosystem BVOC emissions from a subtropical plantation in China, Atmos. Environ., 161, 176–190, https://doi.org/10.1016/j.atmosenv.2017.05.002, 2017.

Barber, V. P., Pandit, S., Green, A. M., Trongsiriwat, N., Walsh, P. J., Klippenstein, S. J., and Lester, M. I.: Four-Carbon Criegee Intermediate from Isoprene Ozonolysis: Methyl Vinyl Ketone Oxide Synthesis, Infrared Spectrum, and OH Production, J. Am. Chem. Soc., 140, 10866–10880, https://doi.org/10.1021/jacs.8b06010, 2018.

Bernard, F., Fedioun, I., Peyroux, F., Quilgars, A., Daële, V., and Mellouki, A.: Thresholds of secondary organic aerosol formation by ozonolysis of monoterpenes measured in a laminar flow aerosol reactor, J. Aerosol Sci., 43, 14–30, https://doi.org/10.1016/j.jaerosci.2011.08.005, 2012.

Berndt, T., Mentler, B., Scholz, W., Fischer, L., Herrmann, H., Kulmala, M., and Hansel, A.: Accretion Product Formation from Ozonolysis and OH Radical Reaction of α-Pinene: Mechanistic Insight and the Influence of Isoprene and Ethylene, Environ. Sci. Technol., 52, 11069–11077, https://doi.org/10.1021/acs.est.8b02210, 2018.

Bianchi, F., Kurtén, T., Riva, M., Mohr, C., Rissanen, M. P., Roldin, P., Berndt, T., Crounse, J. D., Wennberg, P. O., Mentel, T. F., Wildt, J., Junninen, H., Jokinen, T., Kulmala, M., Worsnop, D. R., Thornton, J. A., Donahue, N., Kjaergaard, H. G., and Ehn, M.: Highly Oxygenated Organic Molecules (HOM) from Gas-Phase Autoxidation Involving Peroxy Radicals: A Key Contributor to Atmospheric Aerosol, Chem. Rev., 119, 3472–3509, https://doi.org/10.1021/acs.chemrev.8b00395, 2019.

Bohn, B., Rohrer, F., Brauers, T., and Wahner, A.: Actinometric measurements of NO_2 photolysis frequencies in the atmosphere simulation chamber SAPHIR, Atmospheric Chem. Phys., 5, 493–503, https://doi.org/10.5194/acp-5-493-2005, 2005.

Boyd, A. A., Villenave, E., and Lesclaux, R.: Self- and cross-reactions of β-hydroxyperoxy radicals of relevance to tropospheric monoterpene oxidation: structure–activity relationships for rate

coefficients, Atmos. Environ., 37, 2751–2760, https://doi.org/10.1016/S1352-2310(03)00253-X, 2003.

Buhr, K., Van Ruth, S., and Delahunty, C.: Analysis of volatile flavour compounds by Proton Transfer Reaction-Mass Spectrometry: fragmentation patterns and discrimination between isobaric and isomeric compounds, Int. J. Mass Spectrom., 221, 1–7, https://doi.org/10.1016/S1387-3806(02)00896-5, 2002.

Butkovskaya, N., Kukui, A., and Le Bras, G.: Pressure and Temperature Dependence of Methyl Nitrate Formation in the CH_3O_2 + NO Reaction, J. Phys. Chem. A, 116, 5972–5980, https://doi.org/10.1021/jp210710d, 2012.

Calvert, J. G., Kerr, J. A., Demerjian, K. L., and McQuigg, R. D.: Photolysis of Formaldehyde as a Hydrogen Atom Source in the Lower Atmosphere, Science, 175, 751–752, https://doi.org/10.1126/science.175.4023.751, 1972.

Carrasco, N., Rayez, M. T., Rayez, J. C., and Doussin, J. F.: Experimental and theoretical study of the reaction of OH radical with sabinene, Phys. Chem. Chem. Phys., 8, 3211, https://doi.org/10.1039/b604489a, 2006.

Chen, J., Møller, K. H., Wennberg, P. O., and Kjaergaard, H. G.: Unimolecular Reactions Following Indoor and Outdoor Limonene Ozonolysis, J. Phys. Chem. A, https://doi.org/10.1021/acs.jpca.0c09882, 2021.

Chiappini, L., Carrasco, N., Temine, B., Picquet-Varrault, B., Durand-Jolibois, R., Wenger, J. C., and Doussin, J.-F.: Gaseous and Particulate Products from the Atmospheric Ozonolysis of a Biogenic Hydrocarbon, Sabinene, Environ. Chem., 3, 286, https://doi.org/10.1071/EN06037, 2006.

Cho, C., Hofzumahaus, A., Fuchs, H., Dorn, H.-P., Glowania, M., Holland, F., Rohrer, F., Vardhan, V., Kiendler-Scharr, A., Wahner, A., and Novelli, A.: Characterization of a chemical modulation reactor (CMR) for the measurement of atmospheric concentrations of hydroxyl radicals with a laser-induced fluorescence instrument, Atmospheric Meas. Tech., 14, 1851–1877, https://doi.org/10.5194/amt-14-1851-2021, 2021.

Coggon, M. M., Gkatzelis, G. I., McDonald, B. C., Gilman, J. B., Schwantes, R. H., Abuhassan, N., Aikin, K. C., Arend, M. F., Berkoff, T. A., Brown, S. S., Campos, T. L., Dickerson, R. R., Gronoff, G., Hurley, J. F., Isaacman-VanWertz, G., Koss, A. R., Li, M., McKeen, S. A., Moshary, F., Peischl, J., Pospisilova, V., Ren, X., Wilson, A., Wu, Y., Trainer, M., and Warneke, C.: Volatile chemical product emissions enhance ozone and modulate urban chemistry, Proc. Natl. Acad. Sci., 118, e2026653118, https://doi.org/10.1073/pnas.2026653118, 2021.

Coggon, M. M., Stockwell, C. E., Claflin, M. S., Pfannerstill, E. Y., Lu, X., Gilman, J. B., Marcantonio, J., Cao, C., Bates, K., Gkatzelis, G. I., Lamplugh, A., Katz, E. F., Arata, C., Apel, E. C., Hornbrook, R. S., Piel, F., Majluf, F., Blake, D. R., Wisthaler, A., Canagaratna, M., Lerner, B. M., Goldstein, A. H., Mak, J. E., and Warneke, C.: Identifying and correcting interferences to PTR-ToF-MS measurements of isoprene and other urban volatile organic compounds, Gases/In Situ Measurement/Instruments and Platforms, https://doi.org/10.5194/egusphere-2023-1497, 2023.

Cox, R. A. and Tyndall, G. S.: Rate constants for the reactions of CH_3O_2 with HO_2, NO and NO_2 using molecular modulation spectrometry, J. Chem. Soc. Faraday Trans. 2, 76, 153, https://doi.org/10.1039/f29807600153, 1980.

Cox, R. A., Ammann, M., Crowley, J. N., Herrmann, H., Jenkin, M. E., McNeill, V. F., Mellouki, A., Troe, J., and Wallington, T. J.: Evaluated kinetic and photochemical data for atmospheric chemistry: Volume VII – Criegee intermediates, Atmospheric Chem. Phys., 20, 13497–13519, https://doi.org/10.5194/acp-20-13497-2020, 2020.

Criegee, R.: Mechanism of Ozonolysis, Angew. Chem. Int. Ed. Engl., 14, 745–752, https://doi.org/10.1002/anie.197507451, 1975.

Crounse, J. D., Paulot, F., Kjaergaard, H. G., and Wennberg, P. O.: Peroxy radical isomerization in the oxidation of isoprene, Phys. Chem. Chem. Phys., 13, 13607–13613, https://doi.org/10.1039/C1CP21330J, 2011.

Dorn, H.-P., Brandenburger, U., Brauers, T., and Hausmann, M.: A New In Situ Laser Long-Path Absorption Instrument for the Measurement of Tropospheric OH Radicals, J. Atmospheric Sci., 52, 3373–3380, https://doi.org/10.1175/1520-0469(1995)052<3373:ANISLL>2.0.CO;2, 1995.

Duan, C., Liao, H., Wang, K., and Ren, Y.: The research hotspots and trends of volatile organic compound emissions from anthropogenic and natural sources: A systematic quantitative review, Environ. Res., 216, 114386, https://doi.org/10.1016/j.envres.2022.114386, 2023.

Dunker, A. M., Yarwood, G., Ortmann, J. P., and Wilson, G. M.: Comparison of Source Apportionment and Source Sensitivity of Ozone in a Three-Dimensional Air Quality Model, Environ. Sci. Technol., 36, 2953–2964, https://doi.org/10.1021/es011418f, 2002.

Eddingsaas, N. C., Loza, C. L., Yee, L. D., Seinfeld, J. H., and Wennberg, P. O.: α-pinene photooxidation under controlled chemical conditions – Part 1: Gas-phase composition in low- and high-NO_x; environments, Atmospheric Chem. Phys., 12, 6489–6504, https://doi.org/10.5194/acp-12-6489-2012, 2012.

Ehn, M., Thornton, J. A., Kleist, E., Sipilä, M., Junninen, H., Pullinen, I., Springer, M., Rubach, F., Tillmann, R., Lee, B., Lopez-Hilfiker, F., Andres, S., Acir, I.-H., Rissanen, M., Jokinen, T., Schobesberger, S., Kangasluoma, J., Kontkanen, J., Nieminen, T., Kurtén, T., Nielsen, L. B., Jørgensen, S., Kjaergaard, H. G., Canagaratna, M., Maso, M. D., Berndt, T., Petäjä, T., Wahner, A., Kerminen, V.-M., Kulmala, M., Worsnop, D. R., Wildt, J., and Mentel, T. F.: A large source of low-volatility secondary organic aerosol, Nature, 506, 476–479, https://doi.org/10.1038/nature13032, 2014.

Exton, D. A., McGenity, T. J., Steinke, M., Smith, D. J., and Suggett, D. J.: Uncovering the volatile nature of tropical coastal marine ecosystems in a changing world, Glob. Change Biol., 21, 1383–1394, https://doi.org/10.1111/gcb.12764, 2015.

Faiola, C. and Taipale, D.: Impact of insect herbivory on plant stress volatile emissions from trees: A synthesis of quantitative measurements and recommendations for future research, Atmospheric Environ. X, 5, 100060, https://doi.org/10.1016/j.aeaoa.2019.100060, 2020.

Farmer, D. K., Boedicker, E. K., and DeBolt, H. M.: Dry Deposition of Atmospheric Aerosols: Approaches, Observations, and Mechanisms, Annu. Rev. Phys. Chem., 72, 375–397, https://doi.org/10.1146/annurev-physchem-090519-034936, 2021.

Fuchs, H., Bohn, B., Hofzumahaus, A., Holland, F., Lu, K. D., Nehr, S., Rohrer, F., and Wahner, A.: Detection of HO_2 by laser-induced fluorescence: calibration and interferences from RO_2 radicals, Atmospheric Meas. Tech., 4, 1209–1225, https://doi.org/10.5194/amt-4-1209-2011, 2011.

Fuchs, H., Dorn, H.-P., Bachner, M., Bohn, B., Brauers, T., Gomm, S., Hofzumahaus, A., Holland, F., Nehr, S., Rohrer, F., Tillmann, R., and Wahner, A.: Comparison of OH concentration measurements by DOAS and LIF during SAPHIR chamber experiments at high OH reactivity and low NO concentration, Atmospheric Meas. Tech., 5, 1611–1626, https://doi.org/10.5194/amt-5-1611-2012, 2012.

Fuchs, H., Hofzumahaus, A., Rohrer, F., Bohn, B., Brauers, T., Dorn, H.-P., Häseler, R., Holland, F., Kaminski, M., Li, X., Lu, K., Nehr, S., Tillmann, R., Wegener, R., and Wahner, A.: Experimental evidence for efficient hydroxyl radical regeneration in isoprene oxidation, Nat. Geosci., 6, 1023–1026, https://doi.org/10.1038/ngeo1964, 2013.

Fuchs, H., Novelli, A., Rolletter, M., Hofzumahaus, A., Pfannerstill, E. Y., Kessel, S., Edtbauer, A., Williams, J., Michoud, V., Dusanter, S., Locoge, N., Zannoni, N., Gros, V., Truong, F., Sarda-Esteve, R., Cryer, D. R., Brumby, C. A., Whalley, L. K., Stone, D., Seakins, P. W., Heard, D. E., Schoemaecker, C., Blocquet, M., Coudert, S., Batut, S., Fittschen, C., Thames, A. B., Brune, W. H., Ernest, C., Harder, H., Muller, J. B. A., Elste, T., Kubistin, D., Andres, S., Bohn, B., Hohaus, T., Holland, F., Li, X., Rohrer, F., Kiendler-Scharr, A., Tillmann, R., Wegener, R., Yu, Z., Zou, Q., and Wahner, A.: Comparison of OH reactivity measurements in the atmospheric simulation chamber SAPHIR, Atmospheric Meas. Tech., 10, 4023–4053, https://doi.org/10.5194/amt-10-4023-2017, 2017.

Gkatzelis, G. I., Coggon, M. M., McDonald, B. C., Peischl, J., Aikin, K. C., Gilman, J. B., Trainer, M., and Warneke, C.: Identifying Volatile Chemical Product Tracer Compounds in U.S. Cities, Environ. Sci. Technol., https://doi.org/10.1021/acs.est.0c05467, 2021a.

Gkatzelis, G. I., Coggon, M. M., McDonald, B. C., Peischl, J., Gilman, J. B., Aikin, K. C., Robinson, M. A., Canonaco, F., Prevot, A. S. H., Trainer, M., and Warneke, C.: Observations Confirm that Volatile Chemical Products Are a Major Source of Petrochemical Emissions in U.S. Cities, Environ. Sci. Technol., https://doi.org/10.1021/acs.est.0c05471, 2021b.

Glowania, M., Rohrer, F., Dorn, H.-P., Hofzumahaus, A., Holland, F., Kiendler-Scharr, A., Wahner, A., and Fuchs, H.: Comparison of formaldehyde measurements by Hantzsch, CRDS and DOAS in the SAPHIR chamber, Atmospheric Meas. Tech., 14, 4239–4253, https://doi.org/10.5194/amt-14-4239-2021, 2021.

Gong, Y., Chen, Z., and Li, H.: The oxidation regime and SOA composition in limonene ozonolysis: roles of different double bonds, radicals, and water, Atmospheric Chem. Phys., 18, 15105–15123, https://doi.org/10.5194/acp-18-15105-2018, 2018.

Griffin, R. J., Cocker, D. R., Flagan, R. C., and Seinfeld, J. H.: Organic aerosol formation from the oxidation of biogenic hydrocarbons, J. Geophys. Res. Atmospheres, 104, 3555–3567, https://doi.org/10.1029/1998JD100049, 1999.

Grosjean, D., Williams, E. L., Grosjean, E., Andino, J. M., and Seinfeld, J. H.: Atmospheric oxidation of biogenic hydrocarbons: reaction of ozone with .beta.-pinene, D-limonene and trans-caryophyllene, Environ. Sci. Technol., 27, 2754–2758, https://doi.org/10.1021/es00049a014, 1993.

Guenther, A. B., Monson, R. K., and Fall, R.: Isoprene and monoterpene emission rate variability: Observations with eucalyptus and emission rate algorithm development, J. Geophys. Res., 96, 10799, https://doi.org/10.1029/91JD00960, 1991.

Guenther, A. B., Jiang, X., Heald, C. L., Sakulyanontvittaya, T., Duhl, T., Emmons, L. K., and Wang, X.: The Model of Emissions of Gases and Aerosols from Nature version 2.1 (MEGAN2.1): an extended and updated framework for modeling biogenic emissions, Geosci. Model Dev., 5, 1471–1492, https://doi.org/10.5194/gmd-5-1471-2012, 2012.

Hakola, H., Arey, J., Aschmann, S. M., and Atkinson, R.: Product formation from the gas-phase reactions of OH radicals and O_3 with a series of monoterpenes, J. Atmospheric Chem., 18, 75–102, https://doi.org/10.1007/BF00694375, 1994.

Hantschke, L., Novelli, A., Bohn, B., Cho, C., Reimer, D., Rohrer, F., Tillmann, R., Glowania, M., Hofzumahaus, A., Kiendler-Scharr, A., Wahner, A., and Fuchs, H.: Atmospheric photooxidation and ozonolysis of Δ^3-carene and 3-caronaldehyde: rate constants and product yields, Atmospheric Chem. Phys., 21, 12665–12685, https://doi.org/10.5194/acp-21-12665-2021, 2021.

Hasan, G., Valiev, R. R., Salo, V.-T., and Kurtén, T.: Computational Investigation of the Formation of Peroxide (ROOR) Accretion Products in the OH- and NO_3 -Initiated Oxidation of α-Pinene, J. Phys. Chem. A, 125, 10632–10639, https://doi.org/10.1021/acs.jpca.1c08969, 2021.

Hausmann, M., Brandenburger, U., Brauers, T., and Dorn, H.: Detection of tropospheric OH radicals by long-path differential-optical-absorption spectroscopy: Experimental setup, accuracy, and precision, J. Geophys. Res. Atmospheres, 102, 16011–16022, https://doi.org/10.1029/97JD00931, 1997.

Hendrick, F., Müller, J.-F., Clémer, K., Wang, P., De Mazière, M., Fayt, C., Gielen, C., Hermans, C., Ma, J. Z., Pinardi, G., Stavrakou, T., Vlemmix, T., and Van Roozendael, M.: Four years of ground-based MAX-DOAS observations of HONO and NO₂ in the Beijing area, Atmospheric Chem. Phys., 14, 765–781, https://doi.org/10.5194/acp-14-765-2014, 2014.

Hens, K., Novelli, A., Martinez, M., Auld, J., Axinte, R., Bohn, B., Fischer, H., Keronen, P., Kubistin, D., Nölscher, A. C., Oswald, R., Paasonen, P., Petäjä, T., Regelin, E., Sander, R., Sinha, V., Sipilä, M., Taraborrelli, D., Tatum Ernest, C., Williams, J., Lelieveld, J., and Harder, H.: Observation and modelling of HO_x radicals in a boreal forest, Atmospheric Chem. Phys., 14, 8723–8747, https://doi.org/10.5194/acp-14-8723-2014, 2014.

Hofzumahaus, A., Rohrer, F., Lu, K., Bohn, B., Brauers, T., Chang, C.-C., Fuchs, H., Holland, F., Kita, K., Kondo, Y., Li, X., Lou, S., Shao, M., Zeng, L., Wahner, A., and Zhang, Y.: Amplified Trace Gas Removal in the Troposphere, Science, 324, 1702–1704, https://doi.org/10.1126/science.1164566, 2009.

Hohaus, T., Kuhn, U., Andres, S., Kaminski, M., Rohrer, F., Tillmann, R., Wahner, A., Wegener, R., Yu, Z., and Kiendler-Scharr, A.: A new plant chamber facility, PLUS, coupled to the atmosphere simulation chamber SAPHIR, Atmospheric Meas. Tech., 9, 1247–1259, https://doi.org/10.5194/amt-9-1247-2016, 2016.

Holopainen, J. K. and Gershenzon, J.: Multiple stress factors and the emission of plant VOCs, Trends Plant Sci., 15, 176–184, https://doi.org/10.1016/j.tplants.2010.01.006, 2010.

Inman, M.: Carbon is forever, Nat. Clim. Change, 1, 156–158, https://doi.org/10.1038/climate.2008.122, 2008.

IPCC: Climate Change 2022: Impacts, Adaptation, and Vulnerability. Contribution of Working Group II to the Sixth Assessment Report of the Intergovernmental Panel on Climate Change, Cambridge University Press, Cambridge, UK/New York, NY, USA, 3056 pp., 2022.

Jenkin, M. E., Saunders, S. M., and Pilling, M. J.: The tropospheric degradation of volatile organic compounds: a protocol for mechanism development, Atmos. Environ., 31, 81–104, https://doi.org/10.1016/S1352-2310(96)00105-7, 1997.

Jenkin, M. E., Young, J. C., and Rickard, A. R.: The MCM v3.3.1 degradation scheme for isoprene, Atmospheric Chem. Phys., 15, 11433–11459, https://doi.org/10.5194/acp-15-11433-2015, 2015.

Jenkin, M. E., Valorso, R., Aumont, B., Rickard, A. R., and Wallington, T. J.: Estimation of rate coefficients and branching ratios for gas-phase reactions of OH with aliphatic organic compounds for use in automated mechanism construction, Atmospheric Chem. Phys., 18, 9297–9328, https://doi.org/10.5194/acp-18-9297-2018, 2018.

Jenkin, M. E., Valorso, R., Aumont, B., and Rickard, A. R.: Estimation of rate coefficients and branching ratios for reactions of organic peroxy radicals for use in automated mechanism construction, Atmospheric Chem. Phys., 19, 7691–7717, https://doi.org/10.5194/acp-19-7691-2019, 2019.

Jenkin, M. E., Valorso, R., Aumont, B., Newland, M. J., and Rickard, A. R.: Estimation of rate coefficients for the reactions of O_3 with unsaturated organic compounds for use in automated mechanism construction, Atmospheric Chem. Phys., 20, 12921–12937, https://doi.org/10.5194/acp-20-12921-2020, 2020.

Kaminski, M.: Untersuchung des photochemischen Terpenoidabbaus in der Atmosphärensimulationskammer SAPHIR, Forschungszentrum Jülich GmbH Zentralbibliothek, Jülich, 148 pp., 2014.

Kaminski, M., Fuchs, H., Acir, I.-H., Bohn, B., Brauers, T., Dorn, H.-P., Häseler, R., Hofzumahaus, A., Li, X., Lutz, A., Nehr, S., Rohrer, F., Tillmann, R., Vereecken, L., Wegener, R., and Wahner, A.: Investigation of the α-pinene photooxidation by OH in the atmosphere simulation chamber SAPHIR, Atmospheric Chem. Phys., 17, 6631–6650, https://doi.org/10.5194/acp-17-6631-2017, 2017.

Kappers, I. F., Aharoni, A., Van Herpen, T. W. J. M., Luckerhoff, L. L. P., Dicke, M., and Bouwmeester, H. J.: Genetic Engineering of Terpenoid Metabolism Attracts Bodyguards to *Arabidopsis*, Science, 309, 2070–2072, https://doi.org/10.1126/science.1116232, 2005.

Kessler, A. and Baldwin, I. T.: Defensive Function of Herbivore-Induced Plant Volatile Emissions in Nature, Science, 291, 2141–2144, https://doi.org/10.1126/science.291.5511.2141, 2001.

Kim, K.-H., Jahan, S. A., and Lee, J.-T.: Exposure to Formaldehyde and Its Potential Human Health Hazards, J. Environ. Sci. Health Part C, 29, 277–299, https://doi.org/10.1080/10590501.2011.629972, 2011.

Kim, S., VandenBoer, T. C., Young, C. J., Riedel, T. P., Thornton, J. A., Swarthout, B., Sive, B., Lerner, B., Gilman, J. B., Warneke, C., Roberts, J. M., Guenther, A., Wagner, N. L., Dubé, W. P., Williams, E., and Brown, S. S.: The primary and recycling sources of OH during the NACHTT-2011 campaign: HONO as an important OH primary source in the wintertime, J. Geophys. Res. Atmospheres, 119, 6886–6896, https://doi.org/10.1002/2013JD019784, 2014.

Kleist, E., Mentel, T. F., Andres, S., Bohne, A., Folkers, A., Kiendler-Scharr, A., Rudich, Y., Springer, M., Tillmann, R., and Wildt, J.: Irreversible impacts of heat on the emissions of monoterpenes, sesquiterpenes, phenolic BVOC and green leaf volatiles from several tree species, Biogeosciences, 9, 5111–5123, https://doi.org/10.5194/bg-9-5111-2012, 2012.

Knote, C., Hodzic, A., and Jimenez, J. L.: The effect of dry and wet deposition of condensable vapors on secondary organic aerosols concentrations over the continental US, Atmospheric Chem. Phys., 15, 1–18, https://doi.org/10.5194/acp-15-1-2015, 2015.

Kramshøj, M., Albers, C. N., Holst, T., Holzinger, R., Elberling, B., and Rinnan, R.: Biogenic volatile release from permafrost thaw is determined by the soil microbial sink, Nat. Commun., 9, 3412, https://doi.org/10.1038/s41467-018-05824-y, 2018.

Kuwata, K. T., Luu, L., Weberg, A. B., Huang, K., Parsons, A. J., Peebles, L. A., Rackstraw, N. B., and Kim, M. J.: Quantum Chemical and Statistical Rate Theory Studies of the Vinyl Hydroperoxides Formed in *trans*-2-Butene and 2,3-Dimethyl-2-butene Ozonolysis, J. Phys. Chem. A, 122, 2485–2502, https://doi.org/10.1021/acs.jpca.8b00287, 2018.

Larsen, Bo. R., Di Bella, D., Glasius, M., Winterhalter, R., Jensen, N. R., and Hjorth, J.: Gas-Phase OH Oxidation of Monoterpenes: Gaseous and Particulate Products, J. Atmospheric Chem., 38, 231–276, https://doi.org/10.1023/A:1006487530903, 2001.

Lee, A., Goldstein, A. H., Kroll, J. H., Ng, N. L., Varutbangkul, V., Flagan, R. C., and Seinfeld, J. H.: Gas-phase products and secondary aerosol yields from the photooxidation of 16 different terpenes, J. Geophys. Res., 111, D17305, https://doi.org/10.1029/2006JD007050, 2006.

Lelieveld, J., Butler, T. M., Crowley, J. N., Dillon, T. J., Fischer, H., Ganzeveld, L., Harder, H., Lawrence, M. G., Martinez, M., Taraborrelli, D., and Williams, J.: Atmospheric oxidation capacity sustained by a tropical forest, Nature, 452, 737–740, https://doi.org/10.1038/nature06870, 2008.

Leungsakul, S., Jeffries, H. E., and Kamens, R. M.: A kinetic mechanism for predicting secondary aerosol formation from the reactions of d-limonene in the presence of oxides of nitrogen and natural sunlight, Atmos. Environ., 39, 7063–7082, https://doi.org/10.1016/j.atmosenv.2005.08.024, 2005.

Li, X., Rohrer, F., Hofzumahaus, A., Brauers, T., Häseler, R., Bohn, B., Broch, S., Fuchs, H., Gomm, S., Holland, F., Jäger, J., Kaiser, J., Keutsch, F. N., Lohse, I., Lu, K., Tillmann, R., Wegener, R., Wolfe, G. M., Mentel, T. F., Kiendler-Scharr, A., and Wahner, A.: Missing Gas-Phase Source of HONO Inferred from Zeppelin Measurements in the Troposphere, Science, 344, 292–296, https://doi.org/10.1126/science.1248999, 2014.

Librando, V. and Tringali, G.: Atmospheric fate of OH initiated oxidation of terpenes. Reaction mechanism of α-pinene degradation and secondary organic aerosol formation, J. Environ. Manage., 75, 275–282, https://doi.org/10.1016/j.jenvman.2005.01.001, 2005.

Lim, Y.-J., Armendariz, A., Son, Y.-S., and Kim, J.-C.: Seasonal variations of isoprene emissions from five oak tree species in East Asia, Atmos. Environ., 45, 2202–2210, https://doi.org/10.1016/j.atmosenv.2011.01.066, 2011.

Lindinger, W., Hansel, A., and Jordan, A.: On-line monitoring of volatile organic compounds at pptv levels by means of proton-transfer-reaction mass spectrometry (PTR-MS) medical applications, food control and environmental research, Int. J. Mass Spectrom. Ion Process., 173, 191–241, https://doi.org/10.1016/S0168-1176(97)00281-4, 1998.

Liu, X., Mason, M., Krebs, K., and Sparks, L.: Full-Scale Chamber Investigation and Simulation of Air Freshener Emissions in the Presence of Ozone, Environ. Sci. Technol., 38, 2802–2812, https://doi.org/10.1021/es030544b, 2004.

Long, B., Bao, J. L., and Truhlar, D. G.: Atmospheric Chemistry of Criegee Intermediates: Unimolecular Reactions and Reactions with Water, J. Am. Chem. Soc., 138, 14409–14422, https://doi.org/10.1021/jacs.6b08655, 2016.

Loreto, F. and Schnitzler, J.-P.: Abiotic stresses and induced BVOCs, Trends Plant Sci., 15, 154–166, https://doi.org/10.1016/j.tplants.2009.12.006, 2010.

Loreto, F., Mannozzi, M., Maris, C., Nascetti, P., Ferranti, F., and Pasqualini, S.: Ozone Quenching Properties of Isoprene and Its Antioxidant Role in Leaves, Plant Physiol., 126, 993–1000, https://doi.org/10.1104/pp.126.3.993, 2001.

Lou, S., Holland, F., Rohrer, F., Lu, K., Bohn, B., Brauers, T., Chang, C. C., Fuchs, H., Häseler, R., Kita, K., Kondo, Y., Li, X., Shao, M., Zeng, L., Wahner, A., Zhang, Y., Wang, W., and Hofzumahaus, A.: Atmospheric OH reactivities in the Pearl River Delta – China in summer 2006: measurement and model results, Atmospheric Chem. Phys., 10, 11243–11260, https://doi.org/10.5194/acp-10-11243-2010, 2010.

Lu, X., Wang, Y., Li, J., Shen, L., and Fung, J. C. H.: Evidence of heterogeneous HONO formation from aerosols and the regional photochemical impact of this HONO source, Environ. Res. Lett., 13, 114002, https://doi.org/10.1088/1748-9326/aae492, 2018.

Lüpke, M., Steinbrecher, R., Leuchner, M., and Menzel, A.: The Tree Drought Emission MONitor (Tree DEMON), an innovative system for assessing biogenic volatile organic compounds emission from plants, Plant Methods, 13, 14, https://doi.org/10.1186/s13007-017-0166-6, 2017.

Ma, Y. and Marston, G.: Multifunctional acid formation from the gas-phase ozonolysis of β-pinene, Phys. Chem. Chem. Phys., 10, 6115, https://doi.org/10.1039/b807863g, 2008.

McDonald, B. C., De Gouw, J. A., Gilman, J. B., Jathar, S. H., Akherati, A., Cappa, C. D., Jimenez, J. L., Lee-Taylor, J., Hayes, P. L., McKeen, S. A., Cui, Y. Y., Kim, S.-W., Gentner, D. R., Isaacman-VanWertz, G., Goldstein, A. H., Harley, R. A., Frost, G. J., Roberts, J. M., Ryerson, T. B., and Trainer, M.: Volatile chemical products emerging as largest petrochemical source of urban organic emissions, Science, 359, 760–764, https://doi.org/10.1126/science.aaq0524, 2018.

McGillen, M. R., Percival, C. J., Shallcross, D. E., and Harvey, J. N.: Is hydrogen abstraction an important pathway in the reaction of alkenes with the OH radical?, Phys. Chem. Chem. Phys., 9, 4349, https://doi.org/10.1039/b703035e, 2007.

Mellouki, A., Ammann, M., Cox, R. A., Crowley, J. N., Herrmann, H., Jenkin, M. E., McNeill, V. F., Troe, J., and Wallington, T. J.: Evaluated kinetic and photochemical data for atmospheric chemistry: volume VIII – gas-phase reactions of organic species with four, or more, carbon atoms (≥ C_4), Atmospheric Chem. Phys., 21, 4797–4808, https://doi.org/10.5194/acp-21-4797-2021, 2021.

Mentel, T. F., Springer, M., Ehn, M., Kleist, E., Pullinen, I., Kurtén, T., Rissanen, M., Wahner, A., and Wildt, J.: Formation of highly oxidized multifunctional compounds: autoxidation of peroxy radicals formed in the ozonolysis of alkenes – deduced from structure–product relationships, Atmospheric Chem. Phys., 15, 6745–6765, https://doi.org/10.5194/acp-15-6745-2015, 2015.

Møller, K. H., Otkjær, R. V., Chen, J., and Kjaergaard, H. G.: Double Bonds Are Key to Fast Unimolecular Reactivity in First-Generation Monoterpene Hydroxy Peroxy Radicals, J. Phys. Chem. A, 124, 2885–2896, https://doi.org/10.1021/acs.jpca.0c01079, 2020.

Nazaroff, W. W. and Weschler, C. J.: Cleaning products and air fresheners: exposure to primary and secondary air pollutants, Atmos. Environ., 38, 2841–2865, https://doi.org/10.1016/j.atmosenv.2004.02.040, 2004.

Nguyen, T. B., Tyndall, G. S., Crounse, J. D., Teng, A. P., Bates, K. H., Schwantes, R. H., Coggon, M. M., Zhang, L., Feiner, P., Millller, D. O., Skog, K. M., Rivera-Rios, J. C., Dorris, M., Olson, K. F., Koss, A., Wild, R. J., Brown, S. S., Goldstein, A. H., de Gouw, J. A., Brune, W. H., Keutsch, F. N., Seinfeld, J. H., and Wennberg, P. O.: Atmospheric fates of Criegee intermediates in the ozonolysis of isoprene, Phys. Chem. Chem. Phys., 18, 10241–10254, https://doi.org/10.1039/C6CP00053C, 2016.

Nguyen, T. L., Peeters, J., and Vereecken, L.: Theoretical study of the gas-phase ozonolysis of β-pinene ($C_{10}H_{16}$), Phys. Chem. Chem. Phys., 11, 5643, https://doi.org/10.1039/b822984h, 2009.

Novelli, A., Vereecken, L., Bohn, B., Dorn, H.-P., Gkatzelis, G. I., Hofzumahaus, A., Holland, F., Reimer, D., Rohrer, F., Rosanka, S., Taraborrelli, D., Tillmann, R., Wegener, R., Yu, Z., Kiendler-Scharr, A., Wahner, A., and Fuchs, H.: Importance of isomerization reactions for OH radical regeneration from the photo-oxidation of isoprene investigated in the atmospheric simulation chamber SAPHIR, Atmospheric Chem. Phys., 20, 3333–3355, https://doi.org/10.5194/acp-20-3333-2020, 2020.

Oswald, R., Behrendt, T., Ermel, M., Wu, D., Su, H., Cheng, Y., Breuninger, C., Moravek, A., Mougin, E., Delon, C., Loubet, B., Pommerening-Röser, A., Sörgel, M., Pöschl, U., Hoffmann, T., Andreae, M. O., Meixner, F. X., and Trebs, I.: HONO Emissions from Soil Bacteria as a Major Source of Atmospheric Reactive Nitrogen, Science, 341, 1233–1235, https://doi.org/10.1126/science.1242266, 2013.

Pagonis, D., Sekimoto, K., and De Gouw, J.: A Library of Proton-Transfer Reactions of H_3O^+ Ions Used for Trace Gas Detection, J. Am. Soc. Mass Spectrom., 30, 1330–1335, https://doi.org/10.1007/s13361-019-02209-3, 2019.

Pang, J. Y. S., Novelli, A., Kaminski, M., Acir, I.-H., Bohn, B., Carlsson, P. T. M., Cho, C., Dorn, H.-P., Hofzumahaus, A., Li, X., Lutz, A., Nehr, S., Reimer, D., Rohrer, F., Tillmann, R., Wegener, R., Kiendler-Scharr, A., Wahner, A., and Fuchs, H.: Investigation of the limonene photooxidation by OH at different NO concentrations in the atmospheric simulation chamber SAPHIR (Simulation of Atmospheric PHotochemistry In a large Reaction Chamber), Atmospheric Chem. Phys., 22, 8497–8527, https://doi.org/10.5194/acp-22-8497-2022, 2022.

Pang, J. Y. S., Berg, F., Novelli, A., Bohn, B., Färber, M., Carlsson, P. T. M., Dubus, R., Gkatzelis, G. I., Rohrer, F., Wedel, S., Wahner, A., and Fuchs, H.: Atmospheric photooxidation and ozonolysis of sabinene: reaction rate coefficients, product yields, and chemical budget of radicals, Atmospheric Chem. Phys., 23, 12631–12649, https://doi.org/10.5194/acp-23-12631-2023, 2023.

Paulson, S. E. and Orlando, J. J.: The reactions of ozone with alkenes: An important source of HO_x in the boundary layer, Geophys. Res. Lett., 23, 3727–3730, https://doi.org/10.1029/96GL03477, 1996.

Peeters, J., Boullart, W., Pultau, V., Vandenberk, S., and Vereecken, L.: Structure−Activity Relationship for the Addition of OH to (Poly)alkenes: Site-Specific and Total Rate Constants, J. Phys. Chem. A, 111, 1618–1631, https://doi.org/10.1021/jp066973o, 2007.

Peeters, J., Müller, J.-F., Stavrakou, T., and Nguyen, V. S.: Hydroxyl Radical Recycling in Isoprene Oxidation Driven by Hydrogen Bonding and Hydrogen Tunneling: The Upgraded LIM1 Mechanism, J. Phys. Chem. A, 118, 8625–8643, https://doi.org/10.1021/jp5033146, 2014.

Pfeifle, M., Ma, Y.-T., Jasper, A. W., Harding, L. B., Hase, W. L., and Klippenstein, S. J.: Nascent energy distribution of the Criegee intermediate CH2OO from direct dynamics calculations of primary ozonide dissociation, J. Chem. Phys., 148, 174306, https://doi.org/10.1063/1.5028117, 2018.

Piccot, S. D., Watson, J. J., and Jones, J. W.: A global inventory of volatile organic compound emissions from anthropogenic sources, J. Geophys. Res. Atmospheres, 97, 9897–9912, https://doi.org/10.1029/92JD00682, 1992.

Platt, U. F., Winer, A. M., Biermann, H. W., Atkinson, Roger., and Pitts, J. N.: Measurement of nitrate radical concentrations in continental air, Environ. Sci. Technol., 18, 365–369, https://doi.org/10.1021/es00123a015, 1984.

Reissell, A., Harry, C., Aschmann, S. M., Atkinson, R., and Arey, J.: Formation of acetone from the OH radical- and O_3-initiated reactions of a series of monoterpenes, J. Geophys. Res. Atmospheres, 104, 13869–13879, https://doi.org/10.1029/1999JD900198, 1999.

Reissell, A., Aschmann, S. M., and Arey, J.: Products of the OH radical- and O_3 -initiated reactions of myrcene and ocimene, J. Geophys. Res., 107, 4138, https://doi.org/10.1029/2001JD001234, 2002.

Rindelaub, J. D., McAvey, K. M., and Shepson, P. B.: The photochemical production of organic nitrates from α-pinene and loss via acid-dependent particle phase hydrolysis, Atmos. Environ., 100, 193–201, https://doi.org/10.1016/j.atmosenv.2014.11.010, 2015.

Roberts, J. M.: The atmospheric chemistry of organic nitrates, Atmospheric Environ. Part Gen. Top., 24, 243–287, https://doi.org/10.1016/0960-1686(90)90108-Y, 1990.

Rohrer, F., Bohn, B., Brauers, T., Brüning, D., Johnen, F.-J., Wahner, A., and Kleffmann, J.: Characterisation of the photolytic HONO-source in the atmosphere simulation chamber SAPHIR, Atmospheric Chem. Phys., 5, 2189–2201, https://doi.org/10.5194/acp-5-2189-2005, 2005.

Rohrer, F., Lu, K., Hofzumahaus, A., Bohn, B., Brauers, T., Chang, C.-C., Fuchs, H., Häseler, R., Holland, F., Hu, M., Kita, K., Kondo, Y., Li, X., Lou, S., Oebel, A., Shao, M., Zeng, L., Zhu, T., Zhang, Y., and Wahner, A.: Maximum efficiency in the hydroxyl-radical-based self-cleansing of the troposphere, Nat. Geosci., 7, 559–563, https://doi.org/10.1038/ngeo2199, 2014.

Rolletter, M., Kaminski, M., Acir, I.-H., Bohn, B., Dorn, H.-P., Li, X., Lutz, A., Nehr, S., Rohrer, F., Tillmann, R., Wegener, R., Hofzumahaus, A., Kiendler-Scharr, A., Wahner, A., and Fuchs, H.: Investigation of the α-pinene photooxidation by OH in the atmospheric simulation chamber SAPHIR, Atmospheric Chem. Phys., 19, 11635–11649, https://doi.org/10.5194/acp-19-11635-2019, 2019.

Rollins, A. W., Smith, J. D., Wilson, K. R., and Cohen, R. C.: Real Time In Situ Detection of Organic Nitrates in Atmospheric Aerosols, Environ. Sci. Technol., 44, 5540–5545, https://doi.org/10.1021/es100926x, 2010.

Romer, P. S., Duffey, K. C., Wooldridge, P. J., Allen, H. M., Ayres, B. R., Brown, S. S., Brune, W. H., Crounse, J. D., de Gouw, J., Draper, D. C., Feiner, P. A., Fry, J. L., Goldstein, A. H., Koss, A., Misztal, P. K., Nguyen, T. B., Olson, K., Teng, A. P., Wennberg, P. O., Wild, R. J., Zhang, L., and Cohen, R. C.: The lifetime of nitrogen oxides in an isoprene-dominated forest, Atmospheric Chem. Phys., 16, 7623–7637, https://doi.org/10.5194/acp-16-7623-2016, 2016.

Rosales, C. M. F., Jiang, J., Lahib, A., Bottorff, B. P., Reidy, E. K., Kumar, V., Tasoglou, A., Huber, H., Dusanter, S., Tomas, A., Boor, B. E., and Stevens, P. S.: Chemistry and human exposure implications of secondary organic aerosol production from indoor terpene ozonolysis, Sci. Adv., 8, eabj9156, https://doi.org/10.1126/sciadv.abj9156, 2022.

Sander, S. P. and Watson, R. T.: Kinetics studies of the reactions of methyldioxy with nitric oxide, nitrogen dioxide, and methyldioxy at 298 K, J. Phys. Chem., 84, 1664–1674, https://doi.org/10.1021/j100450a002, 1980.

Saunders, S. M., Jenkin, M. E., Derwent, R. G., and Pilling, M. J.: Protocol for the development of the Master Chemical Mechanism, MCM v3 (Part A): tropospheric degradation of non-aromatic volatile organic compounds, Atmospheric Chem. Phys., 3, 161–180, https://doi.org/10.5194/acp-3-161-2003, 2003.

Saunier, A., Ormeño, E., Wortham, H., Temime-Roussel, B., Lecareux, C., Boissard, C., and Fernandez, C.: Chronic Drought Decreases Anabolic and Catabolic BVOC Emissions of (*Quercus pubescens*) in a Mediterranean Forest, Front. Plant Sci., 8, https://doi.org/10.3389/fpls.2017.00071, 2017.

Schlosser, E., Bohn, B., Brauers, T., Dorn, H.-P., Fuchs, H., Häseler, R., Hofzumahaus, A., Holland, F., Rohrer, F., Rupp, L. O., Siese, M., Tillmann, R., and Wahner, A.: Intercomparison of Two Hydroxyl Radical Measurement Techniques at the Atmosphere Simulation Chamber SAPHIR, J. Atmospheric Chem., 56, 187–205, https://doi.org/10.1007/s10874-006-9049-3, 2007.

Sekimoto, K., Li, S.-M., Yuan, B., Koss, A., Coggon, M., Warneke, C., and De Gouw, J.: Calculation of the sensitivity of proton-transfer-reaction mass spectrometry (PTR-MS) for organic trace gases using molecular properties, Int. J. Mass Spectrom., 421, 71–94, https://doi.org/10.1016/j.ijms.2017.04.006, 2017.

Sharkey, T. D., Wiberley, A. E., and Donohue, A. R.: Isoprene Emission from Plants: Why and How, Ann. Bot., 101, 5–18, https://doi.org/10.1093/aob/mcm240, 2007.

Sindelarova, K., Granier, C., Bouarar, I., Guenther, A., Tilmes, S., Stavrakou, T., Stefani, P., and Knorr, W.: Global data set of biogenic VOC emissions calculated by the MEGAN model over the last 30 years, Atmos Chem Phys, 25, https://doi.org/10.5194/acp-14-9317-2014, 2014.

Solberg, S., Hov, Ø., Søvde, A., Isaksen, I. S. A., Coddeville, P., De Backer, H., Forster, C., Orsolini, Y., and Uhse, K.: European surface ozone in the extreme summer 2003, J. Geophys. Res., 113, D07307, https://doi.org/10.1029/2007JD009098, 2008.

Staudt, M. and Bertin, N.: Light and temperature dependence of the emission of cyclic and acyclic monoterpenes from holm oak (*Quercus ilex L.*) leaves, Plant Cell Environ., 21, 385–395, https://doi.org/10.1046/j.1365-3040.1998.00288.x, 1998.

Steiner, A. H. and Goldstein, A. L.: Biogenic VOCs, in: Volatile Organic Compounds in the Atmosphere, edited by: Koppmann, R., Blackwell Publishing Ltd, Oxford, UK, 82–128, https://doi.org/10.1002/9780470988657.ch3, 2007.

Tan, Z., Hantschke, L., Kaminski, M., Acir, I.-H., Bohn, B., Cho, C., Dorn, H.-P., Li, X., Novelli, A., Nehr, S., Rohrer, F., Tillmann, R., Wegener, R., Hofzumahaus, A., Kiendler-Scharr, A., Wahner, A., and Fuchs, H.: Atmospheric photo-oxidation of myrcene: OH reaction rate constant, gas-phase oxidation products and radical budgets, Atmospheric Chem. Phys., 21, 16067–16091, https://doi.org/10.5194/acp-21-16067-2021, 2021.

Tollsten, L. and Müller, P. M.: Volatile organic compounds emitted from beech leaves, Phytochemistry, 43, 759–762, https://doi.org/10.1016/0031-9422(96)00272-5, 1996.

Tu, P., Hall, W. A., and Johnston, M. V.: Characterization of Highly Oxidized Molecules in Fresh and Aged Biogenic Secondary Organic Aerosol, Anal. Chem., 88, 4495–4501, https://doi.org/10.1021/acs.analchem.6b00378, 2016.

Valorso, R., Aumont, B., Camredon, M., Raventos-Duran, T., Mouchel-Vallon, C., Ng, N. L., Seinfeld, J. H., Lee-Taylor, J., and Madronich, S.: Explicit modelling of SOA formation from α-pinene

photooxidation: sensitivity to vapour pressure estimation, Atmospheric Chem. Phys., 11, 6895–6910, https://doi.org/10.5194/acp-11-6895-2011, 2011.

Van Meeningen, Y., Schurgers, G., Rinnan, R., and Holst, T.: BVOC emissions from English oak (<i>Quercus robur</i>) and European beech (*Fagus sylvatica*) along a latitudinalgradient, Biogeosciences, 13, 6067–6080, https://doi.org/10.5194/bg-13-6067-2016, 2016.

Vaughan, S., Ingham, T., Whalley, L. K., Stone, D., Evans, M. J., Read, K. A., Lee, J. D., Moller, S. J., Carpenter, L. J., Lewis, A. C., Fleming, Z. L., and Heard, D. E.: Seasonal observations of OH and HO₂ in the remote tropical marine boundary layer, Atmospheric Chem. Phys., 12, 2149–2172, https://doi.org/10.5194/acp-12-2149-2012, 2012.

Vereecken, L. and Nozière, B.: H migration in peroxy radicals under atmospheric conditions, Atmospheric Chem. Phys., 20, 7429–7458, https://doi.org/10.5194/acp-20-7429-2020, 2020.

Vereecken, L. and Peeters, J.: H-atom abstraction by OH-radicals from (biogenic) (poly)alkenes: C–H bond strengths and abstraction rates, Chem. Phys. Lett., 333, 162–168, https://doi.org/10.1016/S0009-2614(00)01347-6, 2001.

Vereecken, L. and Peeters, J.: Decomposition of substituted alkoxy radicals—part I: a generalized structure–activity relationship for reaction barrier heights, Phys. Chem. Chem. Phys., 11, 9062–9074, https://doi.org/10.1039/B909712K, 2009.

Vereecken, L., Vu, G., Wahner, A., Kiendler-Scharr, A., and Nguyen, H. M. T.: A structure activity relationship for ring closure reactions in unsaturated alkylperoxy radicals, Phys. Chem. Chem. Phys., 23, 16564–16576, https://doi.org/10.1039/D1CP02758A, 2021.

Vickers, C. E., Gershenzon, J., Lerdau, M. T., and Loreto, F.: A unified mechanism of action for volatile isoprenoids in plant abiotic stress, Nat. Chem. Biol., 5, 283–291, https://doi.org/10.1038/nchembio.158, 2009.

Wang, L. and Wang, L.: Mechanism of gas-phase ozonolysis of sabinene in the atmosphere, Phys. Chem. Chem. Phys., 19, 24209–24218, https://doi.org/10.1039/C7CP03216A, 2017.

Wang, L. and Wang, L.: Atmospheric Oxidation Mechanism of Sabinene Initiated by the Hydroxyl Radicals, J. Phys. Chem. A, 122, 8783–8793, https://doi.org/10.1021/acs.jpca.8b06381, 2018.

Wang, L. and Wang, L.: The oxidation mechanism of gas-phase ozonolysis of limonene in the atmosphere, Phys. Chem. Chem. Phys., 23, 9294–9303, https://doi.org/10.1039/D0CP05803C, 2021.

Whalley, L. K., Edwards, P. M., Furneaux, K. L., Goddard, A., Ingham, T., Evans, M. J., Stone, D., Hopkins, J. R., Jones, C. E., Karunaharan, A., Lee, J. D., Lewis, A. C., Monks, P. S., Moller, S. J., and Heard, D. E.: Quantifying the magnitude of a missing hydroxyl radical source in a tropical rainforest, Atmos. Chem. Phys., 11, 7223–7233, https://doi.org/10.5194/acp-11-7223-2011, 2011.

Wild, O.: Modelling the global tropospheric ozone budget: exploring the variability in current models, Atmospheric Chem. Phys., 7, 2643–2660, https://doi.org/10.5194/acp-7-2643-2007, 2007.

Wiß, F., Ghirardo, A., Schnitzler, J., Nendel, C., Augustin, J., Hoffmann, M., and Grote, R.: Net ecosystem fluxes and composition of biogenic volatile organic compounds over a maize field–interaction of meteorology and phenological stages, GCB Bioenergy, 9, 1627–1643, https://doi.org/10.1111/gcbb.12454, 2017.

Xu, L., Møller, K. H., Crounse, J. D., Otkjær, R. V., Kjaergaard, H. G., and Wennberg, P. O.: Unimolecular Reactions of Peroxy Radicals Formed in the Oxidation of α-Pinene and β-Pinene by Hydroxyl Radicals, J. Phys. Chem. A, 123, 1661–1674, https://doi.org/10.1021/acs.jpca.8b11726, 2019.

Xue, C., Ye, C., Zhang, C., Catoire, V., Liu, P., Gu, R., Zhang, J., Ma, Z., Zhao, X., Zhang, W., Ren, Y., Krysztofiak, G., Tong, S., Xue, L., An, J., Ge, M., Mellouki, A., and Mu, Y.: Evidence for Strong HONO Emission from Fertilized Agricultural Fields and its Remarkable Impact on Regional O_3 Pollution in the Summer North China Plain, ACS Earth Space Chem., 5, 340–347, https://doi.org/10.1021/acsearthspacechem.0c00314, 2021.

Yu, J., Cocker III, D. R., Griffin, R. J., Flagan, R. C., and Seinfeld, J. H.: Gas-Phase Ozone Oxidation of Monoterpenes: Gaseous and Particulate Products, J. Atmos. Chem., 34, 207–258, https://doi.org/10.1023/A:1006254930583, 1999.

Yu, Z.: Chamber study of biogenic volatile organic compounds: plant emission, oxidation products and their OH reactivity, Forschungszentrum Jülich, 139 pp., 2018.

Yuan, B., Koss, A., Warneke, C., Gilman, J. B., Lerner, B. M., Stark, H., and De Gouw, J. A.: A high-resolution time-of-flight chemical ionization mass spectrometerutilizing hydronium ions (H_3O^+; ToF-CIMS) for measurements of volatile organic compounds in the atmosphere, Atmos. Meas. Tech., 9, 2735–2752, https://doi.org/10.5194/amt-9-2735-2016, 2016.

Zhao, D., Schmitt, S. H., Wang, M., Acir, I.-H., Tillmann, R., Tan, Z., Novelli, A., Fuchs, H., Pullinen, I., Wegener, R., Rohrer, F., Wildt, J., Kiendler-Scharr, A., Wahner, A., and Mentel, T. F.: Effects of NO_x and SO_2 on the secondary organic aerosol formation from photooxidation of α-pinene and limonene, Atmospheric Chem. Phys., 18, 1611–1628, https://doi.org/10.5194/acp-18-1611-2018, 2018.

Zhao, Y., Zhang, R., Wang, H., He, M., Sun, X., Zhang, Q., Wang, W., and Ru, M.: Mechanism of atmospheric ozonolysis of sabinene: A DFT study, J. Mol. Struct., 942, 32–37, https://doi.org/10.1016/j.theochem.2009.11.029, 2010.

Supplementary material for Section 4

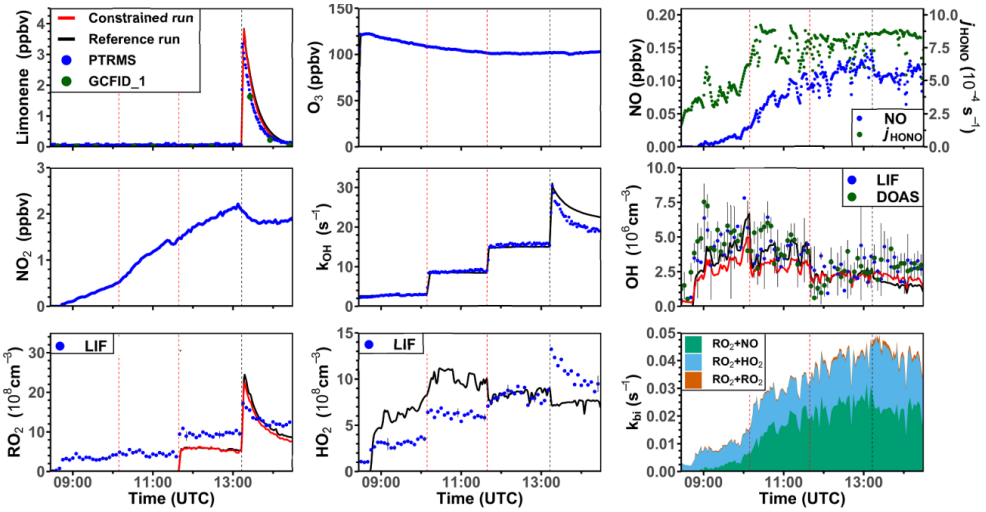

Figure S4-1. Time series of radicals, inorganic and organic species during the limonene oxidation experiment at low NO mixing ratio on 13 June 2015. The black line denoted the modelled results from the reference model with O_3, NO_x and HONO are constrained; the red line denoted the modelled results from the constrained model with HO2 constrained and k_{OH} adjusted to the measurement, and the dots are the measurements. RO_2 bi-molecular reaction loss rate constant (k_{bi}) are calculated based on the measured NO, HO_2, and RO_2 concentrations using reaction rate constants from the MCM model. The first red dashed line indicates the injection of 750 ppb of CO; the second red dashed line indicates the injection of 60 ppm of CH_4.

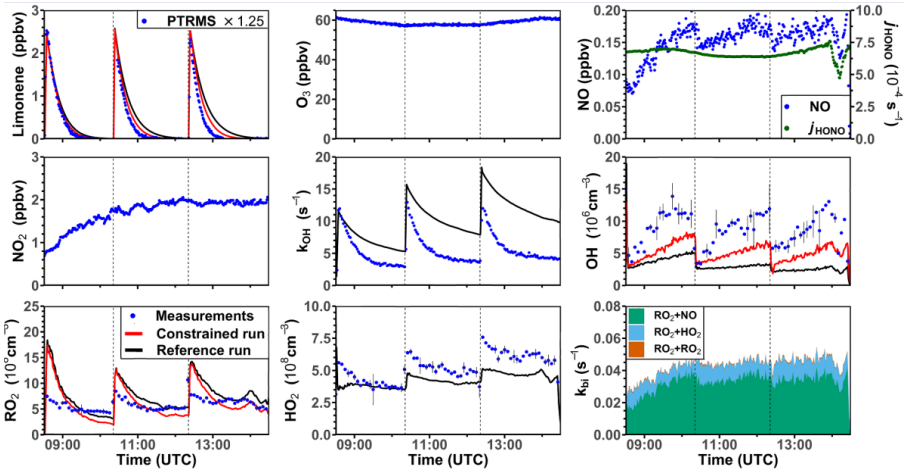

Fig. S4-2 Time series of radicals, inorganic and organic species during the limonene oxidation experiment at low NO mixing ratio on 04 July 2019. Limonene concentrations measured by PTRMS are scaled by a factor of 1.25 to match the increase of OH reactivity during limonene injections. The black line denoted the modelled results from the reference model with O_3, NO_x and HONO being constrained; the red line denoted the modelled resulted from the constrained model with HO2 constrained and k_{OH} adjusted to the measurement. RO_2 bi-molecular reaction loss rate constant (k_{bi}) are calculated based on the measured NO, HO_2, and RO_2 concentrations using reaction rate constants from the MCM model.

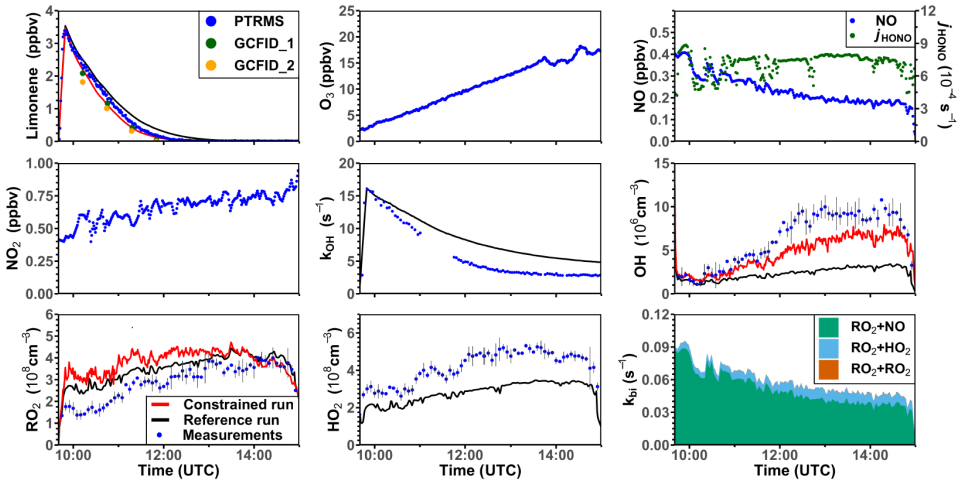

Figure S4-3. Time series of radicals, inorganic and organic species during the limonene oxidation experiment at medium NO mixing ratio on 10 August 2012. The black line denoted the modelled results from the reference model with O_3, NO_x and HONO being constrained; the red line denoted the modelled resulted from the constrained model with HO_2 constrained and k_{OH} adjusted to the measurement. RO_2 bi-molecular reaction loss rate constant (k_{bi}) are calculated based on the measured NO, HO_2, and RO_2 concentrations using reaction rate constants from the MCM model.

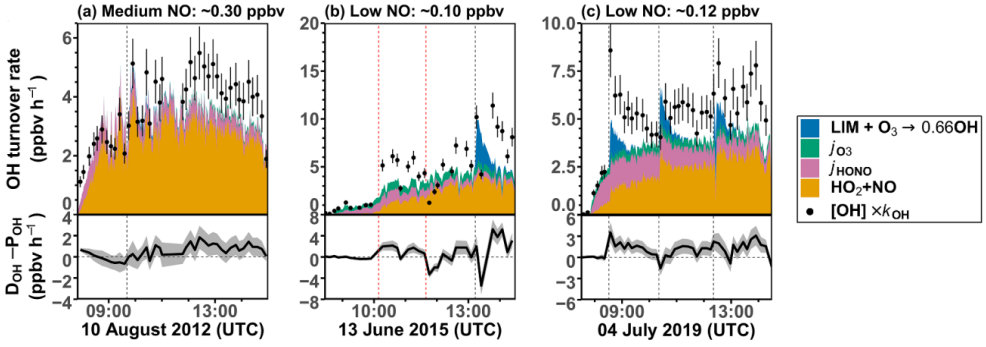

Figure S4-4. The chemical budget of OH radicals during the oxidation of limonene simliar to Fig. 4-20. 10-minutes-average values of total OH destruction rates compared to the sum of OH production rates from the main OH sources that can be calculated from measurements. Shaded areas in the difference plots give the uncertainties of the calculations. Production of OH from the reaction of O_3 and HO_2 was negligible (< 0.01 ppbv h^{-1}) for conditions of the experiments.

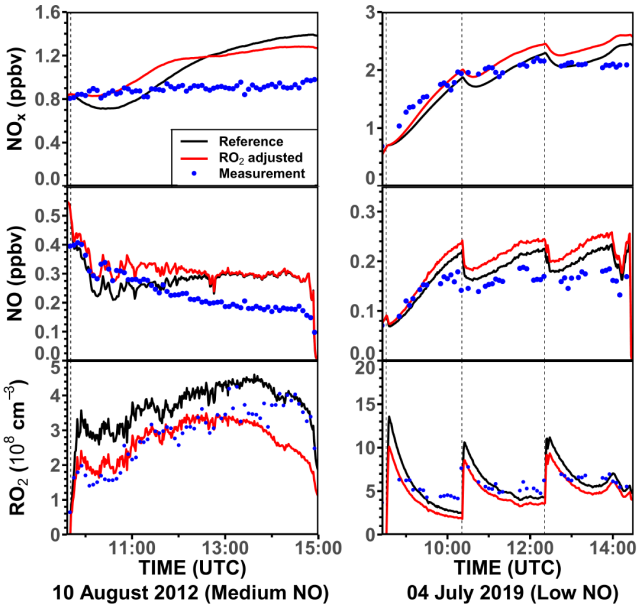

Figure S4-5. Example of the impact of modelled RO_2 on the modelled NO_x and NO concentrations in the experiments with medium NO (10 August 2012) and low NO (04 July 2019) concentrations similar to Fig. 4-19. In both cases, the organic nitrate yield for the first-generation RO_2 from the limonene+OH reaction is taken from the analysis in this work (34%).

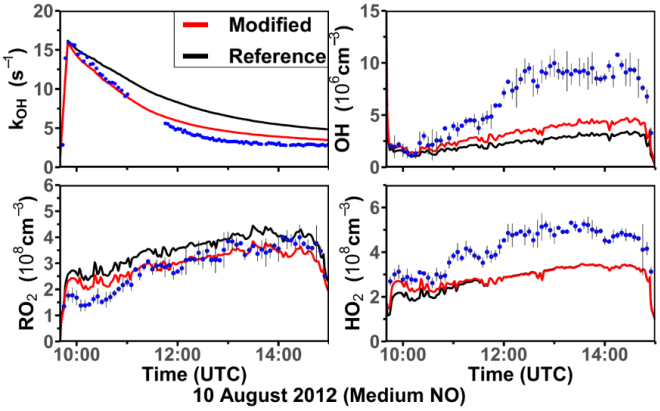

Figure S4-6. Comparison of the modelled OH reactivity k_{OH}, OH, HO_2, RO_2 radical concentrations in the photooxidation experiment with medium NO mixing ratio on 10 Aug 2012 using the MCM model (reference model) and the model with additional reaction pathways from Table 4-5 implemented (modified model).

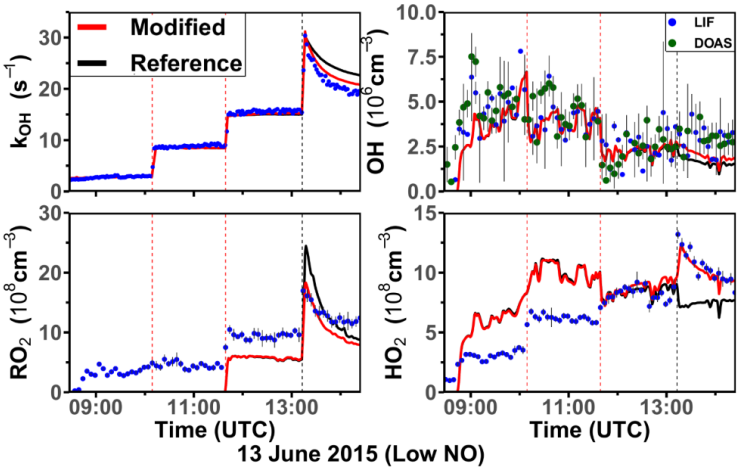

Figure S4-7. Comparison of the modelled OH reactivity k_{OH}, OH, HO_2, RO_2 radical concentrations in the photooxidation experiment with low NO mixing ratio on 13 June 2015 using the MCM model (reference model) and the model with additional reaction pathways from Table 4-5 implemented (modified model).

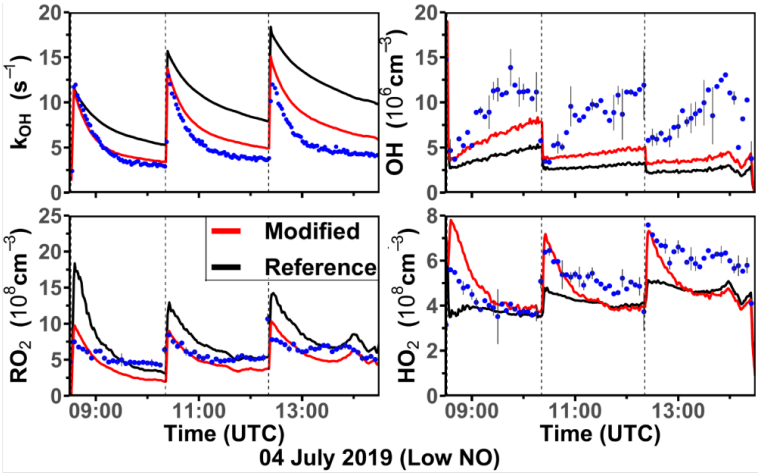

Figure S4-8. Comparison of the modelled OH reactivity k_{OH}, OH, HO_2, RO_2 radical concentrations in the photooxidation experiment with medium NO mixing ratio on 04 Jul 2019 using the MCM model (reference model) and the model with additional reaction pathways from Table 4-5 implemented (modified model).

Supplementary material for Section 6

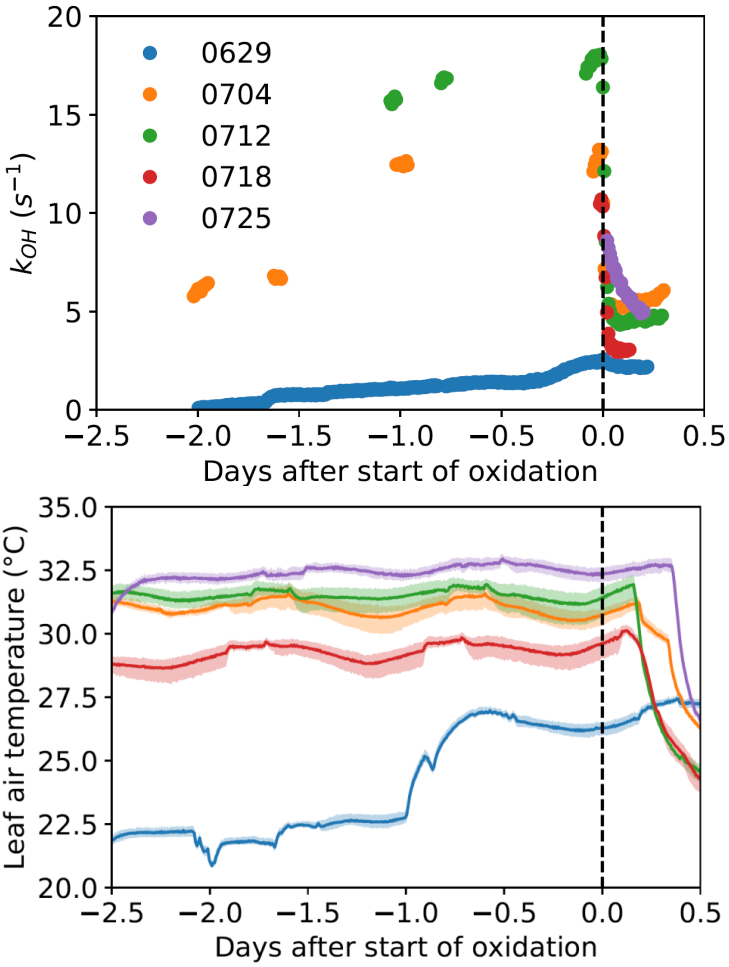

Figure S6-1. The OH reactivity in the SAPHIR chamber (top) and the leaf air temperature in the SAPHIR-PLUS chamber during the coupling phase of the experiment before the start of the oxidation of VOC in the SAPHIR chamber (bottom). The coloured areas of the leaf air temperature indicate the range of temperatures measured at four different plants. The colours indicate the day of the start of the VOC oxidation (Table 2.2). In the ambient air experiment on 29 June 2022, temperature of the SAPHIR-PLUS was raised one day before the start of the oxidation to induce more emissions of VOCs.

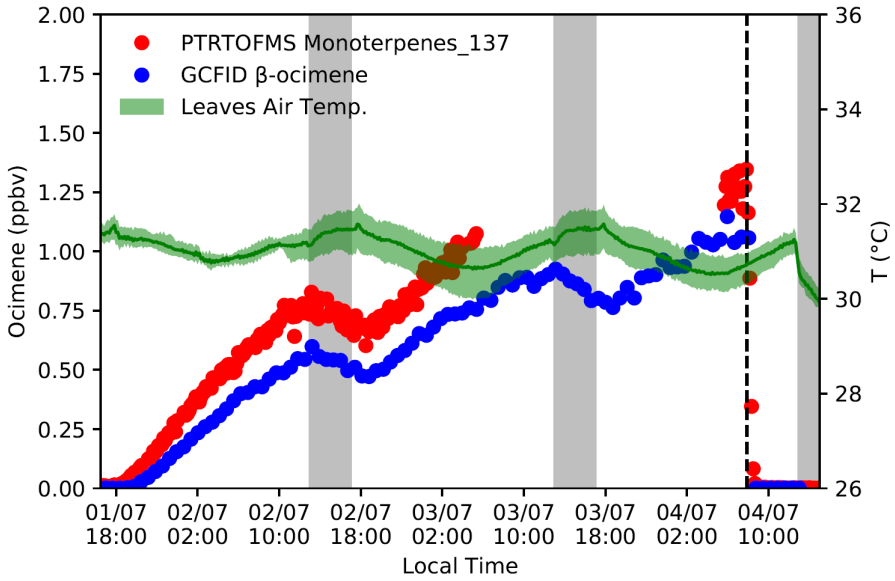

Figure S6-2. The mean leaf temperature measured in the SAPHIR-PLUS chamber and monoterpene concentrations measured by PTR-TOF-MS and β-ocimene concentrations measured by GC-FID in the SAPHIR chamber during the coupling phase between the SAPHIR-PLUS and the SAPHIR chambers for the experiment on 04 July 2022. The coloured areas of the leaf air temperature indicate the range of temperatures measured at four different plants. The grey shaded area indicates when the light in the SAPHIR-PLUS chamber was turned off. The dotted line indicates the decoupling of the two chambers followed by the start of the oxidation of VOCs.

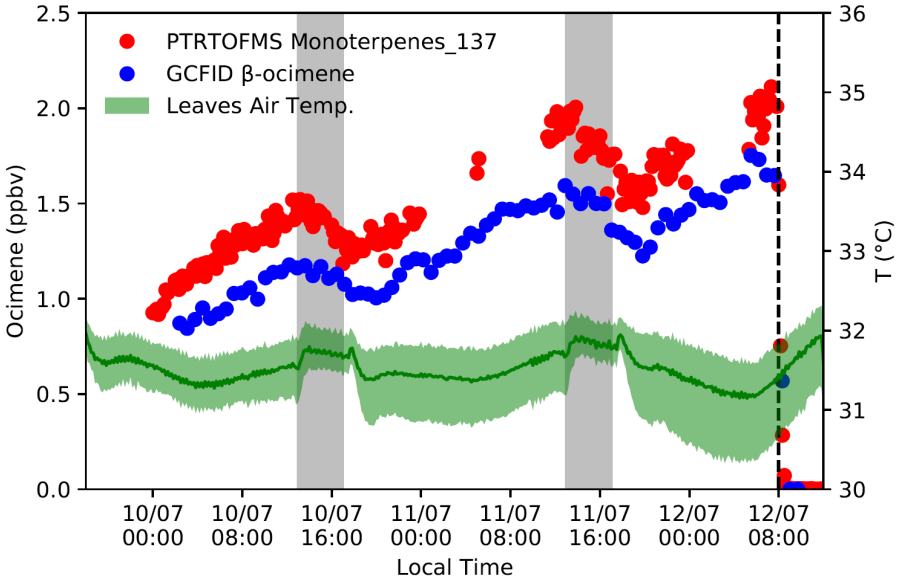

Figure S6-3. Same as Fig. S6-2 but for the experiment on 12 July 2022.

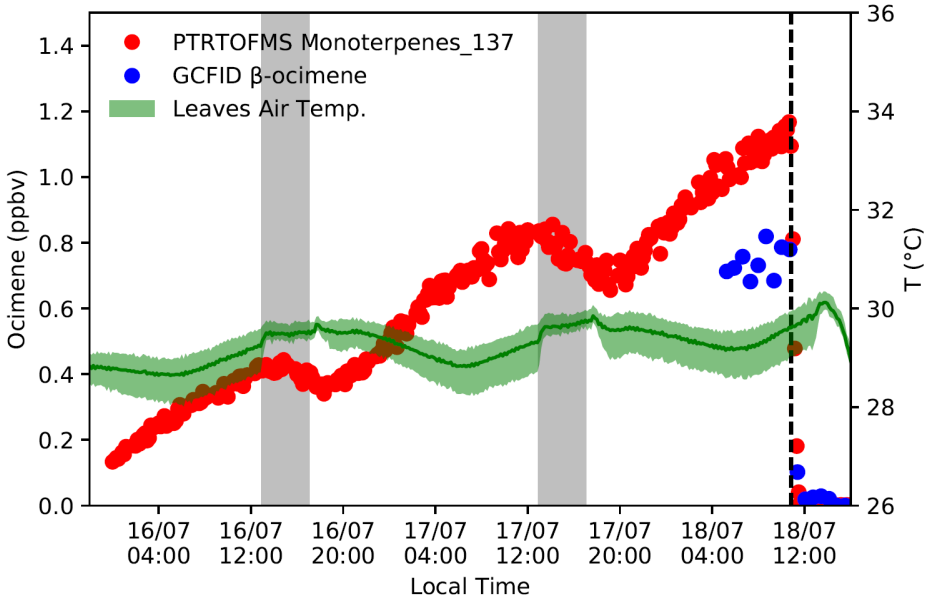

Figure S6-4. Same as Fig. S6-2 but for the experiment on 18 July 2022.

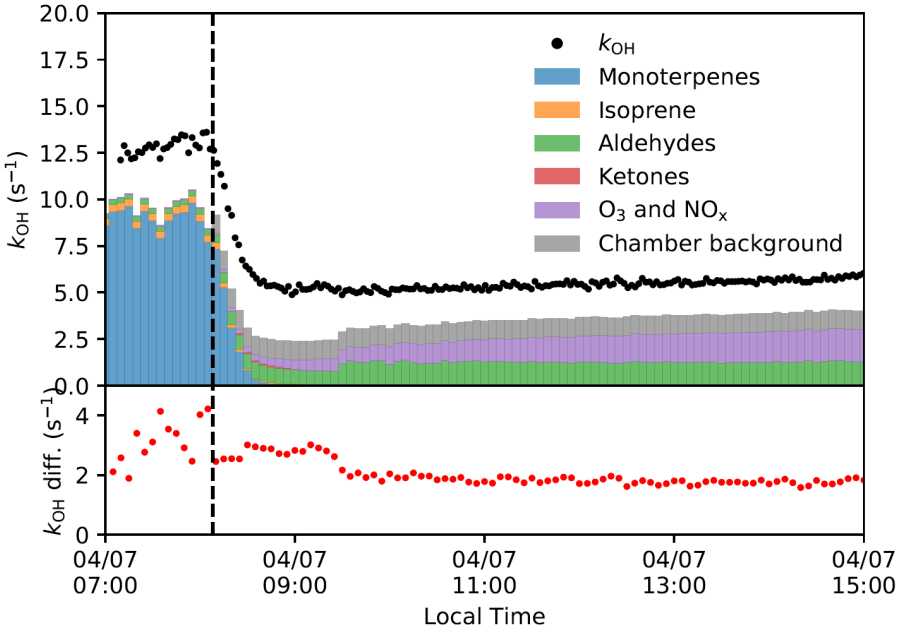

Figure S6-5. Comparison of the measured OH reactivity (black dots) and calculated OH reactivity using PTR-TOF-MS measurements of single reactants (top panel, and their differences (bottom panel) for the photooxidation experiment on 04 July 2022. The vertical dashed line indicates the time when the chamber roof was opened, which initiated the photooxidation of VOCs. The constant contribution from "chamber background" of 1 s^{-1} refers to the background OH reactivity expected to be present in the illuminated chamber. The value of 1 s^{-1} is taken from other VOC photooxidation experiments conducted within the time period of the plant emission experiments.

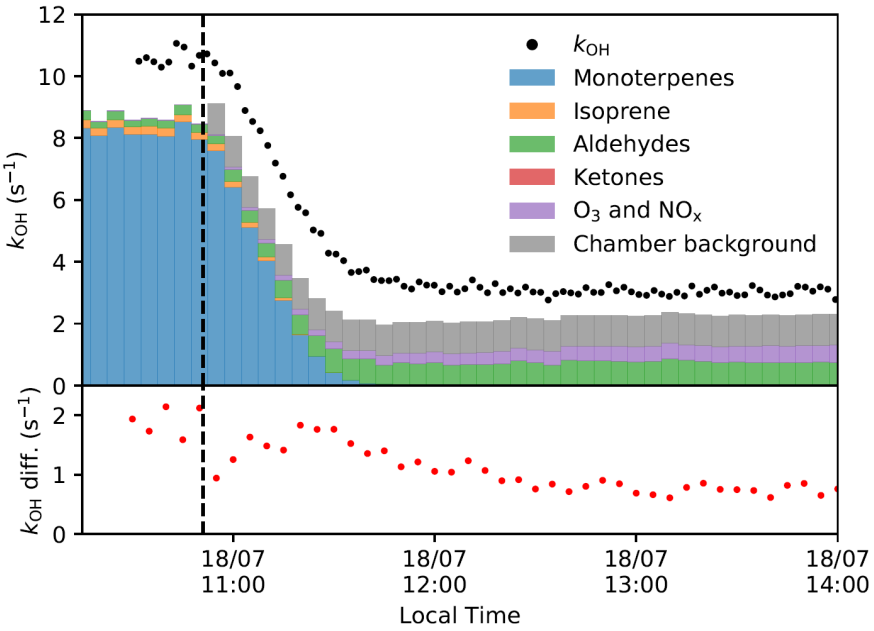

Figure S6-6. Same as Figure S6-5 but for the experiment on 18 July 2022.

Band / Volume 609
Mechanisches Verhalten von Polymer-Elektrolyt-Membran-Elektrolysezellen und -Stacks
S. Holtwerth (2023), x, 251 pp
ISBN: 978-3-95806-697-7

Band / Volume 610
Membrane Reactor Concepts for Power-to-Fuel Processes
H. Huang (2023), VI, 197 pp
ISBN: 978-3-95806-703-5

Band / Volume 611
Deployment of Fuel Cell Vehicles in Road Transport and the Expansion of the Hydrogen Refueling Station Network: 2023 Update
R. C. Samsun, M. Rex (2023), i, 39 pp
ISBN: 978-3-95806-704-2

Band / Volume 612
Behavior/performance of tungsten as a wall material for fusion reactors
M. Gago (2023), X, 120 pp
ISBN: 978-3-95806-707-3

Band / Volume 613
Strategieentwicklung zur Umsetzung der Klimaschutzziele im Verkehrssektor mit dem Fokus Kraftstoffe
M. Decker (2023), ix, 243 pp
ISBN: 978-3-95806-714-1

Band / Volume 614
Joining of tungsten and steel for the first wall of a future fusion reactor
V. Ganesh (2023), xxx, 142, a-v pp
ISBN: 978-3-95806-715-8

Band / Volume 615
Polluter group specific emission optimisation for regional air quality analyses using four-dimensional variational data assimilation
P. M. Backes (2023), xxi, 115 pp
ISBN: 978-3-95806-717-2

Band / Volume 616
Effect of organic soil amendments on increasing soil N retention and reducing N losses from agricultural soils
Z. Li (2023), XI, 134 pp
ISBN: 978-3-95806-721-9

Band / Volume 617
Radiolytic Stability of BTBP-, BTPhen- and DGA-based Ligands for the Selective Actinide Separation by Solvent Extraction
H. Schmidt (2023), ca. 200 pp
ISBN: 978-3-95806-723-3

Band / Volume 618
$Na_5YSi_4O_{12}$-type Na^+ superionic conductors for solid-state batteries
A. Yang (2023), X, 150 pp
ISBN: 978-3-95806-731-8

Band / Volume 619
Development of industry-scalable processes for nanocrystalline silicon oxide in silicon heterojunction solar cells
D. Qiu (2023), 202 pp
ISBN: 978-3-95806-734-9

Band / Volume 620
Photonic Sintering of Garnet-Based Solid-State Batteries
W. S. Scheld (2024), XII, 153 pp
ISBN: 978-3-95806-737-0

Band / Volume 621
Ceria-based composites for application in Oxygen transport membranes
L. Fischer (2024), xiii, 216 pp
ISBN: 978-3-95806-739-4

Band / Volume 622
Investigations of Air Quality Aspects with the Urban Climate Model PALM4U
R. Wegener, U. Javed, R. Dubus, and D. Klemp (2024), 93 pp
ISBN: 978-3-95806-741-7

Band / Volume 623
The Chemical Budget of Radicals and Reaction Mechanisms of the Atmospheric Oxidation of Monoterpenes Investigated in the Atmospheric Simulation Chamber SAPHIR
Y. S. Pang (2024), VI, 158 pp
ISBN: 978-3-95806-742-4

Weitere ***Schriften des Verlags im Forschungszentrum Jülich*** unter
http://wwwzb1.fz-juelich.de/verlagextern1/index.asp

Energie & Umwelt / Energy & Environment
Band / Volume 623
ISBN 978-3-95806-742-4

Mitglied der Helmholtz-Gemeinschaft

JÜLICH
Forschungszentrum